

AD-B186 649



Research Summary No. 36-8

for the period February 1, 1961 to April 1, 1961

*SN-32926
Res. Summary 36-8
Feds. - Apr. 1961*

DTIC
ELECTE
JUN 17 1994
S G D

COPY 5

DTIC QUALITY INFO

LIBRARY COPY

JUL 19 1961



JET PROPULSION LABORATORY
CALIFORNIA INSTITUTE OF TECHNOLOGY
PASADENA, CALIFORNIA

May 1, 1961

94-18021



118021

94 6 10 168

SN-32926

NATIONAL AERONAUTICS AND SPACE ADMINISTRATION
CONTRACT NO. NASw-6

Research Summary No. 36-8

for the period February 1, 1961 to April 1, 1961

Accession For	
NTIS CRA&I	<input type="checkbox"/>
DTIC TAB	<input checked="" type="checkbox"/>
Unannounced	<input type="checkbox"/>
Justification	
By	
Distribution /	
Availability Codes	
Dist	Avail and/or Special
12	

JET PROPULSION LABORATORY
CALIFORNIA INSTITUTE OF TECHNOLOGY
PASADENA, CALIFORNIA

May 1, 1961

Preface

The *Research Summary* is a report of supporting research and development activities at the Jet Propulsion Laboratory, California Institute of Technology. This bimonthly periodical is usually published in two volumes. However, for this issue, all the material has been combined into one volume. To foster a more rapid interchange of original ideas and information throughout the scientific and technical community, all authors' names have been added as bylines to the material they contributed.



W. H. Pickering, Director
Jet Propulsion Laboratory

Research Summary No. 36-8

Copyright © 1961
Jet Propulsion Laboratory
California Institute of Technology

Contents

SYSTEMS DIVISION

I. Systems Analysis	1
A. Trajectory Analysis by V. C. Clarke	1
B. Orbit Determination by D. L. Cain	2
C. Space Flight Studies by J. O. Maloy	4
D. Low-Thrust Trajectory Optimization by W. G. Melbourne	6
E. Powered Flight Studies by H. S. Gordon	7

GUIDANCE AND CONTROL DIVISION

II. Guidance and Control Research	11
A. Cryogenic Gyros by J. T. Harding	11
B. Gas-Supported Spinning Spheres by F. F. Batsch	13
C. Ferromagnetic Flux Reversal Mechanisms by F. B. Humphrey	15
D. Closed-Cycle Gas Supply System by H. D. McGinness	18

TELECOMMUNICATIONS DIVISION

III. Communications Elements Research	21
A. Low-Noise Amplifiers by T. Sato	21
B. Antennas for Space Communications by D. Schuster and C. T. Stelzried	22
C. Thin-Film Techniques by J. Maserjian and H. Erpenbach	31
IV. Communications Systems Research	35
A. Communications Research by W. V. Rusch, K. W. Linnes, S. Frankel, and A. J. Viterbi	35
B. Information Processing by N. Zierler	51
C. Digital Communications Techniques by M. F. Easterling, C. E. Gilchrist, and R. L. Choate	52
D. Venus Radar Experiment by M. H. Brockman, L. R. Malling, and H. R. Buchanan	65

PHYSICAL SCIENCES DIVISION

V. Chemistry Research	74
A. High-Resolution Nuclear Magnetic Resonance Spectroscopy by D. D. Elleman and S. L. Manatt	74
VI. Physics Research	80
A. Fission Electric Cells by W. F. Krieve	80
VII. Gas Dynamics Research	82
A. Stability of a Shear Layer in a Magnetic Field by J. Menkes	82
B. Similarity Solution for Stagnation Point Heat Transfer in Low-Density, High-Speed Flow by M. Chahine	82
C. Hot-Wire Anemometer in Hypersonic Flow by T. Vrebalovich	84

ENGINEERING MECHANICS DIVISION

VIII. Materials Research 86
 A. Graphite by W. V. Kotlensky and D. B. Fischbach 86
 B. Endothermal Materials by W. V. Kotlensky and R. G. Nagler . . . 91
 C. Behavior of Materials in Space by J. B. Rittenhouse 94
 D. Structural Materials by W. W. Gerberich 94
IX. Engineering Research 98
 A. Liquid Surface Shapes by H. E. Williams, Consultant 98
 B. Free-Fall Capsule to Study Weightless
 Liquid Behavior by E. A. Zeiner 99

ENGINEERING FACILITIES DIVISION

X. Wind Tunnel and Environmental Facilities 102
 A. 20-Inch Supersonic Wind Tunnel by G. Goranson 102
XI. Instrumentation 103
 A. Instrumentation Facilities by J. Z. Inskeep 103
 B. Instrument Performance Studies by J. Earnest 104

PROPULSION DIVISION

XII. Liquid Propellant Propulsion 108
 A. Combustion and Injection by G. I. Jaivin 108
 B. Heat Transfer and Fluid Mechanics by A. B. Witte 110
References 112

SYSTEMS DIVISION

I. Systems Analysis

A. Trajectory Analysis

V. C. Clarke

1. Interplanetary Trajectories

Minimum energy interplanetary trajectories are usually associated with the Hohmann transfer orbit. But, in reality, this type of orbit is rarely possible. In its place are two minimum-energy type trajectories, denoted Type I and Type II. Type I trajectories have heliocentric central angles^a less than 180 degrees, and Type II trajectories have heliocentric central angles greater than 180 degrees. The two types of minimum are a result of the fact that the orbits of the launch and target planets are not coplanar.

A computer study is in progress to determine the characteristics of ballistic interplanetary trajectories launched from Earth to Mars, to Venus, to Mercury, and to Jupiter. Thus far, trajectories have been obtained for each launch period (approximately 3 months about the minimum

energy dates) for Mars and Venus through 1971. In addition, trajectories have been computed for Mercury from October 1967 to January 1969.

Partial preliminary results of this study are given in Table 1, which lists pertinent parameters for the Type I and II minimum energy transfers. Several interesting characteristics of these trajectories may be noted. The first is the 8-year cyclic behavior of the Venus trajectories. The parameters for 1970 Venus trajectories are virtually the same as those for 1962. The reason for this is that approximately the same space-fixed geometry of Earth and Venus recurs every 8 years, or after five Cytherean synodic periods (1.5987 years). A similar cyclic behavior will occur for Mars trajectories every 15 years, or after seven Martian synodic periods (2.1353 years). A second interesting characteristic occurs for the Mercury trajectories. Here, based on coplanar theory it would be expected that transfers requiring approximately equal energy would be possible about every 4 months (or every synodic period of 115.88 days). However, as noted from Table 1, the energies required in April and July of 1968 are approximately twice those required in November of 1967 and 1968. The reason for this vast difference is two-fold; (1) Mercury is quite far out of the ecliptic, and (2) its orbit is closer to the Sun at arrival in April and July.

^aHeliocentric central angle is defined as the angle subtended at the Sun between the Sun-launch planet line at launch time and the Sun-target planet line at arrival time.

Table 1. Characteristics of minimum-energy transfer trajectories

Target planet	Trajectory type	Launch date	Flight time, days	Geocentric injection energy ^a , $10^8 \text{ m}^2/\text{sec}^2$	Heliocentric central angle, deg	Earth-planet distance at arrival, 10^8 km	Celestial latitude of planet at arrival, deg
Venus	I	8-23-62	114	0.087	132.4	58	1.46
	II	9-19-62	166	0.104	234.0	145	1.53
	I	3-30-64	112	0.123	126.8	61	-2.93
	II	4-9-64	170	0.081	225.4	137	-0.698
	I	11-12-65	108	0.132	129.5	60	3.31
	II	11-10-65	156	0.073	205.3	112	0.218
	I	6-11-67	142	0.065	175.6	92	-0.082
	II	5-30-67	156	0.059	190.4	94	0.110
	I	1-13-69	126	0.077	150.5	70	-0.393
	II	2-12-69	174	0.125	243.7	161	-2.59
	I	8-19-70	116	0.085	134.5	58	1.36
	II	9-16-70	166	0.106	233.6	145	1.71
Mars	I	10-30-62	232	0.151	158.2	246	1.06
	I	11-19-64	244	0.090	174.1	222	-0.047
	I	1-5-67	202	0.091	152.2	160	-0.833
	I	3-2-69	178	0.088	139.3	117	-1.75
Mercury	I	11-23-67	107	0.412	169.6	130	-0.163
	II	11-7-67	121	0.464	183.7	130	-0.163
	I	4-4-68	92	0.832	123.3	108	-6.98
	II	4-12-68	102	0.857	199.3	168	-0.849
	I	7-30-68	89	1.044	144.2	130	4.7
	II	7-30-68	109	0.820	244.6	197	4.25
	I	11-12-68	103	0.448	177.4	143	0.107
	II	11-2-68	113	0.441	187.4	143	0.107

^aActually, twice the total energy per unit mass, or vis viva integral.

It should be clear from these results and by comparison of the Mars and Venus minimum transfers of Table 1 to the Hohmann cases that coplanar theory can lead to gross inaccuracy except in rare special cases (one being the June trajectory to Venus in 1967).

It is planned to compute the Martian trajectories to 1977 to include the 15-year cycle. No computation of Type II Martian trajectories is planned because they are deemed impractical due to the long flight times and error sensitivity. The results of this study will be published in a JPL report in about 6 months. This report will include about 200 graphs of the more important trajectory parameters for Venus from 1962 to 1970 and for Mars from 1962 for 1977. This work should provide a comprehensive picture of these trajectories useful for preliminary analysis of ballistic interplanetary flight. Further, its usefulness will extend far beyond the periods covered because of the cyclic nature of the trajectories.

B. Orbit Determination

D. L. Cain

1. Shipboard Observation Errors

It has been demonstrated that coasting, or parking, orbits are useful in meeting the geometric constraints of lunar and interplanetary trajectories. This type of powered-flight trajectory, however, has the disadvantage that the location of the last stage of the vehicle powered flight may be dispersed over a wide area of the Earth.

For lunar and planetary flights launched from the Atlantic Missile Range, injection of the spacecraft can occur over large portions of the Indian and Atlantic Oceans, often out of sight of any land masses. It is desirable to track the vehicle in order to obtain acquisition information for

the Deep Space Instrumentation Facility (DSIF) and to get preliminary estimates of the orbit path for the orbit determination iterative procedure. This tracking can possibly be done by a ship at sea with tracking radars aboard. The feasibility of this procedure has undergone a preliminary study in order to determine the errors in predicted spacecraft position angles that result from uncertainties in a tracking ship's position at sea and other data errors.

The orbit considered in this study consisted of a typical lunar trajectory. To get the maximum propagation of errors in the orbit determination and prediction process, the ship was assumed to have observed the vehicle early in this orbit at injection, at Latitude 15.66°N and Longitude 36.42°W. The hypothetical orbit geometry was not particularly favorable, the ship obtaining the first data point at about 43 degrees elevation angle after the vehicle had passed overhead. Spacecraft range as well as azimuth and elevation angles were assumed to be available, a total of 10 observed time points (30 measured data) spaced at 20-second intervals.

The distance of the ship from the center of the Earth was assumed to be perfectly known, but the latitude and longitude were assumed to be contaminated with noise having an rms value of 0.017 degree (1 nm). Data noise was assumed to have the same variance for all times. All data were assumed uncorrelated, with no biases.

The orbit was determined from the observed data by the method of least-squares. The uncertainty in the data then was reflected as uncertainty in the orbital parameters. This uncertainty was then transformed, by a linear transformation, to the uncertainty in the predicted position where the probe would be seen by the South African Station (low on horizon). The results are plotted in Figures 1 and 2. The calculations presented were made assuming a range data error of 200 meters rms. A few calculations using a range error of 100 meters rms were made, showing no improvement of predicted angles. The position of the ship was one of the parameters to which the data was fitted. It is notable that the 1-nautical mile uncertainty in the position of the ship does not cause inordinate uncertainties in the predicted angles.

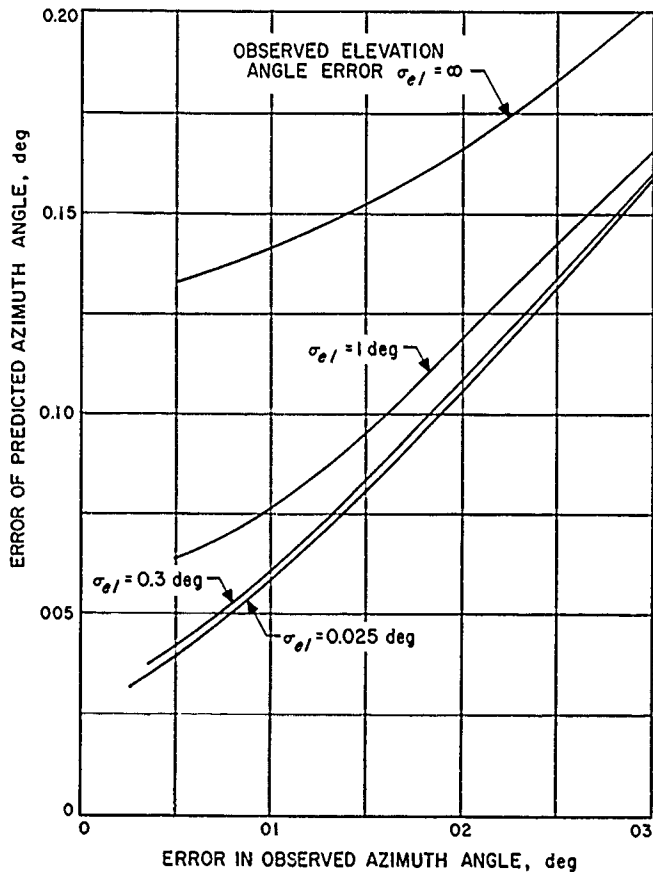


Figure 1. Error of predicted azimuth angle vs errors in observed azimuth and elevation angles

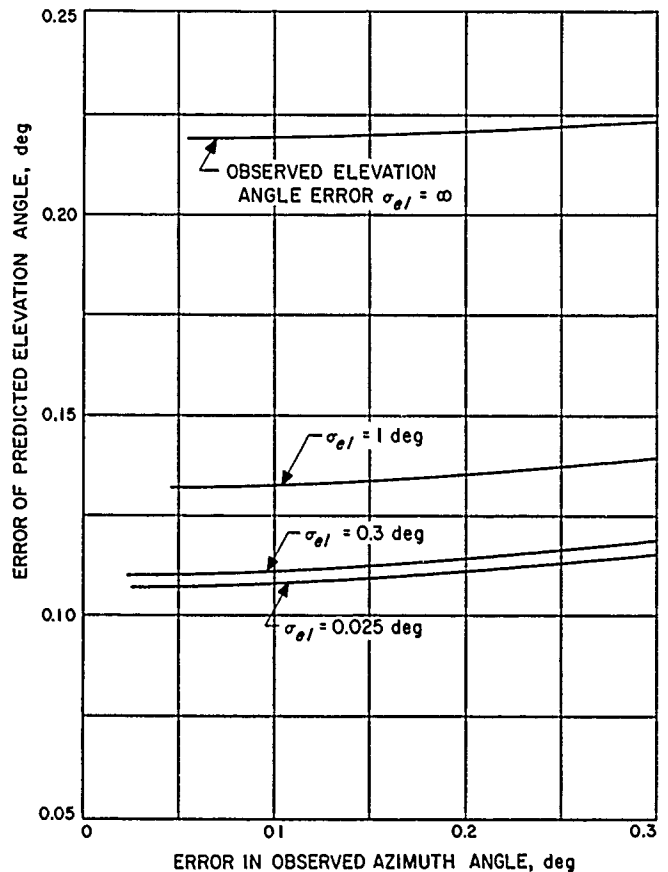


Figure 2. Error of predicted elevation angle vs errors in observed azimuth and elevation angles

C. Space Flight Studies

J. O. Maloy

1. Midcourse Guidance

Midcourse guidance of deep space probes will probably be effected by means of one or two brief applications of thrust applied with a small liquid-fueled rocket at a time when the spacecraft can receive commands from the Goldstone tracking station. The magnitude and direction of the impulse will be chosen so as to correct dispersions in the position of the spacecraft at a later time. For example, the lunar landing spacecraft will be guided so that if there were no landing maneuver, impact would occur at a specified selenographic latitude and longitude at an acceptable time. Planetary flyby spacecraft will be guided to reach the desired point of closest approach at the desired time.

Previous discussions of midcourse guidance have often assumed that the final velocity must be controlled as well as position; but it has been found that the correction of velocity dispersions is unnecessary for the space missions so far considered. In fact, the variations in final velocities which result from normal injection errors are too small to be measured accurately. According to the tracking analysis published earlier (RS 36-5, p 13), the standard deviation of the impact speed on a 66-hour lunar trajectory may be determined with an accuracy of about 17 meters/sec from the tracking data taken before the midcourse maneuver. The standard deviation in the impact speed resulting from injection errors is conservatively estimated at 18 meters/sec. On the other hand, it has been found that control of the time of flight will be mandatory if (1) tracking and scientific data are to be received, (2) if commands are to be sent, and (3) if the lunar landing or planetary flyby is to be observed without risking loss of communication during the final view period.

2. Computation of Differential Correction for Time of Flight

It is now well understood that the guidance analysis for both impact and flyby trajectories is facilitated by use of the impact parameter (the perpendicular distance from the center of the target body to the incoming asymptote) as a measure of the position dispersion normal to the line of motion.

The time to reach closest approach is a convenient generalized measure of the flight time, but one must proceed with care in computing the differential coeffi-

cients which give the sensitivity of the flight time to earlier perturbations in position or velocity. The attraction of the target body produces a variation of the time to closest approach on two trajectories which differ only in the magnitude of the impact parameter. The nature of the effect is shown in Figure 3. The trajectory with the larger value of the impact parameter B_1 requires a longer time to reach closest approach even if both trajectories cross the sphere at radius R at the same time.

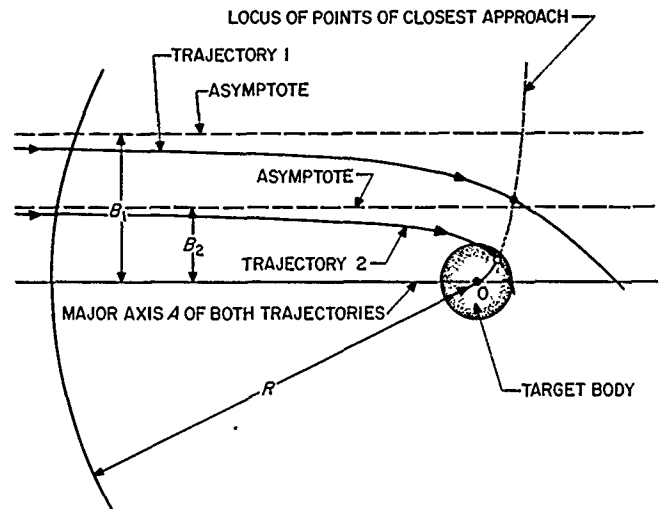


Figure 3. Near-target geometry showing varied trajectories

The dependence of the time of flight to closest approach upon the impact parameter B can easily be calculated if one neglects the influence of bodies other than the target, and treats the target-centered coordinates as an inertial system. If the distance R is much greater than the major axis A of the hyperbolic approach orbit, one obtains the following relation between the time of flight $T(A,B,R)$ from the distance R to closest approach, which displays the expected minimum for $B = 0$:

$$T(A,B,R) = \left(\frac{A^3}{\mu}\right)^{1/2} \left[\frac{R}{A} - \log \frac{2R}{A} + \delta + o\left(\frac{A}{R}\right) \right]$$

where μ is the gravitational constant of the target body, and

$$\sinh \delta = \frac{(B/A)^2}{2[1 + (B/A)^2]^{1/2}}$$

Note that $\sinh \delta$ (and, therefore, δ as well) has a minimum for $B = 0$. One can also write the last formula in terms of the eccentricity

$$e = [1 + (B/A)^2]^{1/2}$$

of the hyperbolic orbit; i.e.,

$$\sinh \delta = \frac{e^2 - 1}{2e}$$

If the differential coefficients for time of flight are derived by taking first differences of the closest approach times obtained by running perturbed trajectories using an integrating trajectory program (a common method), erroneous results may be obtained because of the strong nonlinear dependence of the time on the value of the impact parameter B . This dependence has no significance in performance calculations because the value of B will be controlled. Several methods of generating the required coefficients can be devised which avoid the nonlinear effect. One may, for example, run more than one perturbed trajectory to isolate the nonlinear effect. Another method is suggested by the formula above; one may linearize the time to closest approach by subtracting from it the B -dependent term

$$\Delta T = \left(\frac{A^3}{\mu} \right)^{1/2} \delta$$

before taking differences. The formula is evaluated using the elements of the target-centered osculating conic. Both of these methods are presently in use.

3. Extension of Error Analysis of Orbit Determination

The accuracies now being attained by the radio tracking system are high enough so that sources of error previously neglected must be considered; namely, the bias in angular and range rate measurements and also the uncertainties in physical constants.

The calibration of the DSIF antennas in hour angle and declination by star tracking is subject to a small residual error of about 0.005 degree, or 20 seconds of arc. The statistical error is only two or three times as large (RS 36-5, p 32). If a spacecraft were tracked by only one antenna, without simultaneous range-rate measurements, the entire uncertainty in hour angle would be propagated directly into the position of the orbit. Except for the small perturbations from the Sun, the Moon, and other bodies, there is no way to distinguish between a displacement of the station and the trajectory in hour angle, because the main forces on the spacecraft are independent of hour angle. If several stations track, only their relative calibration errors can be determined. If range-rate data is included, the effect is reduced, because only

the uncertainty in the station longitude (typically 1 to 3 seconds of arc) is relevant in the range-rate data. The amount of reduction obtained depends on the relative weights of the range rate and angle data in eliminating bias effects. This problem is being examined further.

It has been shown that the uncertainty in the Earth's gravitational radius (the geocentric quantity corresponding to the heliocentric astronomical unit), roughly 1 part in 10^5 , can produce deviations in the impact point of a lunar trajectory by as much as 150 km (Ref 1). Similarly, the impact time is uncertain by roughly 2 minutes. If the orbit determination process were equally sensitive to this effect, the lunar landing missions would be impossible using the present system design. Fortunately, the orbit determination is a curve fitting process; if enough late tracking data is obtained, the uncertainty in impact location can be reduced to a few kilometers and the uncertainty in impact time to a few seconds (Ref 2). Provided that the effect can be isolated, the tracking of a lunar spacecraft may furnish a strong determination of the absolute value of the Earth's gravitational constant. Further study of these questions is clearly necessary.

Besides the angular biases referred to earlier, the principal error in planetary tracking arises from the uncertainty in the astronomical unit of length; i.e., the mean distance of the Earth from the Sun. Although a number of measurements have been made, they disagree by quite unacceptable amounts, usually well outside the quoted probable errors. An excellent review of the problem has been given by Herrick, Westrom, and Makemson (Ref 3). If one takes the disagreement between the best astronomical determination of Rabe (Ref 4) and the 1959 radar measurements of Price, Green, et al (Ref 5) as a representative value of the uncertainty, one finds that the uncertainty in the closest approach distance is about 13,000 km at Venus and 40,000 km at Mars. It is hoped that the extensive efforts to refine the measurements being made by the JPL Telecommunications Division and by others will clarify matters. If the uncertainty in the astronomical unit could be reduced to 1 part in 10^4 , the residual uncertainty would at least be acceptable.

It is not yet clear how well one can determine the effects of tracking biases and systematic uncertainties from tracking planetary trajectories. If the effects can be detected, it may be possible to correct the trajectory by use of a late midcourse maneuver. In any event, it is clearly necessary to include these uncertainties in calculating the performance requirements for midcourse and approach guidance. Programs for performing these computations (which are exceedingly complex) are presently being designed.

D. Low-Thrust Trajectory Optimization

W. G. Melbourne

For the past year, the Laboratory has engaged in a study of the utilization of advanced propulsion systems in spacecraft. Consonant with this effort, mission feasibility studies and trajectory analyses with advanced propulsion vehicles are being conducted. Low-thrust trajectory optimization studies are being performed in order to assess the payload capabilities of power-limited advanced propulsion vehicles for the various interplanetary missions under consideration for the coming decade. This summary describes two types of optimum thrust programs which are currently being used in these studies.

The rocket equation for power-limited propulsion is

$$\frac{1}{m_1} = \frac{1}{m_0} + \int_0^{t_1} \frac{a^2}{2P} dt \quad (1)$$

where m_0 and m_1 are the vehicle masses at the beginning and end, respectively, of the flight, a is the thrust acceleration, and P is the power expended in the rocket exhaust. The exhaust power is determined by the power rating of the power plant carried by the vehicle and by the efficiency of conversion by the propulsion system. It is evident that m_1 is maximized by minimizing the above integral. The value of this integral depends upon the flight time, the mission involved (namely, the specification of the kinematic conditions of the vehicle initially, and, terminally), the force field in which the vehicle travels, the nature of the thrust program used to accomplish this mission and, finally, the engineering design of the propulsion system.

For the present mission feasibility studies, it is desirable to employ optimum thrust programs which exclude the complexity imposed by the engineering design but which bracket or isolate that class of trajectories and vehicle performances which an actual vehicle would be capable of achieving. Two such thrust programs which serve this purpose are obtained by satisfying the following criteria:

$$\int_0^{t_1} a^2 dt = \text{minimum, variable thrust vector}$$

and, alternately

$$\int_0^{t_1} a^2 dt = \text{minimum, thrust magnitude} = \text{constant or 0}$$

The former thrust program yields the absolute minimum that

$$\int_0^{t_1} a^2 dt$$

may have and gives rise to the so-called optimum thrust equations of power-limited flight (Refs 6, 7). Its justification stems from the fact that over a wide range of specific impulse the exhaust power is nearly constant, although this is generally not the case for low specific impulse. The second thrust program is constrained to constant-thrust or coast periods but minimizes

$$\int_0^{t_1} a^2 dt$$

over the propulsion periods by optimum programming of the thrust vector. The resulting value is always higher than the first case and, therefore, yields more conservative estimates of final vehicle weight. For a particular mission, then, the generation of a pair of trajectories and vehicle performances using these two thrust programs is extremely valuable in determining mission feasibility, payload capability, and trajectory design.

The present studies employ an inverse-square central force field model in two and three dimensions. The equations of motion of a vehicle in such a field may be written in vectorial form as

$$\ddot{\mathbf{r}} + \nabla V - \mathbf{a} = 0 \quad (2)$$

where \mathbf{r} is the position vector, and V is the potential in this force field. The minimization of

$$\int_0^{t_1} a^2 dt$$

may be accomplished by calculus-of-variations methods in which this integral is minimized subject to certain constraints, namely, the equations of motion, the thrust program constraints, and the initial and terminal kinematic conditions specified by the mission.

For the variable thrust program, it may be shown that the thrust acceleration equations which must be satisfied as necessary conditions for minimizing

$$\int_0^{t_1} a^2 dt$$

are

$$\ddot{\mathbf{a}} + (\mathbf{a} \cdot \nabla) \nabla V = 0 \quad (3)$$

These equations admit a first integral in scalar form which may be expressed as

$$\dot{\mathbf{a}} \cdot \dot{\mathbf{r}} - \frac{1}{2} a^2 + \mathbf{a} \cdot \nabla V = \text{constant} \quad (4)$$

For the constant thrust program, the analogous expressions are

$$\ddot{\lambda} + (\lambda \cdot \nabla) \nabla V = 0 \quad (5)$$

$$\dot{\lambda} \cdot \dot{\mathbf{r}} - \lambda \cdot (\mathbf{a} - \nabla V) + a(\lambda - \alpha_m L) = \text{constant} \quad (6)$$

$$\mathbf{a} = \frac{a}{\lambda} \lambda \quad (7)$$

$$a = a_0 \frac{\alpha_p}{\alpha_m} \quad (8)$$

where $\lambda(t)$ is an auxiliary variable, $\alpha_m(t)$ is a normalized variable proportional to the instantaneous vehicle mass, and α_p is a switching parameter with the value 1 during propulsion periods and 0 during coasting periods. The function $L(t)$ generated by the equation

$$\dot{L} = \frac{\dot{\lambda}}{\alpha_m} \quad (9)$$

determines the periods of propulsion and coast by conditions

$$\begin{aligned} L > 0, \alpha_p &= 1 \\ L < 0, \alpha_p &= 0 \end{aligned} \quad (10)$$

For a particular mission, any initial acceleration above some minimal value yields an optimum trajectory satisfying the end conditions. These trajectories possess different coast periods and values of

$$\int_0^{t_1} a^2 dt$$

It is convenient to define an additional function $R(t)$, in order to isolate the optimum initial acceleration. This function is generated by the equation

$$\dot{R} = \alpha_p \left(2L - \frac{\lambda}{\alpha_m} \right) \quad R(0) = 0 \quad (11)$$

and must be zero at t_1 as a necessary condition for optimum initial acceleration.

Both of these sets of equations along with Equation (2) have been programmed for numerical solution on an IBM 7090 computer. Equations (4) and (6) are used to check the accuracy of the numerical integrations. To overcome the two-point boundary value problem associated with this type of equations, an iterative routine designed to efficiently carry out parametric analyses has

been developed. This routine has been remarkably successful in the large-scale production of interplanetary flyby and rendezvous trajectories to nearly all the planets with flight times ranging from 30 days to 3 years. Numerical studies with the variable thrust program have been reported elsewhere (Ref 7). Studies with the constant thrust program are in progress and will be reported in a later publication.

E. Powered Flight Studies

H. S. Gordon

1. A Study of Guidance System Errors

In *Research Summary 36-6*, an analytic technique was described for determining injection errors that arise from guidance system inaccuracy. The particular guidance system to be studied was described, and several error terms were derived. The analysis assumed that all nonstandard conditions sensed by the guidance system are adequately compensated, so that the only errors remaining are those due to guidance system component inaccuracy (Table 2).

Table 2. Component 1σ errors, assuming gaussian distribution

k	Description	σ_1
1	A-accelerometer scale factor error	5×10^{-4}
2	B-accelerometer scale factor error	5×10^{-4}
3	A-accelerometer null shift error	$4 \times 10^{-2} \text{ m/sec}^2$
4	B-accelerometer null shift error	$4 \times 10^{-2} \text{ m/sec}^2$
5	C-accelerometer null shift error	$4 \times 10^{-2} \text{ m/sec}^2$
6	A-accelerometer alignment error	0°
7	B-accelerometer alignment error	$4 \times 10^{-4} \text{ rad}$
8	C-accelerometer alignment error	$4 \times 10^{-4} \text{ rad}$
9	Gyro 1 initial offset	$5 \times 10^{-4} \text{ rad}$
10	Gyro 2 initial offset	$5 \times 10^{-4} \text{ rad}$
11	Gyro 3 initial offset	$5 \times 10^{-4} \text{ rad}$
12	Gyro 1 random drift	$3 \times 10^{-6} \text{ rad/sec}$
13	Gyro 2 random drift	$3 \times 10^{-6} \text{ rad/sec}$
14	Gyro 3 random drift	$3 \times 10^{-6} \text{ rad/sec}$
15	Gyro 1 g-sensitive drift	$5 \times 10^{-7} \text{ rad-sec/m}$
16	Gyro 2 g-sensitive drift	$5 \times 10^{-7} \text{ rad-sec/m}$
17	Gyro 3 g-sensitive drift	$5 \times 10^{-7} \text{ rad-sec/m}$
18	Clock error	0^b

^aNote that σ_6 is taken to be zero as it is considered that the A-accelerometer alignment defines a reference direction for all other alignments; the other values of alignment accuracy are considered to be valid estimates of present techniques.

^bPessimistic estimates give negligible errors

This technique has been used to determine uncorrected rms target errors σ_m for several representative lunar and interplanetary missions (Table 3). Here, σ_m is defined as the rms value of the magnitude of the impact parameter, which is the distance from the center of the target to the incoming asymptote (Refs 8, 9). The flow chart of computations performed to get the end result is shown in Figure 4; Figure 5 describes the coordinate system used. Results of the study are given in Tables 3 and 4 and in Figures 6 to 9. The component errors assumed (Table 2) were taken from the open literature (Refs 10 to 13). They represent reasonable values, but do not reflect the performance of any specific system. Thus, the results

published here are to be interpreted as giving only an order-of-magnitude indication of rms target error.

To calculate the rms target error, the six-dimensional joint distribution of normally distributed injection errors is calculated from the assumed statistical knowledge of the guidance system components. This distribution is described by a covariance matrix of injection deviations Λ' ; Λ' is then transformed by appropriate transforma-

Table 3. Trajectory description and uncorrected 1σ target error due to injection errors

Trajectory Nos.	Trajectory type	Flight time	Parking orbit interval, sec	σ_m , km
1	Slow lunar	90 hr	659.976	15,650
2	Nominal lunar	66 hr	721.648	6,380
3	Fast lunar	42 hr	859.978	2,530
4	Slow Venus	118 days	784.3957	346,900
5	Fast Venus	88 days	768.8225	212,100
6	Slow Mars	235 days	1,575.6735	454,800
7	Fast Mars	216 days	1,548.0000	351,300

Table 4. Statistics of injection errors for Trajectory 1 of Table 3

Standard deviations ^a	Cross correlation coefficients ^a
$\sigma_x = 16.000$ km	$\rho_{rr} = -0.86676$
$\sigma_r = 10.942$ km	$\rho_{rc} = 0.98355$
$\sigma_c = 14.443$ m/sec	$\rho_{x\Gamma} = -0.74795$
$\sigma_{\Gamma} = 0.0020501$ rad	$\rho_{rc} = -0.91866$
$\sigma_z = 10.268$ km	$\rho_{r\Gamma} = 0.95163$
$\sigma_{\dot{z}} = 18.255$ m/sec	$\rho_{c\Gamma} = -0.81131$
	$\rho_{z\dot{z}} = 0.40330$
	$\rho_{zz} = \rho_{\dot{z}\dot{z}} =$
	$\rho_{rz} = \rho_{r\dot{z}} =$
	$\rho_{cz} = \rho_{c\dot{z}} =$
	$\rho_{rz} = \rho_{r\dot{z}} = 0$

^aThis data is representative of the seven trajectories studied.

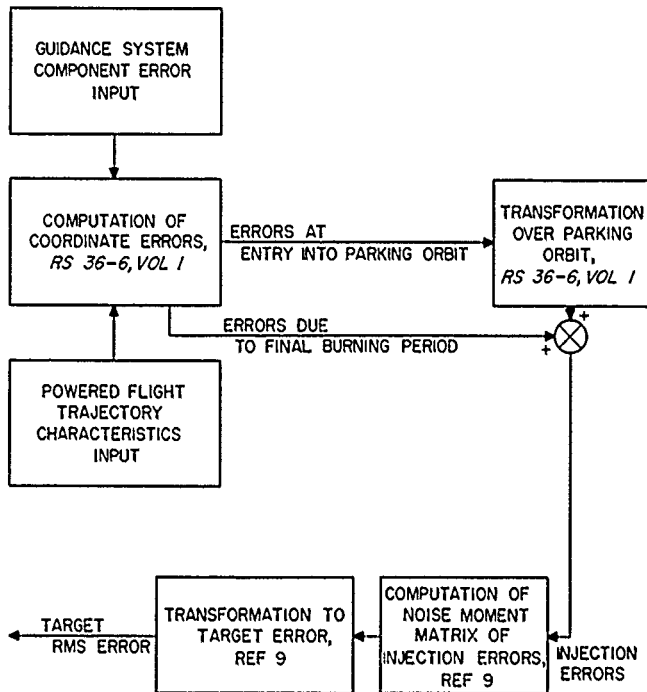


Figure 4. Computation of target miss distances resulting from component errors

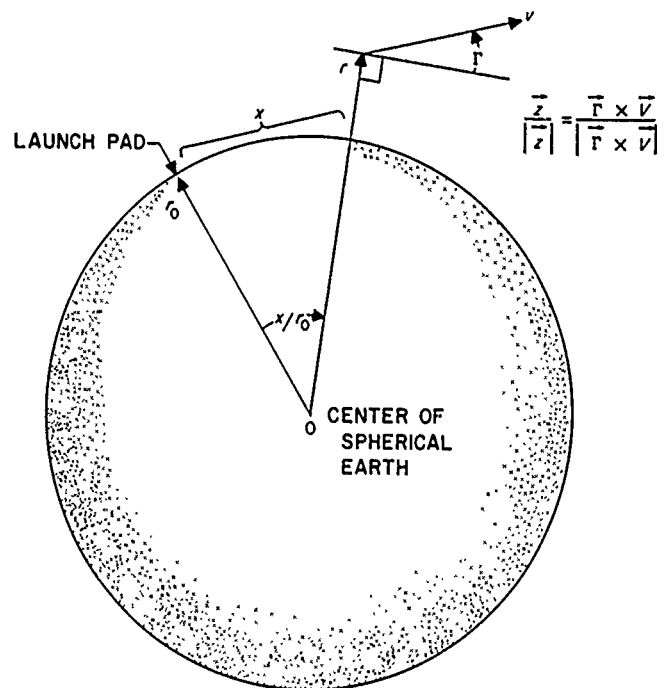


Figure 5. Coordinate system used in parking orbit error study

tions, which are functions of the standard trajectory, to the covariance matrix of target miss components Λ^M (Ref 9).

One result of the study was to evaluate the effect of parking orbit interval on guidance errors. Launching from a given location at a certain time defines a specific trajectory geometry, which requires a definite coast arc in the parking orbit. A launch delay changes the geometry and requires a change in the coast arc to inject

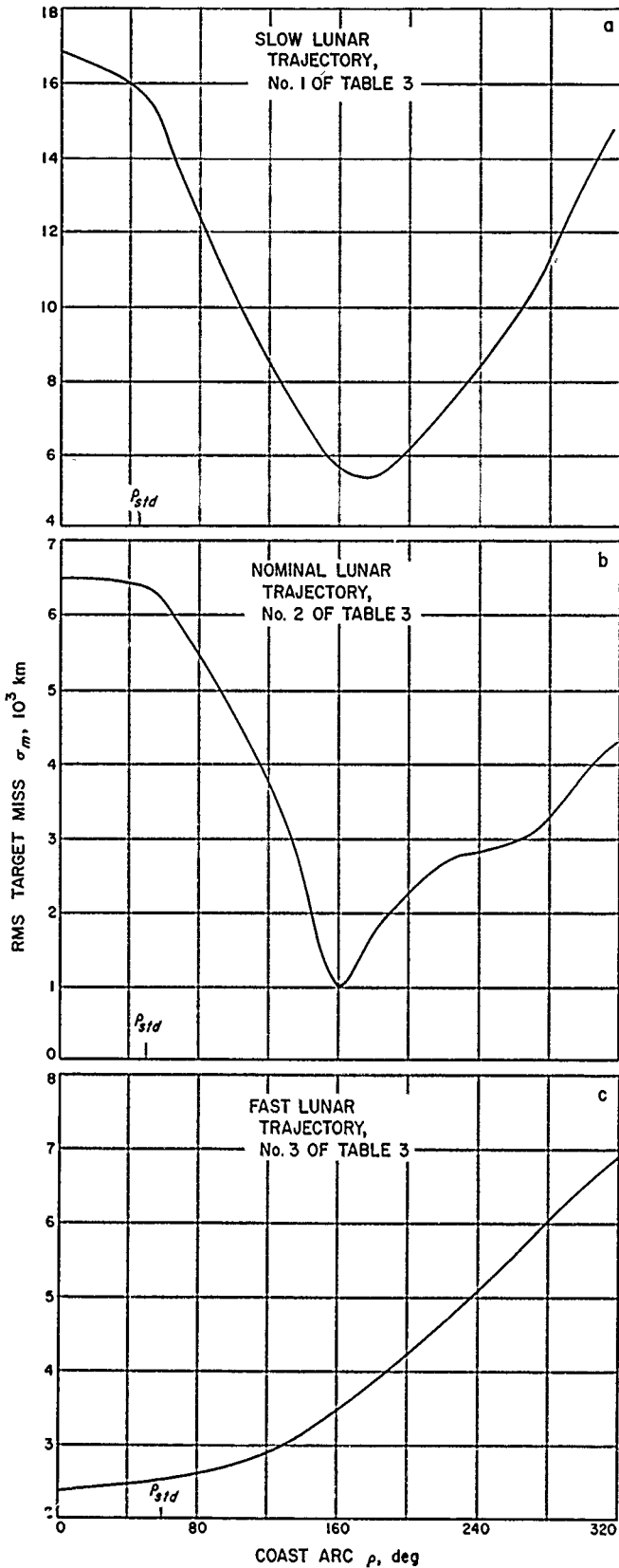


Figure 6. Moon miss distances vs coasting arc

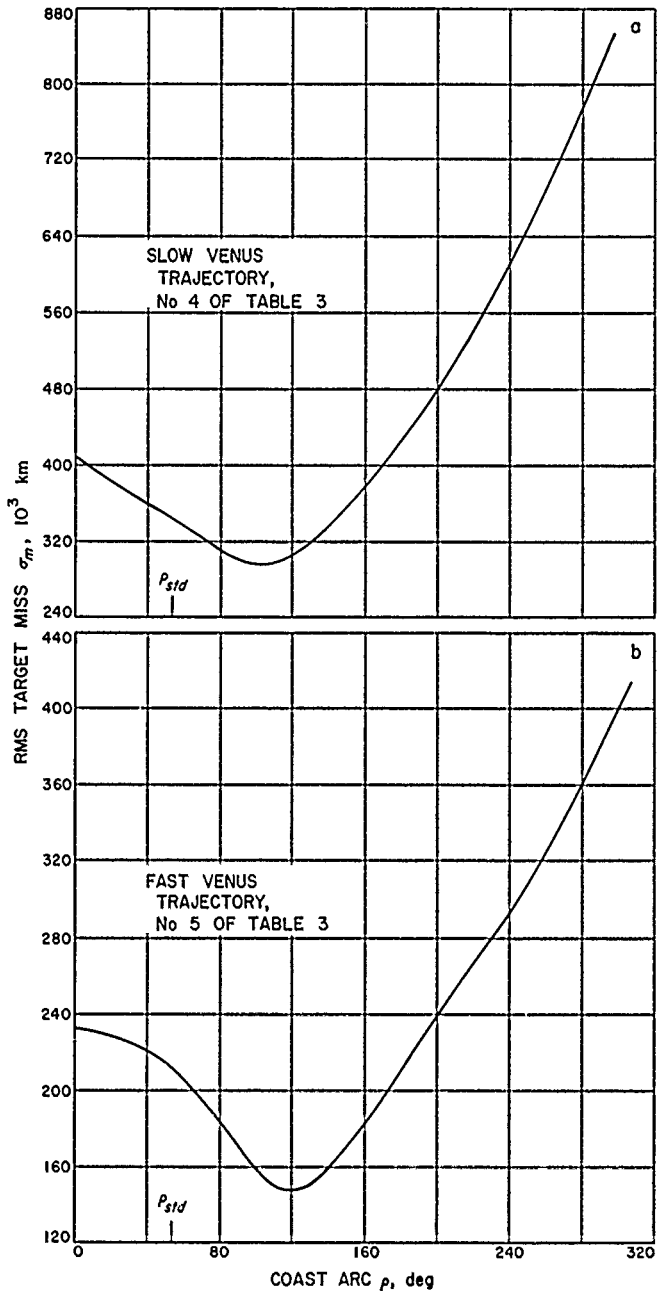


Figure 7. Venus miss distances vs coasting arc

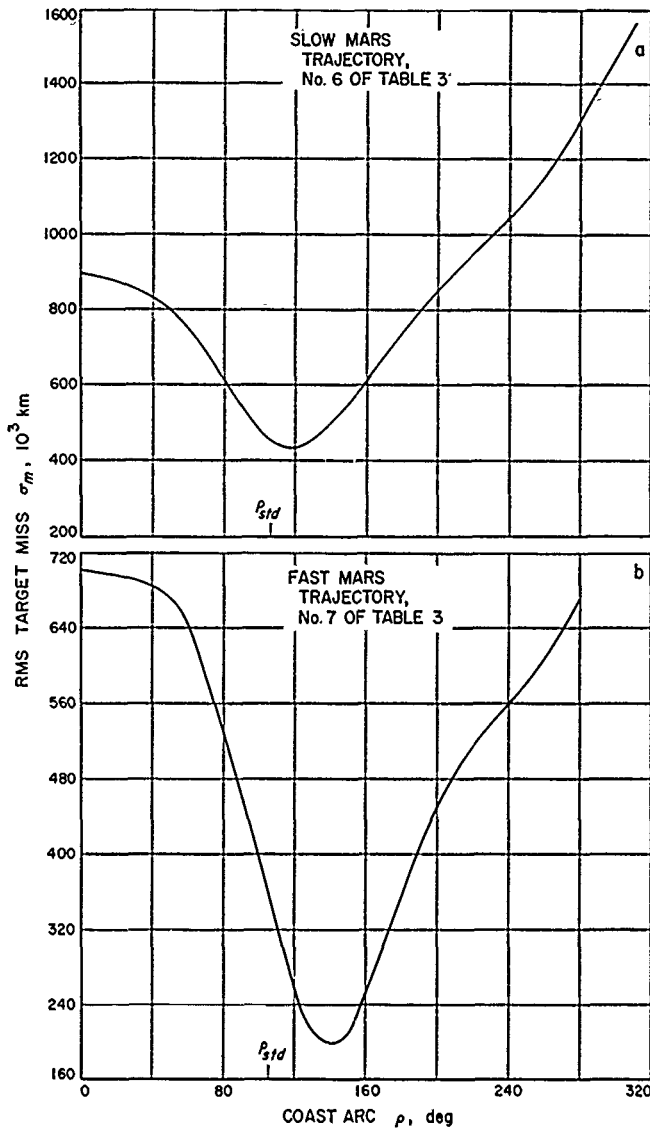


Figure 8. Mars miss distances vs coasting arc

properly. Figures 6 to 8 present the rms values of target error σ_m vs coast arc, showing that a change in this quan-

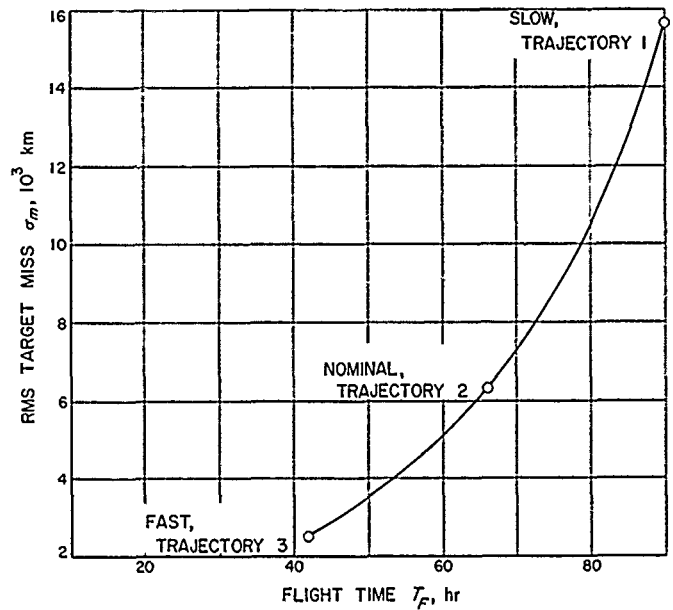


Figure 9. Moon miss distances vs flight time

tity affects guidance accuracy. It is clear that there is an optimum value of the coast arc. This is because correlations between coordinate deviations change as a function of the parking orbit interval, and certain errors may cancel each other.

Figure 9 presents the rms values of target error vs flight time for the three lunar trajectories. These trajectories impact at roughly the same time, thus having similar geometrical properties. It is seen that the faster trajectories tend to have smaller target error. A similar conclusion would be reached for the interplanetary cases.

This does not mean that a larger midcourse maneuver would necessarily be required on the slower trajectories, for the higher error sensitivities mean that less correction is required for a given error.

GUIDANCE AND CONTROL DIVISION

II. Guidance and Control Research

A. Cryogenic Gyros

J. T. Harding

1. Restoring Forces on Spherical Gyro Rotor

In order to determine the oscillation frequency of a magnetically supported superconducting sphere, the restoring force for small displacements from equilibrium has been calculated for the special case of an axially symmetric support field.

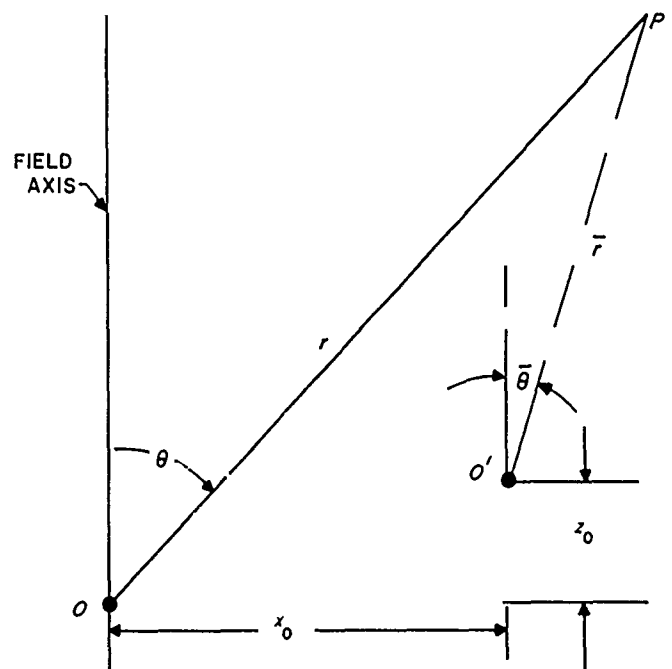
The applied support field B_a is first expressed as the gradient of a scalar potential which is expanded in Legendre polynomials. The origin O is the equilibrium position of the ball,

$$B_a = -\nabla \sum_{n=0}^{\infty} b_n r^n P_n(\cos \theta) \quad (1)$$

where $\theta = 0$ is the symmetry axis of the applied field.

The normal component of the magnetic field must vanish at the surface of a superconductor. In order to determine the induced field required to satisfy this boundary condition, it is desirable to express both the applied and

induced fields in spherical coordinates with origin O at the center of the superconducting sphere, as shown in the sketch:



The induced field B_I must have the form

$$B_I = -\nabla \sum_{n=0}^{\infty} \sum_{m=0}^n \frac{a_{nm}}{r^{n+1}} P_n^m(\cos \bar{\theta}) \cos m\bar{\phi} \quad (2)$$

B_A is transformed into barred coordinates by a Taylor series in powers of x_0, z_0 , the displacements from equilibrium. If terms higher than linear are neglected,

$$B_A(\bar{r}, \bar{\theta}) = -\nabla \sum_{n=0}^{\infty} b_n [\bar{r}^n P_n(\cos \bar{\theta}) + z_0 n \bar{r}^{n-1} P_{n-1}(\cos \bar{\theta}) - x_0 \bar{r}^{n-1} P_{n-1}^1(\cos \bar{\theta}) \cos \bar{\phi} + \dots]$$

The net field $B = B_A + B_I$, which satisfies the boundary condition, is

$$B_A(R, \bar{\theta}) = -\frac{2n+1}{n+1} R^{n-1} \sum_{n=0}^{\infty} \left[b_n \frac{dP_n}{d\bar{\theta}} + z_0(n+1) b_{n+1} \frac{dP_{n+1}}{d\bar{\theta}} - x_0 b_{n+1} \frac{dP_{n+1}^1}{d\bar{\theta}} \cos \bar{\phi} \right] \bar{\theta} + \frac{1}{\sin \bar{\theta}} [x_0 b_{n+1} P_n^1 \sin \bar{\phi}] \bar{\phi}$$

To compute the force exerted on the sphere by this field, the Maxwell stress tensor is integrated over the surface.

$$F = \oint \frac{1}{\mu_0} (BB - \frac{1}{2}B^2) \cdot dS = -\frac{1}{2\mu_0} \oint B^2 dS$$

since $B \cdot r = 0$.

Axial component of force:

$$F_z = -\frac{1}{2\mu_0} \iint B^2 \cos \bar{\theta} R^2 d \cos \bar{\theta} d\bar{\phi} \\ = -\frac{4\pi}{\mu_0} \sum_{n=0}^{\infty} b_n [nR^{2n+1} b_{n+1} + z_0 n(n+2) R^{2n+1} b_{n+2} + z_0(n-1) nR^{2n-1} b_n]$$

Radial component of force:

$$F_r = -\frac{1}{2\mu_0} \iint B^2 \sin \bar{\theta} \cos \bar{\phi} R^2 d \cos \bar{\theta} d\bar{\phi} \\ = -\frac{2\pi x_0}{\mu_0} \sum_{n=0}^{\infty} b_n [-n(n+2) R^{2n+1} b_{n+2} + (n-1)^2 R^{2n-1} b_n]$$

where terms quadratic in x_0, z_0 have been neglected.

Example. If $b_n = 0$ for $n > 2$

$$F_z = -\frac{4\pi}{\mu_0} [R^3 b_1 b_2 + 2z_0 R^3 b_2^2] \\ F_r = -\frac{2\pi x_0}{\mu_0} R^3 b_2^2$$

The restoring force constants are

$$k_z = \frac{8\pi}{\mu_0} R^3 b_2^2 = 4k_r$$

2. Damping of a Cryogenic Gyro

A proposed cryogenic gyro consists of a superconducting sphere supported by currents in superconducting coils (RS 36-5). Such a system is lossless so that, once set in motion, the sphere will bounce almost endlessly, limited only by radiation. To provide damping, the sphere may be surrounded by a lossy shield. The ac magnetic field induced by the motion of the sphere in the support field will generate eddy currents in the resistive shield, which will dampen the oscillation. The magnitude of this effect has been calculated for the case of a thin spherical shell when the oscillation is along the axis of an axially symmetric support field. The calculation consists of the following steps:

- (1) Expressing the applied field B_A as the gradient of a scalar potential which is expanded in Legendre polynomials; the origin O is at the center of the resistive shell, which is assumed to be the equilibrium position of the ball;

$$B_A = -\nabla \sum_{n=0}^{\infty} b_n r^n P_n(\cos \theta) \quad (1)$$

where $\theta = 0$ is the symmetry axis of the applied field.

- (2) Transforming B_A to coordinates fixed with respect to the oscillating sphere.
- (3) Determining the induced field produced by the sphere to satisfy the boundary condition for a superconductor:

$$B_{normal} = 0$$

- (4) Calculating the power dissipated due to eddy currents induced in the resistive shell by the time-varying field determined in (3); this is done by employing a formula developed by Smythe for the dissipation rate in a thin spherical resistive shell due to a sinusoidally time-varying magnetic field (Ref 14).

The damping has been worked out in detail for the following special cases: (1) The spherical rotor is oscillating sinusoidally with a small amplitude c_0 at its resonant frequency. (2) The applied field involves only b_1 and b_2 , all other coefficients being zero. (3) Values of b_1 and b_2 are determined by the two conditions that the magnetic

pressure at equilibrium position will support the mass of the ball against gravity, and the torque due to oblateness is made to vanish (Ref 15).

Under these assumptions, the fraction of the total energy lost per period of oscillation is

$$\frac{dE}{E} = \frac{\pi s}{\mu R_0 \omega \tau} \left[\frac{6 \left(\frac{R_1}{R_0}\right)^3}{1 + \left(\frac{3s}{\mu R_0 \omega}\right)^2} + \frac{250 \left(\frac{R_1}{R_0}\right)^5}{1 + \left(\frac{5s}{\mu R_0 \omega}\right)^2} + \frac{112 \left(\frac{R_1}{R_0}\right)^7}{1 + \left(\frac{7s}{\mu R_0 \omega}\right)^2} \right] \quad (2)$$

where R_1 is the radius of the rotor, R_0 the radius of the shield, and s the surface resistivity of the shell. The value of s which permits maximum power dissipation may be found by determining the value of $s/\mu R_0 \omega$ that maximizes Equation (2). As an approximation, $3s/\mu R_0 \omega$ is set equal to 1. Then

$$\frac{dE}{E} = \pi \left[\left(\frac{R_1}{R_0}\right)^3 + \frac{125}{119} \left(\frac{R_1}{R_0}\right)^5 + \frac{56}{29} \left(\frac{R_1}{R_0}\right)^7 \right] > \pi \left(\frac{R_1}{R_0}\right)^3 > 1$$

which represents an overdamped condition.

Since an eddy current shield of appropriate resistivity is capable of overdamping the transient oscillations of a magnetically supported superconducting sphere, it is a practical method for eliminating such oscillations.

B. Gas-Supported Spinning Spheres

F. F. Batsch

A sphere supported and lubricated by a gas or vapor is of considerable interest in the field of guidance and control of space vehicles. It can be used, for instance, for the transfer of momentum in a system for the control of the attitude or as an inertial reference in a gyroscope.

In order to study some of the design parameters of a rotatable gas-supported sphere and to verify the results of the previous analytical treatment, published in RS 36-3 and 36-4, a preliminary test model has been constructed (Figs 10, 11) and is now in process of being tested.

A 2-inch diameter solid steel (440C stainless) ball weighing 1.19 pounds was used in this test model. The

ball is supported by six equally spaced gas bearing pads. Although a sphere may be completely supported by a minimum of four pads, a six-pad system was selected in order to accommodate three pairs of orthogonally placed electromagnetic driving coils. Each of the pads is 0.75 inch in diameter, with a recess 0.375 inch in diameter and 0.001 inch deep. In order to reduce the aerodynamic drag of the sphere in the vicinity of the pressure pads, they were lapped to an internal spherical radius of 0.003 inch greater than the radius of the ball and located so that the centers of the spherical radii were coincident.

The case holding the pads was made from 303 stainless steel in the form of a cube accurately machined on all six faces so that further adjustment would not be necessary (Figs 10 and 11).

The driving coils are wound in such a manner that each coil slips snugly around a pad and is contiguous to the adjacent coils. Each pair of diametrically opposed coils is connected electrically, resulting in three pairs of coils located on the three orthogonal axes. This arrangement will provide a means for spinning the sphere about any axis chosen. The electrical details will be described in a subsequent report.

In order to protect the ball and bearing pads during transport and when the ball is not floating, a simple caging system was incorporated. A manually operated cam raises a nylon pad which, in turn, raises the sphere to its concentric position. An opposing pad is then screwed down until the sphere is firmly clamped between the two nylon pads.

As can be seen in Figure 11a, the case is supported on one corner of the cube. This corner and the opposing one

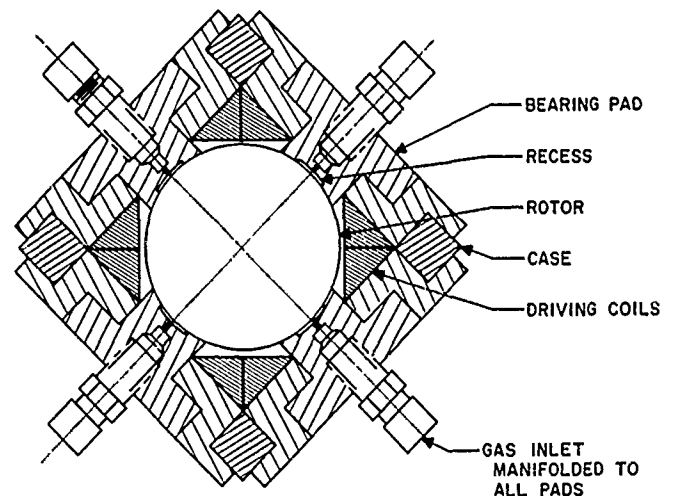


Figure 10. Section drawing of six-pad spinning sphere

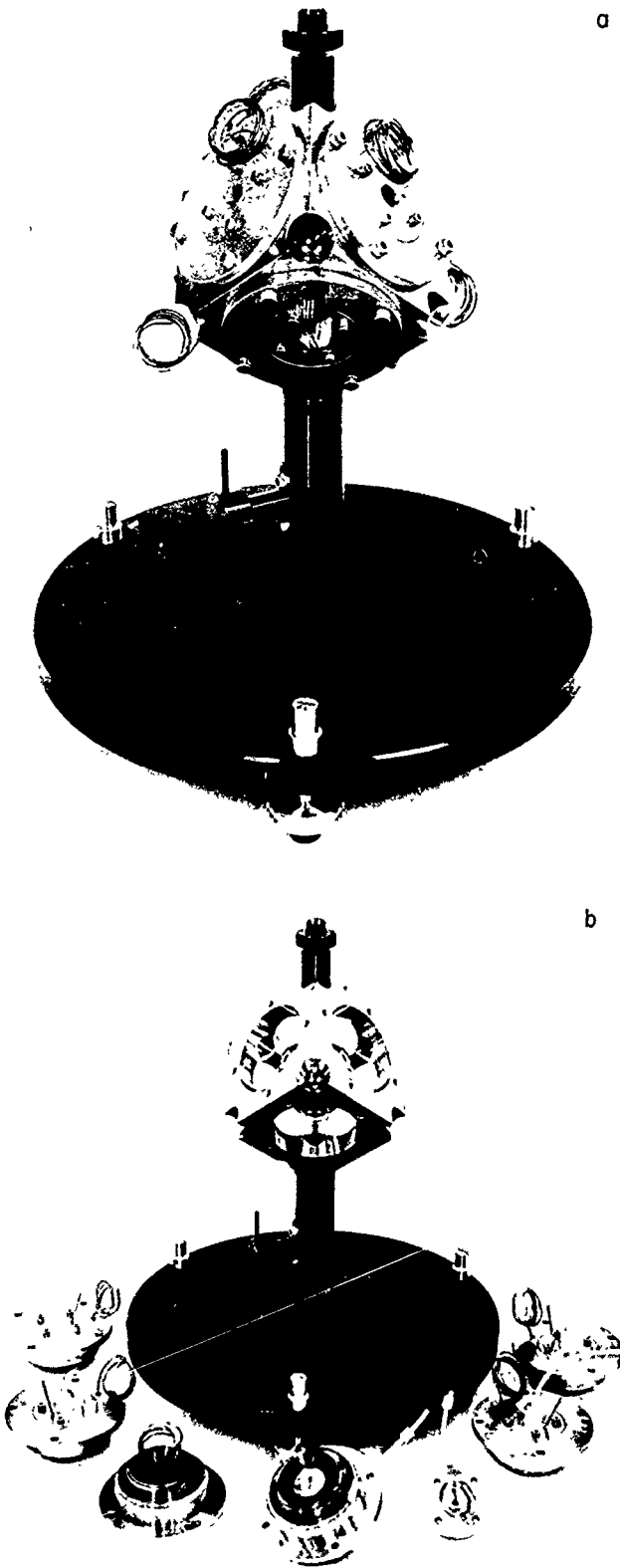


Figure 11. Six-pad spinning sphere, assembled and disassembled

contain the caging mechanism. The pads are positioned so that the three load-carrying pads are equally spaced in a horizontal plane. Figure 11b is a photograph of the model with the pads removed.

The first test was made to determine the flow rate and the pressure in the pad of compressed gas (nitrogen). The total flow rate (all six pads) is shown in Figure 12 as a function of the plenum pressure.

The average or effective gap between the sphere and the pads can be computed from the formula for radial flow in a slit:

$$h^3 = W \frac{12\mu \ln\left(\frac{R}{R_0}\right) RT}{\pi (P_0^2 - P_1^2)}$$

where h is the gap in inches, W is the weight rate of flow in lb/sec, μ is the absolute viscosity in lb-sec/in², R/R_0 is the ratio of the radius of the pad to the radius of the recess, RT the gas constant in inch per degree Rankine, T the temperature in degrees Rankine, P_0 the pad-recess pressure in psia, and P_1 the exit pressure in psia (Ref 16). Figure 13 shows the effective gap for each of the bottom three pads as a function of the plenum pressure.

Knowing the gap, the torque and power required to maintain any given spin velocity can be computed. For an eccentric position of the sphere, the following equations give an approximate value for three pads above the equator and three pads below:

$$\text{Torque } T = \frac{3\mu\pi\sigma^2(\sin\alpha)r^4\omega}{4} \left(\frac{1}{h_b} + \frac{1}{h_t} \right)$$

$$\text{Power} = T \times \omega$$

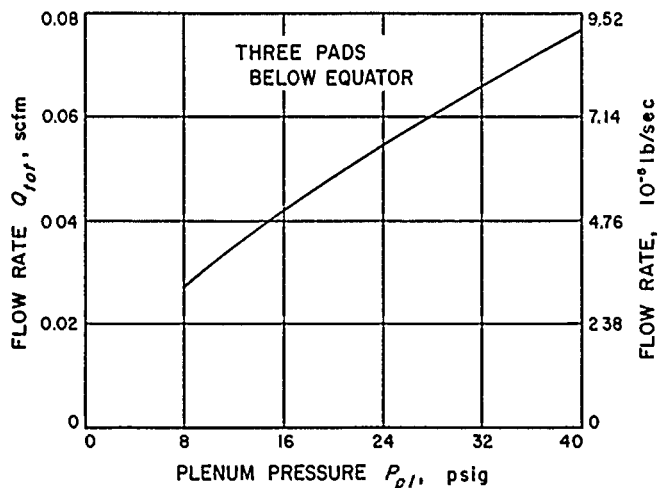


Figure 12. Flow rate of the six-pad spinning sphere

where h_b and h_t are the bottom and top gaps, respectively.

Figure 14 shows the computed power in watts (solid line) and torque in gm-cm (dashed lines) as a function of speed with plenum pressure as a parameter.

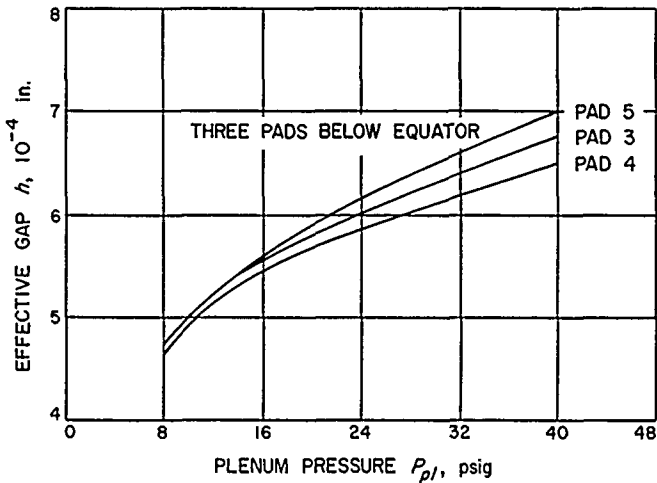


Figure 13. Six-pad spinning sphere, gap as a function of plenum pressure

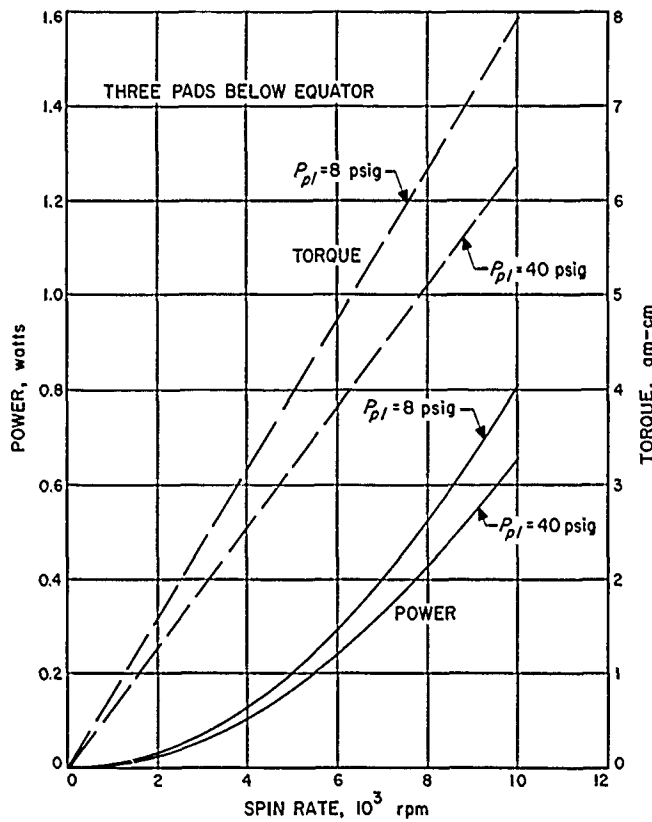


Figure 14. Six-pad spinning sphere, torque and power as a function of speed

The program of tests to be performed on this model includes the determination and possible control of turbine torque, determination of viscous drag and power losses in spinning the sphere, control and readout of the spin axis attitude, and performance characteristics using Freon vapor as a lubricant.

C. Ferromagnetic Flux Reversal Mechanisms

F. B. Humphrey

Ferromagnetic components are particularly well-suited to the requirements of space-borne digital circuitry. At the present time they offer the best solution to the component longevity and reliability problem. For the future when a nuclear reactor might be aboard the spacecraft, ferromagnetic devices can withstand a higher neutron flux and a higher neutron dose than any other digital devices. It is, therefore, desirable to understand the physics involved in the operation of these devices. Research into the details of the mechanism of rapid magnetic flux reversal in these components is now under way at this Laboratory. A short review of the work done thus far is presented here to form the foundation for future reports on this project.

Menyuk and Goodenough (Ref 17) formulated a domain wall motion model of flux reversal for ferrite and metallic tape memory cores. Gyorgy (Ref 18) recognized that such a model was good only for low drives and proposed a nonuniform rotation model for the flux reversal in cores. It was then recognized by Humphrey and Gyorgy (Refs 19, 20) that the reversal was even more complicated, requiring three mechanisms, and that such a model was applicable to all soft ferromagnetics. It is this current model for flux reversal which will be discussed in more detail.

Since this model is, in general, applicable to all soft ferromagnets, the liberty will be taken of discussing mostly thin ferromagnetic films. These films are typically 2000 Å thick of 83% nickel and 17% iron evaporated onto a hot (300°C) glass substrate. If there is a magnetic field in the plane of the film when the film is made, there will be a uniaxial magnetic anisotropy with the easy axis in the direction of the field. The origin of the anisotropy is not understood. It greatly influences the magnetic characteristics of the film. As is indicated schematically

in Figure 15, the direction parallel to the easy axis of the anisotropy is called the longitudinal direction, and the direction perpendicular is called the transverse direction. When there are no external fields, the magnetization will be parallel to the easy axis, that is, magnetized in the longitudinal direction.

A typical flux reversal experiment consists of setting the film in the longitudinal direction with a field many times the coercive force and then removing the field so that the film remains in one of the two remanent states fully magnetized along one easy direction. A uniform field, of magnitude H , is then applied instantaneously in the direction opposite to the setting field. The magnetization will reverse to the other remanent state. Loops are placed around the film, as indicated in Figure 15, to infer the flux change as a function of time by observing the voltage induced in the loops. The time τ is defined as the time to reverse from 10 to 90% of the integrated flux into the new remanent state. Figure 16 illustrates the results of a typical experiment. Here, one over the reversal time τ has been plotted against the drive field H , with a dc transverse field H_T as a parameter. The three regions are indicated as Region I at low drives where the plot is curved, Region II at intermediate drives where the points are connected by straight solid lines, and Region III at high drives where the points are connected by straight dashed lines. It takes three different mechanisms to describe this behavior, one mechanism for each region.

Region I. In the first region, the low-drive region, the mechanism of flux reversal is thought to be by domain wall motion, much the way Menyuk and Goodenough described (Ref 17). When a field H over a certain

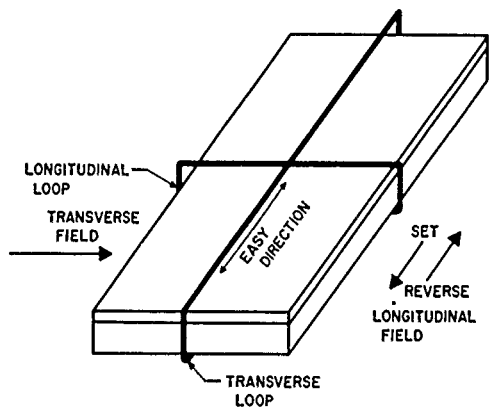


Figure 15. Relative direction of external fields on thin film and position of loops used to observe flux changes

threshold is applied to the sample, domain walls sweep through the sample as one domain grows at the expense of another. The threshold can be recognized as being related to the coercive force. Over this threshold H_0 , the velocity of the walls increases as the drive increases, reducing the reversal time. To account for the nonlinear behavior in this region, as indicated in Figure 16, it is

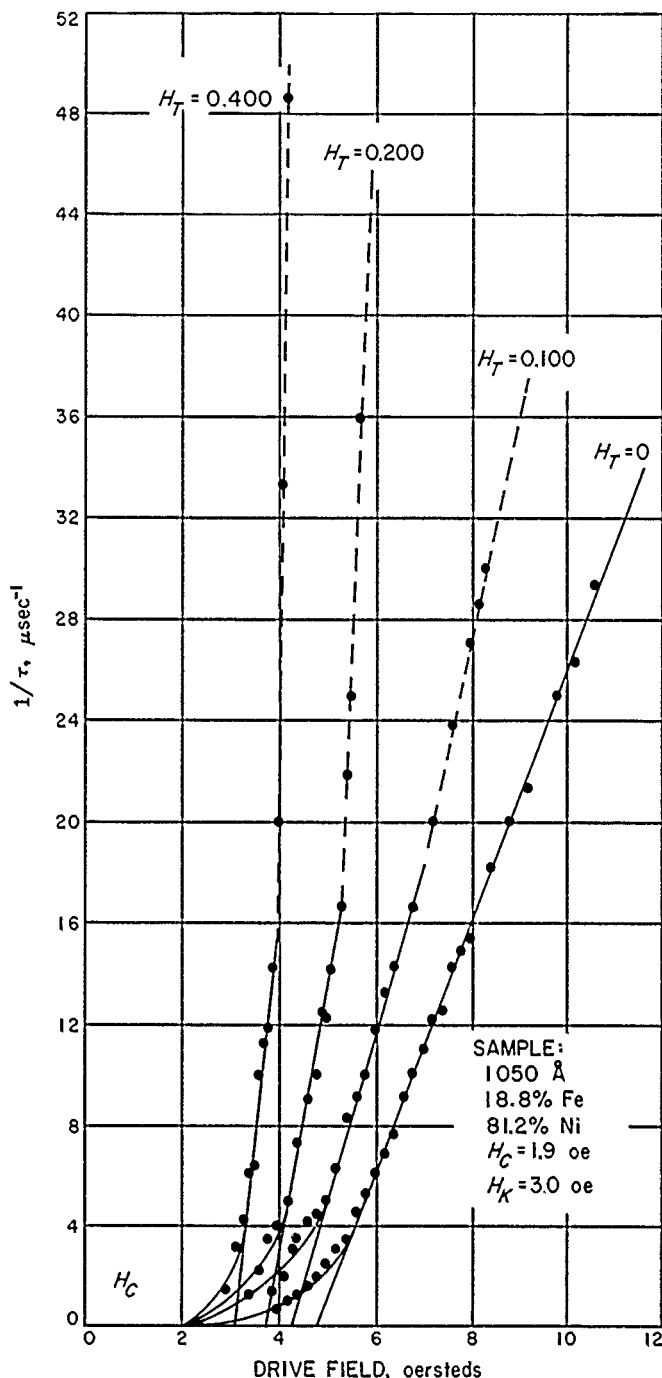


Figure 16. Typical reversal time vs drive field plot with transverse field as a parameter

necessary to slightly modify the Menyuk and Goode-nough model to make the number of walls nucleated be a function of drive. The most striking *indirect* evidence for wall motion is the interrupted pulse experiment first done on toroids by Gyorgy and Rogers (Ref 21) and repeated on films by Hagedorn (Ref 22). With the drive adjusted so that the reversal is in the domain wall motion region, the field pulse was interrupted in the middle of a reversal. The model predicts that the walls will stop and then start again when the field is reapplied and move as if there had not been an interruption. Figure 17 illustrates the results of this experiment. This is the data of Hagedorn (Ref 22). The upper trace is a typical voltage transient observed during a flux reversal. If the field is interrupted as in the lower trace and then restarted, it can be seen that the induced voltage follows on as if nothing had happened.

The most convincing *direct* evidence for domain wall motion is to see the domain walls move. Thin films are particularly adaptable to such an experiment since they can be used, without any surface preparation, to see domains using the Kerr magneto-optical technique or the Bitter powder pattern technique. Both methods provide striking evidence for the existence of domains and domain walls. The Bitter method is used for the microscopic

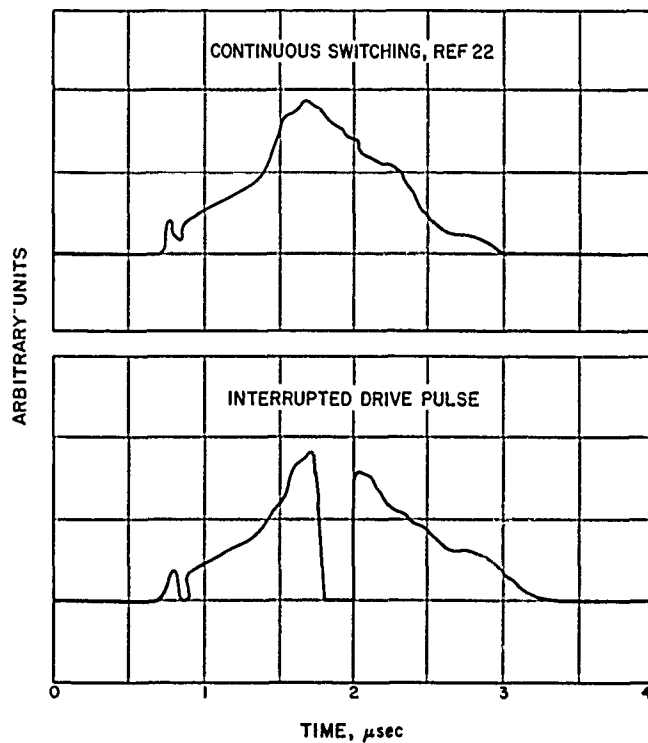


Figure 17. Typical voltage transient observed with longitudinal loop while switching films in Region I

examination of domain walls and is limited to essentially static configurations. No such limitation exists for the Kerr technique, where domain pattern pictures have been taken with exposures as short as 10^{-8} second.

Region II. Referring to Figure 16, the second region that is at intermediate drive field and is always linear is called the nonuniform rotation region. Here the interrupted pulse experiment is considerably different from that in Figure 17. It takes as much time to complete the reversal after the interruption as it did for the whole sample. Such evidence clearly suggests a mechanism different from domain wall motion. The nonuniform rotation model proposes flux reversal in the intermediate drive region by a rotation process where the phase of the precession is not preserved throughout the sample but changes from one spot to another in the material. This breakup is similar to magnetization modes or spin waves. Their presence allows local cancellation of the demagnetization field, resulting in a lower energy path—that is, lower than that of the uniform rotation. The model predicts that the shape of the switching transient will be proportional to the hyperbolic secant squared. The fit is quite good, as can be seen in Figure 18, which is the case for films (Ref 20). In the figure, the sample used was a thin evaporated film 1050 Å thick, 18.8% Fe, 81.2% Ni; the drive conditions were 5.7 oe with previously applied 15 oe setting field and zero transverse field. The model also predicts that the maximum slope of the $1/\tau$ vs H curve (with zero transverse field) will be dependent on the g -factor (spectroscopic splitting factor) of the material; for most ferromagnetics where $g = 2$, the maximum slope = 5. Such seems to be the case, since films (with zero transverse field), ferrites, garnets, and tape cores all have slopes close to but less than 5 (Refs 19, 20).

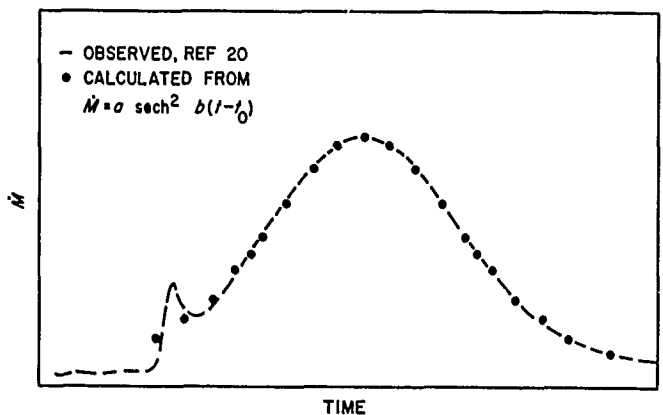


Figure 18. Observed voltage transient during reversal compared with that calculated from nonuniform rotation model

Region III. In the high-drive region, the mechanism of flux reversal is uniform rotation. Here a *single vector* can be used to represent the *entire magnetization* of the sample. The motion of this magnetization vector in the presence of an applied field is described by the Landau-Lifshitz equation. The motion of the magnetization is very much like the motion of a gyroscope consisting of the $[M \times H]$ term plus a damping term. In a thin film, then, it would be expected that the magnetization would precess up out of the plane of the film and then just swing around, damped only by the intrinsic damping of the material. Such a process should allow very fast flux reversals. For loops arranged as in Figure 15, the voltage induced in the transverse loop should change sign when the film is half-switched in the longitudinal direction. The longitudinal and transverse voltage transients for drive fields of sufficient magnitude to be in Region III have been observed by Olson and Pohm (Ref 24) and also by Dietrich, Proebster, and Wolf (Ref 25). The latter data is reproduced in Figure 19. The evidence supporting the uniform rotational mode is generally not this good. The fault is only partly the model since most of the data is taken in times so short that the experimental problems are formidable. The model gives a reasonable explanation for the existence of the short reversal times observed, although it generally predicts times shorter than those measured, and detailed agreement between the theoretical and observed switching waveforms in the longitudinal direction is very poor.

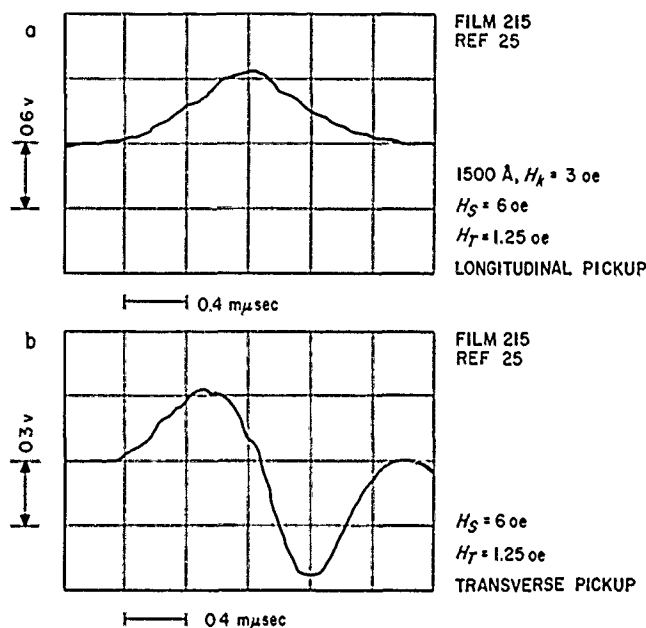


Figure 19. Comparison of observed longitudinal and transverse flux changes during reversal of thin film in Region III

Conclusion. It has been shown that at least three mechanisms must be considered in describing flux reversal in soft ferromagnets. In Region I, where the drive field is only slightly larger than the coercive force, flux reversal takes place by domain wall motion. The most convincing evidence is the direct observation of the domain or domain walls and the interrupted pulse experiment. Larger drive fields lead to Region II, where most of the experimental observations are consistent with a nonuniform rotation model. In particular, such a model predicts the linear relation between drive field and the inverse of the reversal time, the observed shape of the flux reversal transient, and the observed value of the maximum slope. Uniform rotation provides the best description of the observations of flux reversal in Region III, where a still larger drive field and a transverse magnetic field are required. The observed fast reversal is accounted for as is the transverse switching transient.

D. Closed-Cycle Gas Supply System

H. D. McGinness

An apparatus for testing a closed-cycle gas supply system, incorporating an actual gas thrust bearing, was described in RS 36-7 (Vol I). It was demonstrated, by feeding nitrogen gas through the bearing, that the experimental results agreed very well with the theoretical prediction and that subsequent experimentation with Freon vapors would be valid.

The objectives of the Freon tests were to determine whether a Freon vapor in a slightly superheated state could be made to operate a gas bearing without producing any liquid flow at the bearing and also to determine whether certain formulas, which were derived by employing the equation of state, would apply to Freon vapor bearings.

In the preliminary experiments it was found that the superheater, located just upstream of the control orifice (pictured in RS 36-7, Vol I, Fig 30), could not reliably prevent some liquid flow through the control orifice when the evaporator temperature was substantially higher than the ambient temperature. Apparently, the heat capacity of the bearing housing was too large for the small superheater to overcome. Therefore, another technique was developed which proved to be satisfactory and is thought

to be more readily adaptable to spacecraft applications. This method consists of maintaining the evaporator temperature below the ambient and letting the saturated vapor become superheated as it flows through the tubing (at room temperature) leading to the bearing.

Freon C318 was selected, because its pressure near room temperature is suitable for many gas bearing applications. At 45°F its pressure is 10.5 psig, and increases approximately linearly to 30 psig at 76°F. The evaporator may be cooled by blowing off some of the Freon; it may be heated by applying electric current to heating coils placed within the container. Thus, the temperature is easily adjusted to the desired value. Several tests were made over this temperature range; in each case as the evaporator temperature approached ambient, the entrance to the pad bearing was visually observed in order to see when there was liquid flow. In all instances where the temperature of the evaporator was very slowly raised, liquid flow did not occur until the evaporator temperature was approximately 0.5°F more than the bearing temperature. When the evaporator temperature was rapidly increased, a small amount of liquid flow would appear and then disappear, even at evaporator temperatures as much as 8°F below the bearing temperature. A possible explanation for this is that, due to vigorous boiling, small droplets are thrown upward into the open end of the evaporator discharge pipe (RS 36-7, Vol I, Fig 30). When the temperature difference between the evaporator and the bearing was not more than 8°F, the droplets were not vaporized before entering the bearing, whereas for a greater temperature difference such droplets were vaporized.

It is well known that the equation of state ($pV = \text{IRT}$) does not apply over a large range of temperatures and pressures which include those near the saturation line. However, over a small range in the superheat region near the saturation line, but considerably below the critical point, the equation of state gives values agreeing fairly well with those of thermodynamic charts for Freon. Tests were made to compare the actual weight flows of Freon C318 (as measured with a flowmeter) with two different calculated flows; namely, the isentropic flow through the control orifice, and the isothermal viscous flow between the faces of the flat circular pad thrust bearing. Both flow calculations made use of a given gas constant IR ; that is, the equation of state was assumed to apply. These equations are:

$$W_{or} = \left(\frac{2}{k+1} \right)^{\frac{k+1}{2(k-1)}} \left(\frac{k g}{\text{IRT}} \right)^{\frac{1}{2}} P_{pl} A C \quad (1a)$$

when

$$\frac{P_{pl}}{P_0} \leq \left(\frac{2}{k+1} \right)^{\frac{k}{k-1}}$$

$$W_{or} = \left[\left(\frac{\left(\frac{P_{pl}}{P_0} \right)^{\frac{k-1}{k}} - 1}{\left(\frac{P_{pl}}{P_0} \right)^{\frac{k+1}{k}}} \right) \frac{2 k g}{(k-1) \text{IRT}} \right]^{\frac{1}{2}} P_{pl} A C \quad (1b)$$

when

$$\frac{P_{pl}}{P_0} > \left(\frac{2}{k+1} \right)^{\frac{k}{k-1}}$$

$$W_B = \frac{\pi b^3 (P_0^2 - P_1^2)}{12 \mu \text{IRT} \log \frac{R}{R_0}} \quad (2)$$

where

W_{or} = weight flow through control orifice

W_B = weight flow through pad bearing

$k = C_p/C_v$ = ratio of specific heats

g = acceleration of gravity

T = absolute temperature

IR = gas constant in units of length per degree absolute temperature

P_{pl} = absolute pressure upstream of control orifice

P_0 = absolute pressure at bearing entrance

P_1 = absolute pressure at bearing exit

A = orifice area

C = orifice coefficient

b = uniform gap between bearing faces

μ = coefficient of absolute viscosity

R = bearing outer radius

R_0 = bearing radius at inner edge of gap

The following values pertain to the bearing tested and to Freon C318: $k = 1.05$, $g = 386 \text{ in./sec}^2$, $\text{IR} = 93 \text{ in./}^\circ\text{R}$, $P_1 = 14.7 \text{ psia}$, $A = 1.25 \cdot 10^{-5} \text{ in.}^2$, $C = 1$, $\mu = 1.7 \cdot 10^{-9} \text{ lb-sec/in.}^2$, and $\log R/R_0 = 3.56$. In Figure 20, W_{or} is plotted against P_0 for two different P_{pl} values, using the above values of the parameters. The symbols represent measured points; thus, it is seen that Equation (1) applies reasonably well.

In order to check Equation (2), the two faces of the pad bearing were spaced apart by three small shims approximately 0.0625 inch square, equally spaced near the outer edge of the bearing. The thicknesses of the shim stock were determined by measuring across several thicknesses with a micrometer and computing the average.

In Figure 21, W_B vs P_0 is plotted, using the above values of the parameters, for four shim thicknesses. The symbols represent the measured flow values. Equation (2) shows that W_B varies as the cube of h ; thus, a very small error in the measurement of h would produce a substantial change in W_B . For instance, in the case of the 0.000285-inch shim, a decrease in h of 0.00001 inch would decrease the calculated flow to 90% of the value shown. With this in mind, it is thought that Equation (2) applies very well to slightly superheated Freon vapors.

Thus, the conclusion is justified that the performance of gas bearings operating on Freon vapor within the limits investigated can be satisfactorily predicted by the analytical treatment developed.

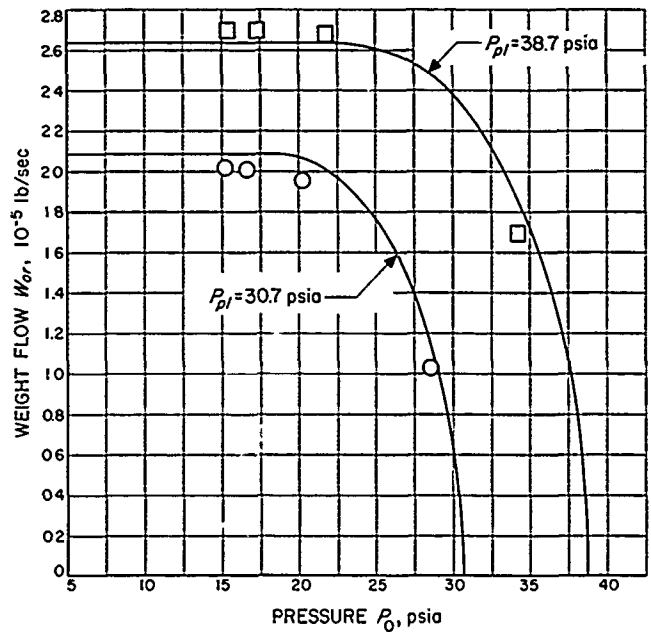


Figure 20. Weight flow through orifice vs absolute pressure at bearing entrance

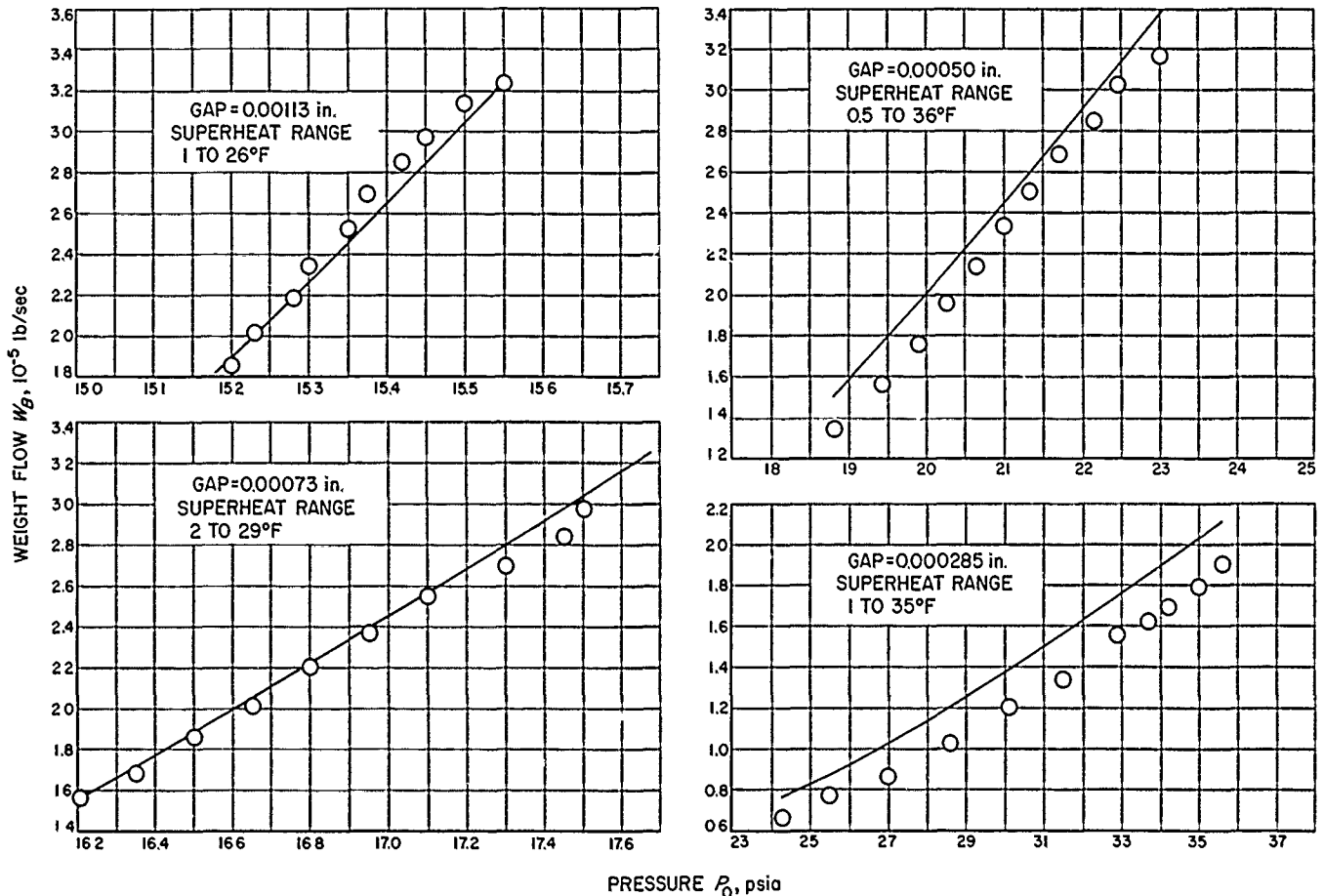


Figure 21. Weight flow through bearing vs absolute pressure at bearing entrance

TELECOMMUNICATIONS DIVISION

III. Communications Elements Research

A. Low-Noise Amplifiers

T. Sato

1. Solid State Maser

A 2388-mc, cavity-type ruby maser has been constructed and installed at the Goldstone Tracking Station for use in the 1961 Venus radar experiment. The maser is similar in design to the 960-mc research and development maser described in *Research Summary 36-6* and has been described in *RS 36-7 (Vol I)*. Various refinements have been incorporated to improve the general system performance. Figure 22 shows the maser prior to installation at the apex of the Goldstone Ha-Dec antenna.

Since the previous report, improved performance of the maser was obtained by raising the pump frequency from 12.6 to 12.9 kmc while keeping the magnetic field to about 2500 gauss. At 20 db gain, it is now possible to obtain a bandwidth of 2.5 mc, an improvement by 1 mc over the previous value. The maser noise temperature was measured to be around 25°K. This value is slightly less than that measured previously.

The liquid helium dewar system performs as expected, with a useful life of 24 hours. Daily filling on the antenna maintains the maser in operating condition. The ion pump, used to maintain the dewar vacuum, also performs very

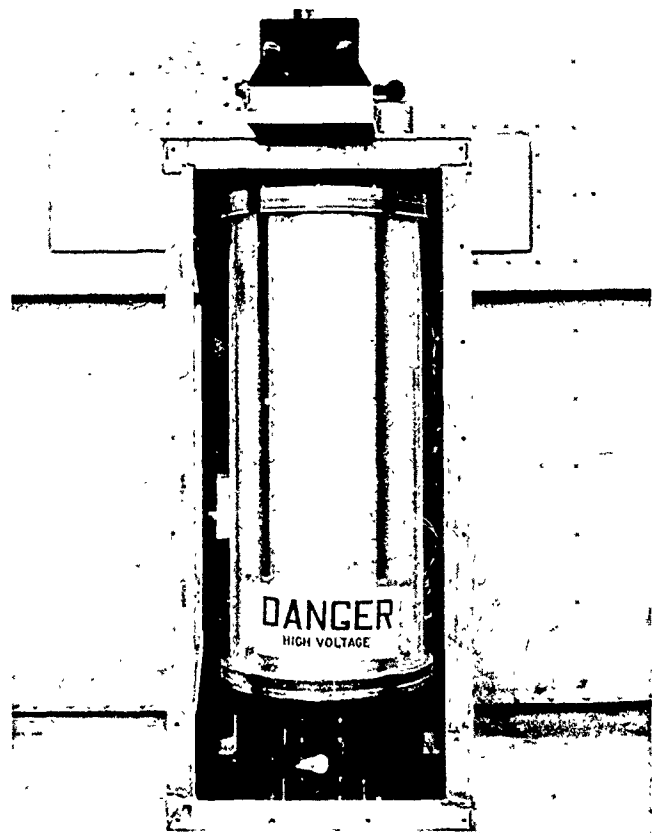


Figure 22. The 2388-mc maser system with side panels removed

well; it has maintained the vacuum to better than 10^{-7} mm Hg after 1 month of continuous operation. The unique design of this pump enables it to outperform ion pumps twice the volume and four times the weight.

The performance of the maser was checked after installation on the receiving antenna. The gain-bandwidth product and noise temperature were substantially the same as those measured in the laboratory. The presence of gain variations with antenna position was detected. The source of this gain variation is believed to be small changes in the magnetic field resulting from the mechanical shifting of the magnet system relative to the ruby crystal. Gain fluctuations observed are of the order of ± 2 db when the antenna is rapidly scanned across the sky. When tracking a slowly moving object such as Venus, a periodic adjustment of the magnet current allows the gain fluctuations to be kept under ± 0.5 db.

B. Antennas for Space Communication

D. Schuster and C. T. Stelzried

1. Shaped Beam Feed Research

In November 1960, research in low-noise antenna systems was directed to aid development of a low-noise temperature, high-gain, circularly polarized feed to be ready for the Venus radar experiment. The research was directed toward shaping the primary pattern of the feed to provide better dish illumination and less spillover.

Figure 23 shows a typical waveguide horn primary pattern with tapered aperture illumination. A considerable amount of power is wasted in the region outside of the dish illumination angle. For a 10-db taper, this may cause a loss in efficiency of 15%. Also, a significant amount of power (perhaps 8 to 10%) falls within the ground illumination angle. (The angular distribution of this part of the primary pattern power will be changed somewhat due to diffraction at the dish edge.) Since ground temperature radiation is usually the largest contributor to the antenna temperature, it is important to reduce the percentage of pattern power in the ground illumination region. This principle was verified during the 960-mc maser test program at Goldstone (*Research Summary 36-6, Vol I*).

The first pattern shaping experiments were conducted using crude models, and several possible approaches were

tested. The initial ideas included the use of RF chokes of various types around the horn mouth, a variation of the flange size in order to shape the pattern (Ref 26), the placing of obstacles and chokes in the horn mouth to simulate multiple tilted horns, and the use of large tilted ground planes at approximately the edge illumination angle of the dish. The idea of using a metallic lens in front of the horn was considered briefly. The use of an array of horns was considered but was discarded because of the required additional waveguide feedlines which would contribute additional excess temperature.

By late December, some progress had been achieved with the use of chokes around the horn mouth. Experimental data showed this to be a promising approach, but insufficient data was available to design the feed. The use of obstacles in a horn mouth was tried without promising results for this application. Next, an experiment was carried out with a large wide-angle (120 deg) tilted groundplane, flaring out from the horn mouth, that provided good results for linear polarization in the E-plane. Later, very good shaping of an H-plane pattern was obtained using a very large flat groundplane around the horn mouth. A combination of these two ideas was tested

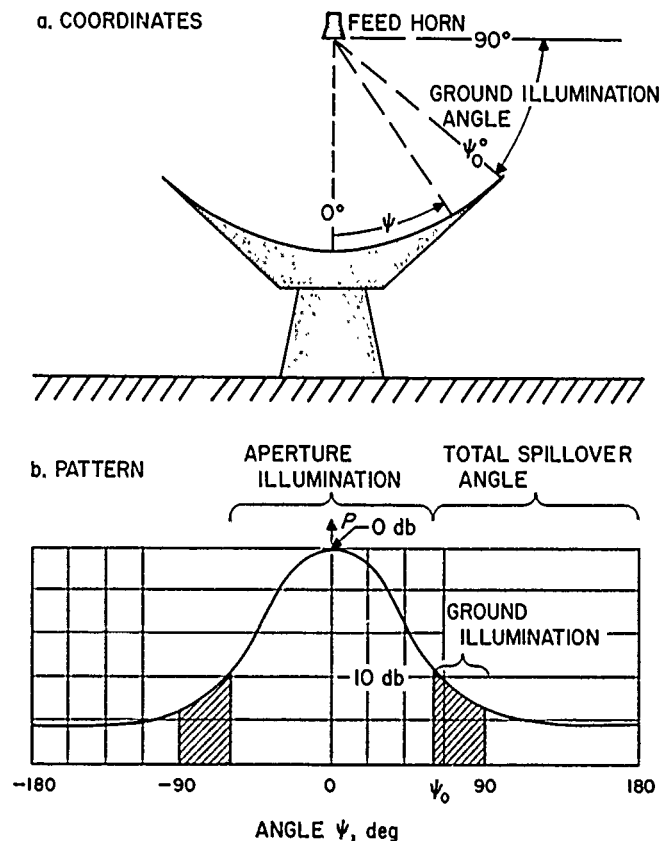


Figure 23. Typical primary feed pattern

and provided a good technique for shaping the pattern of a linearly polarized horn.

During January, numerous tests were carried out on combinations of various finned, choked and flat or tilted groundplanes; by late January, a promising technique had been developed to provide good pattern shaping for a circularly polarized feed. This involved the use of a square groundplane with raised RF chokes along the outer edge. To improve the symmetry of the patterns, a new feed was built using a round groundplane with multiple raised chokes, i.e., a surface-wave structure on the outer edge. After testing the critical spacing of the inside choke and designing a small-aperture horn to work with this system, the design dimensions of the present Venus radar feeds were determined. By this time, the heuristic ideas explaining the operation of the feed were believed to be valid.

In order to confirm satisfactory operation of a shaped-beam feed from primary pattern measurements, it was necessary to measure the phase center of the feed versus polarization. To accomplish this, work was started at the end of November to develop and build a phase-measuring

antenna range. Some pieces of equipment were purchased, and some were designed and built specifically for this purpose. By January, this range was operating with high accuracy but required slow and tedious adjustments. A special rotator mount to reduce the time required for a phase measurement was in the design stage and has now been completed and installed. (See discussion in Section III-B-4 of this summary.)

By early February, the first Goldstone shaped-beam feed had been fabricated, tested for primary patterns, phase centers, VSWR, and primary pattern ellipticity and was ready for installation on the receiver site 85-foot antenna. Figures 24 and 25 provide a comparison between the E- and H-plane patterns of a conventional feed horn and those of the shaped-beam feed.

By mid-February, this feed had been installed (Fig 26) and had been tested for antenna temperature, gain,

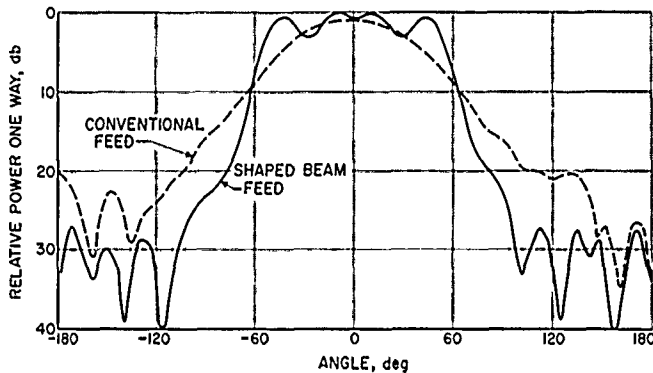


Figure 24. Conventional and shaped beam E-plane patterns

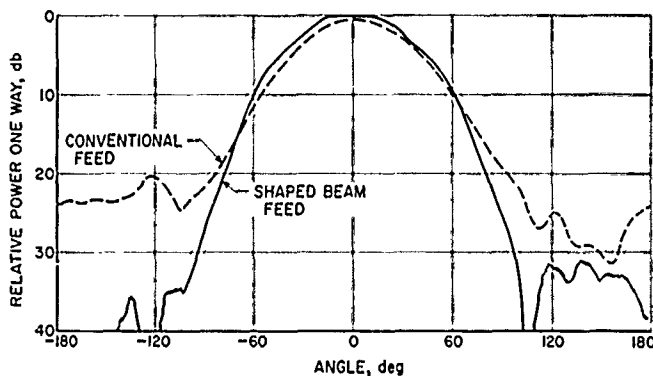


Figure 25. Conventional and shaped beam H-plane patterns

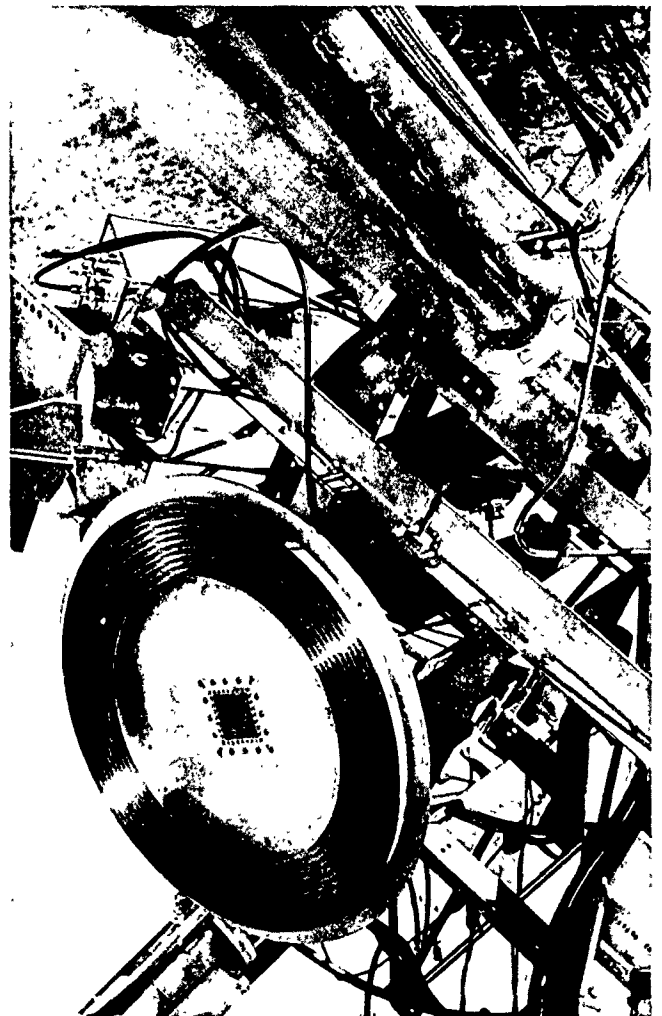


Figure 26. Shaped beam feed installation

ellipticity, and secondary patterns. The results of the experimental measurements are included in Section III-B-2 on the Venus radar feeds.

At the present time, research on shaped-beam feed design is continuing. The immediate aim is to see if further improvements can be made in the gain and figure of merit of paraboloidal antennas.

2. Feed System for Venus Radar Experiment

Several proposed feed systems to provide a low-noise listening feed for the Venus radar experiment were described in *Research Summary 36-7* (Vol 1). The primary design objective was to obtain a circularly polarized 2388-mc feed that would produce the highest figure of merit (the quotient of gain and system temperature) for

the 85-foot receiving antenna. In order to achieve this purpose, three horns were provided. Two of these were conventional horns to produce edge illuminations of 10 and 14 db (and with fin loading to obtain equal E- and H-plane patterns). The third was a shaped-beam feed horn which was developed at JPL. (See discussion in Section III-B-1 on research leading to this development.) All three horns were designed to use the same waveguide phase shifter and transformer sections to achieve circular polarization.

During the installation period, the three horns were tested for gain, ellipticity, antenna temperature, and secondary patterns. The shaped-beam feed was found to have from 0.8 to 1.1 db more gain than the conventional feeds. The axial ratio of the elliptical polarization was 0.75 db for the shaped-beam feed. The measured antenna

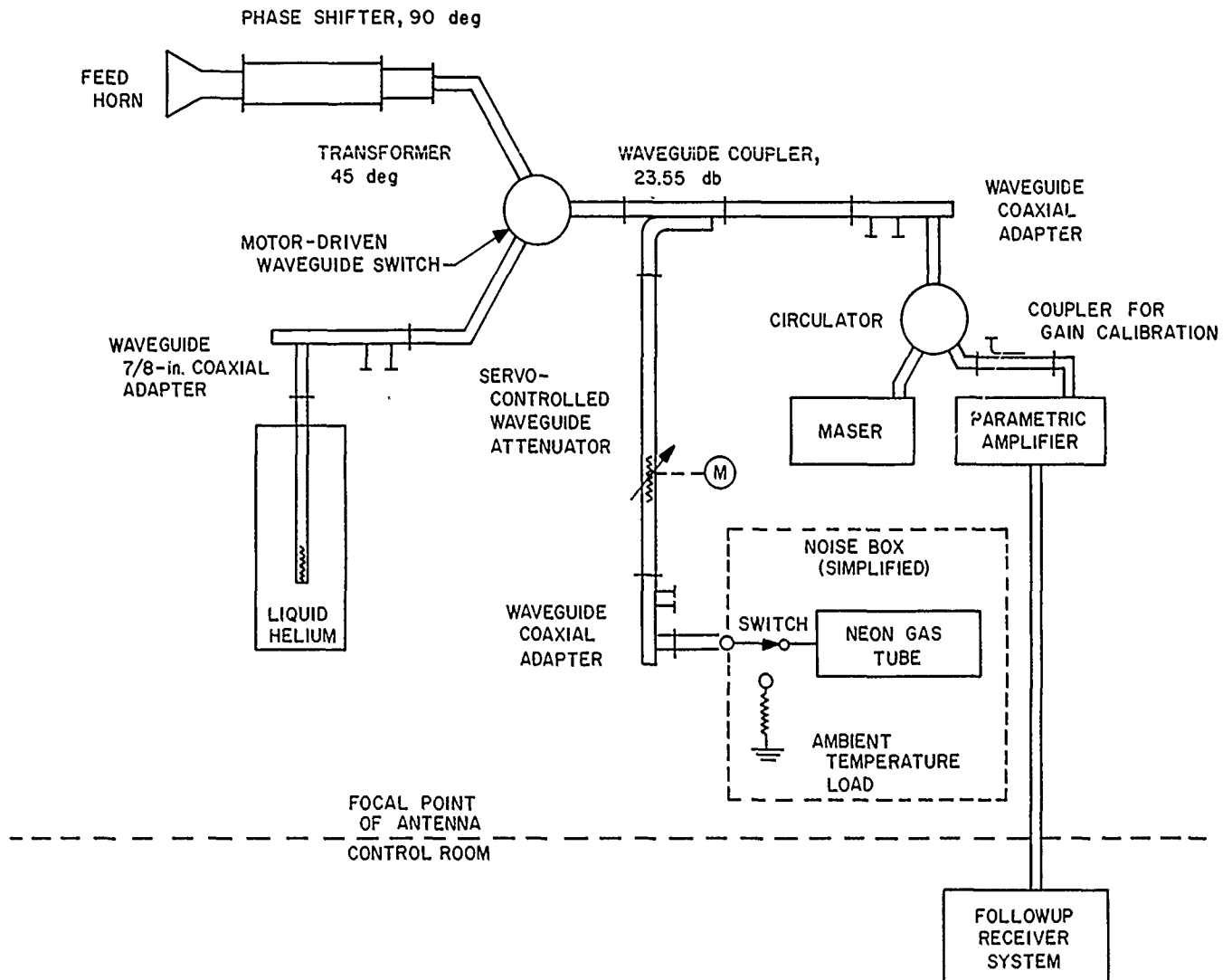


Figure 27. Feed system for Venus radar receiver

temperatures with the antenna pointed at zenith (and with a quiet sky background) were as follows:

Horn with 10-db taper, 30°K.

Horn with 14-db taper, 16°K.

Shaped-beam feed, 14°K (absolute accuracy 4°K).

The best estimate of the far field gain, based on measurements taken in the near field at $0.3D^2/\lambda$, is 53.5 db for a matched polarization isotropic source. Because of its superior performance, the shaped-beam feed is being used in the Venus radar experiment.

A block diagram of the Venus radar feed and transmission line system is shown in Figure 27; Figure 28 is a photo of the antenna focal point with the feed system, maser, helium load, and parametric amplifier installed. Antenna temperatures are measured by comparing the recorded noise signal from the antenna to that from the liquid helium cooled load. A calibrated amount of additional noise is injected into the system to raise the apparent temperature of the helium load to equal that of the antenna. The switching is done after several integration time constants on either the antenna or helium load position. Very good short-term gain and temperature stability are required of the receiving system. (See additional dis-

cussion of the noise temperature measurement techniques in Section III-B-3 of this summary.)

An alternate feed system design includes a bimodal combiner and an additional waveguide switch to allow rapid changing between right- and left-handed circular polarization. The bimodal combiner has not yet been installed; it still remains as a possible modification later in the Venus radar experiment.

To maintain the lowest possible system temperature, the feed and transmission line system up to the maser circulator was made entirely of waveguide. All parts of the low-loss transmission line system were tested for VSWR before installation. The maximum VSWR for any component used in the system was 1.09 before matching. Then the input ports to the antenna feed and to the transmission lines joining the antenna feed, the helium load, and the circulator were all matched to apparent VSWR's = 1.02 after installation on the antenna. Because of residual errors in the measurement techniques, the real VSWR at these ports may be as much as 1.04. All flanges used in the system were lapped flat to improve measurement repeatability; also, wherever possible, MIL standard guide pins were used in the flanges.

The waveguide attenuator in use in the noise injection line is an FXR Model R-160B that has been modified at JPL for precise control by a remote servosystem. The attenuator is a flexible vane type and is extremely well matched over the entire attenuation range. The apparent VSWR is less than 1.03 over at least a 20-db range. The minimum insertion loss was measured and found to be 0.08 db; the attenuation repeatability was excellent.

After the successful tests on the shaped-beam feed for the receiver antenna, the test model of the shaped-beam feed was temporarily mounted on the transmitting antenna. Gain tests again indicated at least 0.8 db more gain than for the other available transmitter feeds. After this, another shaped-beam feed was fabricated for use with the 10-kw transmitting system. The feed section was designed to attach to the standard circularly polarized phase shifter section.

A modified waveguide 90-degree phase shifter and square-to-rectangular transformer were fabricated, tuned, and installed at the same time that the newly fabricated shaped-beam feed was installed on the antenna. The new phase shifter was installed to improve the ellipticity of the transmitter feed system. The old phase shifter provided broad bandwidth operation, but the polarization axial ratio was 1.2 db at best. Both phase shifters are of the same basic design; five double-waveguide irises spaced apart in a square waveguide section, with sharp corners

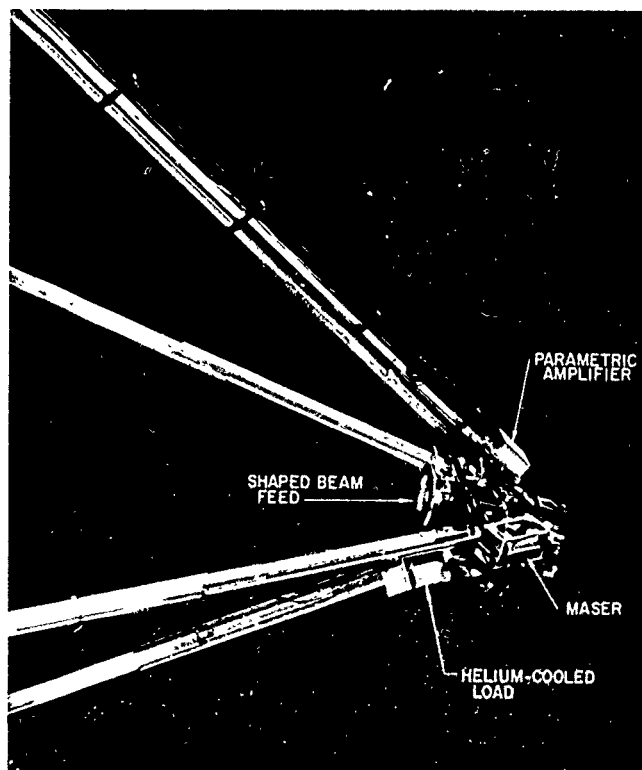


Figure 28. Maser and low-noise feed installation

rounded to prevent corona arcing. After installation of the new shaped-beam feed, phase shifter, and transformer, the ellipticity was measured for right-hand secondary polarization and the axial ratio was less than 0.3 db. The present best estimate of the far-field gain of the transmitter antenna, under the same conditions that apply to the receiving antenna, is 53.8 db.

3. Noise Temperature Measurements

Evaluation of low-noise feeds for the Goldstone receiving antenna requires an accurate technique for measurement of the system equivalent noise temperature. Figure 29 shows a block diagram of the technique used. Calibration is obtained by recording the system noise level with the input switched to the liquid helium cooled termination, and with the noise source fired and not fired. The input is then switched to the antenna, and the antenna temperature is interpolated from the recording. Utilizing this technique, the measured equivalent noise temperature of the antenna with the 2388-mc feed used for the Venus radar experiment was about 14°K.

The liquid helium dewar previously used for the 960-mc maser was used for the cooled load; over 24 hours of continuous operation between refills has been obtained with the cooled load installed on the antenna. A 0.75-inch diameter stainless steel gold-plated transmission line was installed with a modified coaxial termination immersed in the liquid helium. The measured temperature distribution along the line and the insertion loss as a function of temperature are shown in Figures 30 and 31. The temperature distribution was made independent of the liquid helium level by providing a jacket of copper around the outer conductor and inside the inner conductor of the coaxial line. The approximate equivalent temperature of

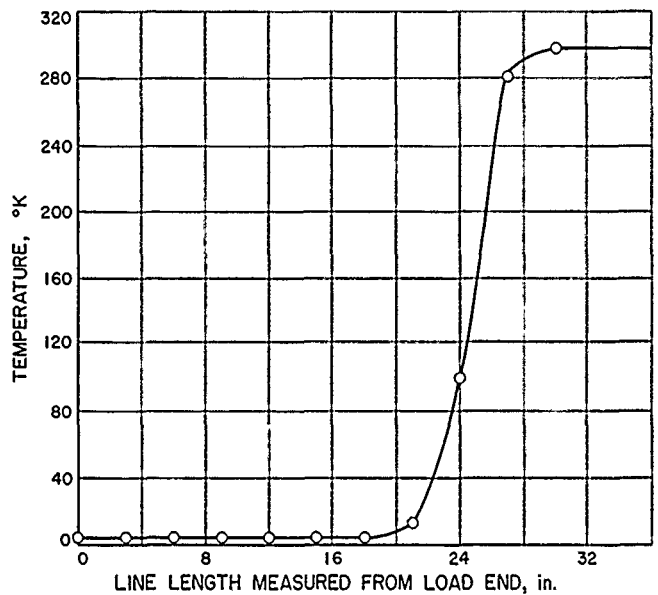


Figure 30. Temperature distribution along helium load transmission line

the transmission line was calculated by dividing it into five segments; the result was 5.5°K.

The cavity bandpass filter (Fig 30) reduces the image and harmonic response of the mixer. The 3-db pad and circulator reduce the effect of any slight mismatch on the amplifier gain when switching between the cooled termination and antenna. The 2388-mc mixer and IF amplifier were designed for low noise and high gain stability (RS 36-7, Vol I, p 83).

The 2388-mc mixer was also used to evaluate the excess noise of a Bendix TD40 argon noise source. This source is used as a standard noise source for system noise temperature measurements in the Venus radar experiment. A

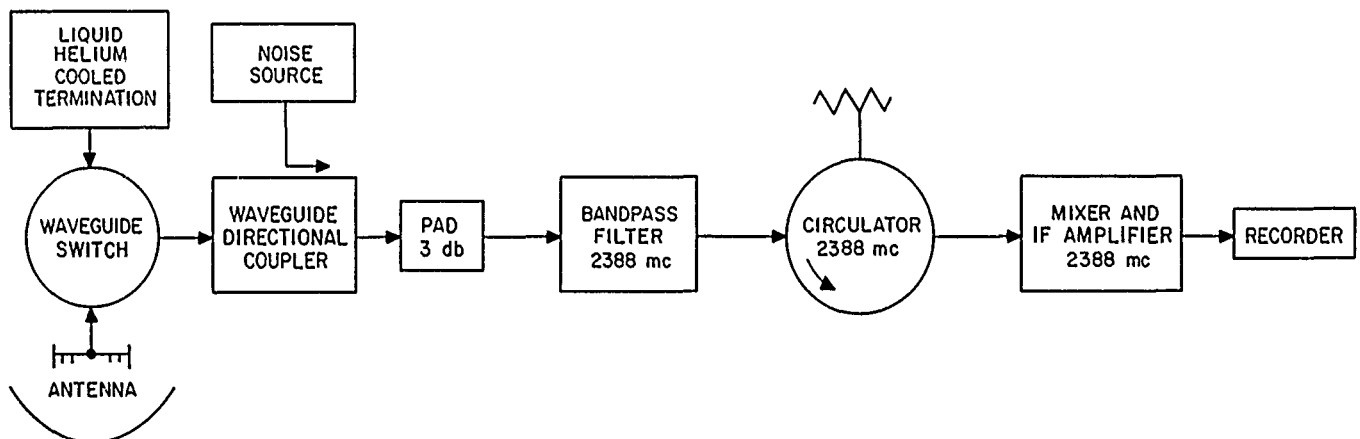


Figure 29. Block diagram of 2388-mc antenna temperature measurement setup

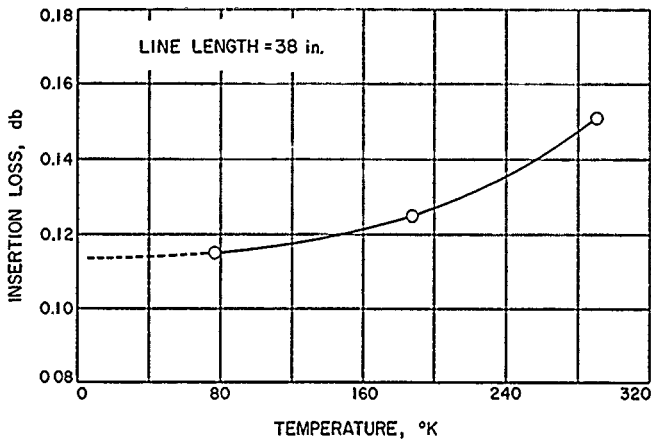


Figure 31. Insertion loss of 0.75-inch transmission line vs temperature

block diagram of the noise source calibration equipment is shown in Figure 32. The circulator is used to reduce the gain change of the amplifier when switching loads. The effectiveness of this measure was checked by switching between mismatched loads with a VSWR of 1.04 and 1.50; the gain change was not measurable with the recording system. The second and third harmonic response was measured and found to be below 25 db. The measurement technique consisted of setting equal readings on the recorder with the precision attenuator. Calibration is obtained by measuring the power ratio between the cooled and ambient temperature load. The excess noise is then obtained from the power ratio between the cooled load with the noise source on and off. A typical recording

is shown in Figure 33; the effect of gas-tube current variations is also shown in the figure.

A radiometer was set up for calibration purposes and to obtain Venus black-body radiation data at 2388 mc. It utilized the 2388-mc maser and the 2388-mc mixer as shown in Figure 34. The operating parameters of the system are:

- Center frequency, 2388 mc.
- Bandwidth, 2 mc.
- System temperature, 80°K.

The waveguide attenuator can be set to obtain a calibrating pulse when the noise source is turned on. Typical radiation drift curves from Venus and M87 (a standard radiometer source) are shown in Figures 35 and 36. The curves were obtained by setting the antenna at the declination of the source and about 0.5 degree ahead in hour angle and letting the source drift through the antenna beam.

The hour angle and declination are shown on the recording, and the GMT is indicated at the peak of the radiation intensity. Separation of the half-power points is about 0.35 degree. The relative antenna temperature increases determined in these preliminary measurements are approximately 0.5°K for Venus and 10°K for M87.

Figure 37 shows a block diagram of the operational 2388-mc Venus radar receiver system temperature measurement equipment. The system temperature on both the

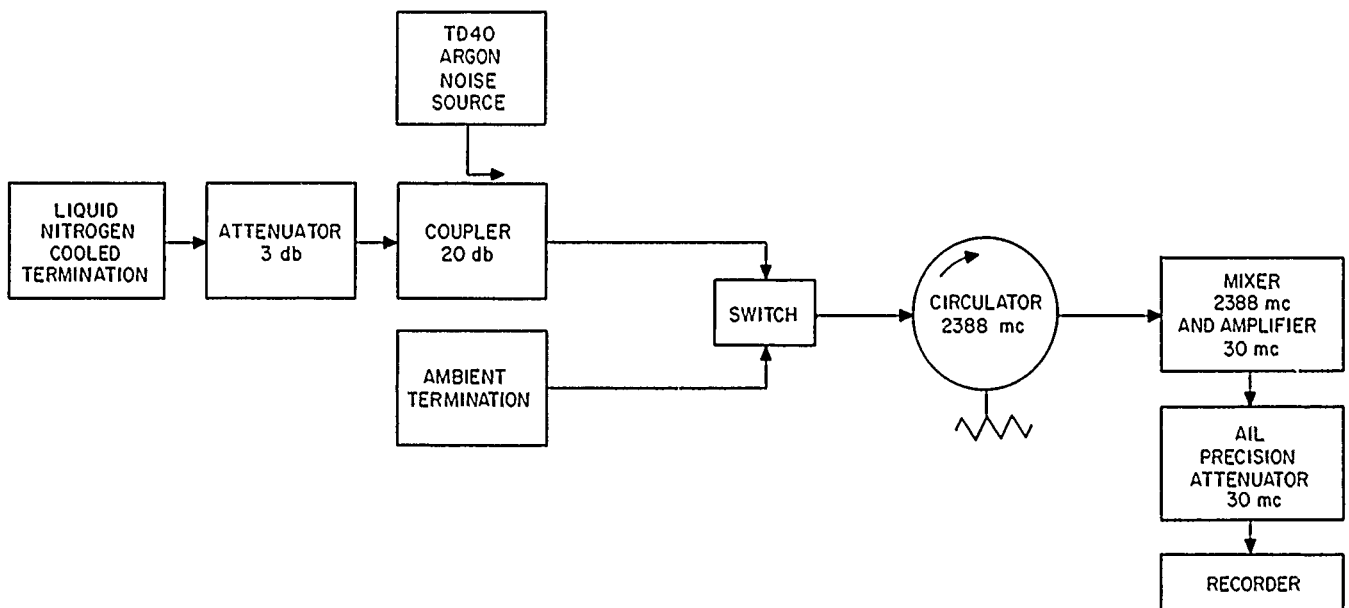


Figure 32. Noise source evaluation setup

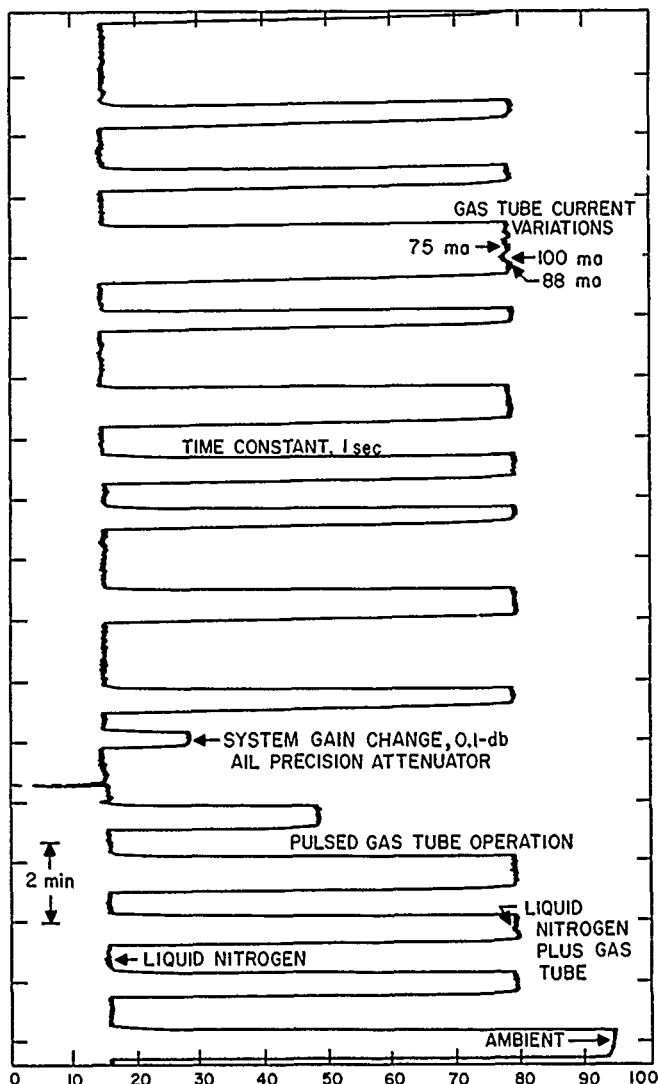


Figure 33. Recording of excess noise of argon TD40 noise source at 2388 mc

antenna and liquid helium cooled termination are measured on a periodic basis by the Y-factor method. The method (Fig 30) consists of setting the precision attenuator so that the indicated noise level is the same after the noise source is turned on as before. If T_s is the total system temperature, T_e the excess noise from the noise source, and Y the measured power ratio

$$\frac{T_s + T_e}{T_s} = Y$$

Typical values for the system temperature are 60°K with the antenna pointed in the vicinity of Venus, and 55°K on the helium load. Since the helium load has an equiv-

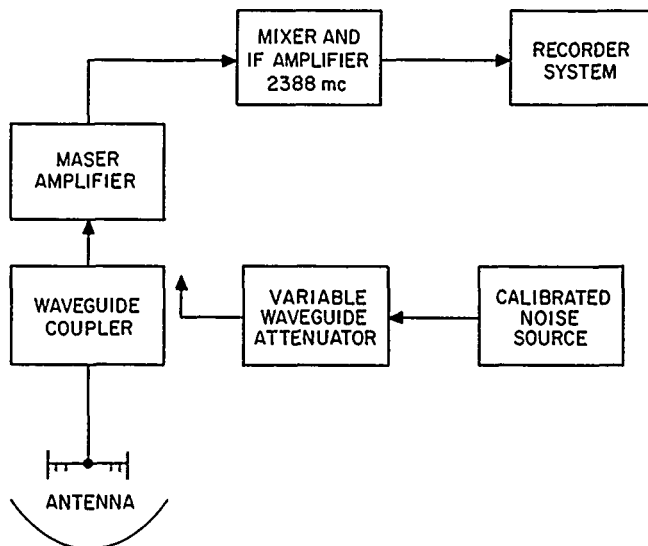


Figure 34. Radiometer setup using 2388-mc maser amplifier

alent temperature of about 10°K, this indicates about 15°K for the antenna. The excess noise (20°K) was accurately measured by calibrating the noise tube with a liquid nitrogen cooled termination (discussed in preceding paragraphs).

The sensitivity of the nonsynchronous receiver system is also measured periodically, using the equipment of Figure 29. A remote-controlled coaxial relay switches the waveguide directional coupler between the noise source and an ambient termination. The level of the pulse is determined by the remote-controlled waveguide attenuator.

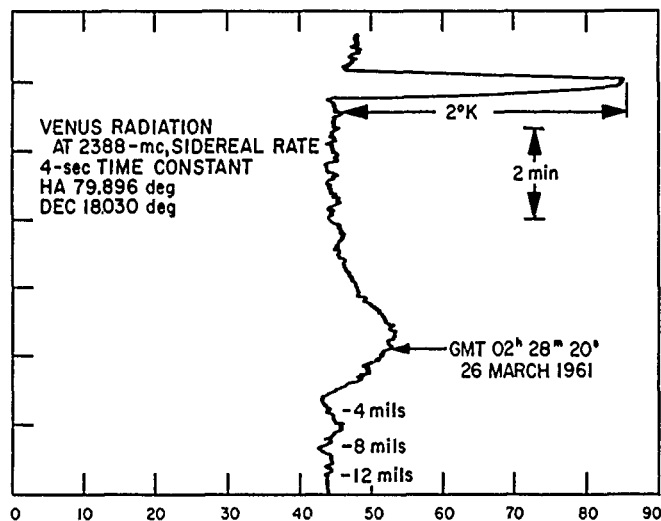


Figure 35. Drift curve of 2388-mc radiation for Venus

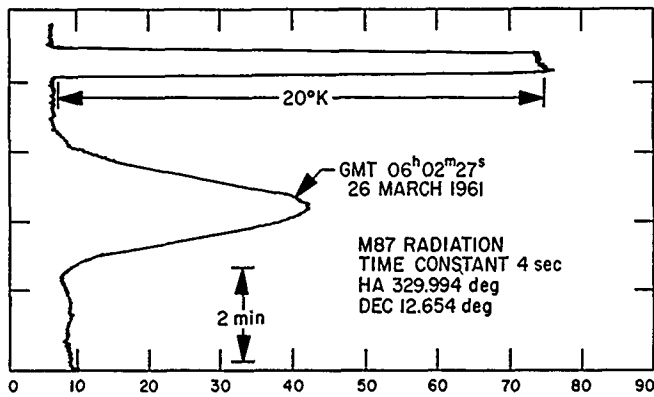


Figure 36. Drift curve of 2388-mc radiation for M87

4. Phase Measurement Range

As part of a primary feed testing program, phase-center measurements have been required on several different

feeds intended for use in the Goldstone antennas. To perform the measurements, an antenna phase-center test range has been set up using a Serrrodyne single-sideband and carrier mixing system (Refs 27 and 28). One of the major advantages of the system for antenna work is that accurate phase measurements can be performed for a very large variation in signal (or antenna pattern) amplitude. The Serrrodyne generator, in this case, is a traveling wave tube amplifier with the helix modulated by a 1-kc sawtooth wave (Fig 38). The output of the Serrrodyne is a CW signal at the carrier frequency f_c , shifted by 1 kc. The shifted signal, $f_c + 1$ kc, is passed through the antennas and mixed with the carrier signal. The 1-kc difference frequency output of the mixer exhibits the same phase shifts as the microwave frequency. In addition, the 1-kc signal has stable amplitude and phase characteristics. The phase shift measurement is carried out by comparing this signal to the 1-kc master oscillator signal.

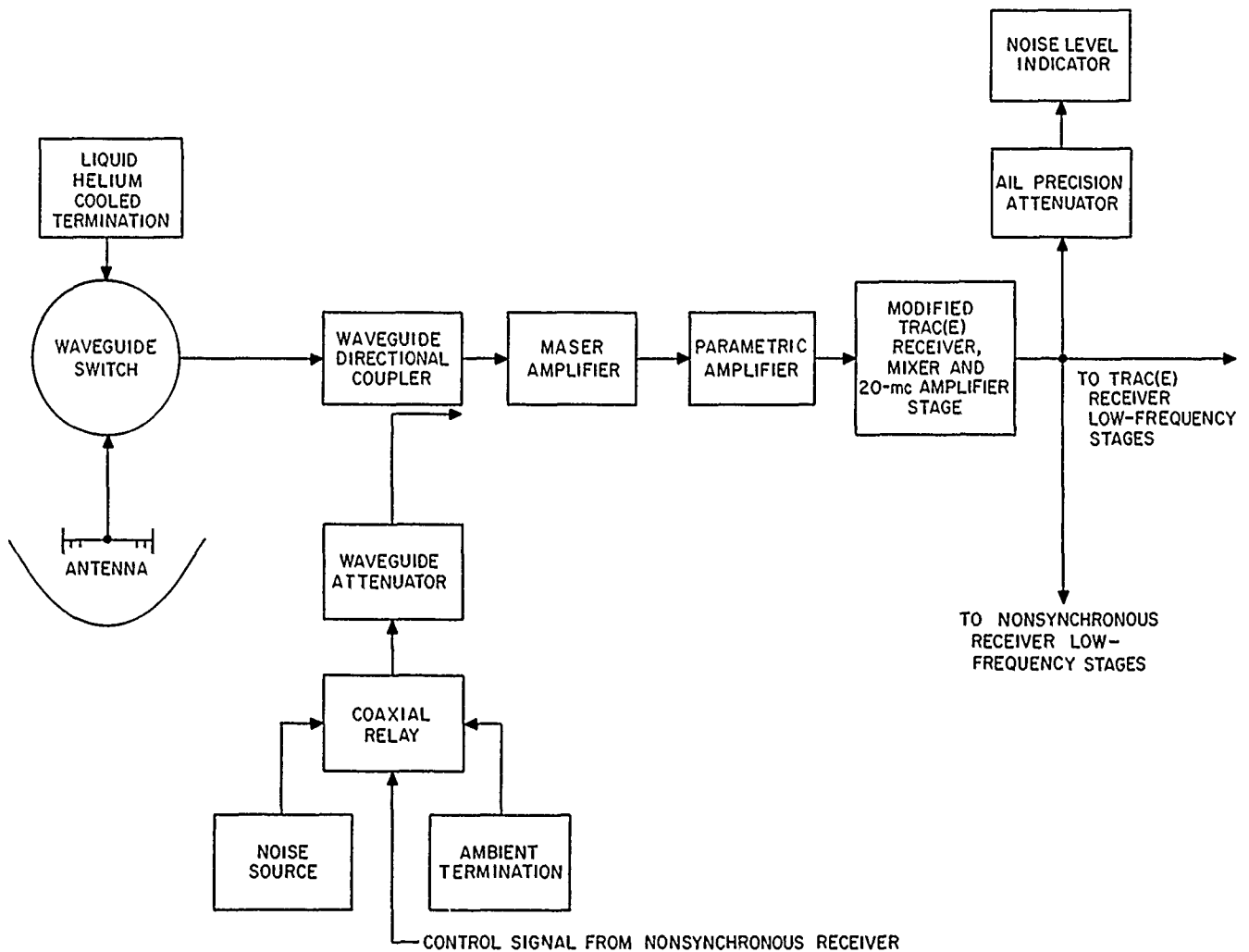


Figure 37. Venus radar system temperature measurement equipment

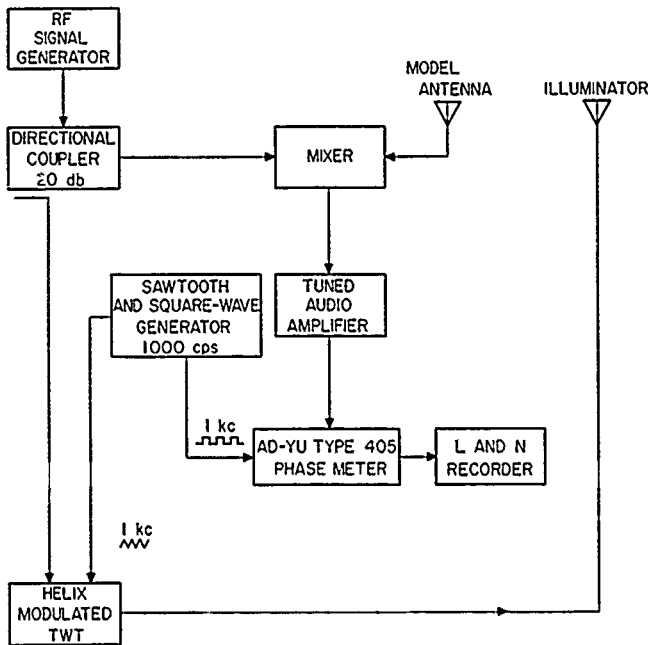


Figure 38. Phase measurement setup

Results of a phase-center measurement on a 960-mc feed horn are shown in Figures 39 and 40. Over the primary illumination angle of 120 degrees, with the phase center over the center of rotation, the phase shift is about ± 2.5 degrees. The accuracy of the system is about ± 2 degrees at present, limited by multipath reflections. The potential accuracy is much better. Figure 41 shows the simple horn positioning device used for the measurements.

Other advantages of the system are the wide frequency range capability due to the use of a traveling wave tube and the fact that the Serrodyne may be used to measure phase shift through waveguide or coaxial components.

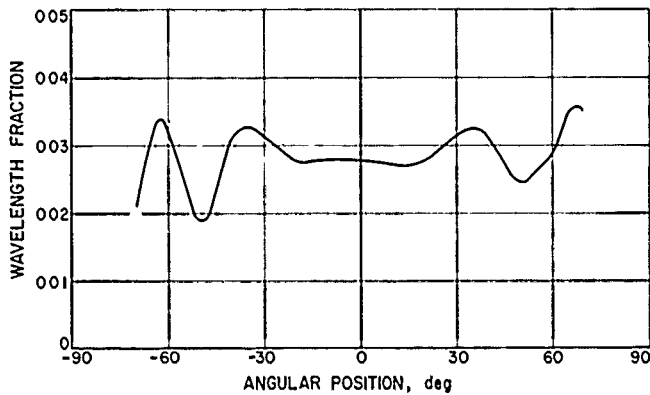


Figure 39. Antenna E-plane phase pattern

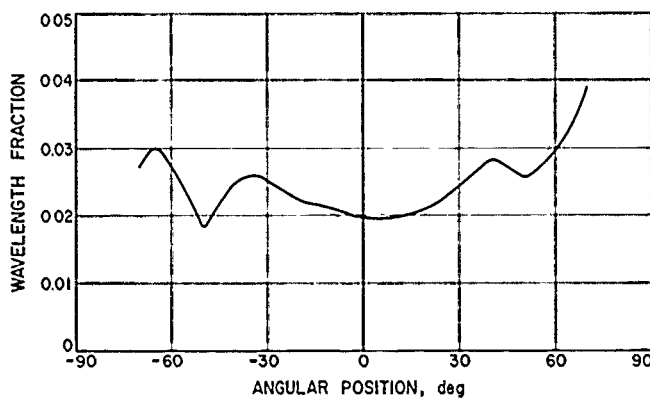


Figure 40. Antenna H-plane phase pattern

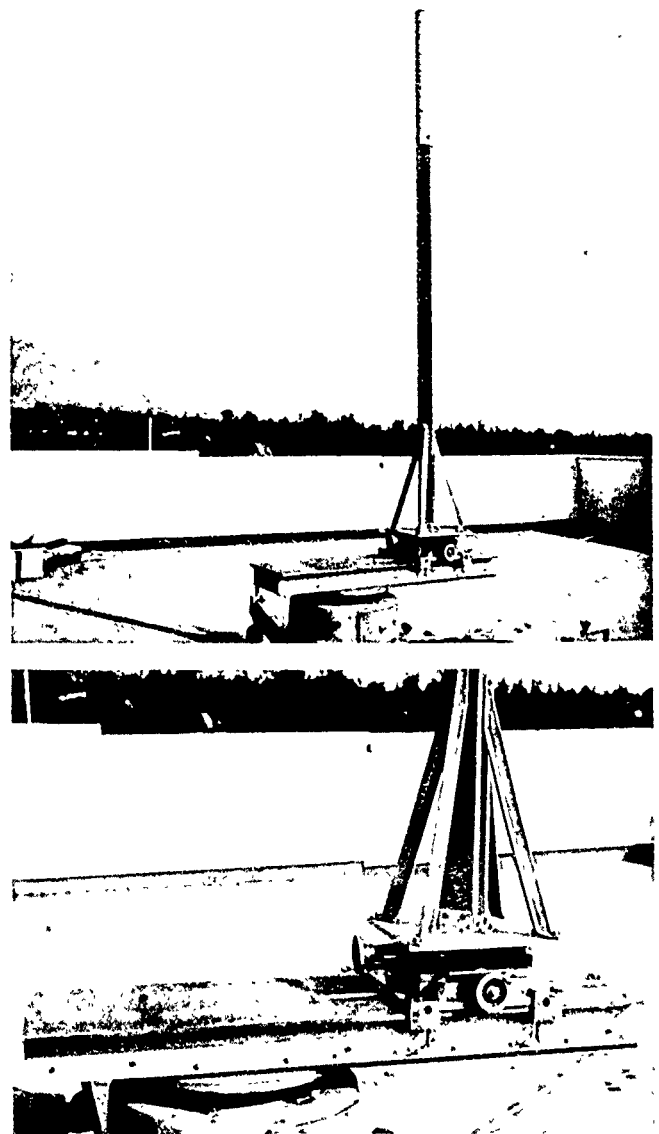


Figure 41. Antenna phase center positioner

C. Thin-Film Techniques

J. Maserjian and H. Erpenbach

1. Thin-Film Single Crystals

The concept of microzone growing of single crystals from semiconductor film has been under investigation for several months (RS 36-4, 36-5, 36-7, and Ref 29). Recent efforts include incorporation into the experimental apparatus of an improved electron-visual optical system. Prior to this, experiments were conducted in a less satisfactory system which did, however, provide some encouraging preliminary results.

The experiment utilizes a finely focused electron beam as a means of melting small areas or zones along a path on the film. The small dimensions (a few microns) require a high-performance electron-visual optical system. The original system, designed inside an EMU 2 electron microscope, provided satisfactory electron optics but lacked good visual optics.

Figure 42 shows a cutaway drawing of the new system incorporated in the electron microscope. The water cooled heater and specimen stage are the same as in the original apparatus. The major difference involves the use of light optics coaxial with the electron optics. In the original system, the light was reflected from a mirror above and to one side of the opening at the top of the heater jacket. The new system permits closer spacing of the electron lenses to the specimen for better beam focusing and allows a larger numerical aperture for the visual microscope objective. The objective also has the advantage of focusing in the plane of the specimen surface. Great care was necessary in selecting a suitable objective lens and preserving its optical alignment in the system. Initial tests on the new system have been highly satisfactory, but melting experiments have not been conducted, as yet.

It was suggested in RS 36-7 that the presence of sufficiently large crystal grains in the original semiconductor film may have a detrimental influence on the single crystal growth process. Efforts to evaporate films at lower substrate temperatures in order to obtain less grainy deposits have been complicated by poor adherence of the film to the substrate.

Improved adherence has been observed when the substrate is thoroughly baked out at high temperatures under high vacuum shortly before evaporation of the film. However, cracking and flaking occur during subsequent heat cycling if there is any significant mismatch of the coefficients of thermal expansion between the film and sup-

porting material. Sapphire has proved to be a good match for germanium; however, no corresponding material has yet been found for silicon. Attention was temporarily turned to silicon because of the availability of excellent preferential etches which can be used in the treatment of the microzone melted specimens. Attempts to use either sapphire or fused quartz with silicon have been unsuccessful. Attempts at using an intermediate film of lead (immiscible with silicon) as a means of relieving the strains were also unsuccessful. The choice of supporting materials is very limited because of all the thermal, electrical, and chemical requirements; the search is being continued.

Some germanium films evaporated with sapphire substrates maintained near room temperature have been successfully used in recent experiments without the occurrence of cracking or flaking. The microzone melted region did not show the rippled texture observed previously that seemed to relate to the grains of the adjacent film (RS 36-7). Figure 43a is a photomicrograph of a melted region which also reveals the very fine-grained or amorphous texture of the adjacent germanium film. The crystallized path, about 27 microns wide, is quite smooth except for the intermittent shrinkage crevices. Narrower paths were also melted, but the subsequent etching treatment makes this wider path a convenient region to study.

A reasonably good preferential etch for germanium may have been found (Ref 30), as indicated by the results seen in the photomicrograph of Figure 43b. The etching action produced a glossy smooth surface on the crystallized path which is more characteristic of single crystals. The texture of the surrounding film is seen to become increasingly rough with etching. The preferential action is noted particularly at the sides of the path where deep crevices have formed.

If the path crystallized with a (111) orientation at the surface, faster etching along the less dense planes at the sides would be expected. In addition, the surface of the path is focused slightly above the surrounding film, indicating the preferential action originally hoped for.

Figure 43c shows that further etching removed some of the crystalline path, indicating that the zone had not melted through to the underlying sapphire support. This is not surprising in view of the rather thick film used (10μ) and the minimum of heat which had been employed during the melting process. It may be a fortunate event if subsequent results indicate the sapphire support to interfere with the growth process. This has been open to speculation thus far. Comparison with the present results should provide some answers.

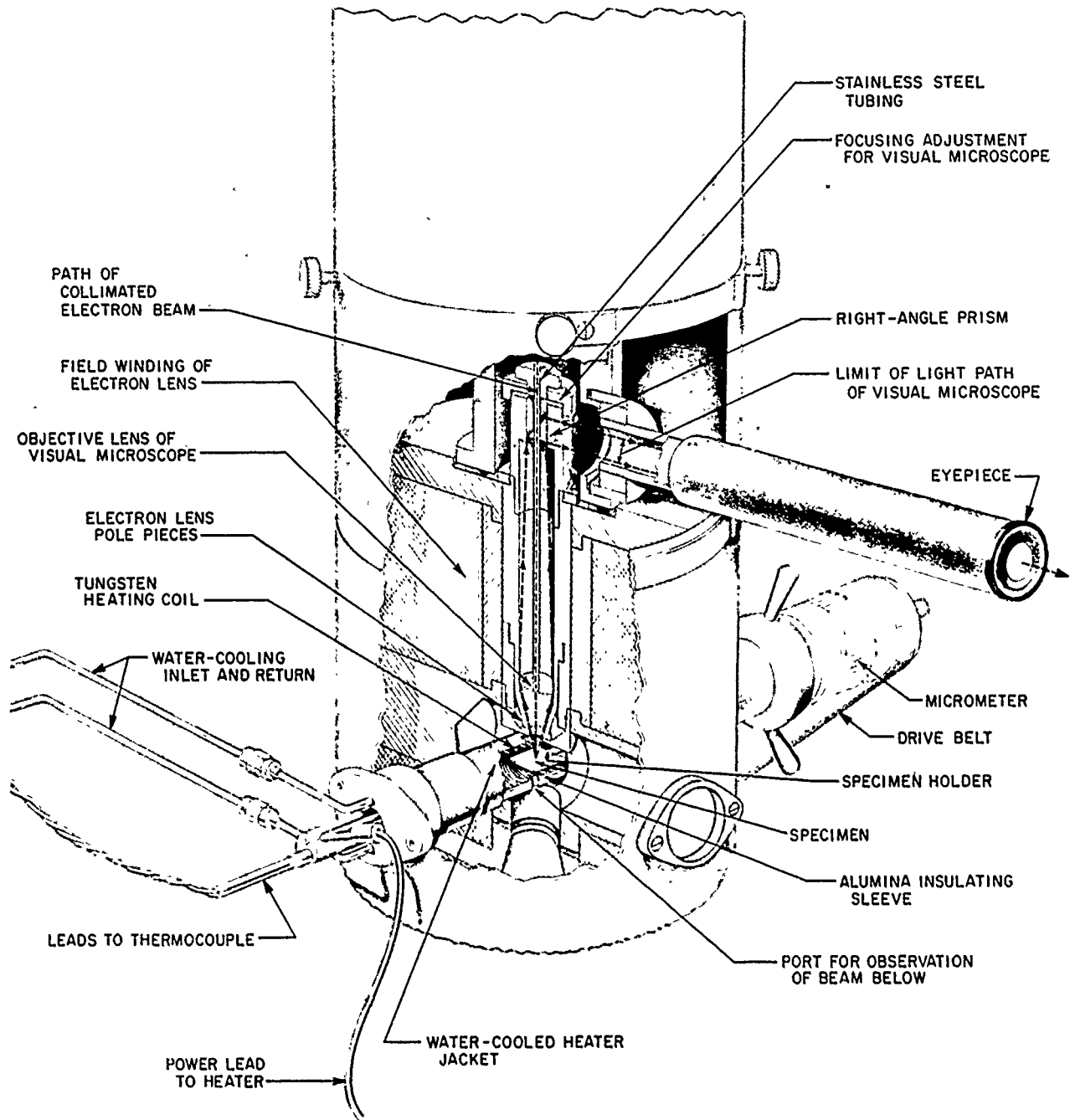


Figure 42. Electron beam melting apparatus in EMU2 electron microscope

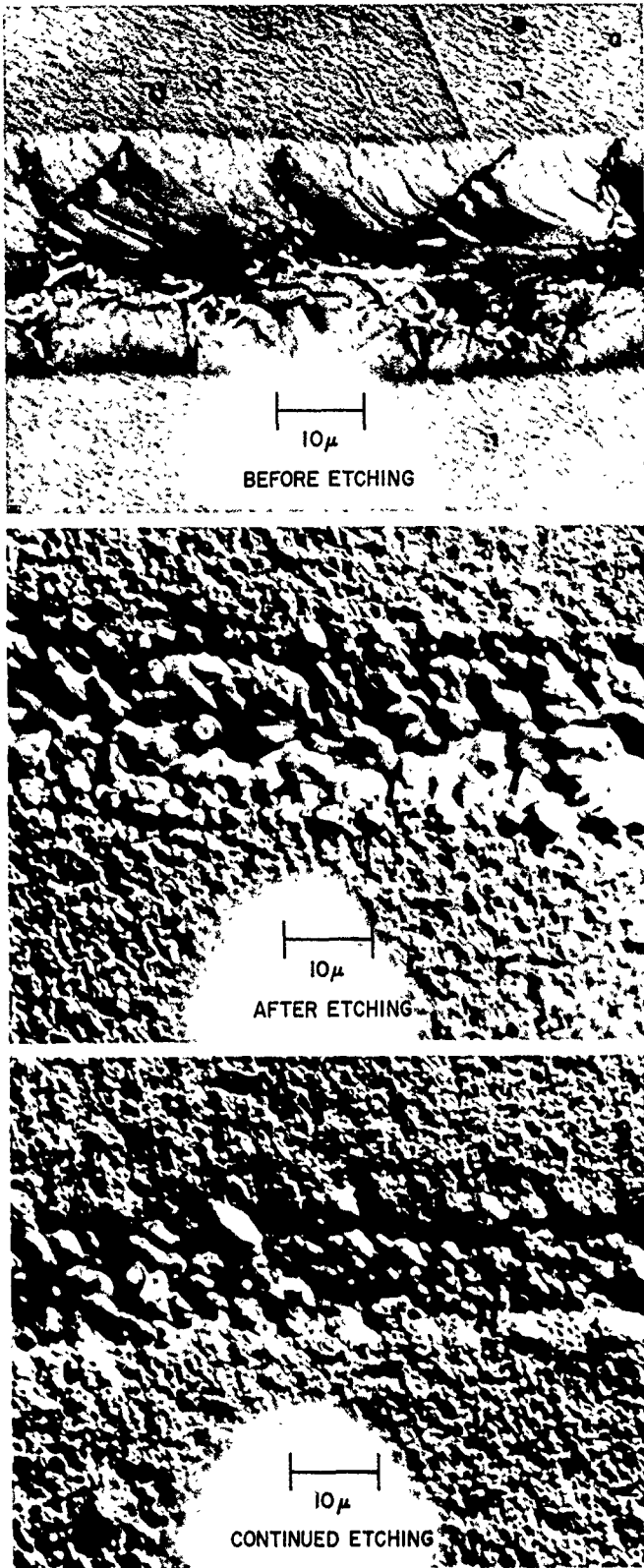


Figure 43. Photomicrograph of microzone melted path on germanium film before and after etching

2. Niobium Superconducting Thin Films

Work is continuing on the problem of depositing thin films of niobium, which are superconducting. Since the last report (RS 36-7), a film of niobium approximately 1.5μ thick has been deposited inside a cylindrical substrate. The deposition of the film was done in high vacuum by sublimation techniques, as shown in Figure 44. The film has been tested for superconductivity, and positive results have been obtained.

A cylindrical alumina (GE Lucalox) substrate was used for the following reasons: (1) The geometry of a cylinder is good for making experimental superconductivity tests. (2) The coaxial geometry and the resulting proximity of the niobium wire evaporant to the substrate wall will heat it to approximately 1000°C without external means. (3) The coefficient of linear expansion of alumina approximates that of niobium, and it may be heated to 1000°C in a vacuum.

Figure 44 shows the water cooled electrode terminals and the cylindrical substrate in place with the 0.025-inch niobium wire inside the cylinder. The electrode terminals are spring-loaded sufficiently to take up the linear expansion of the niobium wire.

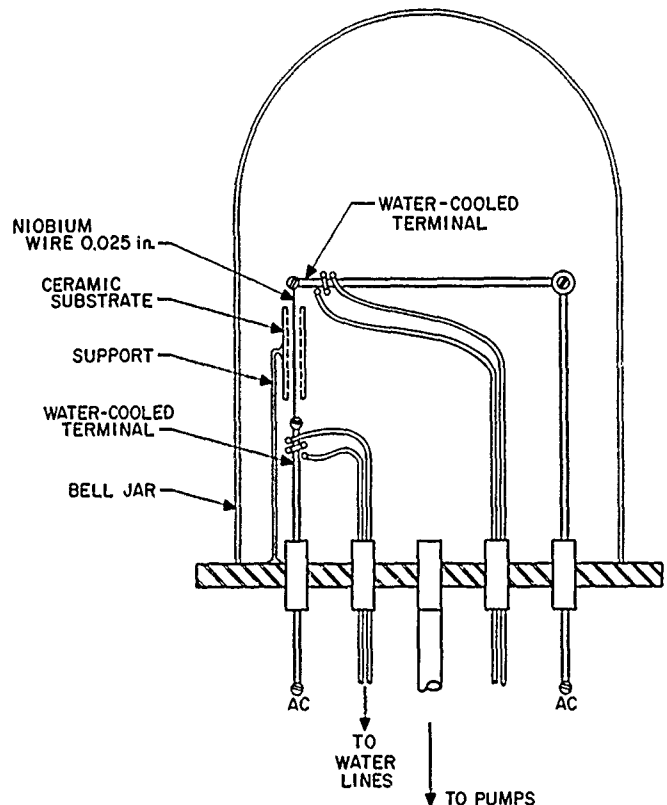


Figure 44. Vacuum chamber arrangement for niobium thin-film deposition

Before evaporation was attempted, a maximum current-temperature relationship for a given size wire is established with the substrate in place. To accomplish that, the vacuum system is pumped down to a pressure of 10^{-6} mm Hg, a current is passed through the wire and is increased slowly until the wire burns out; the number of amperes is then noted. From this information, the maximum current may be used during the evaporation, which is about 5% less than the burnout point.

The vacuum system is equipped with a liquid nitrogen trap and was capable of obtaining and holding a pressure of 10^{-6} mm Hg or better during the evaporation of niobium, which takes approximately 0.5 hour, depending on the size of wire used for the source.

A suitable device for the random rotation of a ceramic sphere at high temperatures for the purpose of evenly depositing refractory metal thin films by vacuum evaporation is shown in Figure 45. The 0.5-inch sphere is in position on top of the ceramic rod; it is held in place by a spherical depression in the end of the rod. By proper adjustment of frequency (about 70 cps) and amplitude (about 0.002-in. displacement) a point is reached where the rotation of the sphere is essentially random. Preliminary measurements of a niobium thin film deposited on a sphere using a four point resistance probe showed that the distribution of the thin film is very even. Tests have shown the deposited film to be superconducting.

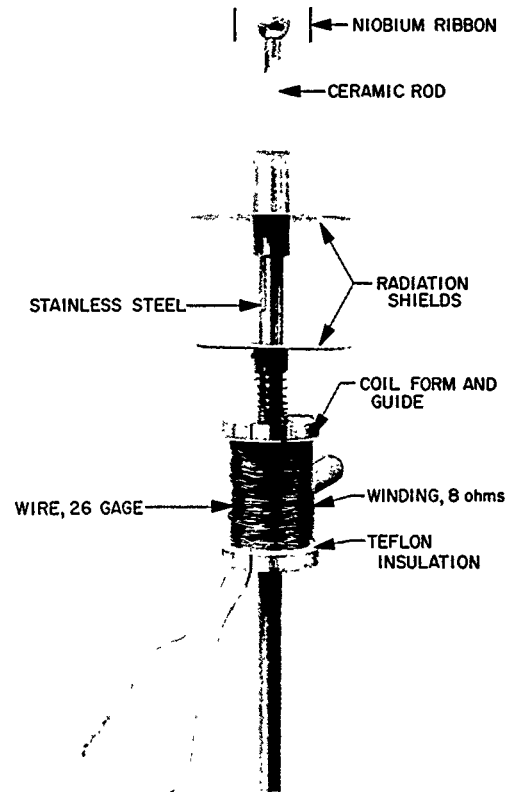


Figure 45. Support for uniform film deposition on spheres

IV. Communications Systems Research

A. Communications Research

W. V. Rusch, K. W. Linnes,
S. Frankel, and A. J. Viterbi

1. Analytical Study of Wide-Angle and Back Lobes of Paraboloidal Antennas

It is customary to treat a paraboloidal antenna as an equivalent radiating aperture in order to determine its radiation pattern. While adequately describing the main beam and small-angle side lobes of the antenna, this aperture field method is unable to reveal the nature of the wide-angle side-lobes or the fields behind the paraboloidal reflector. The minimum excess noise temperature of a UHF receiving antenna is determined primarily by the amount of the Earth's black-body radiation accepted by the back and wide-angle side lobes of the antenna. As part of an investigation of low-noise antennas, a study has been undertaken to provide a useful theoretical representation of the wide-angle and back-lobe radiation from paraboloidal antennas. The results of this study are intended to provide design information to reduce the equivalent noise temperature of DSIF antennas.

a. Obtaining fields from current distribution. The primary antenna feed is located at the paraboloid focus F , chosen also to be the origin of coordinates (Fig 46). The

current distribution over the inside of the paraboloidal reflector may be approximated by applying the laws of geometrical optics to the primary feed pattern (Ref 31). On this ray-optics basis, the current in the *shadow* region on the back of the reflector must be assumed to be zero.

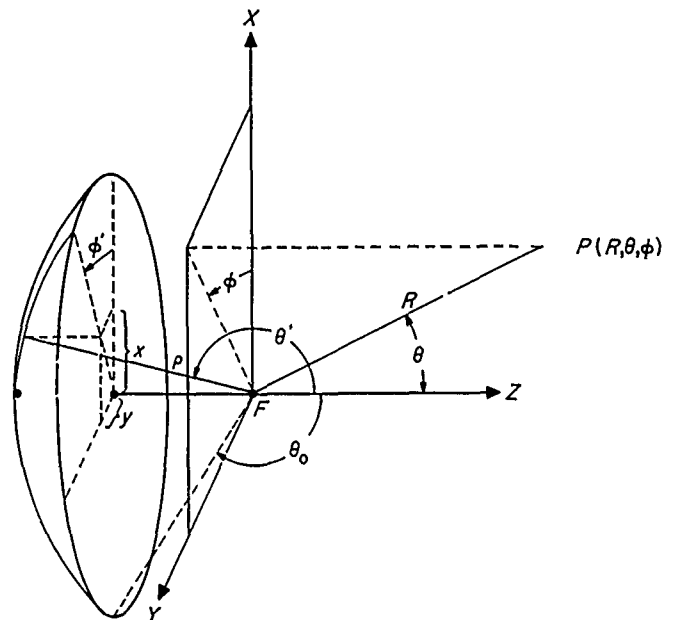


Figure 46. Antenna geometry

For a primary feed polarized along the x -axis, the vector surface current density is:

$$\bar{K} = 2 \sin \frac{\theta'}{2} \left[\bar{a}_x + \cos \phi' \cot \frac{\theta'}{2} \bar{a}_z \right] T(\theta', \phi') \frac{e^{jk\rho}}{\rho} \quad (1)$$

where \bar{a}_x and \bar{a}_z are unit vectors in the x - and z -directions, $\rho = f/\sin^2 \theta'/2$, f is the focal length, and $T(\theta', \phi')$ is the primary feed directivity pattern. No y -component of the current is excited by this feed polarization.

The radiation field is then obtained by integrating Equation (1) over the inner surface of the reflector (Ref 32),

$$E_\phi = \left[\frac{-j e^{jkR}}{\lambda R} \right] e^{jkz/\cos^2 \theta/2} \times \int_{refl} \frac{T(\theta', \phi')}{\rho} \sin \phi e^{jk\psi} \sin \frac{\theta'}{2} dS - \sin \phi T(\theta, \phi) \frac{e^{jkR}}{R} \quad (2)$$

where

$$\psi = \frac{x^2 + y^2}{2f} \sin^2 \frac{\theta}{2} - \sin \theta (x \cos \phi + y \sin \phi)$$

Direct radiation from the primary feed is also included in Equation (2).

If the primary feed directivity pattern is axially symmetric so that

$$T(\theta, \phi) = \frac{1}{2 \sin^2 \frac{\theta}{2}} g \left[\frac{1}{q \tan \frac{\theta}{2}} \right] \quad (3)$$

where $q = 1/\tan \theta_0/2$, then the field distribution in the reflector aperture is given by $g(r)/2f$, where

$$r = (\tan \theta_0/2)/(\tan \theta'/2)$$

the normalized aperture radius. Then, in the plane $\phi = \pi/2$, the total radiation field is:

$$E_\phi(\theta) = \left[-j\alpha q \frac{e^{jkR}}{R} \right] \left[e^{j(z/\beta)} \int_0^1 g(r) J_0(zr) e^{j\beta z r^2/2} r dr - \frac{j}{\beta z} g\left(\frac{1}{\beta}\right) \right] \quad (4)$$

where

- $\alpha = \pi(D/\lambda)$
- $D =$ diameter of antenna aperture
- $\beta = q \tan(\theta/2)$
- $z = \alpha \sin \theta$

The equivalent result for the aperture-field method is:

$$E_\phi(\theta) = \left[-j\alpha q \frac{e^{jkR}}{R} \right] \left[\frac{(1 + \cos \theta)}{2} \times \int_0^1 g(r) J_0(zr) r dr - \frac{j}{\beta z} g\left(\frac{1}{\beta}\right) \right] \quad (5)$$

However, Equation (5) is valid only for small angles, in which case (4) and (5) are in agreement. Equation (4) is valid for all values of θ , both in the directly illuminated region and in the shadow region behind the reflector within the range of validity of the geometrical optics approximation.

b. Evaluation of integrals. When the following aperture field distribution is assumed:

$$g(r) = (1 - r^2)^n, n = 0, 1, 2, \dots \quad (6)$$

the integral form of the field (4) becomes a Lommel function which can be expressed as an infinite power series of Bessel functions (Ref 32). However, since this series solution converges very slowly for large values of D/λ , Equation (4) has been integrated directly on the IBM 7090 computer. Results are presented in Figures 47 and 48 where the absolute gain function $G(\theta)$ is plotted for $n = 0$ (uniform illumination), $n = 1$, and $n = 2$. When axial symmetry is assumed, the gain function may be defined:

$$G(\theta) = 10 \log_{10} \left[\frac{2|E_\phi(\theta)|^2}{\int_0^\pi |E_\phi(\theta)|^2 \sin \theta d\theta} \right] \quad (7)$$

These theoretical results were calculated for the Goldstone DSIF antennas operating at 960 mc (Fig 47) and 2316 mc (Fig 48). The three aperture distributions $g(r)$ considered were: uniform distribution, $(1 - r^2)$, and $(1 - r^2)^2$, as shown in Figure 49. The primary feed patterns completely filled the reflector and were zero elsewhere; consequently, spillover effects were not considered. Local maxima in the gain were found at $\theta = 0$ (main beam), $\theta = \theta_0$ (the shadow boundary), and $\theta = \pi$.

In addition to making the evaluation of radiation patterns for larger D/λ ratios possible, direct numerical integration of Equation (4) also facilitates the evaluation for primary feed aperture field distributions $g(r)$, other than the idealized $(1 - r^2)^n$. The important problem of primary feed spillover can thus be evaluated with no additional mathematical difficulties. The gain function is presently being evaluated for various types of primary feed spillover. The results of this calculation will be translated into equivalent antenna noise temperature.

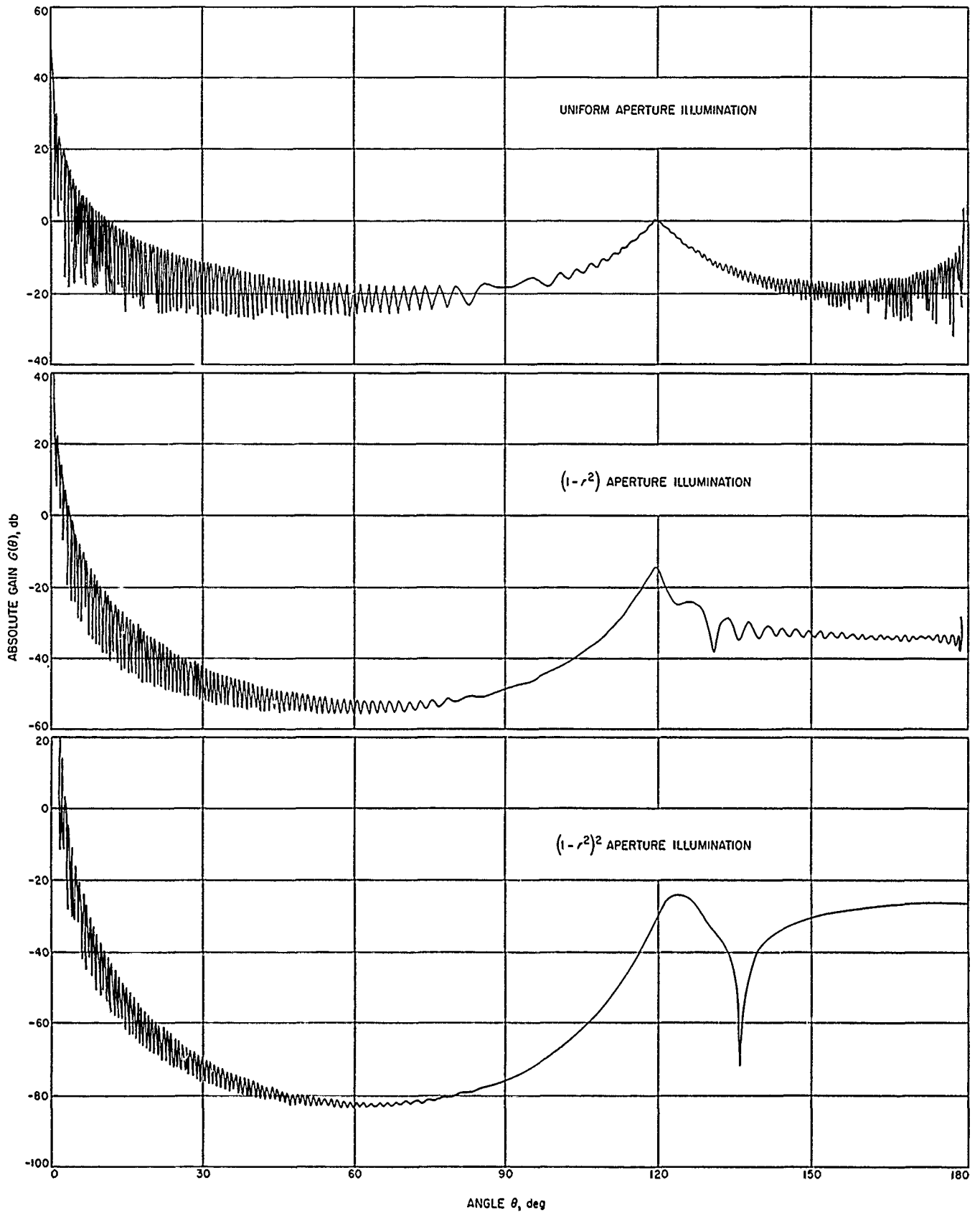


Figure 47. Absolute gain vs angle for $D/\lambda = 83$ and various aperture illuminations

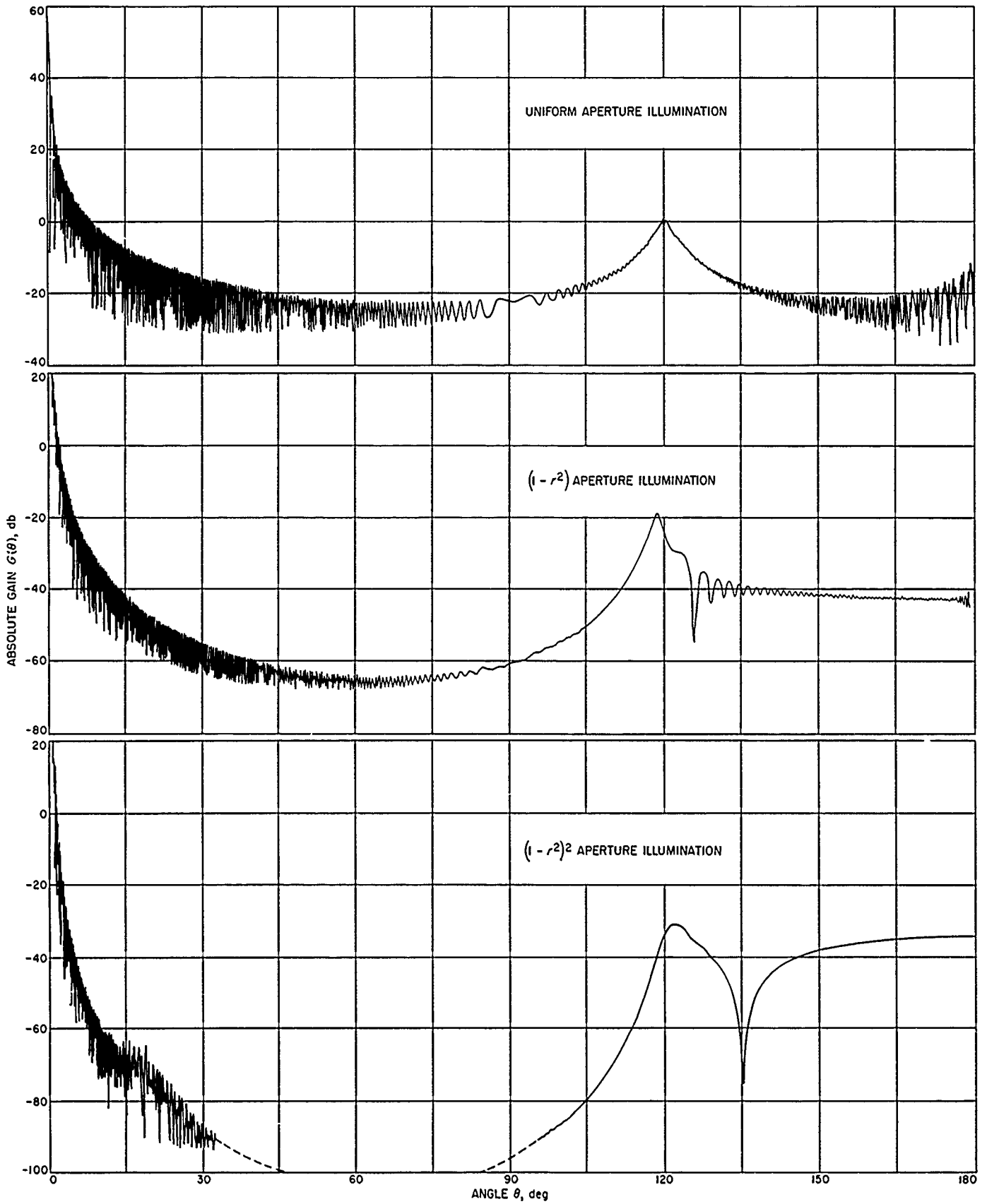


Figure 48. Absolute gain vs angle for $D/\lambda = 200$ and various aperture illuminations

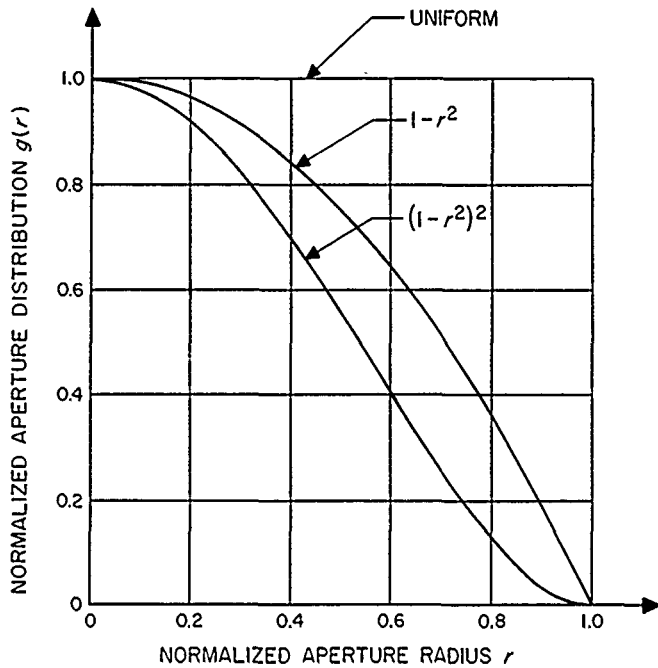


Figure 49. Aperture distributions

Both gain function and antenna temperature will be compared with recent experimental data from the Goldstone antennas.

2. Feasibility of Space Communications Using Optical Masers

a. Comparison of RF and optical systems. Recent publicity about coherent light obtained with optical masers contains statements to the effect that they offer attractive advantages in space communications. Principal among these advantages is the high *antenna gain* available at optical frequencies; however, no convincing and thorough analysis of such systems applied to lunar and planetary communications has been made to support these speculations. Therefore, a study was undertaken to determine the potential capabilities of a communications system using optical masers, commonly called lasers. The approach has been to make fairly optimistic assumptions about the development of optical components which may be made in the next decade and to compare the optical system with an RF system which is a reasonable and conservative extrapolation of the techniques used in the present DSIF. This comparison necessitates looking at the optical concepts and techniques from the point of view of the communications engineer, using such terms as antenna gain, mixer, and bandwidth, which are quite foreign to the field of optics but are perfectly straightforward analogs of the same ideas used at microwaves.

In order to compare the systems independently of modulation and demodulation methods, they are examined on the basis of the ratio of signal-power-to-noise spectral density as shown in Equation (1).

$$\frac{P_r}{\Phi_N} = \frac{P_t G_t G_r}{k T_s} \left(\frac{\lambda}{4\pi R} \right)^2 \quad (1)$$

where P_r is the received power in watts, P_t the transmitter power in watts, G_r the receiver antenna gain, G_t the transmitter antenna gain, Φ_N the noise spectral density in watts/cyc/sec, k the Boltzmann constant, T_s the equivalent system noise temperature, λ the wavelength in meters, and R the range in meters.

Comparing Equation (1) for RF and optical systems gives Equation (2) under the assumption of equal transmitter powers.

$$\frac{\frac{P_r}{\Phi_N} \Big|_{RF}}{\frac{P_r}{\Phi_N} \Big|_{opt}} = \frac{\left[\frac{G_t G_r \lambda^2}{T_s} \right]_{RF}}{\left[\frac{G_t G_r \lambda^2}{T_s} \right]_{opt}} \quad (2)$$

The actual transmitter powers potentially available should be included in a more complete comparison, but so little is known at present of the optical power potentially available that this step must be postponed for a future review of the subject. Modulation methods are also presently incapable of precise definition, and it is for this reason that the comparison made on the basis of Equation (2) is the fairest and most basic measure at this time.

b. Laser characteristics. Notable characteristics of optical masers are the high monochromaticity of their spectral lines and, equivalently, the high coherence of the emitted light. Line widths of 10^{-2} Å at 6900 Å have been reported (Ref 33). Radiating apertures 5 mm in diameter have produced beamwidths of 0.1 degree. Although the operating lasers described are pulsed, CW types are being investigated with encouraging results. Relatively high pulsed power (5 kw) has been reported, but no continuous lasers presently produce powers adequate for long-range communications. Considerable thought and effort is being devoted to components for modulating, mixing, amplifying and detecting light signals (Ref 33), but the state-of-the-art does not yet permit construction of receivers in the RF sense. Photomultiplier tubes are about the most effective detectors at present.

c. Optical transmitter antenna. The high gain desired in a transmitter antenna is directly related to the narrowness of the beam transmitted. It must be obtained either from the radiation characteristics of the laser itself or, if necessary, by assistance of an appropriate lens or mirror

system. A perfectly coherent source radiating through a circular aperture of diameter D would have a beam whose width between first minima is determined through the relation $\theta = 1.22\lambda/D$. The narrowest beam reported, about 0.1 degree for a diameter of about 5 mm, is far greater than the diffraction limit of the aperture. An optical system might be considered for narrowing the beam. In this case, the beam width is $\theta = D/f$, where f is the focal length of the mirror or lens. Laser output apertures on the order of 1 cm would require focal lengths greater than 10^3 cm or 10 meters to produce beams less than 0.1 degree. This is an impractical length for a spacecraft, particularly since it may be expected that experimentally achieved beamwidths of lasers will be reduced even further than the present 0.1 degree.

The optical beamwidth of 0.1 degree or 1.8×10^{-3} radian corresponds to a 3-db beamwidth of 0.085 degree or an antenna gain of 64 db. The diffraction limited beamwidth for the 5-mm aperture is 1.4×10^{-4} radian; the corresponding gain is 87 db. In Table 5, 75 db is taken for the optical transmitting antenna gain; an extra 10 db allows for future improvement.

d. Receiver antenna gain. The receiver antenna is taken as the largest optical telescope which may be considered feasible. For this purpose a 60-inch telescope is assumed because: (1) several exist, and (2) new ones could be built with a lead time of but a few years. The gain of such an aperture is 137 db for uniform illumination. Allowing 10 db for losses, 127 db is used as the value in Table 5. The resolution of a 60-inch telescope is about 2 or 3 seconds of arc on an average night. On nights when observing conditions are much better than average, it is 0.5 to 1 second; and under exceptional conditions it

approaches 0.2 second. The theoretical resolving power of a 60-inch telescope is 0.1 second of arc; therefore, the assumed degradation in gain of 10 db is quite optimistic.

e. System temperature. If a maser operates at a wavelength λ , the minimum noise temperature which could be theoretically attained is given by Reference 34 as

$$T \geq \frac{hc}{k\lambda}$$

where h is Planck's constant, k is Boltzmann's constant, and c is the velocity of light. At 100 kmc, this amounts to only 5°K. However, at 6900A it is 20,800°K. This is one of the most serious disadvantages of optical systems. In Table 5, this value is used for comparison without including other sources of noise except for 10 db for general inefficiency and allowance for deviation from the theoretically ideal. The other major disparity between the systems is the difference in space loss between the two operating wavelengths, displayed in the value dependent on λ . Had Equation (1) been written in terms of the effective radiating apertures, A_r and A_t , through the relation

$$G = 4\pi \frac{A}{\lambda^2} \tag{3}$$

the wavelength advantage would have accrued to the opposite system; however, the values assigned to the apertures would have counteracted to produce the identical end result.

f. The RF system. The system with which the optical system must compete is the RF system which is likely

Table 5. Comparison of RF and optical laser communications systems

Parameter	Symbol	RF system		Optical system		RF compared to optical, db
		Value	db	Value	db	
Transmitter antenna gain	G_t	--	45	--	75	-30
Receiver antenna gain	G_r	---	63	--	127	-64
Operating wavelength	λ	13 cm	22*	6900Å	-83	105
System equivalent noise temperature	T_s	70°K	-18.5 ^b	20,800°K	-53 ^{b,c}	34.5

Advantage of RF over optical system +45.5 db

*Obtained from $20 \log_{10} \lambda$, with λ in centimeters.
^bObtained from $-10 \log_{10} T_s$, with T_s in degrees Kelvin.
^cIncludes 10 db as receiver excess noise.

to exist at the end of a similar period of development. Since much more is known about RF systems than optical systems, it is simpler to estimate parameters conservatively and more accurately. The operating frequency will be about 2300 mc for some years to come. The system temperature presently obtained at Goldstone is about 70°K or less; this value is used in Table 5 although it should certainly drop 3 db or more in the future. The transmitting antenna gain is 45 db to correspond to a diameter of 10 meters. This size and larger is certain to be used in space communications in the next few years and is being investigated now. The ground antenna gain is 63 db, which corresponds to a 250-foot reflector at 2300 mc. Even if any of these values are too optimistic by a few db, inspection of Table 5 shows that the large difference in performance of the two systems will not be significantly affected.

g. Conclusions. The large discrepancy shown in Table 5 in favor of RF systems for long-range communications prompts one to inspect the various parameters to determine in which areas spectacular developments might make the two systems more comparable. The optical transmitter antenna has the greatest margin between probable and theoretically maximum performance. It is conceivable that a laser with an aperture diameter on the order of 10 cm might be developed which could give a gain over 100 db. Moding problems in the interferometer action presently render this unlikely. Whether or not this occurs, the problem of how to point the beam with sufficient accuracy toward the Earth is a practical problem of considerable difficulty which has been omitted in this discussion. The severity of the problem is indicated by the fact that a 75-db antenna gain corresponds to an angle of 0.036 degree or 2.1 minutes of arc.

The space loss could not be drastically reduced by operating at longer wavelengths since there is a limit to how far into the infrared region optical systems can be built.

The power available for transmission will come under scrutiny as the field develops. The present ruby lasers are relatively inefficient, and the CW gas lasers have low output levels.

Consequently, quite aside from such extremely difficult problems as pointing and efficiency, the optical systems do not, at present, appear to promise any advantage over conventional RF systems for deep space tracking and communications. However, since this situation may change drastically because of unforeseen developments, this problem will be reviewed periodically.

3. Coherent Synchronous Sampled Data Telemetry Systems

The consideration of transmission methods for sampled data is a significant communications problem for several reasons. First, by virtue of the well-known sampling theorem (Ref 35), any signal may be presented as sampled data with no loss of information provided the sampling rate is greater than twice its highest frequency. Second, certain types of modulation, notably those involving pulses, require sampling of the signal prior to modulation. Finally, the most practical reason is that certain types of data sources are of a sampled nature; i.e., commutators are employed which sample a given source periodically. Sampled data signals also afford an inherent degree of synchronization which can be used advantageously in a communication system.

For the evaluation and comparison of various modulation and detection systems, a generic performance criterion must first be stipulated. One of the simplest to measure and to calculate is a mean-square error criterion, which will be discussed in the next section. On this basis, a wide class of coherent synchronous communications systems will then be analyzed.

a. Error criteria. A general communication system for sampled data signals is shown in Figure 50. The channel interference is assumed to be white gaussian noise. Clearly, the value of the system depends on how nearly the output signal (within a scale factor) matches the transmitted signal. Path loss and transmitter and receiver gains will, of course, vary the output signal amplitude. Hence, for a comparison with the output signal, the data

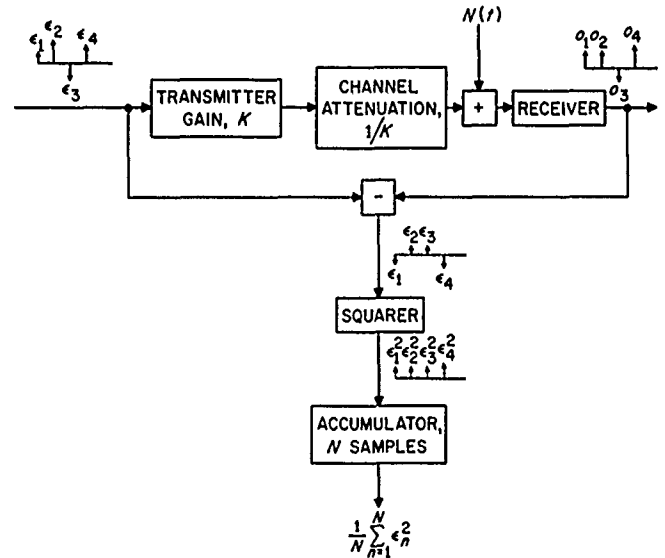


Figure 50. Measurement of mean-square error

signal must be amplified or attenuated by an appropriate factor K . Thus, the error in the n th sample will be $\epsilon_n = s_n - o_n$, where s_n would be the n th output sample in the absence of noise, and o_n is the actual n th output sample. It may be assumed that both the data signal and the output signal levels have been adjusted so that their means are zero. Then the error mean will also be zero.

There are several measures of how nearly the output resembles the data. The most common is the mean-square error which, for stationary signal and noise, is given by

$$\overline{\epsilon_n^2} = \lim_{N \rightarrow \infty} \frac{1}{N} \sum_{n=1}^N \epsilon_n^2$$

A simple method of measuring this is shown in Figure 50. A criterion which is more simply measured and generally equally valid is the mean-absolute error

$$|\overline{\epsilon}| = \lim_{N \rightarrow \infty} \frac{1}{N} \sum_{n=1}^N |\epsilon_n|$$

Although the mean-absolute error is precisely the same as the mean-square error when both the signal and noise are gaussian, it is not readily calculated when one of the two is not gaussian. Likewise, several other error criteria are equivalent to the mean-square error for gaussian distributions (Ref 36) but are hopeless to determine in general. Thus, for the sake of analytical feasibility, only the mean-square error will be considered. Of course, the magnitude of this parameter will depend on the data signal magnitude. For this reason it is necessary to normalize $\overline{\epsilon_n^2}$ by some parameter of the signal. The most significant such parameter is the data signal power or mean-square signal

$$\overline{s_n^2} = \lim_{N \rightarrow \infty} \frac{1}{N} \sum (s_n)^2$$

It is evident that both $\overline{s_n^2}$ and $\overline{\epsilon_n^2}$ have the dimension of power. For the sake of similarity to the well-known signal-to-noise ratio, the ratio $\overline{s_n^2}/\overline{\epsilon_n^2}$, or mean-square signal-to-error ratio, will be used here.

b. Classification of telemetry systems. A number of modulation methods of the continuous wave and pulse variety are in common use. Certain types (such as amplitude modulation) are basically for transmission of continuous signals rather than sampled data. However, even these have an equivalent form for sampled data. The following is a list of the forms of modulation which are generally accepted (Ref 37) and their sampled data equivalents:

- (1) Amplitude modulation, or pulse amplitude modulation (PAM).

- (2) Phase modulation, or phase shift keying (PSK).
- (3) Frequency modulation, or frequency shift keying (FSK).
- (4) Pulse duration modulation (PDM).
- (5) Pulse position modulation (PPM).
- (6) Pulse code modulation (PCM).

In this work, we shall be interested in coherent synchronous detection of the various forms of modulation; that is, the detection process will involve locally generated signals which are coherent to the transmitted carrier and synchronous with the sampled data rate. In this context, it will be shown that the six types of modulation may be detected coherently and synchronously by means of one of the following detection techniques:

- (1) Linear synchronous detection.
- (2) Correlation detection, or matched filtering.

The next two sections will treat the detection of the six forms of modulation by these two methods.

c. Linear synchronous detection. In this section it will be shown that pulse amplitude modulation (PAM), pulse duration modulation (PDM), and phase shift keying (PSK), can all be detected by a pulsed integrator synchronous with the sample transmission time and that the output signal-to-mean-square error ratio is a linear function of the channel signal-to-noise ratio.

Pulse amplitude modulation consists simply of extending the sample amplitude to last over the allotted transmission time of T seconds and multiplying the carrier by this waveform. This is shown in Figure 51a. In pulse duration modulation, a pulse is generated whose width is proportional to the amplitude of the sample. For this purpose, the sample must be amplitude-limited, say between $-A$ and $+A$. Then a sample of amplitude x_n (where $-A < x_n < A$) will produce a pulse of duration $[1 + (x_n/A)](T/2)$ seconds. In order to keep the transmitted power a constant, the pulse waveform is made to alternate between 1 and -1 rather than between 1 and 0. The waveform is then used to multiply the carrier (Fig 51b). In phase shift keying, the amplitude of the sinusoidal carrier is not varied, but rather its phase is varied from $-\pi/2$ to $\pi/2$, depending on the amplitude of the sample. Again, the data is assumed to be amplitude-limited between $+A$ and $-A$, and the phase of the carrier over a given sample transmission time is $\sin^{-1} x_n/A$ when the sample is x_n (where $-A \leq x_n < A$). Since the phase varies between $\pi/2$ and $-\pi/2$ it is, therefore, unambiguous. The phase waveform is shown

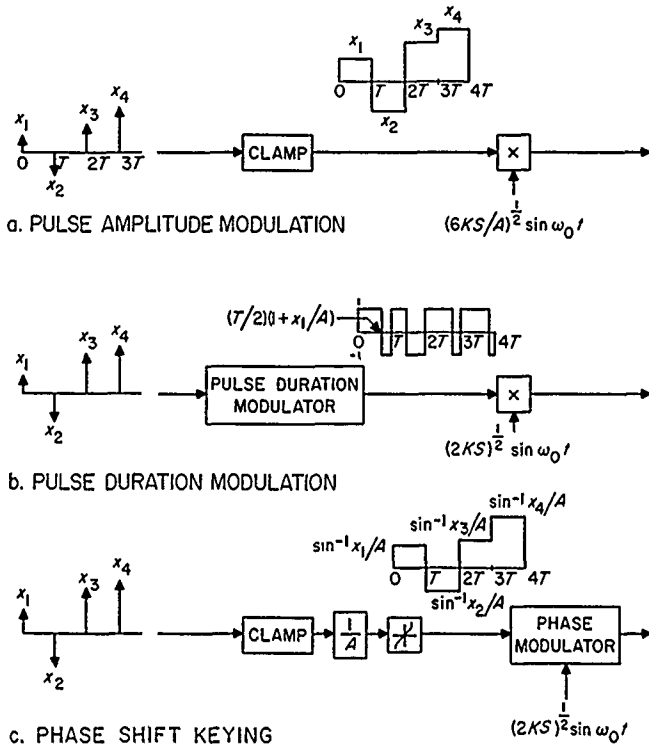


Figure 51. Modulation systems pertinent to linear synchronous detection

In Figure 51c. Both PDM and PSK have the advantage that they maintain a constant transmitted power, but in return they require a limited data amplitude. In PAM, the power varies from one sample transmission period to the next. A stringent limit need not be placed on the data amplitude, but peak power limitations are, nevertheless, present in the transmitter.

Mean-square signal-to-error ratio. The remarkable aspect of these three different modulated signals is that they can all be demodulated by the same synchronous detector; namely, a pulsed integrator (Fig 52). It should be noted, first of all, from Figure 51 that the power transmitted for PDM and PSK is KS watts, where S is the received power and $1/K$ the channel attenuation. Furthermore, if the data signal has a flat distribution between A and $-A$, as will be assumed henceforth, the transmitted power for PAM will also be KS watts. This follows from the fact that the power P in the transmitted signal envelope is

$$\int_{-\infty}^{\infty} x^2 P(x) dx = \frac{1}{2(6KS)^{1/2}} \int_{(6KS)^{1/2}}^{(6KS)^{1/2}} x^2 dx = 2KS$$

since the probability density of the envelope of the transmitted signal is $1/2(6KS)^{1/2}$ between $-(6KS)^{1/2}$ and $(6KS)^{1/2}$ and is zero elsewhere. The envelope power must be

divided by 2 to determine the power in the modulated sinusoid. It should be noted, however, that the power during a given sample transmission period of T seconds will vary from 0 to $3S$ watts; hence, the peak power is three times that for PDM or PSK.

Thus, the average signal power into the synchronous detector will be S . The first stage of the demodulator consists of a multiplier that is phase coherent with the received carrier, which shifts the spectrum to low frequencies. In the case of PAM (Fig 52a), the multiplier output over the n th sample period is

$$\left(\frac{3S}{A}\right)^{1/2} x_n (1 - \cos 2\omega_0 t)$$

The double-frequency term may be neglected since it will be discarded by the integrator, as will be shown. For PDM, the low-frequency output of the multiplier is the same as the modulating signal at the transmitter (Fig 51b) except for the gain factor of $S^{1/2}$ (Fig 52b). For PSK, the output of the multiplier during the n th sample period is

$$(2S)^{1/2} \sin\left(\omega_0 t + \sin^{-1} \frac{x_n}{A}\right) \cdot 2^{1/2} \cos \omega_0 t = S^{1/2} \frac{x_n}{A} \sin\left(2\omega_0 t + \sin^{-1} \frac{x_n}{A}\right)$$

Thus, the low-frequency component is $S^{1/2} x_n/A$ (Fig 52c). The second stage of the synchronous detector is a pulsed integrator which during each sample integrates for T seconds and is followed by an amplifier or attenuator with gain $1/T$. For the case of PAM, the low-frequency

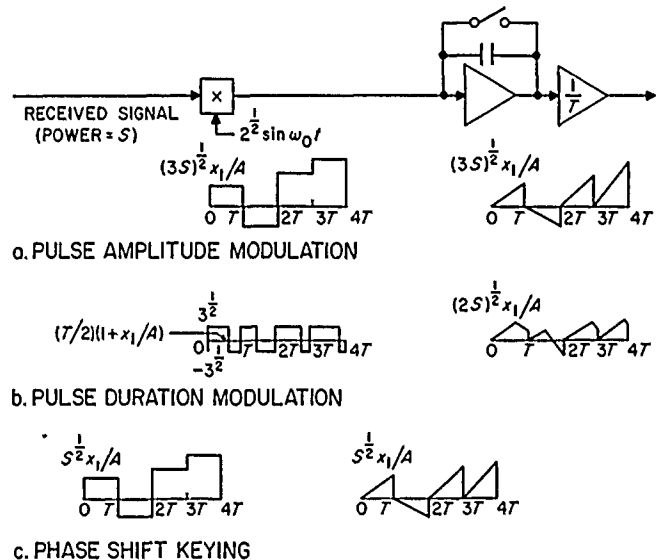


Figure 52. Waveforms at input and output of pulsed integrator for linear synchronous detection

component produces an output at time T of $3S^{1/2}x_n/A$, while the double-frequency term produces

$$-(3S)^{1/2} \frac{x_n \sin 2\omega_0 t}{A 2\omega_0}$$

at time T . If T is chosen such that $T = \pi k/2\omega_0$, where k is an integer (that is, if the data rate is a certain multiple of the carrier frequency) then the double-frequency term is 0 and may properly be neglected for all three types of modulation. For PDM, the integrator will produce a ramp of slope $S^{1/2}/T$ for $[1 + (x_n/A)]T/2$ seconds and a ramp of slope $-S^{1/2}/T$ for the remaining $[1 - (x_n/A)]T/2$ seconds (Fig 52b). Thus, the net output amplitude at the end of the sample transmission period is $S^{1/2}x_n/A$. For PSK, the integrator will produce a ramp of slope $S^{1/2}x_n/TA$ for T seconds, and thus, an amplitude of $S^{1/2}x_n/A$ at the end of the integrating period, the same as for PDM. Since the signal was assumed to have a flat distribution between $-A$ and A , the output signal power or mean-square signal at the end of the sample transmission time will be for PDM and PSK;

$$\overline{s_n^2} = \int_{-1}^1 S \left(\frac{x_n}{A} \right)^2 P(x_n) dx_n = \frac{S}{A} \int_{-1}^1 \frac{x_n^2}{2A} dx_n = \frac{S}{3}$$

For PAM since the output signal is three times as large

$$\overline{s_n^2} = S$$

Clearly, the output error will be the same in all cases since the same detector is used. It is assumed that the received noise $N(t)$ is white gaussian noise and has spectral density $N/2B$, where N is the noise power measured at the output of a bandpass filter of bandwidth B cps. The noise output of the multiplier will be $2^{1/2} N(t) \sin \omega_0 t$. Then the variance or mean-square error at the output of the synchronous detector at the end of the sample transmission period is

$$\begin{aligned} \overline{\epsilon_n^2} = \sigma^2 &= \frac{1}{T^2} \int_0^T \int_0^T \frac{2N(t)N(w) \sin \omega_0 t \sin \omega_0 w}{dt dw} \\ &= \frac{1}{T} (N/2B) \end{aligned}$$

Hence, in the case of PDM and PSK, the ratio of output signal power-to-mean-square error is

$$\overline{s_n^2}/\overline{\epsilon_n^2} = \frac{2ST}{3N/B}$$

For PAM, the ratio is

$$\overline{s_n^2}/\overline{\epsilon_n^2} = \frac{2ST}{N/B}$$

It should be emphasized that the factor of three superiority of PAM over PDM and PSK is due solely to the lack of a constant power restriction in this case. If the restriction were placed on PAM that the energy per sample transmission period were not to exceed that for PDM and PSK (i.e., if a peak power rather than an average power restriction were used) then all three forms of modulation would yield the same result.

The mean-square signal-to-error ratio at the output of the detector is shown in Figure 53 as a function of $ST/(N/B)$, the (received energy per sample)/(noise spectral density). It is now evident that the performance of this form of synchronous detection is a linear function of the channel parameters.

Bandwidth occupancy. A significant consideration in the evaluation of any communication system is the band-

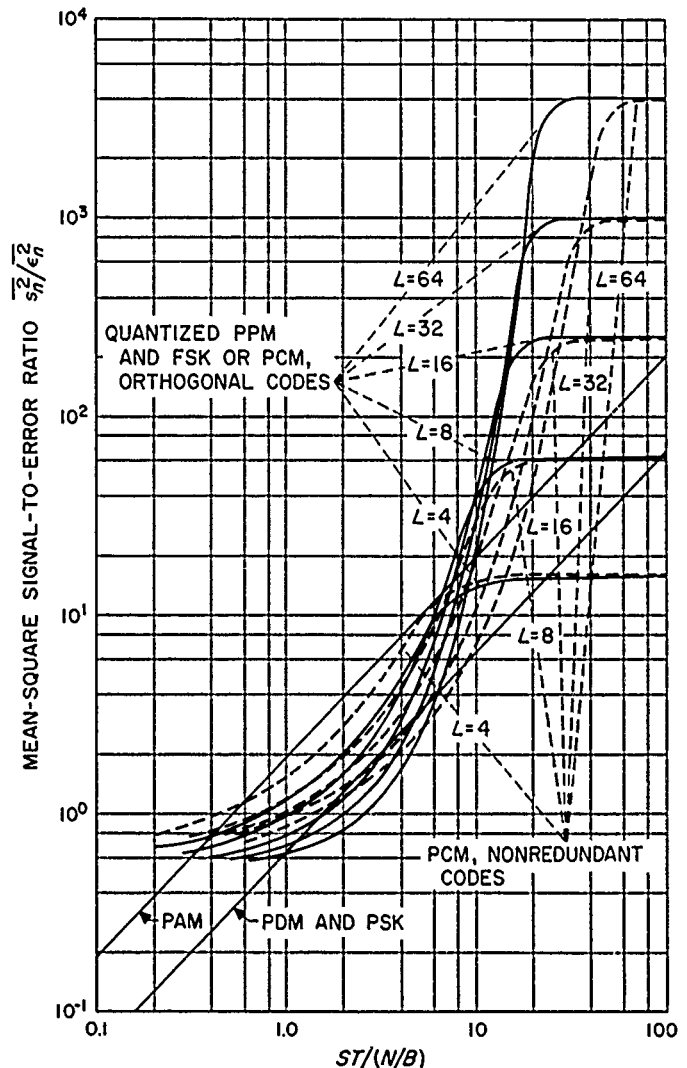


Figure 53. Mean-square signal-to-error ratio

width which it occupies. In this treatment, the bandwidth occupancy of a channel will be defined as the minimum frequency separation required between the given channel and an adjacent channel modulated in precisely the same manner so that the adjacent channel will have no effect on the detector for the given channel. In the case of PAM with a sample transmission period T , an adjacent channel similarly modulated must be placed $1/T$ cps away, or a multiple thereof, in order that the detector for a given channel will not be influenced. This is shown by the fact that the detector at the end of the transmission period will produce an output due to the adjacent channel of

$$\int_0^T 2^{1/2} \sin \omega_0 t \cdot 2^{1/2} \sin \left[\left(\omega_0 + \frac{2\pi}{T} \right) t + \phi \right] dt = 0$$

where ϕ is the arbitrary initial phase difference between the adjacent channel carriers. If ϕ could be made zero so that the various channel carriers were phase coherent, then the bandwidth separation of the channels could be cut in half to $1/2T$ cps.

The situation is the same for PSK since if the adjacent channel is transmitting a sample of amplitude y_n during a given transmission period, the output of the given channel detector at the end of the period will be

$$\int_0^T 2^{1/2} \sin \omega_0 t \cdot 2^{1/2} \sin \left[\left(\omega_0 + \frac{2\pi}{T} \right) t + \sin^{-1} \frac{y_n}{A} + \phi \right] dt = 0$$

However, in this case the bandwidth occupancy cannot be cut in half by making $\phi = 0$, since the phase is modulated and, hence, adjacent channels can not be made phase coherent.

Circumstances are less favorable for PDM. If the adjacent channel carrier is taken ω_D radians from the given channel carrier, a sample of amplitude y_n modulating the adjacent channel will produce a waveform at the given channel detector input which is $\sin [(\omega_0 + \omega_D)t + \phi]$ for the first $[1 + (y_n/A)]T/2$ seconds of the transmission period and is $-\sin [(\omega_0 + \omega_D)t + \phi]$ for the remainder. Thus, the given channel detector will produce an output at the end of the period which is

$$\begin{aligned} & \frac{1}{T} \left\{ \int_0^{(1 + \frac{y_n}{A})\frac{T}{2}} 2^{1/2} \sin \omega_0 t \cdot 2^{1/2} \sin [(\omega_0 + \omega_D)t + \phi] dt \right. \\ & \left. - \int_{(1 + \frac{y_n}{A})\frac{T}{2}}^T 2^{1/2} \sin \omega_0 t \cdot 2^{1/2} \sin [(\omega_0 + \omega_D)t + \phi] dt \right\} \\ & \approx \frac{2 \sin \left[\frac{\omega_D T}{2} \left(1 + \frac{y_n}{A} \right) + \phi \right] - \sin [\omega_D T + \phi]}{\omega_D T} \end{aligned}$$

The approximation is valid since the double frequency terms will be divided by $2\omega_0 + \omega_D \gg \omega_D$. Then the detector output due to the adjacent channel will be at all times less than $3/\omega_D T$, but it can not be made precisely zero because of the random nature of y_n . In order to maintain the channel cross-modulation below 1% at all times, it is necessary to make

$$\omega_D \geq \frac{300 \text{ rad}}{T \text{ sec}}$$

which means that the frequency separation must be greater than about $50/T$ cps. This is a serious handicap for PDM relative to PAM and PSK. These various results are summarized in Table 6.

d. Correlation detection. The forms of modulation which were not treated under linear synchronous detection were pulse position modulation (PPM), frequency shift keying (FSK), and pulse code modulation (PCM). The latter is strictly digital and needs to be considered separately in any case. PPM and FSK, however, could be used to transmit an analog sample. PPM involves varying the position or leading edge of a narrow pulse throughout the sample transmission period according to the sample amplitude. FSK varies the carrier frequency according to the sample amplitude. However, neither of these can be demodulated by a linear synchronous detector because this requires an averaging process over the transmission time. In PPM, the signal exists for only a small portion of this time; for FSK, time averaging can not be used to detect a frequency. On the other hand, the synchronous nature of sampled data can be used to

Table 6. Bandwidth occupancy for various detection and telemetry systems

Detection of modulation	Telemetry system	Bandwidth, cps	
		Adjacent channels not phase coherent*	Adjacent channels phase coherent*
Linear synchronous detection	PAM	$1/T$	$1/2T$
	PSK	$1/T$	$1/T$
	PDM	$50/T$, for less than 1% channel cross-modulation	
Correlation detection	Quantized PPM	L/T	$L/2T$
	Quantized FSK	L/T	$L/2T$
	PCM, orthogonal codes	L/T	$L/2T$
	PCM, nonredundant codes	$\log L/T$	$\log L/2T$

*The symbol T is the transmission time, and L is the number of quantization levels.

advantage if the samples are quantized into n levels, as will now be shown first for PPM and then for FSK.

Quantized PPM. The block diagram for a quantized PPM modulator and demodulator is shown in Figure 54. The sampled data is quantized into L levels (where L will be assumed even); depending upon the level of a given sample, a pulse will be generated in one of L possible positions in the sample transmission interval of duration T . Again, the data is assumed to have a flat amplitude distribution between $-A$ and A . If the amplitude of a given sample lies between $-Ak/(L/2)$ and $-A(k-1)/(L/2)$ (where k is a positive integer $L/2$), a pulse will be sent in the $(L/2 - k)$ th position; while if it lies between $A(k-1)/(L/2)$ and $Ak/(L/2)$, it will be sent as a pulse in the $(L/2 + k)$ th position. This is multiplied by the carrier and transmitted.

The receiver is again considered to be both phase coherent with the transmitted carrier and synchronous to the sampling period. The received signal is assumed to have power S watts. Thus, each pulse of width T/L must be of amplitude $(2SL)^{1/2}$. If the path loss is $1/K$, the transmitted power must be KS watts. The output of the first multiplier in the demodulator has a low-frequency component which is a pulse of amplitude $(SL)^{1/2}$ and of width T/L during a given sample transmission period (Fig 54) plus a double-frequency component which is eliminated in the detection, as will be shown. This signal is fed to a bank of L correlation detectors, each of which is matched to one of the L possible pulse positions. Each detector consists of a multiplier whose other input during the given period is a pulse occurring at one of the L possible positions; this is followed by an integrator of gain L/T which integrates over the sample transmission period and is then discharged. Thus, in the absence of noise the correlator corresponding to the received pulse position will produce an output of magnitude $(SL)^{1/2}$ while all the other correlator outputs will be zero. All these outputs are sampled at the end of the sample transmission period and fed to a decision device which will select the greatest output to be the correct pulse position. This is known as a maximum likelihood detector and was first proposed by Woodward (Ref 38).

Noise in the channel of spectral density $N/2B$ watts/cps will produce a variance at the output of each correlator at the end of the sample transmission period equal to

$$\begin{aligned} \sigma^2 &= \left(\frac{L}{T}\right)^2 \int_0^T \int_0^T (N/2B) (t-u) (2^{1/2} \sin \omega_0 t) (2^{1/2} \sin \omega_0 u) dt du \\ &= \frac{L}{T} (N/2B) \end{aligned}$$

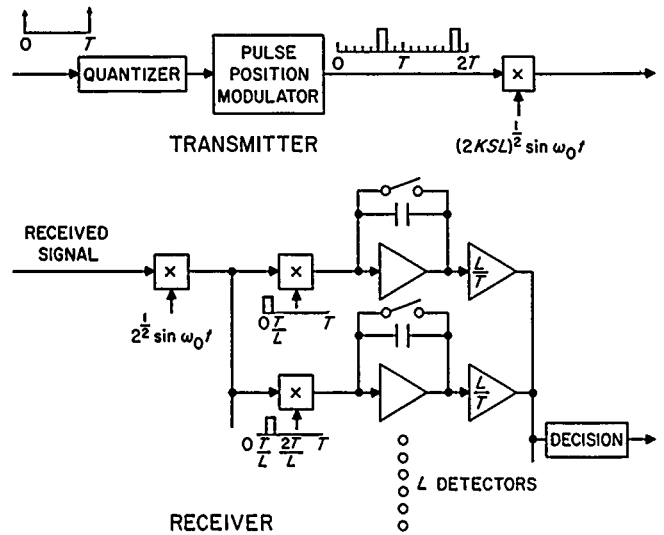


Figure 54. Quantized pulse position modulation system employing correlation detection

since the time over which the noise is integrated is T/L . Then, the ratio of correlator output to rms error for that correlator corresponding to the correct pulse position is

$$\frac{(SL)^{1/2}}{\sigma} = \left(\frac{2ST}{N/B}\right)^{1/2}$$

Furthermore, for white gaussian noise the outputs of the n detectors due to noise will be uncorrelated since each detector integrates over a different time period of duration T/L , and the input noise in each period is independent of the noise over any other because it is white.

Before the mean-square signal-to-error ratio $\bar{s}_n^2/\bar{\epsilon}_n^2$ can be determined, the probability of error in detecting any given sample must be calculated. The probability of detecting a given sample correctly is equal to the probability that the correlator corresponding to the position transmitted will have a greater output than all the others. Thus, for gaussian noise the probability of error, which is 1 minus the probability of correct reception, is given by

$$\begin{aligned} P_E &= 1 - P(x_1 > x_2, x_3, \dots, x_n) \\ &= 1 - \prod_{i=2}^n P(x_i < x_1) \\ &= 1 - \int_{-\infty}^{\infty} \frac{e^{-\frac{(x_1 - \sqrt{SL})^2}{2\sigma^2}}}{(2\pi)^{1/2} \sigma} dx_1 \left[\int_{-\infty}^{x_1} \frac{e^{-\frac{x_i^2}{2\sigma^2}}}{(2\pi)^{1/2} \sigma} dx_i \right]^{n-1} \end{aligned}$$

where

$$\sigma^2 = \frac{L}{T} (N/2B)$$

The second equality holds because the various correlator outputs are independent. By proper substitutions this equation can be shown to become

$$P_E = 1 - \int_{-\infty}^{\infty} \frac{e^{-w^2}}{(2\pi)^{1/2}} dw \left[\int_{-\infty}^{\infty} e^{-\left(\frac{z}{N/B}\right)^2} \frac{e^{-\frac{z^2}{2}}}{(2\pi)^{1/2}} dz \right]^{n-1}$$

Thus, the error probability is a function of the (received energy per sample)/(noise spectral density). This was evaluated by means of an IBM 704 computer for $L = 4, 8, 16, 32,$ and 64 . This is shown in Figure 55.

As a function of probability of error, the output mean-square signal-to-error ratio can now be determined. Since the noise outputs of all the correlators are independent, the probability of the result falling into any particular incorrect level is equal to the probability of its falling

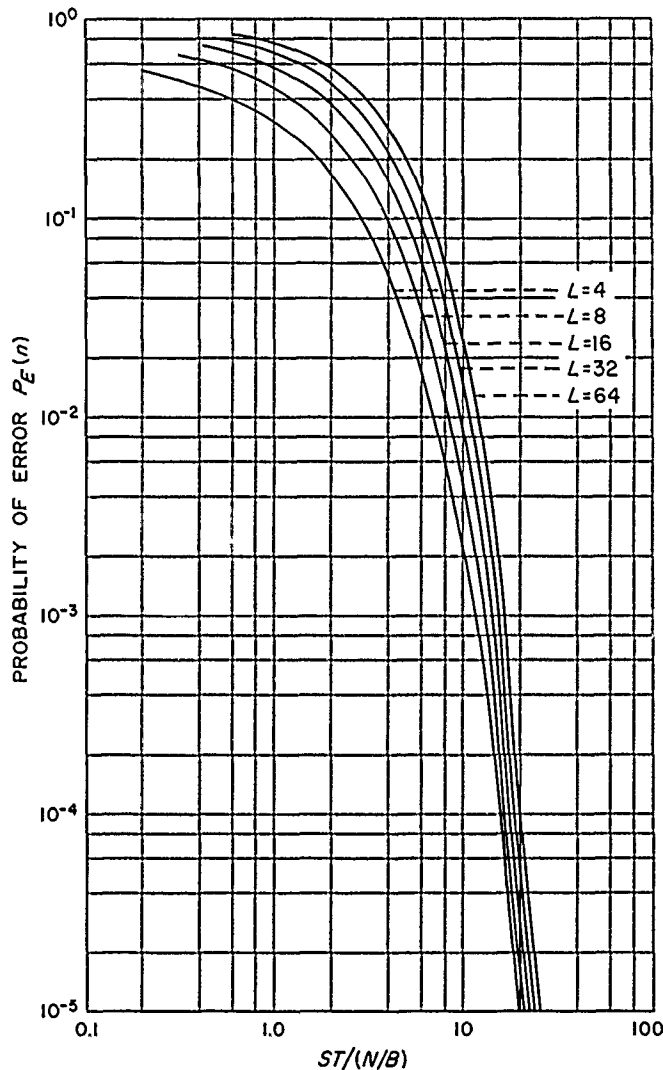


Figure 55. Detection error probabilities for quantized PPM and FSK

into any other incorrect level. However, the error amplitude is not independent of the signal amplitude since; for example, if a sample was sent which was in the highest positive level, only a negative error can result. Figure 56

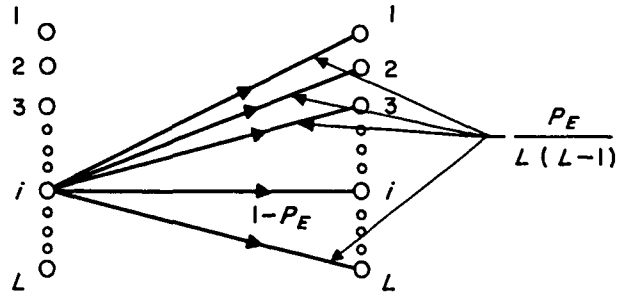


Figure 56. Transition diagram for quantized PPM

shows the transition diagram from transmitted level to detected level. Since P_E is the probability of making any error and there are $L - 1$ possible errors as well as n possible transmitted levels, the probability of any transition other than the correct one is $P_E/[L(L - 1)]$. It is clear from Figure 56 that there are two $(L - 1)$ ways in which a one-level error can be made, two $(L - 2)$ ways in which a two-level error can be made, down to only two ways in which an $(L - 1)$ -level error can be made. Positive errors and negative errors are equally likely. The sample amplitude is again evenly distributed between $-A$ and A . Thus, the probability distribution of errors is as shown in Figure 57a.

Since the sample amplitude is evenly distributed, the error due to quantization is evenly distributed between $-A/L$ and A/L about each level. Thus, the overall error probability density is as shown in Figure 57b.

On this basis, the mean-square error can be computed in terms of P_E :

$$\begin{aligned} \bar{\epsilon}_n^2 &= \int_{-\infty}^{\infty} x^2 p(x) dx \\ &= \frac{1 - P_E}{3} \left(\frac{A}{L}\right)^2 + \frac{P_E}{3(L-1)} \left(\frac{A^2}{L^3}\right) \\ &\quad \times \sum_{i=1}^{L-1} (L-i) [(2i+1)^3 - (2i-1)^3] \\ &= \frac{A^2[1 + 2P_E(L^2 + L)]}{3L^2} \end{aligned}$$

At the same time, since the samples are evenly distributed between $-A$ and A , then

$$\bar{s}_n^2 = \int_{-1}^1 x^2 P(x) dx = \int_{-1}^1 \frac{x^2}{2A} dx = \frac{A^2}{3}$$

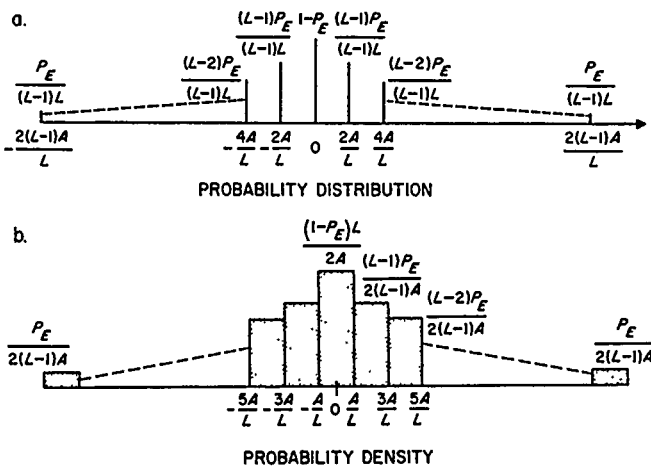


Figure 57. Probability distribution and density of errors for quantized PPM

Then the mean-square signal-to-error ratio is

$$\frac{\overline{S_n^2}}{\overline{\epsilon_n^2}} = \frac{1 + 2 P_E (L^2 + L)}{L^2}$$

Where P_E is given as a function of $ST/(N/B)$ and L in Figure 55. Combining these results $\overline{S_n^2}/\overline{\epsilon_n^2}$ is shown as a function of $ST/(N/B)$ for $L = 4, 8, 16, 32,$ and 64 in Figure 53.

Quantized FSK. The significant feature of the PPM system just described is the orthogonality of its transmitted signals. That is, the pulse signal $x_i(t)$ representing any given level over a sample transmission period is orthogonal to that representing any other level $x_j(t)$; i.e.,

$$\int_0^T x_i(t) x_j(t) dt = 0$$

This orthogonality can be achieved in a multitude of ways. For example, two sinusoidal signals differing in frequency by $1/T$ cps will be orthogonal over an interval of T seconds since

$$\int_0^T \sin \omega t \sin \left[\left(\omega + \frac{2\pi}{T} \right) t + \phi \right] dt = 0$$

This suggests the possibility of encoding the various quantization levels into a set of sinusoids spaced $1/T$ cps apart from one another in frequency and of duration T seconds. This system, which may be called quantized frequency shift keying, is shown in Figure 58. Each sample is quantized and, depending on its level, one of the L stored (or locally generated) sinusoids is transmitted over the sample transmission period T . The demodulator consists of a bank of correlation detectors each of which multiplies the received signal by one of the L frequencies and then integrates the product synchronously for T

seconds and attenuates it by $1/T$. In the absence of noise, the correlator corresponding to the received signal produces an output at time T which is

$$\frac{1}{T} \int_0^T 2S^{\frac{1}{2}} \sin^2 \left(\omega_0 + \frac{2\pi n}{T} \right) dt = S^{\frac{1}{2}} \left[1 - \frac{\sin 2(\omega_0 T + 2\pi n)}{2(\omega_0 T + 2\pi n)} \right]$$

If ω_0 is a multiple of $\pi/2T$, then the output is simply $S^{\frac{1}{2}}$. The output of all the correlators will be zero because of the orthogonality. It should be evident at this point that the operation and evaluation of this FSK system is identical to that of the PPM system described above and that both the error probability and the $\overline{S_n^2}/\overline{\epsilon_n^2}$ ratio will be the same.

Bandwidth occupancy. It will now be shown that both the quantized PPM and FSK systems utilizing correlation detection utilize a bandwidth of L/T cps, where L is the number of quantization levels. It is clear from the previous discussion that this holds for FSK since FSK channels can be placed on both sides of the given channel, provided the frequencies of the adjacent channels are also spaced $1/T$ cps apart and the highest and lowest frequencies of the adjacent channels are placed $1/T$ cps from the lowest and highest frequency of the given channel.

For quantized PPM, if the carrier of the adjacent channel is placed L/T cps from the given channel, then the

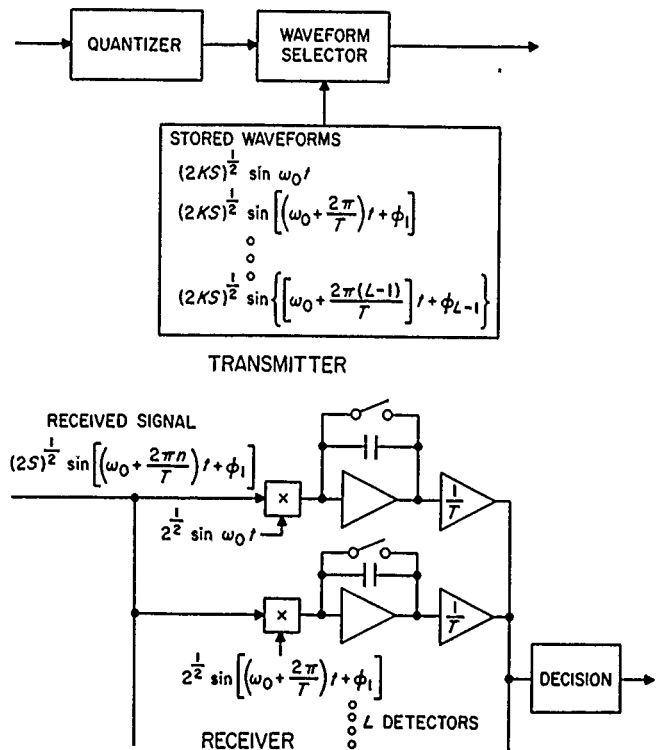


Figure 58. Quantized FSK system employing correlation detection

correlator for the given channel which corresponds to the pulse position of the adjacent channel will produce an output

$$\int_0^T 2 \sin \omega_0 t \sin \left[\left(\omega_0 + \frac{2\pi L}{T} \right) t + \phi \right] dt = 0$$

and, hence, no interaction occurs.

Finally, it should be noted that if the FSK frequencies can be made phase coherent or if the carriers for adjacent PPM channels can be made phase coherent, the same results can be obtained, but now the utilized bandwidth is cut in half and becomes $L/2T$ cps. This can be seen by changing the pertinent equations so that $\phi = 0$, and the second sinusoid is spaced half as far in frequency from the first. It will be seen that the integral of the product over the given time interval is still zero. These results are summarized in Table 6.

e. Pulse code modulation. Nonredundant codes. A pulse code modulation system is defined as one in which the samples are quantized and binary codes are sent to represent the various data levels. The simplest such system transmits the binary equivalent of the numeral value for the given data level by transmitting the pure carrier to represent a *zero* and modulating the carrier by π radians to represent a *one* (Fig 59). Thus, an L -level sample will be represented by a binary code of length $\log_2 L$ bits. The detector is a synchronous integrator which operates on each bit at a time for a period of $T/\log_2 L$ seconds and then decides whether a *zero* or a *one* was sent during that time. As described, this system utilizes correlation detection on a portion of the received sample code and should, therefore, be inferior to a system which detects the entire sample signal at once.

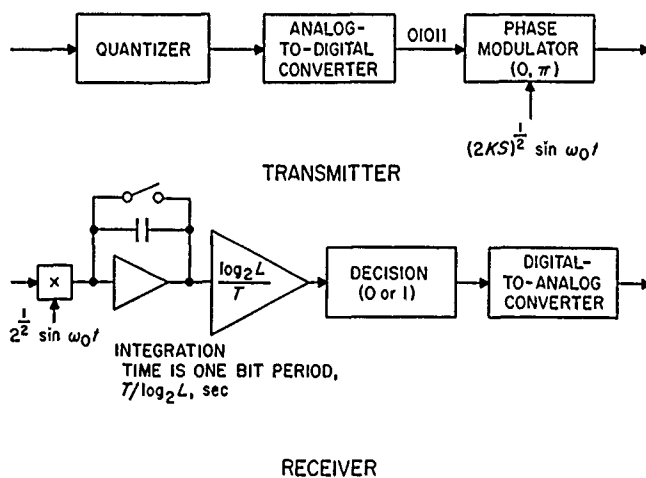


Figure 59. Nonredundant PCM system

To determine the $\overline{s_n^2}/\overline{\epsilon_n^2}$ ratio, the probability of error per bit must be determined first. The signal in the absence of noise at the end of the bit period will be $\pm S^2$, the sign depending upon whether a *zero* or a *one* was set. The variance is

$$\begin{aligned} \sigma^2 &= \left(\frac{\log_2 L}{T} \right)^2 \int_0^{T/\log_2 L} (N/2B) \delta(t-w) (\sqrt{2} \sin \omega_0 t) \\ &\quad \times (\sqrt{2} \sin \omega_0 w) dt dw \\ &= \frac{\log_2 L}{T} (N/2B) \end{aligned}$$

Thus, the signal-to-rms error at time T when a *one* was sent is $[2ST/\log_2 L(N/B)]^{1/2}$. The probability of bit error when a *one* was sent is then the probability that the noise contribution at time T is less than $-S^2$ or

$$P_B = \int_{-\infty}^{-\left[\frac{2ST}{\log_2 L(N/B)} \right]^{1/2}} \frac{e^{-x^2}}{(2\pi)^{1/2}} dx$$

By symmetry, the error probability is the same when a *zero* was sent. This quantity is plotted as a function of $ST/\log_2 L(N/B)$ in Figure 60. The mean-square error can be determined from the probability of error, as was done in Section d. *Correlation detection*. For example, for $L = 4$ levels, the transition diagram is shown in Figure 61. From this diagram, the error distribution can be determined (Fig 62); and from Figure 62, the mean-square error can be determined as

$$\begin{aligned} \epsilon_n^2 &= \int x^2 P(x) dx = \frac{A^2}{3(4)^2} \left[P(0) + 2 \sum_{i=1}^3 P(i) (12i^2 + 1) \right] \\ &= \left(\frac{1 + 60P_B}{48} \right) A^2 \end{aligned}$$

where $P(i)$ is the probability of an i -level error. The mean-square signal is as before

$$\overline{s_n^2} = A^2/3$$

Then

$$\overline{s_n^2}/\overline{\epsilon_n^2} = \frac{16}{1 + 60P_B} \quad (L = 4)$$

Similarly, for $L = 8, 16, 32,$ and 64 the mean-square error can be determined to be

$$\overline{s_n^2}/\overline{\epsilon_n^2} = \frac{64}{1 + 252P_B} \quad (L = 8)$$

$$\overline{s_n^2}/\overline{\epsilon_n^2} = \frac{256}{1 + 1020P_B} \quad (L = 16)$$

$$\overline{s_n^2}/\overline{\epsilon_n^2} = \frac{1024}{1 + 4092P_B} \quad (L = 32)$$

$$\overline{s_n^2}/\overline{\epsilon_n^2} = \frac{4096}{1 + 16,380P_B} \quad (L = 64)$$

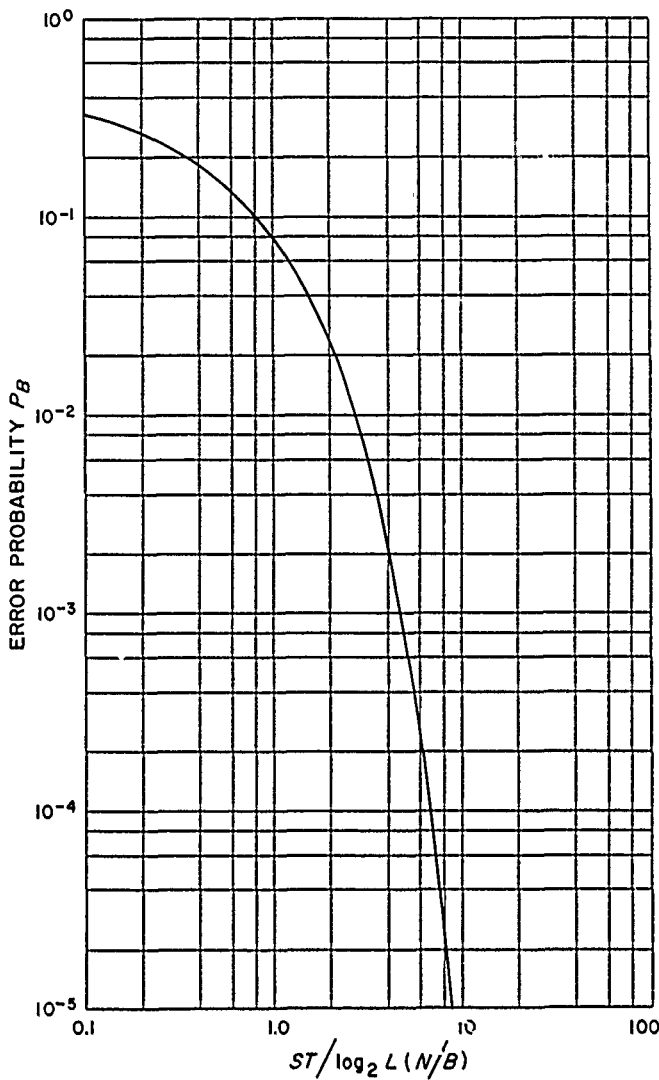


Figure 60. Bit detection error probability for PCM, nonredundant codes

Combination of these results with those of Figure 60 of P_B as a function of $ST/(N/B)$ yields $\overline{s_n^2}/\overline{\epsilon_n^2}$ as a function of $ST/(N/B)$, which is plotted in Figure 53 and is there compared with the other forms of modulation.

The bandwidth occupancy for nonredundant PCM is inversely proportional to the code bit period and hence is $(\log_2 L)/T$ cps.

Orthogonal codes. It can be shown (Ref 39) that a set of orthogonal signals can be generated with binary codes. This suggests the possibility of correlation detection for PCM; that is, each level will correspond to one binary code word which is orthogonal to all the rest. The receiver will consist of L correlation detectors, one for each binary code word (see Ref 39). Such a PCM system is equivalent to the quantized PPM and FSK systems, discussed in

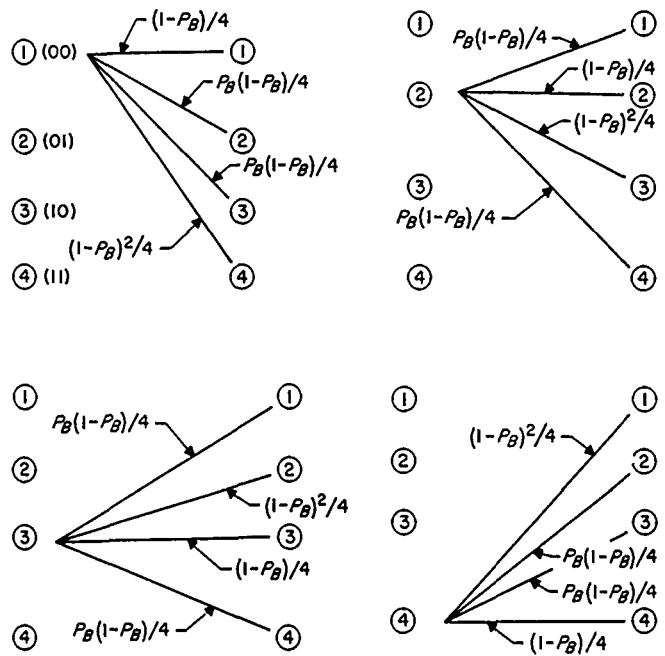


Figure 61. Transition diagram for nonredundant PCM, four levels

Section d , and the results for both $\overline{s_n^2}/\overline{\epsilon_n^2}$ and bandwidth occupancy are the same.

f. Conclusions. Figure 53 and Table 6 present the main results of this paper, and from these the pertinent conclusions can be drawn. It is clear that for reasonably high mean-square signal-to-error ratios, those modulation systems which are demodulated by correlation detection are significantly superior to those demodulated by linear synchronous detection since the former improve exponentially with increasing $ST/(N/B)$, while the latter improve only linearly.

The saturation of the curves for the correlation detection systems of Figure 53 is due to the quantization of the samples. No matter how low the channel noise may

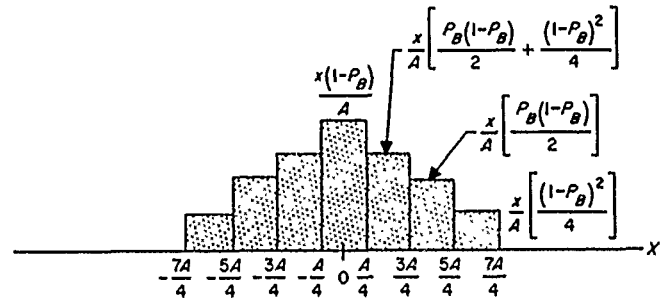


Figure 62. Probability density of errors for nonredundant PCM, four levels

become, the quantization noise will always be present and constant for a fixed number of levels.

Nonredundant PCM, which requires roughly $1/L$ th as much demodulation equipment as the orthogonal systems employing correlation detection, requires only about twice as much received energy to achieve the same results for $L = 64$ quantization levels.

PAM appears to be better than PDM and PSK by a factor of three among the modulation methods which may be demodulated by linear synchronous detection, only because the average power is the criterion. If a peak power criterion were used, the three systems would behave equally well.

PAM and PSK occupy the least bandwidth of all the systems considered, $1/T$ cps, where T is the sample transmission time. The orthogonal systems, quantized PPM, FSK and PCM with orthogonal codes, occupy L/T cps, where L is the number of quantization levels. Nonredundant PCM occupies only $(\log_2 L)/T$ cps. All the systems with the exception of PSK occupy half as much bandwidth if the adjacent channel carriers can be made phase coherent. Because it is impossible to make adjacent channels of PDM orthogonal to one another by appropriate frequency separation, PDM utilizes an excessive amount of bandwidth (approx $50/T$ cps) in order to maintain the channel cross-modulation less than 1%.

B. Information Processing

N. Zierler

1. Decoding Groups for Reed-Muller Codes

In References 40 and 41, a general method for decoding linear codes is described. In spite of the fact that the Reed decoding procedure for the Reed-Muller codes is quite efficient, it is of interest to apply the general method to these codes for the following three reasons. First, the Reed decoding procedure for an r th order code of block length 2^n will correct all errors of norm less than 2^{n-r-1} but almost no others, while the general decoding procedure will correct all correctible errors. Second, the Reed decoder computes first either the original message or its complement and resolves the ambiguity by a further operation; the general procedure computes the message directly and is probably somewhat

easier to instrument for that reason. Finally, the application of the general method to specific codes may be expected to yield further insight into the method with particular regard to its feasibility.

The principal tool in the construction of a decoding procedure by the method of References 40 and 41 is the group G of coordinate permutations of the space V of binary n -tuples which map the code subspace A on itself (actually, a sufficiently transitive subgroup will serve as well). The groups G for the first-order Reed-Muller codes of arbitrary block length 2^n have been characterized both as linear transformations on the spaces on which they act and also with regard to their abstract group-theoretical structure. It should be noted that each such group is a subgroup—and probably sufficiently transitive—of the corresponding group for all higher order codes of the same block length. These characterizations are sufficient for the computation of specific decoding procedures, and are as follows.

Let V be the space of binary 2^n -tuples, and let A be the first-order Reed-Muller code in V ; then A is the linear span of the $n + 1$ vectors

$$\begin{aligned} v_0 &= (1 \ 1 \ \cdots \ 1) \\ v_1 &= (1 \ 0 \ 1 \ 0 \ 1 \ 0 \ \cdots \ 1 \ 0) \\ v_2 &= (1 \ 1 \ 0 \ 0 \ 1 \ 1 \ 0 \ 0 \ \cdots \ 1 \ 1 \ 0 \ 0) \\ v_3 &= (1 \ 1 \ 1 \ 1 \ 0 \ 0 \ 0 \ 0 \ \cdots \ 0 \ 0 \ 0 \ 0) \\ &\vdots \\ v_n &= (1 \ 1 \ \cdots \ 1 \ 0 \ 0 \ \cdots \ 0) \end{aligned}$$

Note that v_0 is mapped on itself by every member g of $G = G_n$, and so g is completely determined by the specification of the images v_1g, \dots, v_ng of v_1, \dots, v_n under g .

Theorem 1. Let u_1, \dots, u_n be any linearly independent members of A whose linear span does not include v_0 . Then there is a (unique) member of G with

$$v_ig = u_i \quad i = 1, \dots, n$$

and every member of G_n is obtained in this way.

Theorem 2. Group G_n is the direct product of subgroups H_n and L_n , where H_n is of the type $(2, 2, \dots, 2)$ (n terms), and L_n is isomorphic to the general linear group of n dimensional space over $GF(2)$.

Corollary. The order of G_n is

$$2^n (2^n - 1) (2^n - 2) \cdots (2^n - 2^{n-1})$$

The proofs and further details will appear in a forthcoming article.

2. Optimal Search Procedures for Acquisition of a Single Target

In an optimal search procedure, it is known that a radiating point P lies within a region A of the celestial sphere. The search objective is to locate Point P within a subregion having an area s and a regular convex shape. The antenna can look at a fairly arbitrary subregion of A , but the integration time, i.e., the time it takes to decide whether or not the point lies in a given subregion, is proportional to the area of the subregion. Although the following assertion will be proved for only a rather special case, there seems little doubt that the assertion holds with essentially the stated generality. Let m be the a-priori distribution of P in A ; that is, if R is any (measurable) subset of A , then $m(R)$ is the a-priori probability that P lies in R . Let A_1, \dots, A_n be subregions of A , all of area s and of the desired shape (i.e., the target has been acquired when it has been determined in which of the regions A_i it lies) such that

- (1) $A \subset A_1 \cup \dots \cup A_n$, and A is not contained in the union of any smaller number of subregions of the same area and shape as A_i .
- (2) $m(A_1) \geq m(A_2) \geq \dots \geq m(A_n)$.

An optimal search procedure (one that minimizes the expected acquisition time) then consists of looking in sequence at the regions A_1, A_2, \dots until the target is acquired.

At first glance, one might expect that improvement could result from covering A with a smaller number of subregions B_1, B_2, \dots of area larger than s , determining in which B_i the point lies, then further locating P within that B_i . That this is not the case is clearly indicated by the following discussion.

Without loss of generality we take $s = 1$ as our unit of distance. Suppose A is a square with integral side. Let B_i be a subregion of A of integral area $b_i, i = 1, \dots, k$, and such that $A \subset B_1 \cup \dots \cup B_k$. Suppose that m is the uniform distribution over A ; i.e., $m(r) = \text{area } R/a$ for any (measurable) subset R of A , where a is the area of A . We shall compute the average time T it takes to determine to which of the sets B_i the point belongs (looking in order at B_1, B_2, \dots) and show that it is at least as large as the average total acquisition time for a procedure of the type described above.

Now the integration time for the region B_i is cb_i , where c is a positive constant, and T is made no larger by assum-

ing that the B_i are pairwise disjoint and exactly cover A ; thus, $a = b_1 + \dots + b_k$ and

$$\begin{aligned} T &= m(B_1)cb_1 + m(B_2)c(b_1 + b_2) + m(B_3)c(b_1 + b_2 + b_3) \\ &\quad + \dots + m(B_k)c(b_1 + \dots + b_k) \\ &= \frac{c}{a}(b_1^2 + b_2(b_1 + b_2) + b_3(b_1 + b_2 + b_3) \\ &\quad + \dots + b_k(b_1 + \dots + b_k)) \\ &= \frac{c}{2a}[(b_1 + \dots + b_k)^2 + b_1^2 + \dots + b_k^2] \\ &= \frac{c}{2a}(a^2 + b_1^2 + \dots + b_k^2) \end{aligned}$$

To minimize T , we must pick the partition b_1, \dots, b_k of a that minimizes $b_1^2 + \dots + b_k^2$; but this is obviously $b_1 = \dots = b_k = 1$ which corresponds precisely to a procedure of the type described above, and we have

$$T \cong \frac{c}{2a}(a^2 + a) = \frac{c}{2}(a + 1)$$

with equality for an optimal procedure, whose average acquisition time is thus $c(a + 1)/2$.

C. Digital Communications Techniques

M. F. Easterling, C. E. Gilchrist, and R. L. Choate

1. Ranging Subsystem

a. History of ranging experiments. A series of radar ranging experiments was conducted at Goldstone during the period October 1960 through January 1961. The overall objective of these experiments was to combine the various parts into an operating system and to test the resulting system in actual ranging operations using convenient Earth satellites. The *Echo* satellite was chosen for the first object to be ranged because it gave a large return signal and was often optically visible, making it easy to acquire. After some preliminary difficulties in getting the parts of the system to work properly together, the first successful ranging was performed on *Echo Pass 1107* on November 11. After 1 minute and 20 seconds of range tracking, the range lock was deliberately broken and re-established. After an additional 2 minutes and 40 seconds of range tracking, RF lock was lost momentarily. When the RF lock was re-established, the ranging code was

acquired again and another 30 seconds of ranging tracking obtained. Preliminary analysis and comparison of the data with the Ephemeris showed that actual ranging had occurred on all three acquisitions.

The following week, a successful ranging pass was obtained on November 17, followed by four consecutive passes on November 18. One of these passes had over 11 minutes in unbroken range tracking, and all four passes had the vernier operating for the entire time. However, in analyzing the data from these passes, it became evident that the range tally was counting the RF doppler with a wrong scale factor. Re-examination of the system showed that while the ratio of the RF VCO frequency in the receiver to the clock VCO frequency in the receiver was indeed 59¼ to 1, the ratio of the dopplers on these two frequencies was 60 to 1. The range tally had been designed using the 59¼ to 1 ratio.

Another set of four passes was obtained on November 23, this time without the vernier except for a short test section on the first pass.

It was desired that the vernier portion of the ranging system be tested, so the range tally, including the vernier, was redesigned and modified to include the correct ratio of dopplers, and another series of tests was run in January. By this time the *Echo* orbit was not being determined with sufficient precision for satisfactory acquisition, and the satellite was not often visible; therefore, another target was sought. The Goddard Space Flight Center was able to provide accurate Ephemerides for the *Courier*

satellite, and the addition of a low-noise parametric amplifier had increased the sensitivity of the receiver by an amount sufficient to permit the tracking of a *Courier*-reflected signal; therefore, the *Courier* was selected as the target. Because of the low level of the returned signal, the operating procedures had to be refined; but after this was done, five successful ranging passes were obtained: one on January 30, three in succession on January 31, and one on February 1. The vernier was in operation on all of these passes.

b. Analysis of Echo ranging data. The *Echo* passes for which ranging data was obtained are listed in Table 7. These passes fall naturally into three groups, as shown in the table. In the following discussion of results, the data from each group is treated separately.

Passes 1107 and 1185. For these *Echo* passes, the experimental range *r* from the Ha-Dec site, in meters, was computed from the formula

$$r = \frac{R^2 - D^2}{2 [R + D \cos(\Omega - z_1) \cos \beta_1]}$$

where *D* is the straight-line distance between the antennas of 10,705 meters (constant), Ω is the azimuth angle of the line between receiver and transmitter of 338.56583 degrees (constant), *z*₁ is the azimuth of the satellite in degrees, β ₁ the elevation of the satellite in degrees, and *R* the range from the Ha-Dec site plus the range from the Az-El site in meters. The respective values of *r* were then com-

Table 7. *Echo* passes ranged by Goldstone Tracking Station

Pass Group	Pass No.	Date	Greenwich mean time, hr: min	Ranging time, min: sec		Comments
				Without vernier	With vernier	
1	1107	11 Nov	10:40	01:20 02:40 00:30	— — —	First good ranging, isolated pass
	1185	17 Nov	11:54	02:00	—	Good ranging, isolated pass
2	1193	18 Nov	03:04	—	03:50	All of these passes have only vernier data and, because of the design error in the vernier, produced only non-reducible data
	1194	18 Nov	05:08	—	11:30	
	1195	18 Nov	07:14	—	01:40	
	1196	18 Nov	09:22	—	02:20	
3	1248	23 Nov	02:38	00:50	02:00	Resolution of ±1 clock cycle ambiguity possible because of three acquisitions on one pass
				01:40	00:40	
				01:20	—	
	1249	23 Nov	04:46	01:34	—	Good data except for possible ±1 clock cycle spurious count
				01:56	—	
	1250	23 Nov	06:54	00:16	—	Data bad, apparent equipment malfunction
02:22				—		
1252	23 Nov	11:01	02:56	—		

pared with the Ephemeris prediction ranges r_E . The values of r and r_E have been plotted in Figures 63 and 64 for the ranging portions of *Echo* Pass 1107 and in Figure 65 for the ranging portion of *Echo* Pass 1185.

It is apparent from these graphs that for each pass there is an appreciable error between r and r_E . However, it is equally apparent that the plots for r and r_E are in essence parallel, i.e., the error is constant to a first approximation. This leads one to believe that a time discrepancy exists between the predicted and measured ranges. The fact that on more than one occasion, before and since, orbital predictions had been found to be off in time by as much as 42 seconds while being correct otherwise lends support to this belief.

Two ranging portions exist for Pass 1107, between which a new RF acquisition took place. The time displacement for the first portion was estimated graphically to be 8.4 seconds. The time displacement for the second portion was estimated graphically to be 8.0 seconds. Obviously, any time error for a given pass must be constant. Therefore, an error of 8.2 seconds was assumed for this pass. Values of r , delayed by 8.2 seconds, were then marked on the graphs by crosses and found to be in excellent agreement with values of r_E .

For Pass 1185, the time displacement was estimated graphically to be 1.6 seconds. Values of r , delayed by 1.6 seconds, were then marked by crosses and found to be in excellent agreement with values of r_E .

Passes 1193, 1194, 1195, and 1196. These *Echo* passes represent some of the best tracking that has been done. Unfortunately, it is not possible to reduce the data since only vernier data with erroneous weighting was obtained. This situation exists because the range measurement is made in essentially two parts. The first part is to acquire the range code and establish a reference range. The second part is to keep the range up to date by counting doppler. In these passes, the reference point was not recorded. It was correct when it was obtained, but it was not recorded. The increments obtained can be corrected for the erroneous scale factor, but the initial point is lost. Checks of the internal consistency of the data and checks against the doppler show that, except for the erroneous scale factor, the system was working well.

Passes 1248, 1249, 1250, and 1252. The first three of these *Echo* passes were good passes. While preparing for the fourth pass, something in the system changed drastically. Attempts were made to rephase, but the fourth pass was not ranged because it was not possible to acquire

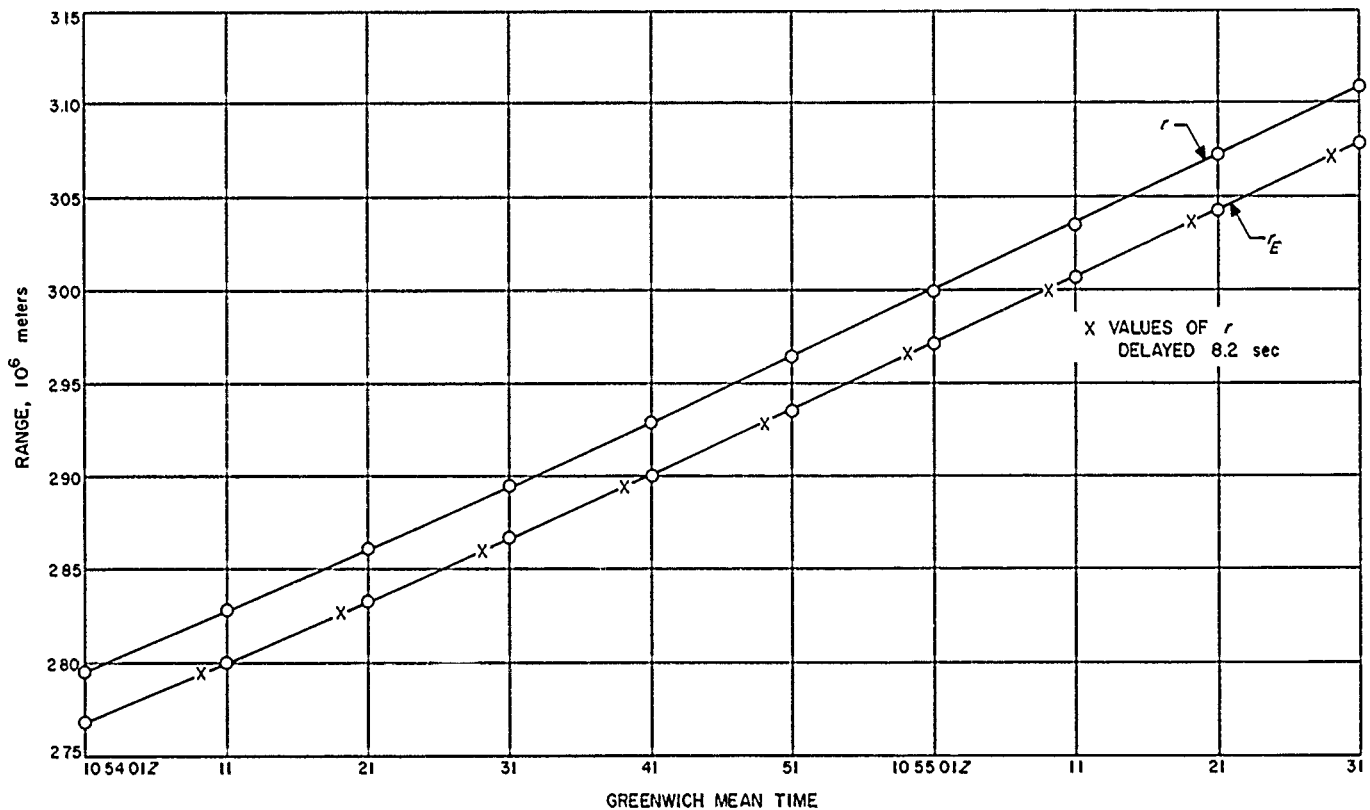


Figure 63. *Echo* pass 1107, first ranging portion

the range code over the passive link; only RF tracking was done during the fourth pass. By the time of the fifth pass, the situation (which was not and still is not, understood) was rectified sufficiently so that the range code could be acquired over the passive link, but not reliably. The ranging of the fifth pass is not good, partly because of the unexplained difficulty already mentioned and partly because of what appears to have been a malfunction in the range tally. Because of these difficulties, the data reduction has been restricted to Passes 1248, 1249, and 1250. An orbit was fitted to the angle and doppler data from these passes, using the IBM 7090 computer. From the orbit, the range to each of the sites was computed. The range measurement was compared with these computed ranges for all times for which good ranging data was available. The error was computed for each point, and the means and standard deviations for each acquisition were determined. These are given in Table 8.

The comparison was made in terms of the average of the ranges to each of the two antennas, with the error

being the measured quantity minus the computed quantity. The increment for the measured quantity is one clock cycle or 301.33 meters. Only two of the errors differed from the mean error by more than the increment, and they were differences of 304 meters and 303 meters. These are easily explainable as one increment plus a small error in the calibration. Checks were also made of the first and second differences of the ranges; it was found that they were in increments of 301 meters and smooth. The increments in the range number between each pair of points were compared with the average of the doppler for each pair of points and found to agree within less than the increment of the range number except for one pair where the error is slightly greater than one increment. This particular error is positive, while the errors for the two adjacent pairs are both negative showing that this particular time interval just caught a count at either end.

The several computations indicate that the data is smooth and self-consistent for each acquisition. How-

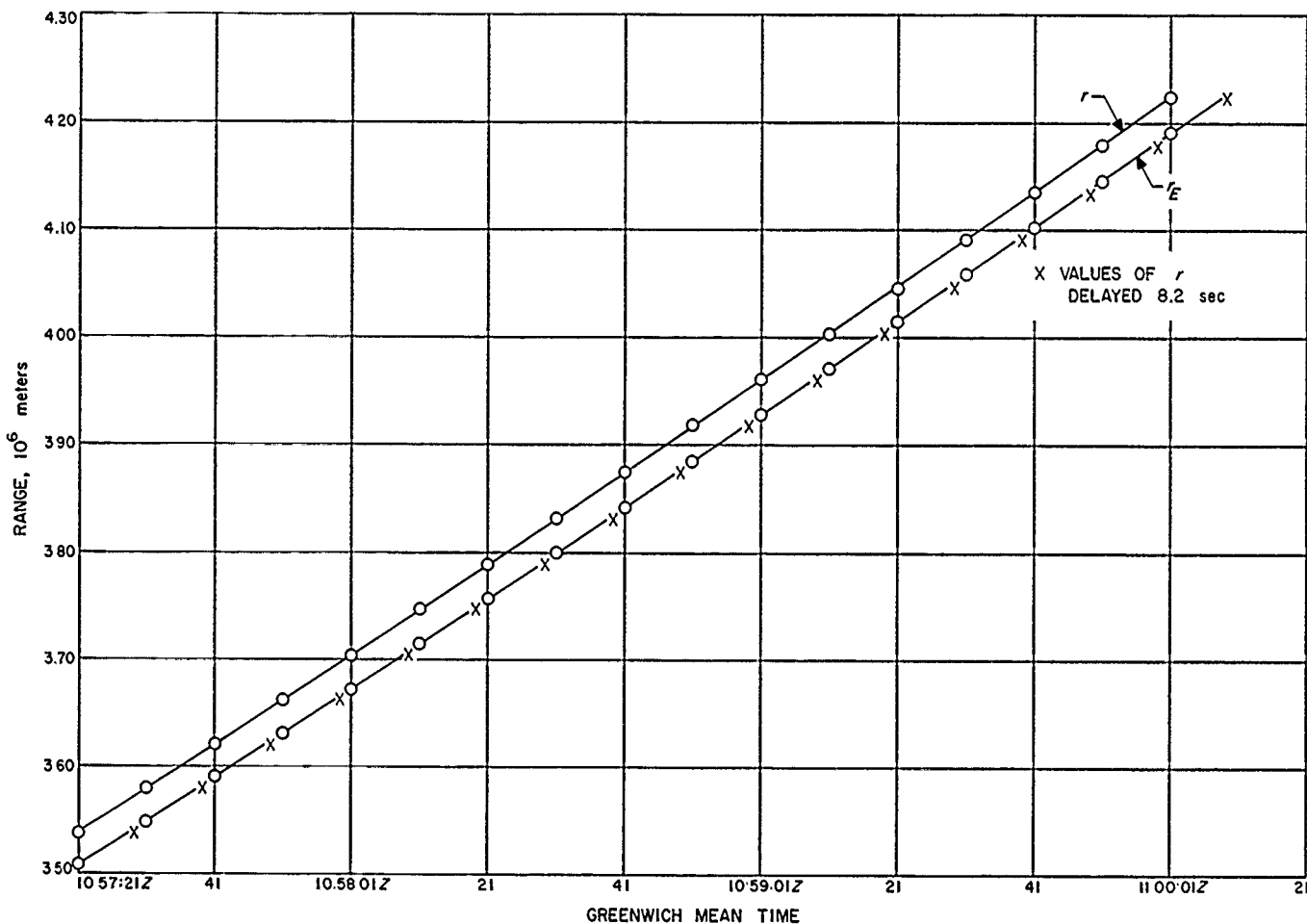


Figure 64. Echo pass 1107, second ranging portion

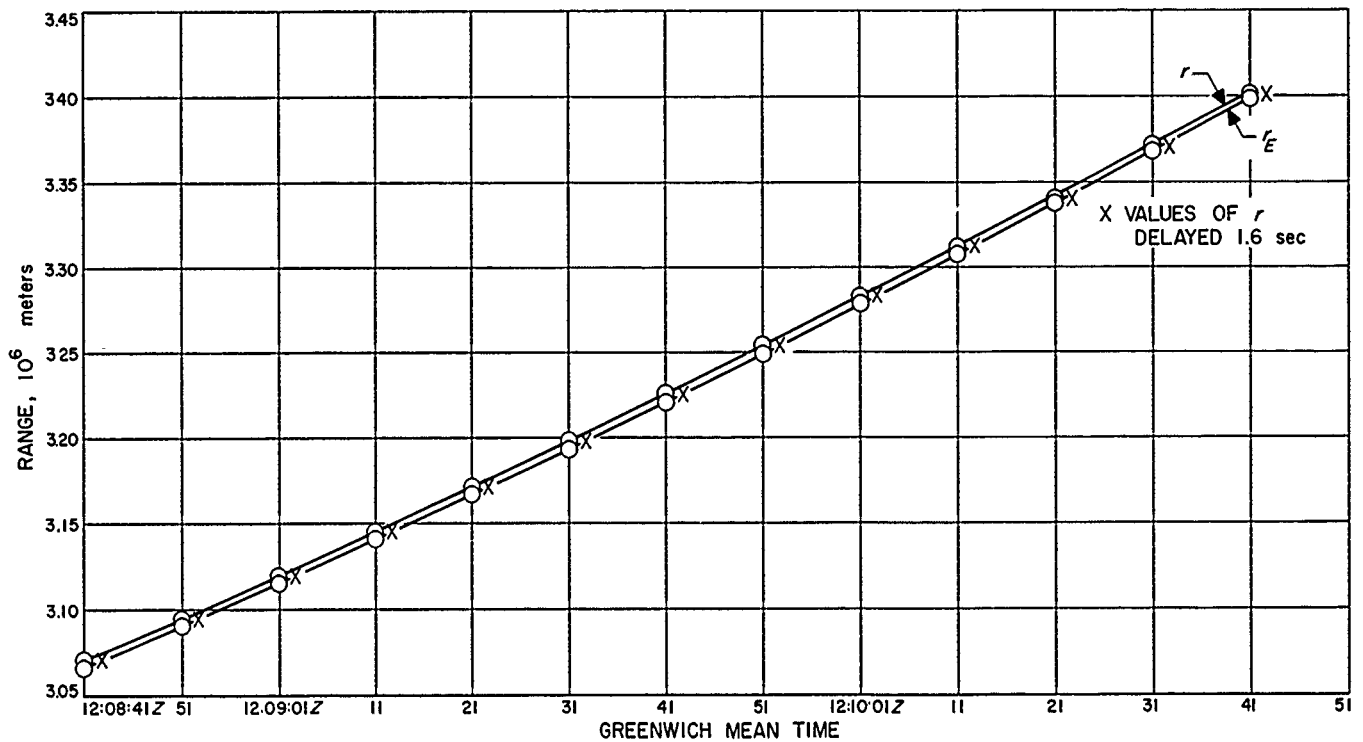


Figure 65. Echo pass 1185, ranging portion

ever, there is a bias between the measured range and that computed from the angles and doppler. Part of the bias is due to an error in the range tally.

After these tests were run, it was discovered that a wire had been omitted in the range tally, apparently during one of the modifications. This had the effect of introducing a logical error, such that an additional count of one clock doppler cycle might be made at the beginning of a run. This means that all of the range numbers in a given run may be in error by 301.33 meters in either direction.

In Pass 1248, if it is assumed that the first acquisition had a spurious count to make the range 301 meters too high and the second acquisition had a spurious count to make the range 301 meters too low, then the means for the three acquisitions became -2384, -2528, and

-2455. If the points in the first and second acquisitions are corrected according to this assumption, the combined mean error is -2464 meters, and no corrected point differs from this amount by more than the increment. There is, unfortunately, no way to tell at this time whether the other two passes have this bias in them.

c. Analysis of Courier ranging data. The Courier passes for which ranging data was obtained are listed in Table 9. An orbit was computed on the IBM 7090 computer from

Table 8. Results of Echo ranging passes

Pass No.	Acquisition No.	Error mean, meters	Error standard deviations, meters	No. of Points
1248	First	-2083	163	6
	Second	-2829	119	11
	Third	-2455	81	9
1249	First	-4152	122	46
1250	First	1677	146	46

Table 9. Courier passes on which successful ranging was obtained

Ranging period	Date	Greenwich mean time, hr: min	Ranging time, min: sec	
			Without vernier	With vernier
A	Jan 30	22:51	00:02	02:58
B1	Jan 31	18:11	00:26	01:12
B2	—	—	00:08	—
B3	—	—	00:26	—
B4	—	—	00:12	01:40
C	Jan 31	20:05	00:26	02:48
D	Jan 31	21:55	00:06	03:46
E1	Feb 1	19:12	00:32	00:32
E2	—	—	00:16	00:06

the angle and doppler data taken in Passes B, C, and D. The computer then determined from this orbit the range to each of the two sites. The average of these two computed ranges was compared with the average of these two ranges as measured by the ranging system with the vernier operative and is given in Table 10. These data points for which the vernier were inoperative were omitted from the comparison. At first glance it appears that the vernier has not improved the measurement accuracy, because it should reduce the increment of range to 5 meters and give a standard deviation of less than 5 meters. An examination of the data shows it to be smooth and to agree with the doppler much better than the large standard deviation would indicate; but the curve of measured range is not just displaced with respect to the curve of computed range but is skewed. The agreement between the range measurements and the doppler measurement indicates that the difficulty is probably in the computed range. It is known that the computed orbit does not fit the angle and doppler data as well as should be expected.

Pass C is obviously in error, apparently due to a malfunction in the range tally which at some point injected a large spurious number. The small standard deviation indicates that the tracking and vernier were operating well.

Passes A and E were compared briefly to the Ephemeris and found to agree within a few kilometers, although Pass A shows evidence of being skewed also.

d. Conclusions. From the foregoing discussion, the following conclusions may be drawn: (1) The experiments were generally successful in that they showed the basic ideas of the ranging system to be correct and workable. (2) The accuracy of the measurement appears to be good, although it is as yet uncertain just how good. The present uncertainties of a few kilometers in several thousand kilometers are fractions of 1% and may well be due more to uncertainties in the computed orbit than to uncertainties in the range measurement itself. More work is

Table 10. Results of Courier ranging passes

Ranging period*	Change in range	Mean error, meters	Standard deviation, meters	No. of points
B1	Decreasing	-6,483	152	35
B2	Increasing	-5,325	380	13
B3	Increasing	-6,002	199	76
C	Increasing	3,721,548	141	76
D	Increasing	-4,715	33	113

* Periods described in Table 9.

being done to try to obtain a better standard for evaluation of the ranging data.

2. Digital Telemetry Testing Program

As indicated in *Research Summary No. 36-7* (Vol I), an evaluation of digital communications techniques is underway at this Laboratory. These tests are being carried out to verify the theoretical evaluations of various systems, some of which are reported in References 42 to 52. Partial results of these tests are being reported here.

Digital systems fall within one of two broad categories, i.e., either bit-by-bit detection or coded-word detection. They are further categorized into types of modulation and various mechanizations. The systems currently under scrutiny are classified as follows:

- (I) Bit-by-bit detection.
 - (A) Phase shift keying (PSK).
 - (1) Matched filter, wired sync, and wired phase reference.
 - (2) Low-pass filter (Wiener Form), wired sync, and wired phase reference.
 - (3) Collins Kineplex, matched filter, using either preceding bit reference, wired reference, or locked-loop reference.
 - (B) Frequency shift keying (FSK), wired sync.
 - (1) Phase locked loop, matched filter.
 - (2) Wiener filter.
 - (3) Rate limited.
- (II) Coded word detection.
 - (A) Phase shift keying (PSK).
 - (1) Space Electronics Corporation, Digilock.

a. Investigation of PSK (matched filter and low-pass filter) data transmission system. To date, only those systems under Category (I-A) have been completely evaluated, while the remainder are currently under test. The method of test for the systems completed is shown in Figure 66. This equipment generates a random sequence of nonreturn to zero (NRZ) bits, 131,071 bits long. Bit error totalizing capacity is sufficient for 2^{16} errors. Further, equipment used for mixing the signal and noise is calculated to be capable of an accuracy of 0.2 db rms. This will be borne out in the test results discussed below.

The system under Category (I-A-1) was mechanized to correspond to the assumptions made in some of the theoretical evaluations of PSK bit-by-bit detection; namely, perfect phase reference for demodulation and perfect synchronization. Results of the tests on this mechanization are shown in Figure 67. It may be seen that the theory and experiment agree quite closely and further

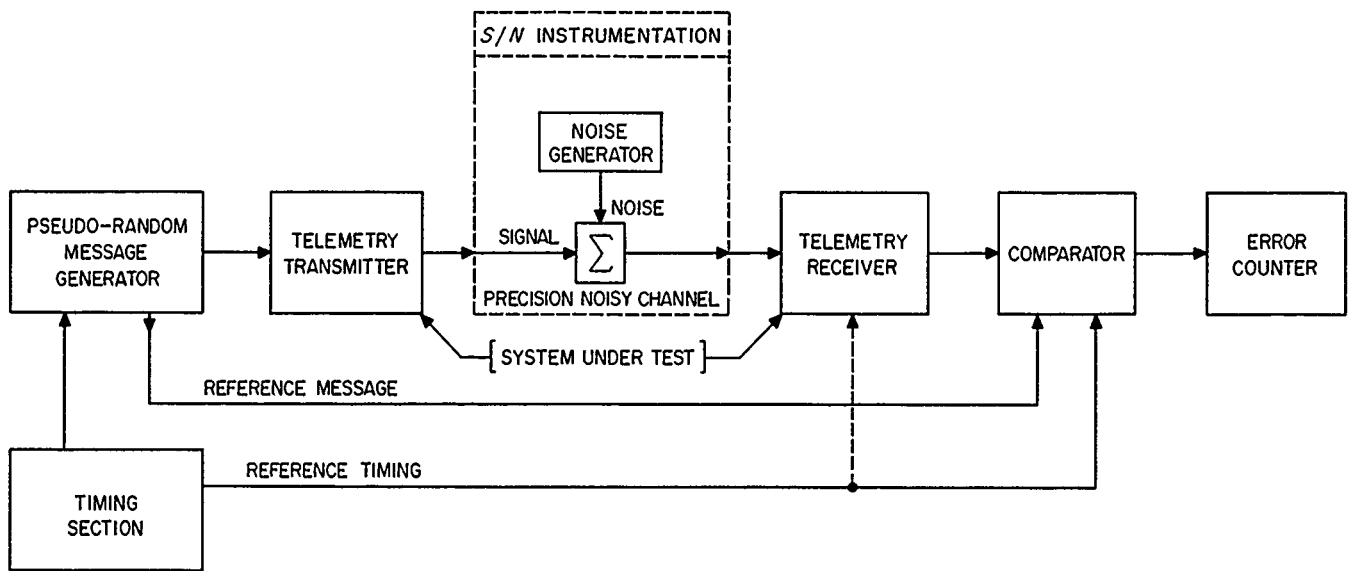


Figure 66. Bit-by-bit telemetry test system

that the estimation of the accuracy of the instrumentation is valid. Points at the lower end of the curve show a

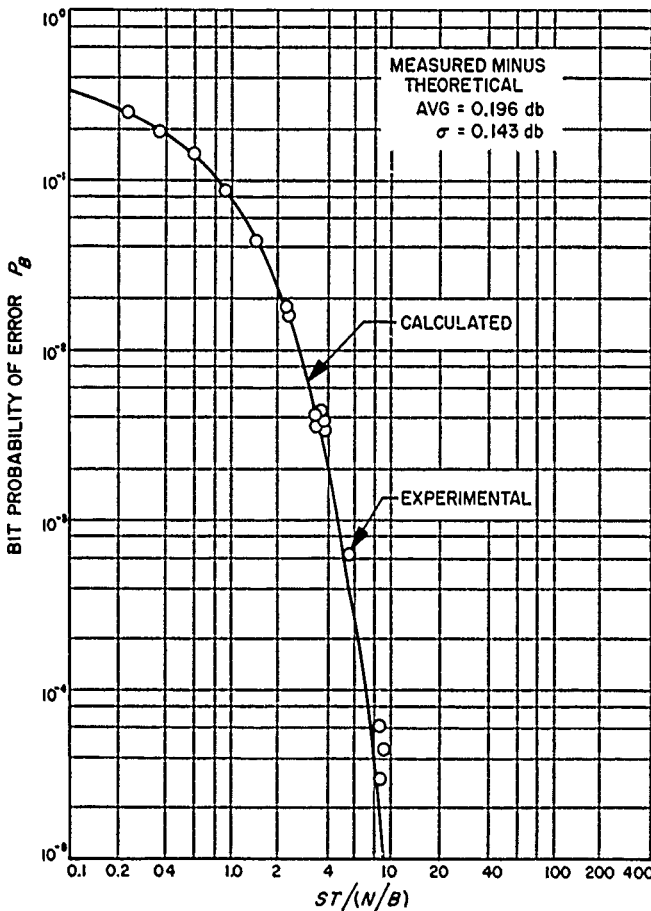


Figure 67. Probability of error for bit-by-bit PSK detection with matched filter

larger deviation from the theory because of the relatively few errors (1 to 5 bits) for the length of the test (131,071 bits) represent a poorer statistical average.

Under Category (I-A-2) is a system mechanized to evaluate how much advantage the matched filter has over a low-pass filter. The particular low-pass filter chosen here is a single RC section which is the same form obtained if one evaluated the Wiener filter for a step function and flat noise (Ref 53).

The conditions imposed by Jaffe and Rechin (Ref 53) in their analysis are difficult to apply to the digital systems evaluated here. Jaffe and Rechin specify the value of the time integral of the squared error for transient signal and minimize rms error due to the noise. For the digital system, the specification of the transient error for an additional condition, that of minimum probability of error, is virtually impossible. As it turns out, the optimum value of the filter time constant is such that the transient has not subsided sufficiently within the bit time to make the bit errors independent from bit to bit; but rather, the errors depend upon the time history of the preceding bits.

No attempt, during the tests, was made to change the time constant as a function of S/N, as would be indicated ordinarily by the solution of a Wiener filter. No difficulty is encountered because of this as an observation of the results shown in Figure 68 will indicate. Had this been a difficulty, the curves would have crossed, indicating the optimum value to be the envelope of the curves rather than a single optimum value as shown. (Both parts a and b of Figure 68 represent a single series of tests; they

are separated only to prevent confusion of overlapping curves.)

Apparently the advantage of the matched filter over the low-pass filter is not too great; but since sync is required for sampling both systems, the matched filter is obtained at small cost.

Extrapolations of the results shown in Figure 68 are shown in Figure 69, which obtains the optimum value for the time constant of the filter. It is interesting to note that the noise bandwidth of this filter is about 1.5 times the fundamental frequency of the bit rate.

One baffling result observed in the results of the above system is the fact that a change in S/N due to a bandpass limiter, as predicted by Davenport (Ref 54) and verified experimentally by various workers, does not show up. Because Davenport assumed an unmodulated carrier, it was thought that this might be the source of the difference. A test was then devised to test his hypothesis. This was accomplished by sending data of the all-ones state (NRZ), which is essentially an unmodulated carrier.

Results are shown in Figure 70, which do not verify the hypothesis. This remains unsolved.

b. Investigation of Kineplex data transmission system.
 The digital telemetry test system as described in RS 36-7 (Section V-D-3) was used in this experiment. A block diagram of the test setup is shown in Figure 66, and a photograph of the test setup is shown in Figure 71. In order to provide synchronous data, the test unit data source was supplied with a 45.45-cps square wave from the Kineplex transmitter. The message data was supplied to the transmitter in sequences of 131,071 bits at the rate of 45.45 bits/sec. In the transmitter, the phase of a 960-cps sine wave was either advanced or retarded by $\pi/2$ radians in accordance with the zeros and ones of the input data. This output signal was passed through a precision noisy channel, which mixed the signal and noise with a calculated accuracy of 0.2 db rms, and then passed to the Kineplex receiving system. After detection, the message bits were compared with the original message suitably delayed to compensate for delays in the system. The errors were counted in a 15-stage binary counter. The sig-

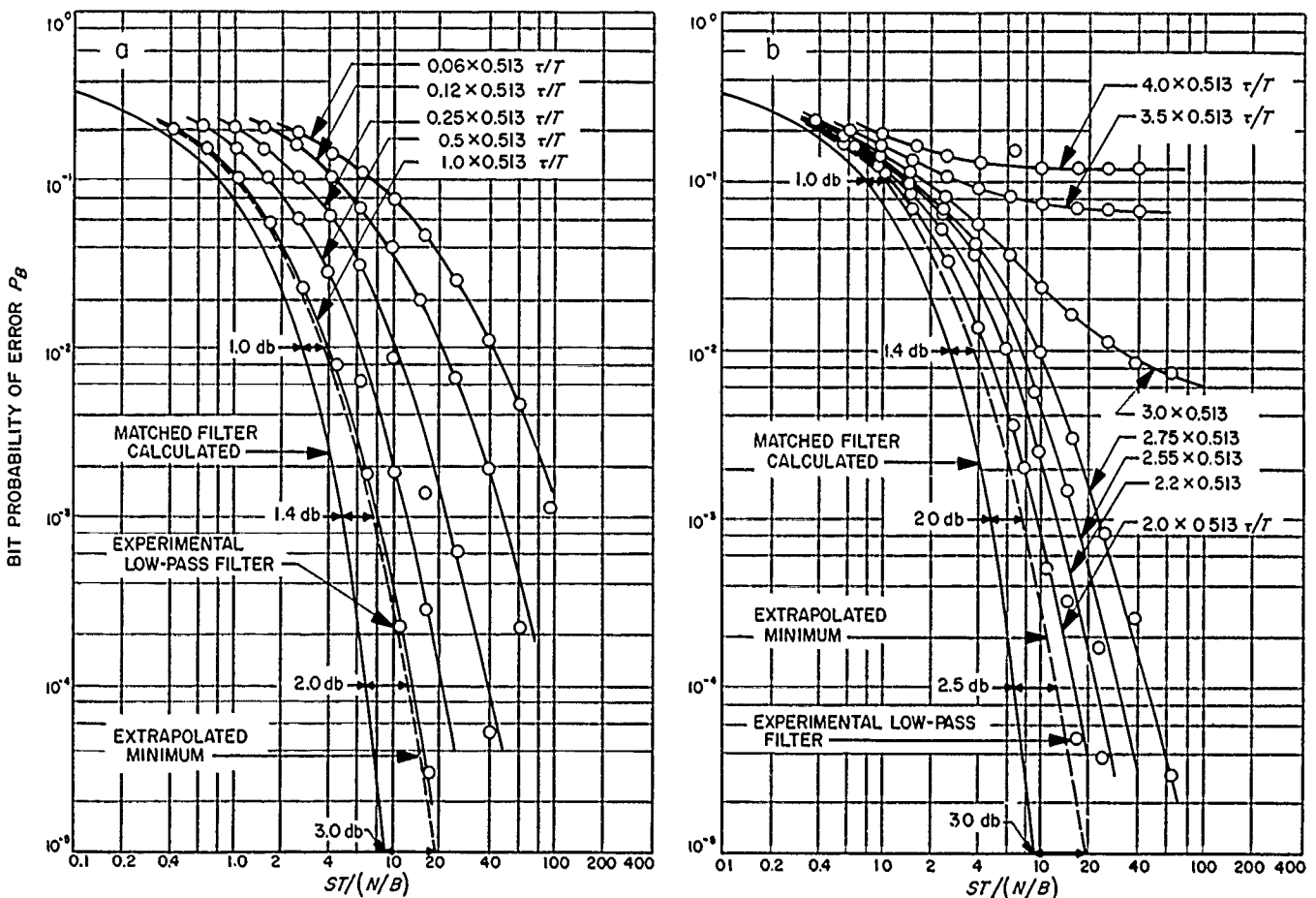


Figure 68. Probability of error for bit-by-bit PSK detection with low-pass filter

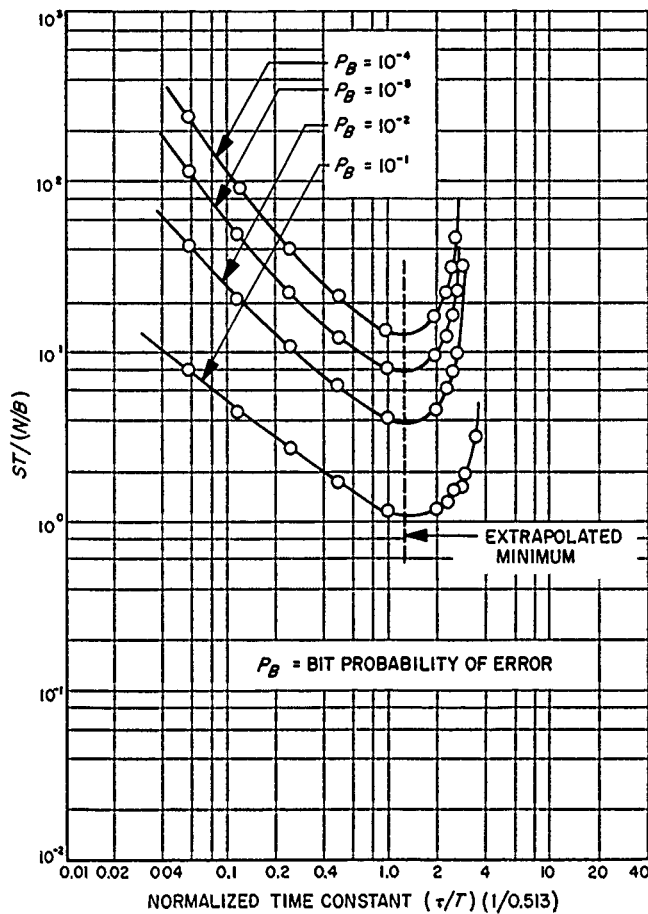


Figure 69. Extrapolated values for filter time constant

nal energy per bit was maintained constant throughout the test, while the noise power was varied by means of precision attenuators.

Description of Kineplex system. The Collins Kineplex transmit and receive terminals, designated respectively TE 290 A-1 and TE 290 B-1, comprise a single-tone, single-channel binary data transmission station. It uses a 960-cps carrier with ± 90 -degree phase shifts representing data zeros and ones. The name Kineplex is derived from the detection technique which utilizes kinematic filtering and from the fact that the equipment is generally used for providing multiplex operation. Figure 72 shows a close-up of the receive terminal mounted in a standard rack. This shows the front panel with controls, input and output jacks, and indicator lights. The major proportion of circuitry is constructed on tiny modules which are mounted on plug-in panels. The photograph shows one of the panels extended by means of an extension plug which permits trouble-shooting procedures while the equipment is operating.

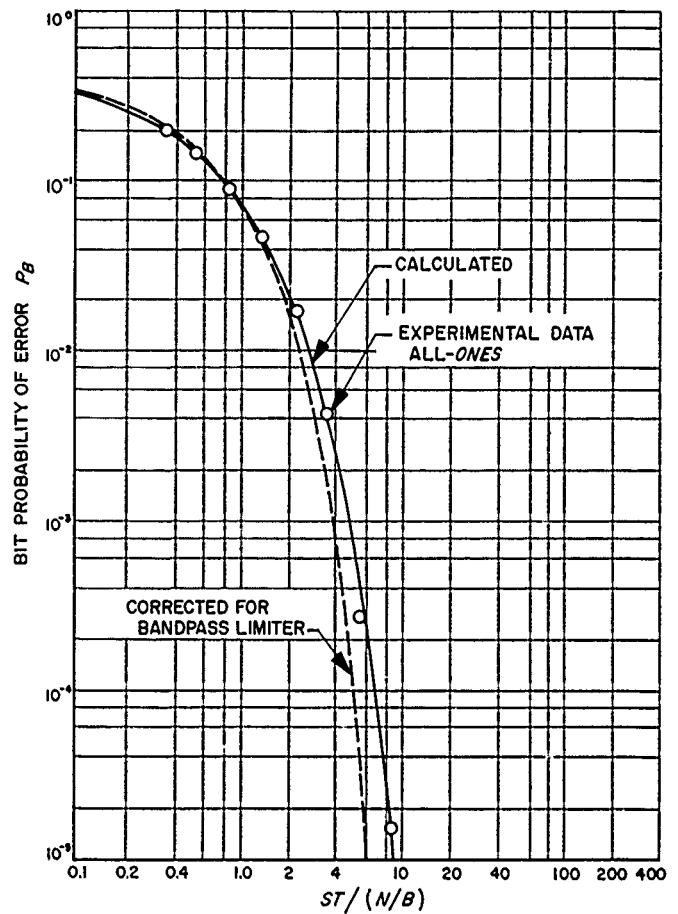


Figure 70. Probability of error for bit-by-bit detection using all-ones data

The simplified block diagram of Figure 73 describes the functional operation of the system. In the transmitter, a 3840-cps, crystal-controlled oscillator drives a quadrature phase generator which provides four 960-cps, square-wave signals which are displaced in phase by $\pi/2$ radians. The output of the digital phase selector is a 960-cps square wave which is phase shifted either $\pi/2$ or $-\pi/2$ radians with respect to the phase reference at 22-millisecond intervals in accordance with the binary input data. When the system is operating in the ideal phase reference mode, the phase reference in the transmitter is shifted -90 degrees after each bit is transmitted (Refs 48, 49). When operating in the modes described as local phase reference and preceding-frame phase reference, the phase of the preceding bit is used as the reference. The encoded 960-cps square wave is then filtered and passed through the precision noisy channel to the receiver.

In the receiver, the encoded 960-cps signal is balanced modulated with a stable 20,975-cps reference to provide the 21,935-cps signal required to pass through the

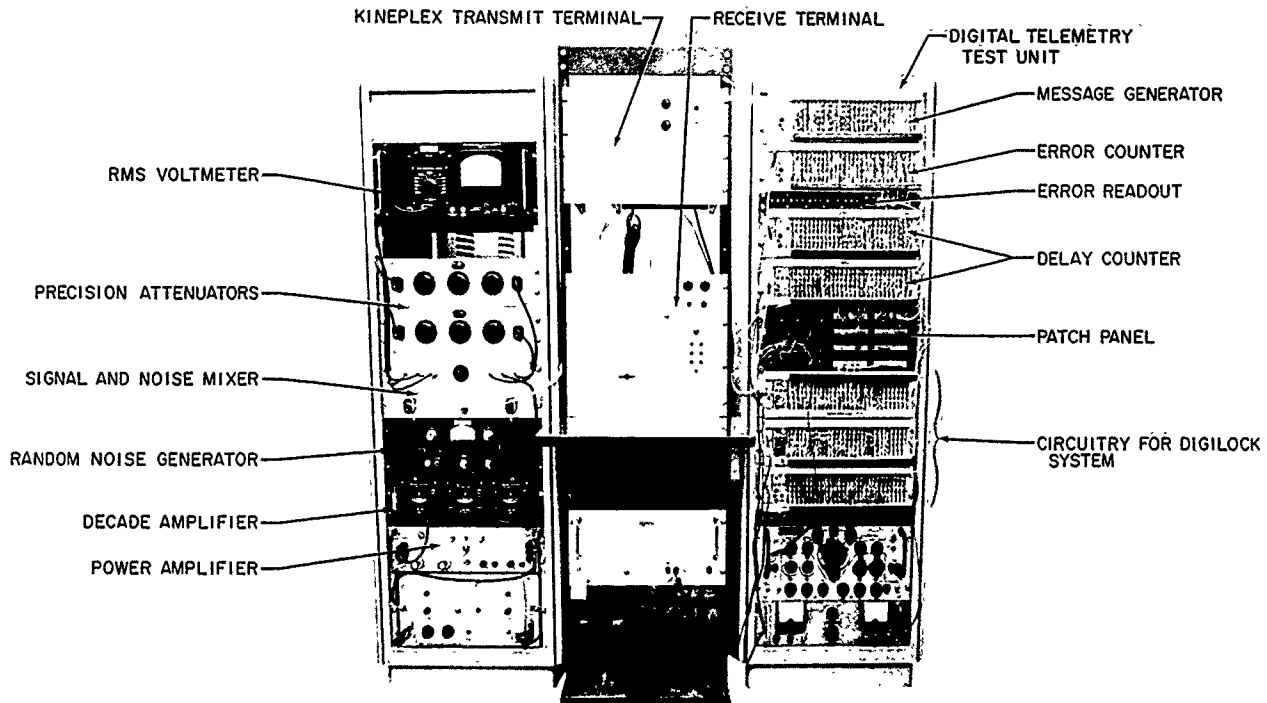


Figure 71. Instrumentation for testing Kineplex data transmission system

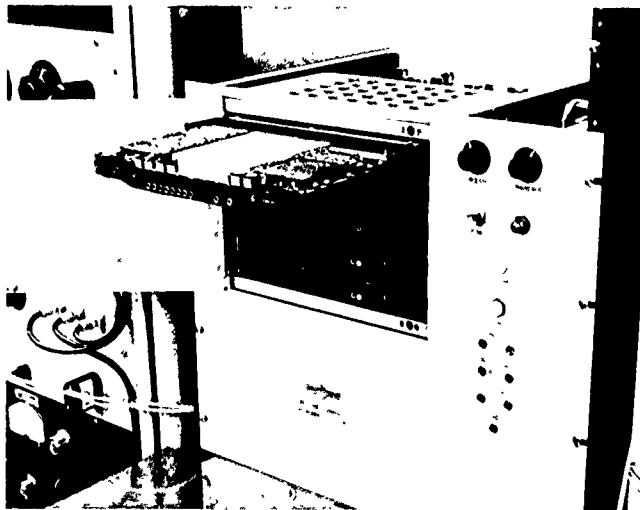


Figure 72. Kineplex receive terminal

narrow-band, matched-filter system. The keyed filters are driven on alternate data frames. During a drive period, one of the resonators builds up energy at the same frequency and phase as the input signal, while the other is storing the amplitude and phase information from the preceding frame. The lower trace of Figure 74 shows the input waveform to a keyed filter, and the upper trace represents the output waveform for the preceding

frame phase reference mode of operation. The lower trace shows the sampling time, the quench pulse, the drive period, and storage. The upper trace shows the integration of the data tone, storage of amplitude and phase information, and quenching of the resonator. The output of one resonator is compared in a phase detector with the output of the other resonator which has been phase shifted 90 degrees. Immediately following the drive period, a sampling pulse gates the output of the phase detector into a shaper which converts the analog phase output to binary levels, thus indicating whether a 0 or 1 has been sent. After the sampling gate, the resonator which stored the amplitude and phase information of the preceding frame is quenched prior to receiving the next data frame. During this period, the other resonator stores the amplitude and phase information for comparison at the end of the period. The period of a data frame consists of the drive gate duration of approximately 18.18 milliseconds and the sampling and quench gate duration of 3.82 milliseconds.

In order for the detection process to be performed efficiently, the gating operation in the receiver must be timed synchronously with the 22-millisecond timing in the transmitter. This synchronization is accomplished in the receiver by determining the time of each phase transition in the 960-cps data signal. The bit timing reference

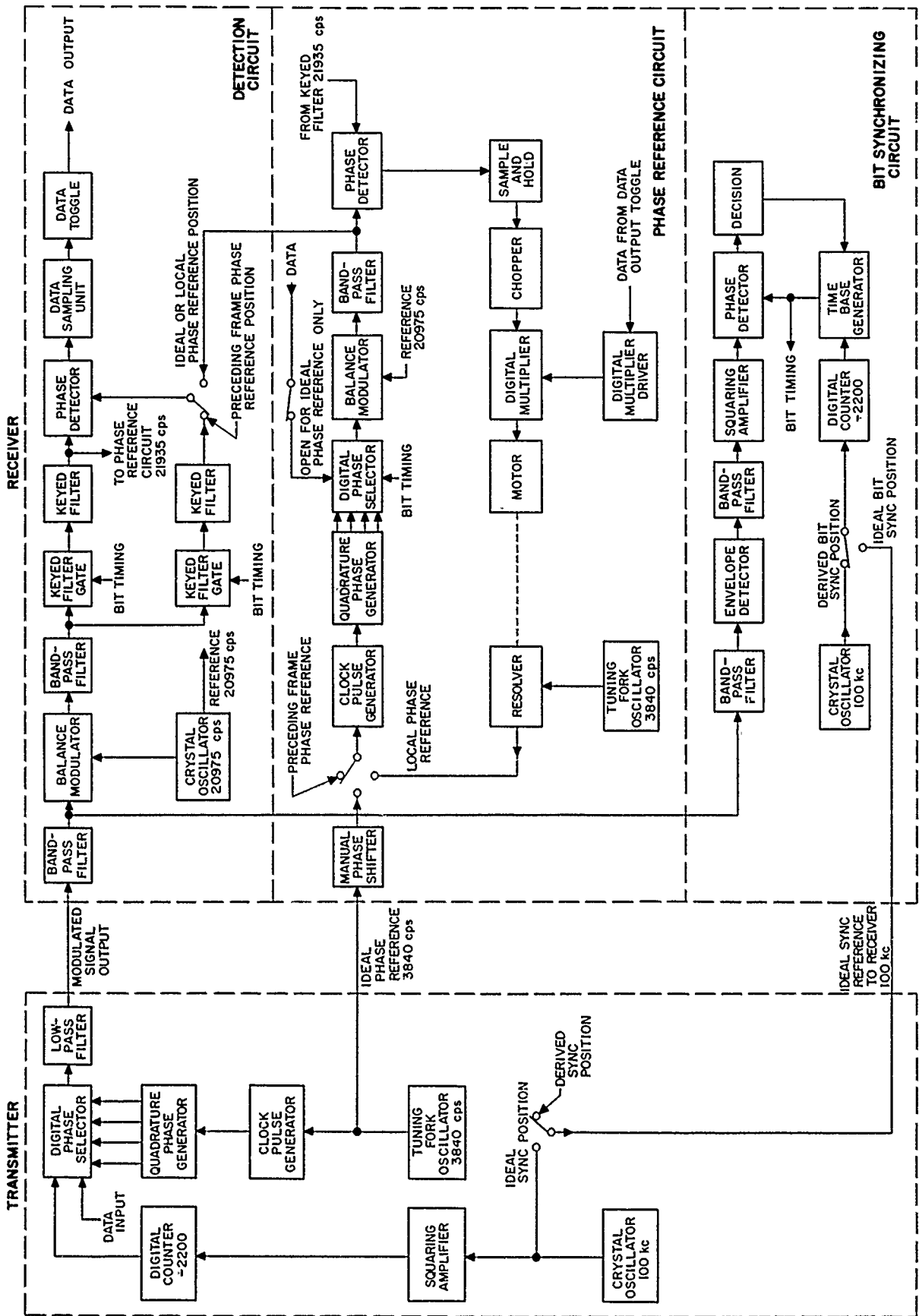


Figure 73. Block diagram of Kineplex data transmission system

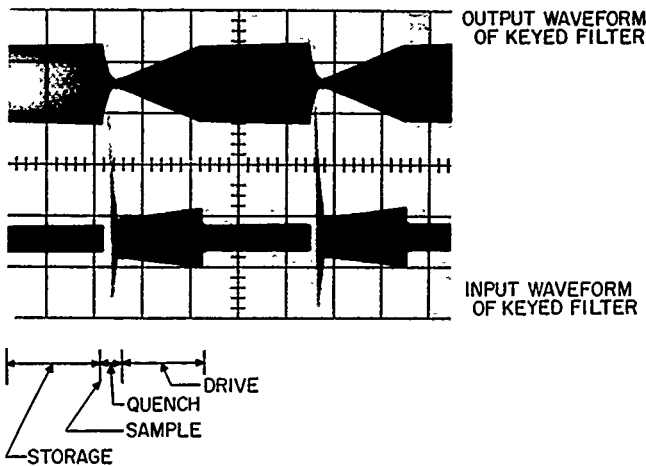


Figure 74. Keyed filter input and output waveforms

is provided by the time base generator which is driven by a 45.45-cps square wave derived from a 100-kc crystal controlled oscillator in the receiver. This reference is compared in a phase detector with a 45.45-cps square wave derived from the 960-cps data signal. The bit timing error is applied to the time base generator causing it to run synchronously with the phase transitions in the 960-cps data signal.

In the detection process, it is also necessary for the system to have a phase reference corresponding to the phase reference in the transmitter. In the standard Kineplex detection system, the phase reference is determined from the phase of the preceding bit. An alternate method (Refs 48, 49) of deriving the phase reference from the preceding bit uses a servo-loop as shown in Figure 73. In this local phase reference mode, the output of a 3840-cps oscillator is phase shifted by the servo which locks the reference tone to the incoming data tone. The output of the servo-loop is phase shifted in response to the received data in order that it will always be in the proper phase to detect the next bit. One important weakness of this method should be noted. Since the preceding bit is used to set the phase reference for the following bit, an error in detection will result in a second error due to a false phase reference.

Summary of results. The performance of the ideal Kineplex system is shown by the graphs of Figure 75. The phase reference and bit synchronizing reference were wired directly from transmitter to receiver. The measured performance agreed with the theoretical curve with an average error of 0.23 db rms and a standard deviation of 0.3 db rms. The performance of the system when operating with a locally derived bit synchronization

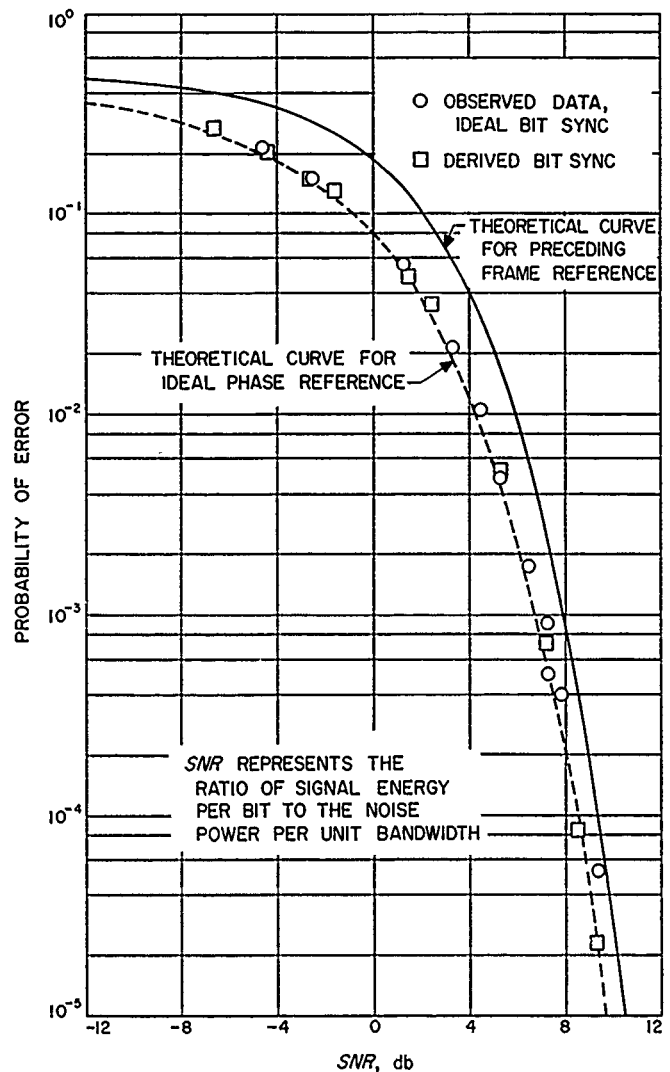


Figure 75. Probability of error vs SNR for Kineplex system with ideal phase reference

(square data points) appeared to be fully as good as the ideal system over the range of operation.

Normally, the Kineplex system uses a phase reference derived from the phase of the preceding data frame after storage in a resonator. The performance for this mode of operation is shown in Figure 76. The observed data agreed with the theoretical curves with an average error of 0.1 db rms and a standard deviation of 0.14 db rms for both the ideal and derived bit synchronization methods.

The graphs of Figure 77 show the performance while utilizing a phase reference which was derived by a servo in the receiver from the phase of the transmitted signal. For this mode of operation, the performance showed an improvement of about 0.5 db over that indicated for the

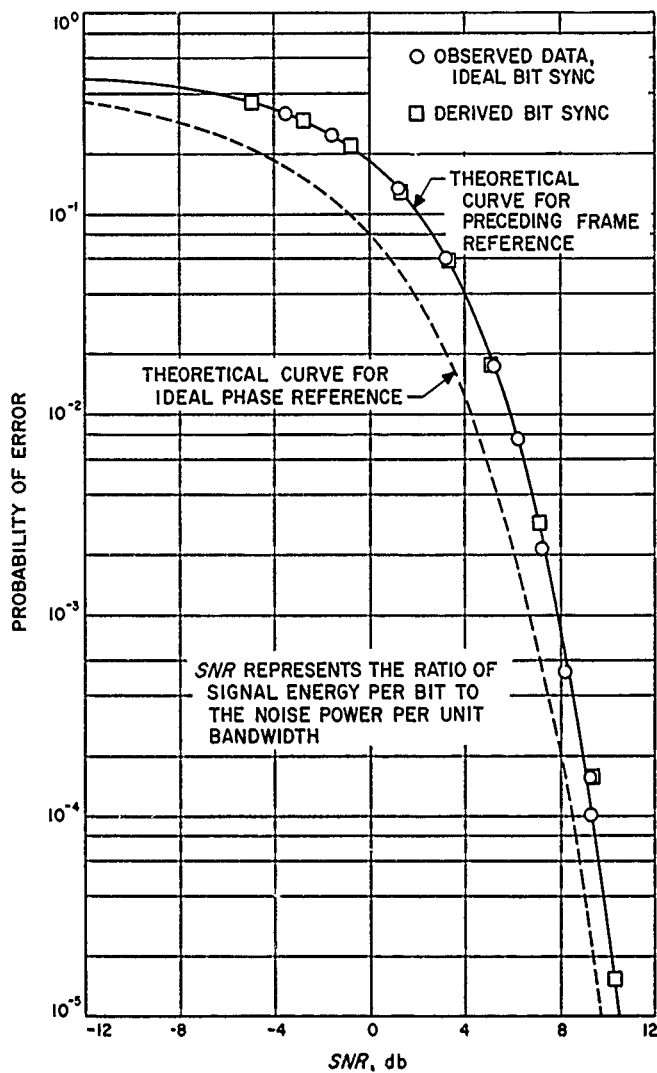


Figure 76. Probability of error vs SNR for Kineplex system with preceding frame reference

preceding-frame phase reference system when the SNR values (ratio of signal energy per bit to the noise power per unit bandwidth) were 0 to 9 db. For SNR's less than 0 db, the observed data indicates a degradation of 1.5 to 2.0 db relative to the preceding-frame reference system.

Conclusions. This report presents the results of an experimental investigation to determine the performance under noise conditions of the Kineplex detection scheme. The probability of error was measured for each of six operational modes as functions of the SNR (signal energy per bit/noise power per unit bandwidth). The theoretical curves (Refs 42 to 47) for ideal phase reference (coherent PSK) and preceding frame phase reference (differentially coherent PSK) are shown for comparison.

The performance for the ideal Kineplex system (Fig 75, circle symbols) shows very good agreement with the

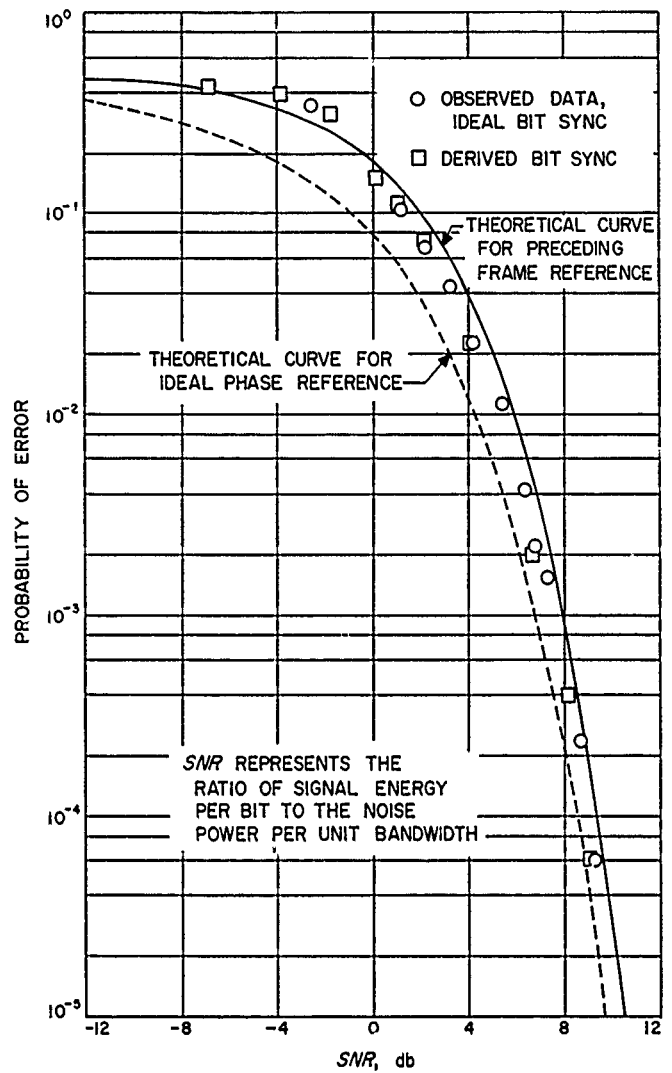


Figure 77. Probability of error vs SNR for Kineplex system with local phase reference

theoretical curves. The average error between experimental data and the theoretical values was 0.23 db rms. This is comparable with a probable error of 0.2 db rms predicted from the measuring equipment specification. Figure 75 also shows the performance obtained when the bit synchronization is derived from the transmitted signal (square symbols). This is in very good agreement with the performance of the ideal bit synchronization system shown in the figure.

The graphs of Figure 76 show the performance of the Kineplex system when the phase reference is derived from the phase information in the preceding data frame. The experimental data shows very good agreement with the theoretical curves with an average error of 0.1 db rms. This is well within the calculated accuracy of 0.2 db rms for the measuring equipment. It is again significant to

note the good agreement shown in Figure 76 for the system utilizing the locally derived bit synchronization (square symbols).

The performance of the Kineplex system with a locally generated version of the phase reference is shown in Figure 77. This shows a slight improvement in noise performance relative to that indicated for the system using the preceding frame reference when the SNR values were in range of 0 to 8 db. A degradation of 1 to 2 db was noted for SNR's less than 0 db. The measured data shows an error rate which is two times the rate predicted for a coherent PSK system in the strong signal region. This indicates a tendency for errors to occur in pairs. While a theoretical analysis of the local phase reference system has not been performed, a study of the system block diagram shows that this double error rate should be expected intuitively. This is due to the fact that each bit is used to establish the phase reference for the following bit and an error in detection results in a false reference for detection of the next bit. For SNR's less than 0 db this result would not be expected. In order to complete the evaluation of the local phase reference system, it would be desirable to determine the experimental performance for SNR's less than 0 db and to calculate the theoretical performance for the entire range of SNR's.

In general the observed data served to verify the calculated theoretical performance within the accuracy of the measuring equipment. It is significant to note the performance of the system when the timing synchronization was derived in the receiver for SNR's from -6.7 db (Fig 75, square symbols) to +9 db. The observed data for error rates less than about 10^{-4} does not represent a good statistical average since the message length was only 131,071 bits.

The performance of the practical Kineplex system (preceding frame reference) shows a 3- to 5-db degradation relative to the ideal coherent PSK system for SNR values from 0 to -50 db. This difference approaches 2 db at an SNR of 4 db and decreases toward zero for higher values of SNR.

D. Venus Radar Experiment

M. H. Brockman, L. R. Malling, and H. R. Buchanan

1. The 2388-mc CW Doppler Radar

a. *Functional description.* The 2388-mc doppler radar system for the 1961 Venus experiment consists of a highly

stable 2388-mc, 10-kw transmitter feeding an 85-foot diameter transmitting antenna and a highly sensitive receiving system fed by an 85-foot diameter receiving antenna. The function of the transmitter is to illuminate Venus and provide a Venus-reflected signal to the receiving system which is located some 7 miles from the transmitter.

A functional block diagram of the 2388-mc doppler radar is shown in Figure 78. A 31.84 (31^{63/100}) mc phase-stable, crystal-controlled oscillator is slaved to an atomic frequency standard to provide a frequency stability of 1 part in 10^9 or better for the transmitted signal (RS 36-7, Vol I, p 73). The oscillator frequency is multiplied to 2388 mc, amplified to a 10-kw power level, and fed to the 85-foot diameter transmitting antenna. At the transmitter site, the 31.84-mc frequency is coherently divided by 64, and the resultant 497.5-kc signal is sent via the microwave relay link to the receiver site to establish coherent reference signals for the 2388-mc receiver.

The synchronous receiver is a narrow-band, phase-coherent double conversion superheterodyne type which obtains its signal from the 85-foot diameter receiving antenna through a low-noise UHF amplifier. The low-noise UHF amplifier consists of a 2388-mc Maser amplifier (Sec III-A-1 of this report) followed by a 2388-mc parametric amplifier (Sec IV-D-3 of this report). The coherent receiver consists essentially of an RF servo-loop operating at 2388 mc, an AGC loop, a UHF doppler detection system, and two auxiliary channels. One channel synchronously detects the Venus reflected signal and provides an input to the waveform measurement equipment. The second channel provides an input signal to the nonsynchronous receiver (RS 36-7, Vol I, Fig 77). This second channel is also utilized, during synchronous operation, to monitor receiver system gain and noise temperature. The output of this channel is detected (square-law diode detector) and recorded to provide a continuous record of system gain variation. Additional noise (55°K) is periodically introduced into the input of the receiving system from a calibrated noise source through a directional coupler (Fig 78) to provide a record of system noise temperature during coherent signal reception from Venus.

During this mode of operation, the 29.85-mc IF amplifier and the second auxiliary channel are operated at fixed gain so that variations in received signal level do not produce corresponding variations in receiver gain due to AGC action. Acquisition of the Venus-reflected RF signal is accomplished by extremely accurate programming of the receiver local oscillator frequency (RS 36-7, Vol I, pp 75-77 and Sec IV-D-2 of this report).

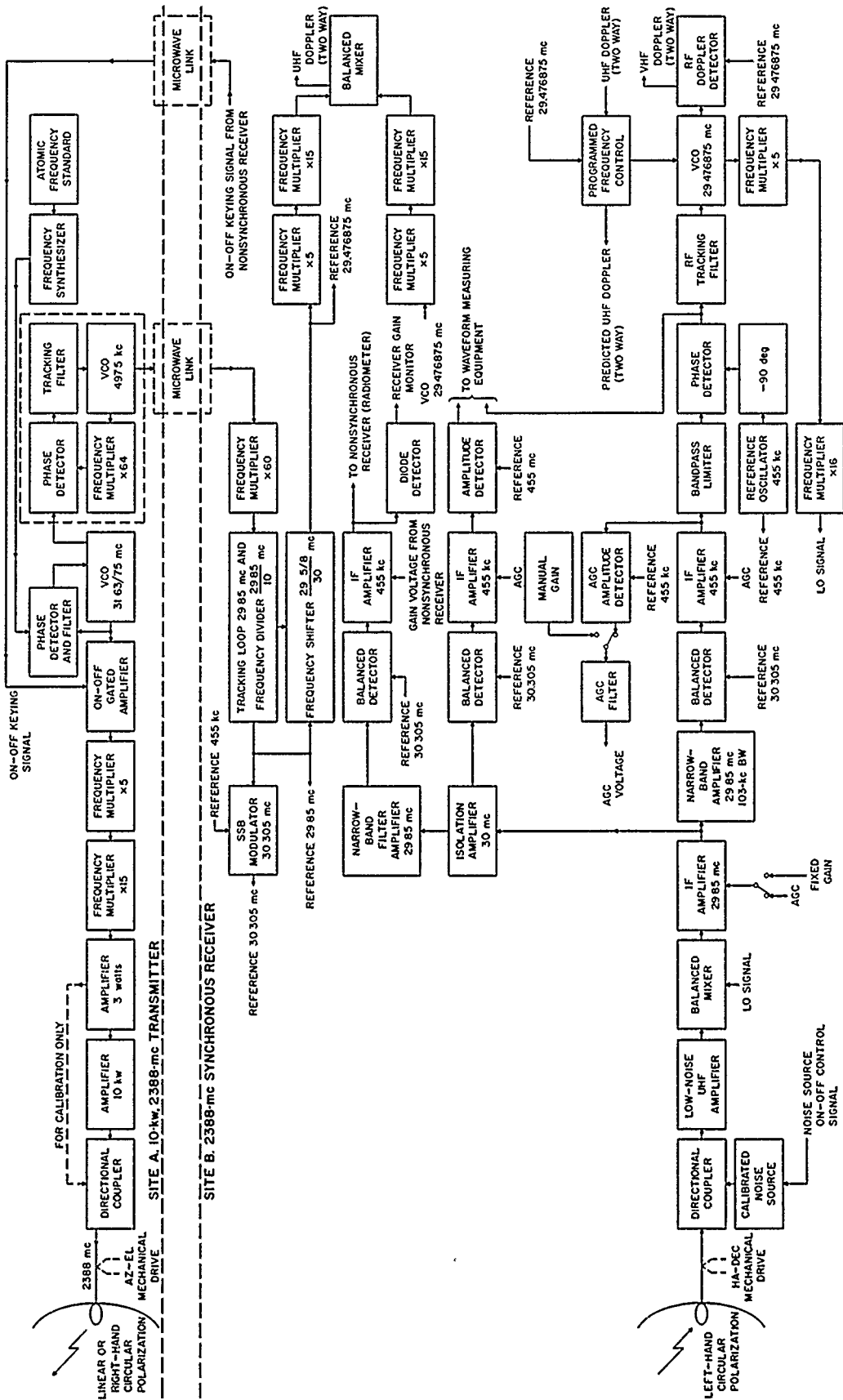


Figure 78. Block diagram of 2388-mc CW doppler radar Venus experiment prior to inferior conjunction

The 2388-mc CW doppler radar was originally designed to track the *Echo I* satellite. Waveform equations which describe the operation of the 2388-mc radar were presented in the *Space Programs Summary* (pp 17-19). The angle error detection portion of the system and the coded ranging subsystem have been deleted since they are not being used in the Venus experiment. Detailed information relating to the various portions of the 2388-mc radar has been presented in earlier reports (RS 36-1, Vol I; RS 36-2, Vol I, Part 1; RS 36-3, Vol I, Part 1; RS 36-4, Vol I; RS 36-5, Vol I; and RS 36-6, Vol I).

b. System design parameters. The characteristics of the 2388-mc CW doppler radar are presented in Table 11. Assuming that the reflectivity of Venus is unity, the received carrier level at the point of closest approach to the Earth (inferior conjunction on April 11, 1961) is -153.7 dbm. But 1 month prior to and 1 month following this time, the signal levels will be approximately 6 db less than the above value (RS 36-7, Vol I, pp 72-73). Threshold for the RF loop for a receiving system noise temperature of 57°K is -174 dbm for a receiver noise bandwidth ($2B_{L_{90}}$) of 5 cps. The AGC system has a closed-loop noise bandwidth of 0.03 cps at the 5-cps receiver bandwidth threshold, and the rms gain error is maintained to 0.3 db at threshold.

Table 11. Characteristics for 2388-mc CW doppler radar system

Characteristic	System values		
Transmitter carrier power, dbm	—	—	71.14 13 kw
Transmitter antenna gain, db	—	—	53.8
Transmission line loss, db	—	—	0.25
Reflection loss at 26.4×10^6 miles ^a , db	—	—	-80.3
Space loss at 26.4×10^6 miles ^b , db	—	—	-251.5
Receiver antenna gain ^c , db	—	—	53.5
Transmission line loss, db	—	—	0.06
Receiving system noise temperature ^d , °K	—	—	57
Receiver bandwidth $2B_{L_{90}}$, cps	5	10	20
Receiver threshold, dbm	-174	-171	-168
Receiver prediction bandwidth, cps	500	500	2000
AGC loop bandwidth $2B_{L_{90}}$, cps	0.03	—	—
AGC loop threshold, dbm	-191	—	—
At 26.4×10^6 miles range	—	—	—
Received RF carrier, dbm	—	—	-153.7
S/N for RF loop, db	13.1	10.1	9.1
S/N for AGC loop, db	37.3	—	—

^aReflectivity of Venus assumed to be unity, diameter of Venus 7954 mi.
^bRange to Venus at point of closest approach (inferior conjunction).
^cAntenna gains are based on assumption that polarizations of the two antennas are matched.
^dTypical measured value with receiver antenna pointed at Venus.

c. Preparation for experiment. Performance of the 2388-mc CW doppler radar was evaluated, prior to March 10, 1961, with closed signal path and space transmission sensitivity measurements. Closed path measurements were made by feeding a stable crystal-controlled 2388-mc signal to the receiver through the directional coupler normally fed by the calibrated noise source (Fig 78). Data of input signal level vs AGC voltage was obtained using precision attenuators between the signal source and the receiver. These closed path measurements provided preliminary data on system performance at signal levels well above threshold. Threshold measurements were not attempted because of the problem of spurious RF leakage.

Space transmission sensitivity measurements were of three types. The first type of measurement consisted of radiating a phase-stable, 2388-mc signal from a collimation antenna at a distance of 5400 feet from the 85-foot diameter receiving antenna. Precision attenuators were inserted in the transmission line between the signal source and collimation antenna to vary the received signal level. Figure 79 presents typical sensitivity curves of input sig-

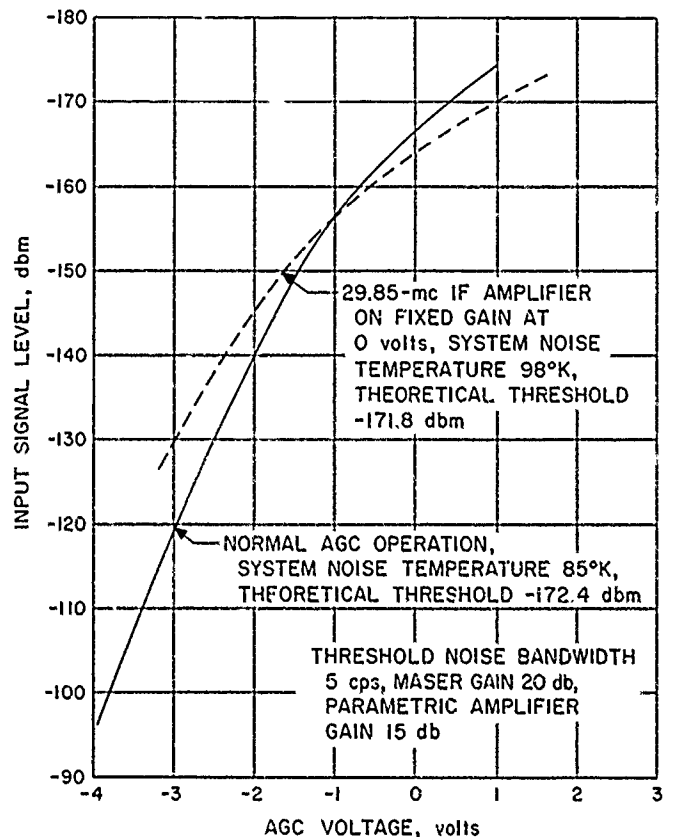


Figure 79. The 2388-mc synchronous receiver sensitivity with a normal AGC and with 29.85-mc amplifier at fixed gain

nal level vs AGC voltage for the synchronous receiver. The IF amplifier was operated on normal AGC to obtain the results shown by the solid line. The curve shown as a dashed line was obtained with the 29.85-mc IF amplifier operating with a fixed gain voltage (0 volt). A second type of measurement consisted of illuminating the passive relay link (RS 36-1, Vol I) with the 85-foot diameter transmitting antenna to provide a signal to the 85-foot diameter receiving antenna. For this measurement, the 10-kw klystron amplifier was inoperative and the 3-watt exciter amplifier fed the power transmission line to the antenna. Precision attenuators were inserted in the transmission line between the 3-watt exciter amplifier and the antenna to vary the radiated 2388-mc signal power.

A third type of measurement was made with essentially the same equipment arrangement as described above for the second type. In this case, however, both the transmitting and receiving antennas were accurately pointed at the Moon to provide a lunar-reflected signal to the synchronous receiving system. Earlier tests, during preparation for the *Echo I* passive satellite (SPS 37-2), had demonstrated that threshold measurements made with lunar-reflected signals were in very close agreement with threshold measurements made from the collimation antenna (first type of space transmission measurement). The sensitivity measurements made in preparation for the Venus experiment corroborated earlier measurements.

d. Preliminary performance. Reception of Venus-reflected signals with the nonsynchronous receiver starting on March 10, 1961, provided data on receiver local oscillator tuning. Phase-coherent reception of a Venus reflected signal was accomplished at approximately 00:02 GMT on March 23, 1961. The measured doppler shift on the Venus-reflected signal was greater than the predicted doppler shift by approximately 1 part in 1600. Earlier attempts at synchronous reception of the Venus-reflected signal had been unsuccessful—possibly due to this discrepancy in doppler shift. Up to the time of this writing, phase-coherent reception of the Venus-reflected signal has been successful whenever it has been attempted. Successful phase-coherent reception has been obtained with threshold noise bandwidths of 5, 10, and 20 cps.

At the time of the first successful phase-coherent reception (March 23, 1961), the synchronous receiver was operating with a 5-cps threshold noise bandwidth, transmitter power was 12.8 kw, and the distance to Venus was approximately 49.7×10^6 km (30.88 million miles).

2. Transmitter and Receiver Oscillators

The 2388-mc receiver must be continuously and accurately tuned to maintain the doppler-shifted, Venus-

reflected signal in the narrow passband of the receiver. This is accomplished during nonsynchronous reception by adding a synthetic doppler component to the receiver local oscillator frequency (RS 36-7, Vol I, pp 73-77). The added UHF doppler component is continuously compared with the computed UHF doppler data obtained from the Venus Ephemeris. Both are displayed on a digital readout in real time at 10-second intervals. If it is assumed that the computed data agrees to within a few cycles of the actual UHF doppler shift and that the reflected signal is specular and above receiver threshold, the receiver should automatically drop into lock when the operations switch is thrown to the synchronous receiver position. Hence, accurate programming of the receiver local oscillator provides a stable acquisition system for phase-coherent reception. Evaluation tests made with lunar-reflected signals, where the Ephemeris is accurately known, have confirmed this operation, and no difficulty has been experienced in switching from nonsynchronous to synchronous operation at signal levels near threshold.

a. Control operations. Closed-loop digital tracking has been planned for controlling the local oscillator frequency. However, since the digital equipment was not immediately available, a manually-operated, aided-track system has been used initially for the Venus experiment. The problem of the operator attention required to control the local oscillator frequency so as to match the computed UHF doppler data continuously to within a few cycles has been alleviated by inserting rate information into the manually operated system by means of a motor-driven potentiometer. (The variable dc voltage from the potentiometer controls a 475-kc voltage-controlled bias oscillator; see RS 36-7, Vol I, pp 75-77.)

The dc control characteristics of the 475-kc, voltage-controlled bias oscillator are shown plotted in Figure 80. The average slope is 10 cps/volt or 0.13 cps/deg rotation of the motor-driven potentiometer. The rotational speed of the motor-driven potentiometer is manually varied by changing the frequency of a 1-cps pulsed oscillator. The resultant control characteristic is shown in Figure 81. Two speeds are available, covering doppler rates from 1 to 40 cps/min. This range covers 95% of the expected doppler rates for any one transit of Venus. Slower rates may be accommodated by switching off the motor and matching the readouts at discrete intervals manually. Little difficulty has been experienced with tracking either Venus or the Moon with a 1- to 2-cycle error, corresponding to a tuning accuracy of 1 part in 10^9 .

b. Equipment and installation. The installation of the Atomichron at the Goldstone transmitter site is shown in Figure 82. The Atomichron has been installed in a

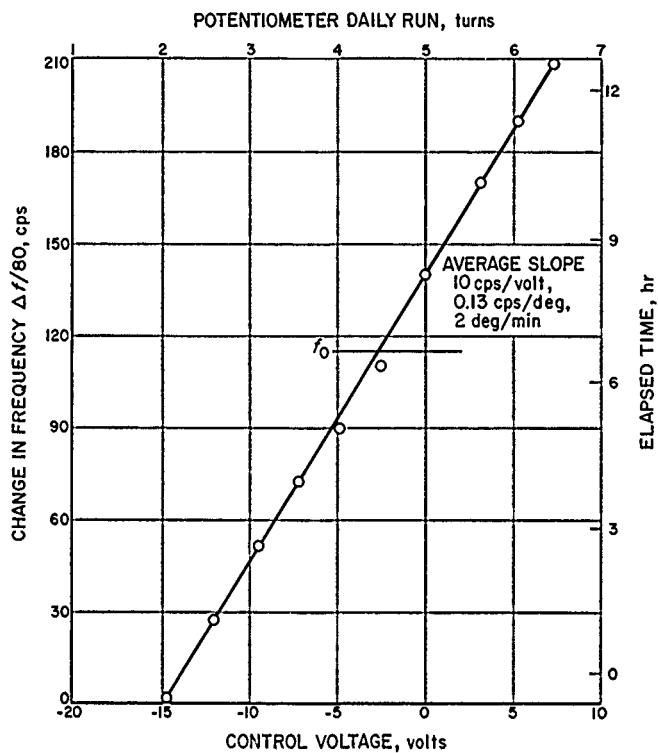


Figure 80. The 475-kc VCO characteristics,
 $f_0 = 474.975$ kc

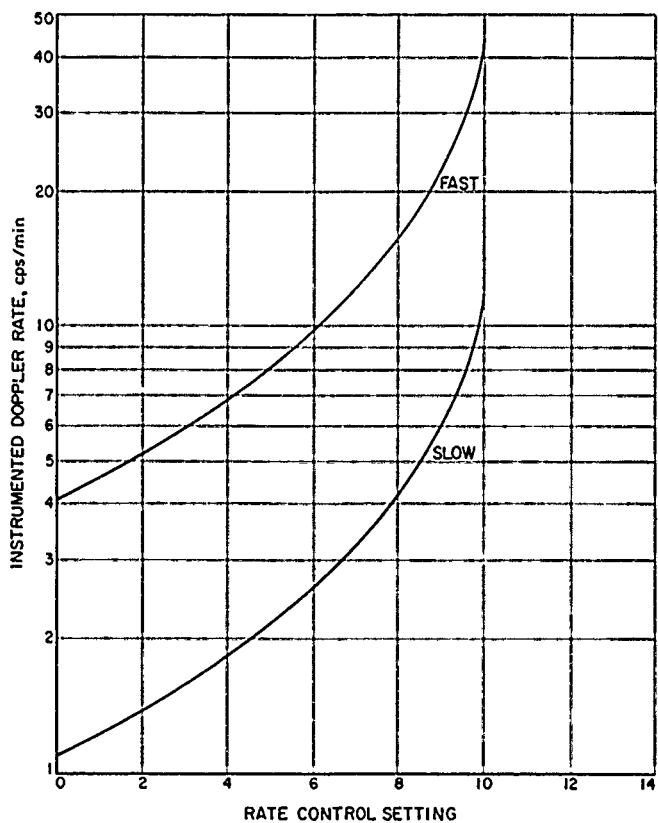


Figure 81. Pulsed oscillator rate control characteristics



Figure 82. Atomichron installation at Goldstone

shielded room to insure extremely low-leakage fields from the RF units that range over a band of frequencies from 100 kc to several kilomegacycles. An in-lock alarm signal informs studio personnel of the stability status of the 1-mc Atomichron reference signal from which is derived the 31.840000-mc synthesized LO signal. The 31.840-mc synthesizer and the transmitter oscillator, with the required instrumentation for determining the lock status, are shown in Figure 83.

Figure 84 shows the two racks that contain equipment for programming and controlling the receiver local oscillator. The left-hand rack contains the local oscillator programming equipment and the filters for determining the bandwidth of the synchronous receiver (Fig 85). The right-hand rack includes the programmed tape-operated digital equipment and the digital readouts. Relay-operated switches permit synchronous or nonsynchronous receiver operation and receiver bandwidth selection from the control panel. The only serious difficulty experienced with the installation of the local oscillator equipment at Goldstone has been heat. Failures due to overheating of components ranged from a klystron failure in the Atomichron to transistor malfunctions in the digital equipment. A generous distribution of cooling fans solved this problem.

The oscillator instrumentation described above has demonstrated a technique for stabilizing the frequency of a UHF radio system with an atomic frequency standard. A technique has also been demonstrated for extremely accurate control of receiver local oscillator tuning to accommodate the time-varying doppler shift on a Venus-reflected VHF signal.

3. The 2388-mc, Low-Noise Parametric Amplifier

The original 2388-mc receiver at the Goldstone Tracking Station has an effective noise temperature of 1580°K, which is typical of crystal mixers at the present state of the art. A fieldworthy low-noise, 2388-mc preamplifier was developed (RS 36-6, Vol I, p 42) and has now been installed at Goldstone, resulting in a receiver noise temperature of 300 to 400°K. This device can serve either as a principal low-noise amplifier or as the postamplifier following a 2388-mc maser amplifier. The latter configuration is used for the Venus experiment.

The amplifier is a one-port nondegenerate type utilizing a circulator in the signal port. The pump frequency of 9600 mc was chosen to make use of the extremely stable source already available at Goldstone as part of the 960-mc parametric amplifier system (RS 36-4, Vol 1, pp 45-47). The parametric element is a silicon varactor diode manufactured by Microwave Associates (Type MA450)

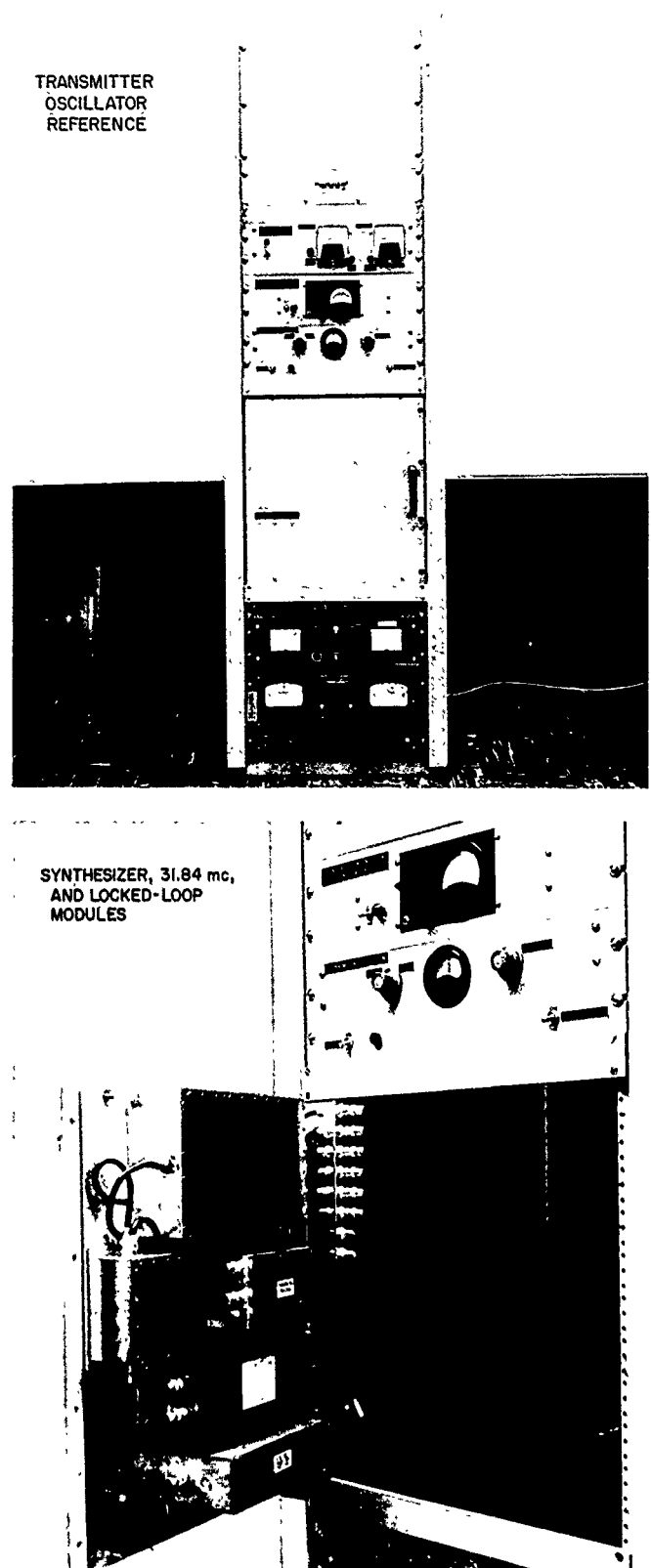


Figure 83. Transmitter oscillator reference for Venus radar experiment with 31.84-mc synthesizer and locked-loop modules

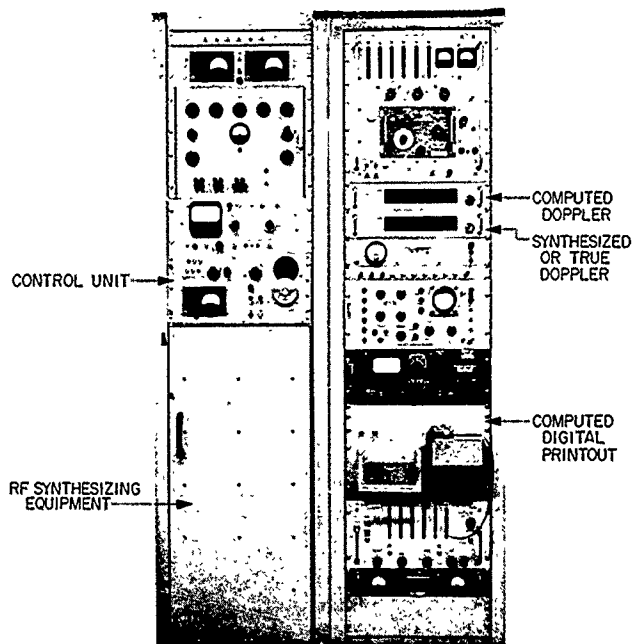


Figure 84. Receiver local oscillator for Venus radar experiment

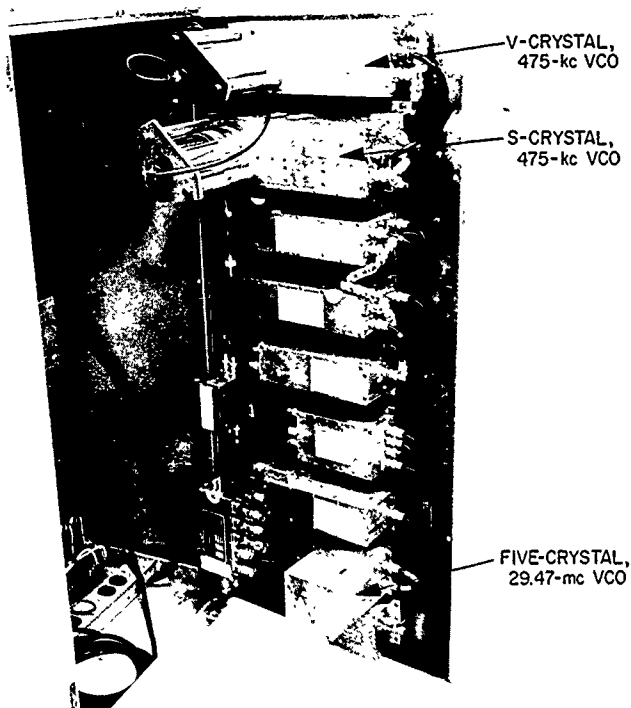


Figure 85. RF modules for synthesized receiver local oscillator

and operated at zero bias. The signal port includes dual radial chokes, one is tuned to the 9600-mc pump frequency, and the other is tuned to the 7212-mc idle frequency. Separate controls are provided for impedance matching at the signal, pump, and idle frequencies. Impedance matching at the signal frequency is accomplished with a quarter-wave sliding transformer having a characteristic impedance of 15 ohms in a nominal 50-ohm line. At the idle frequency, matching is done with an adjustable waveguide short, and at the pump frequency, with a ruggedized slide-screw tuner.

The amplifier is installed at the feed-point of the Goldstone receiving antenna in a weather-tight enclosure, insulated from excessive heat loss, and thermostatically controlled to minimize detuning over the ambient temperature range encountered at the Goldstone site. A photograph of the box mounted at the antenna feed-point is shown in Figure 86. A block diagram and interior photograph of the amplifier were presented in RS 36-6, Volume I, Page 42.

The pump source comprises a 32-mc, crystal-controlled oscillator, a $\times 5$ frequency multiplier, a 160-mc amplifier, a $\times 12$ UHF cavity frequency multiplier, a $\times 5$ microwave diode multiplier, and a 9600-mc klystron amplifier. A block diagram of the pump source is given in Figure 87. A photograph of the pump components mounted in



Figure 86. Parametric amplifier installed at feed-point

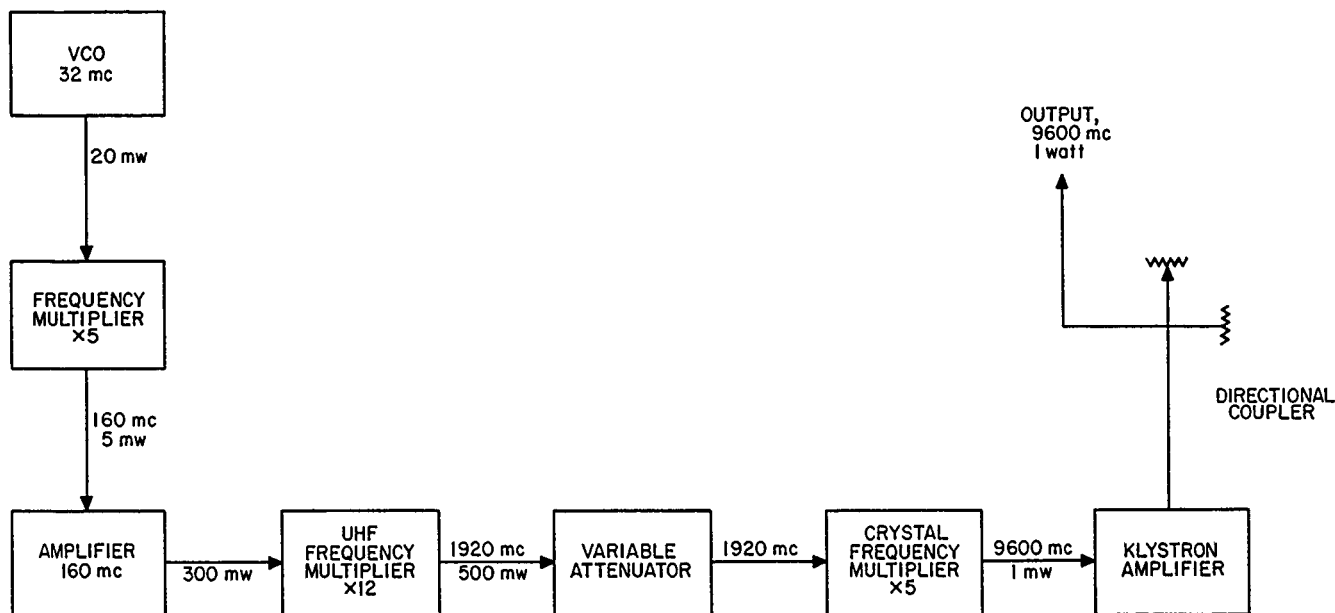


Figure 87. Block diagram of 9600-mc pump source

a weather-tight enclosure is given in Figure 88. The pump box is installed in the west electronics cage at the rear of the antenna reflector on the 85-foot diameter Ha-Dec antenna along with a second box containing a ferrite current-controlled attenuator and pump power

monitor. The pump power indication is repeated remotely in the control room and may be either manually adjusted or automatically maintained at the desired level at the control room console. The pump power is transmitted from the west cage to the parametric amplifier at the feedpoint through X-band waveguide that is supported along the west quadripod leg.

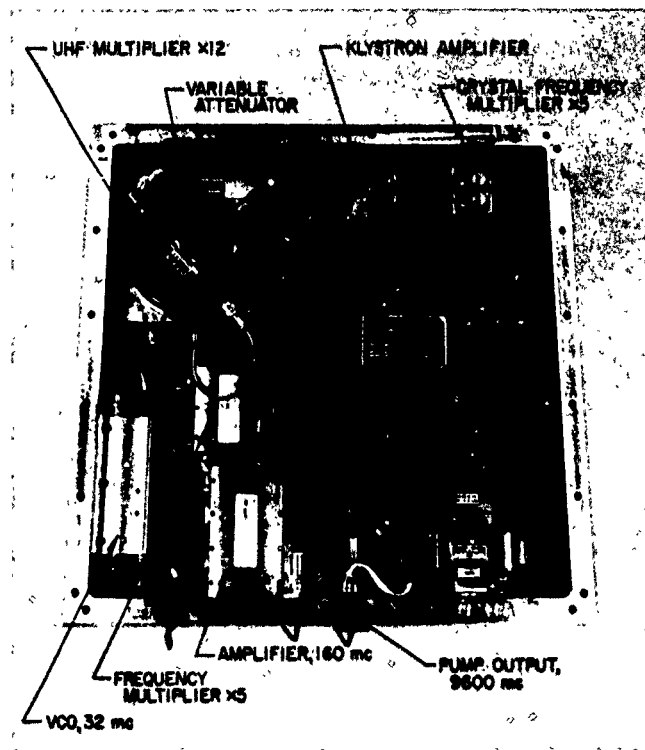


Figure 88. Pump source components

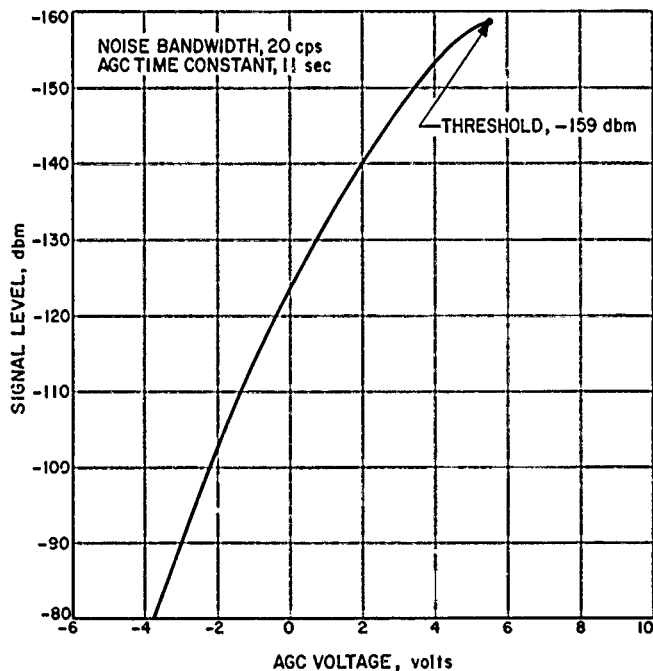


Figure 89. The 2388-mc receiver gain characteristic

The measured noise figure of the Goldstone parametric amplifier and following system was 3.25 db at 20-db gain, referenced to the parametric amplifier input terminal. This indicates a noise temperature of 322°K. The bandwidth is 5 mc. A space path receiver sensitivity curve was made using the parametric amplifier as the principal low-noise amplifier. The results are given in Figure 89.

It is noted that threshold of -159 dbm was obtained. Assuming an antenna temperature of 15°K, an input cable loss of 0.5 db, and a RF loop noise bandwidth of 20 cps, the theoretical threshold is -160 dbm; therefore,

reasonable agreement with theoretical performance has been obtained.

Preliminary gain stability checks have been made on the parametric amplifier. The gain drift measured 0.2 db over a 15-minute period while the antenna was oriented in various positions. Less than 0.5-db gain drift was observed over a 45-minute period. It is anticipated that periodic checks of gain and noise figure will be made during the Venus experiment as frequently as operational experience proves to be desirable. The noise figure test equipment installed for the maser amplifier will be used for this purpose.

PHYSICAL SCIENCES DIVISION

V. Chemistry Research

A. High-Resolution Nuclear Magnetic Resonance Spectroscopy

D. D. Elleman and S. L. Manatt

The theory of nuclear magnetic resonance (NMR) is well known (Refs 55 to 57). Since no previous studies on high-resolution NMR spectroscopy have been given in these summaries, a brief outline of the important effects is given here. In a magnetic field there are three principal factors which determine the magnetic environment of a nucleus having a non-zero nuclear magnetic moment. These are (1) the magnetic dipole interactions, (2) the magnetic shielding by the orbital electrons, and (3) the electron-coupled nuclear spin-spin interactions. In liquids and gases, where the molecules are undergoing very rapid random motion, the magnetic dipole interactions are nearly averaged to zero in most cases so that the latter two effects need only be considered. The magnetic shielding by the electrons manifests itself as an attenuation of the applied magnetic field, and the relative magnitude of this attenuation is referred to as the *chemical shift*. Chemical shift is directly proportional to field strength. The chemical shift can be related to local chemical environment and to local electron density. The

electron-coupled nuclear spin-spin interactions are transmitted by the bonding electrons in molecules in such a manner that they are not averaged to zero by the tumbling of the molecules in a liquid, gas, or solution. This spin-spin coupling is the main cause of the great complexity of the NMR spectra of molecules containing as few as three or four magnetic nuclei. This coupling is described in terms of coupling constants and is field independent. The term *high-resolution NMR spectroscopy* is generally applied to nuclear resonance experiments which permit resolution and measurement of the chemical shifts and spin-spin coupling constants in a molecule.

The high-resolution NMR investigations now in progress are concerned with (1) the determination of structural formulas, (2) the interpretation in detail of the spectra, including numerical evaluation of chemical shifts and coupling constants and the relation of these to molecular structure and symmetry, (3) the determination of the theoretical significance of the chemical shifts and coupling constants as related to electronic structure of molecules, (4) the influence of intra- and intermolecular interactions on the appearance of spectra, (5) the use of double-resonance techniques for the elimination of proton spin-spin coupling, (6) the NMR spectra of elements other than hydrogen, and (7) the improvement of NMR instrumentation. Some results from several of these investigations are briefly described here.

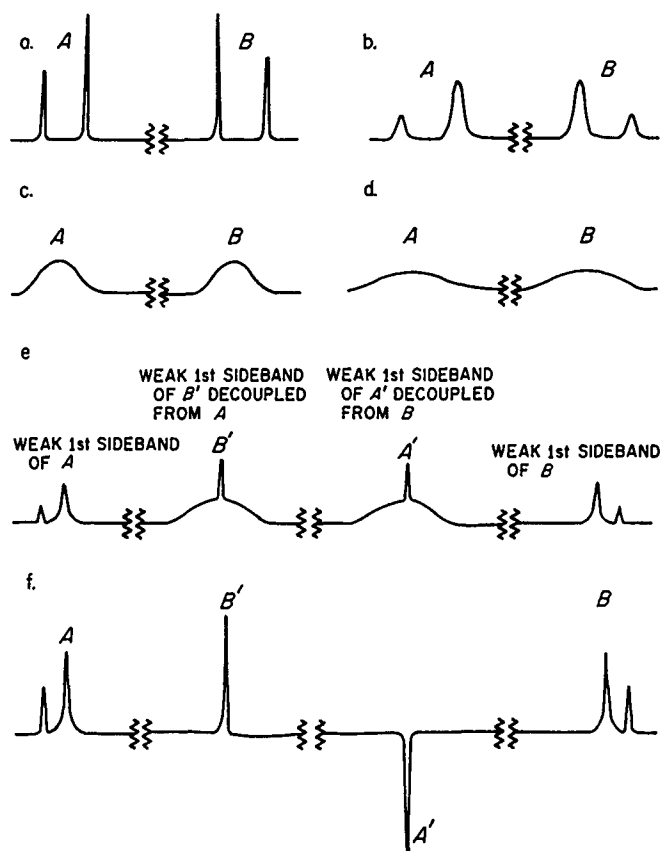
1. Proton-Proton Spin Decoupling

As mentioned above, the complexities of NMR spectra of very simple molecules have their origin in the various spin-spin couplings between the various magnetic nuclei. One way to simplify NMR spectra would be to selectively destroy this coupling. This can be accomplished by the double resonance technique (Refs 58, 59). This technique can be easily illustrated for a system of two types of nuclei, i.e., such as hydrogen (H^1) and fluorine (F^{19}). It is possible to eliminate the effect of the fluorine nuclei on the protons by strongly irradiating the fluorine nuclei at their resonance frequency while observing the proton spectrum. The strong irradiation of the fluorine nuclei destroys the coupling of the fluorine nuclei with the protons which are being observed. This technique has been used on several molecules where the nuclei being decoupled had different magnetogyric ratios. In these cases, the irradiation frequency is considerably different from the resonance frequency of the nuclei being observed. For example, in the case of the boron hydrides, the spin-spin multiplets due to B^{10} and B^{11} were collapsed while the proton resonance spectrum was observed (Ref 57, pp 298-305). There are other examples where complexities due to H^2 , N^{14} , F^{19} , Al^{27} , and P^{31} have been eliminated in NMR spectra by this double irradiation technique. There are many drawbacks and limitations to this technique, and it has only been used once to decouple protons (Ref 58). In this case, the quality of the spectra obtained left much to be desired.

There is another technique for accomplishing proton-proton spin decoupling with relatively simple instrumentation which only recently was described by Kaiser (Ref 60). This technique can be described as the audio sideband phase detection method and is illustrated in Figure 90 for a hypothetical proton two-spin system. Figure 90a shows the high-resolution spectrum for such a two-spin system. As the amplitude of the rotating magnetic RF field, used to simulate nuclear spin transitions, H_1 is increased, the spectrum is broadened due to partial saturation and the fine structure of the spectrum due to spin-spin coupling is lost. Figures 90b through 90d show this effect for increasing H_1 . For the disappearance of the fine structure it is necessary that Bloom and Shoolery's condition (Ref 59) for the scrambling of the spin states be met:

$$\gamma H_1 > \pi J$$

where γ is the gyromagnetic ratio, and J is the spin-spin coupling constant in cps. This condition is reached in Figure 90c. Figure 90e shows what is observed when a very weak audio signal is impressed on the sweep coils of the NMR probe of such a frequency that the first

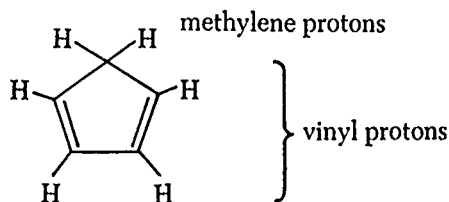


- b. TO d. DC SPECTRUM WITH INCREASING H_1
- e. DC SPECTRUM AT LARGE H_1 WHEN A WEAK AUDIO SIGNAL OF APPROXIMATELY THE CHEMICAL SHIFT BETWEEN A AND B IS ALSO APPLIED
- f. CONDITIONS DESCRIBED IN e. EXCEPT PHASE DETECTOR LOCKED TO AUDIO OSCILLATION EMPLOYED

Figure 90. High-resolution dc spectrum for hypothetical two-proton system, A-lines due to one proton, B-lines due to second proton

sideband corresponds approximately to the chemical shift difference between the two protons or groups of protons. This sideband signal will be decoupled, but its intensity will only be slightly above the noise level. Figure 90e also shows the other undecoupled sidebands. In the case of more complex systems where the decoupled proton (or protons) may still be coupled with other magnetic nuclei, the complete multiplet structure will probably not be discernible above the noise level. Figure 90f shows the quality of spectrum obtained if a phase detector locked to the audio oscillator is used to amplify the extremely weak sideband signals. The quality and resolution obtainable is just that realizable in a normal high-resolution experiment. On each side of the decoupled

spectrum, the undecoupled spectrum is observed. Instrumentation for performing this type of experiment has been added and is in operation with a 60-mc Varian Associates V4311 NMR spectrometer. Some improvements in performance over those reported in the literature (Ref 60) have been realized with the present system; a more detailed report on the instrumentation and results will be given elsewhere. Using this technique we have investigated the spectra of a number of complex molecules. Work is in progress to completely analyze their NMR spectra. Figure 91a shows the 60-mc spectrum of the three protons on the epoxide ring of propylene oxide, and the complexity of the undecoupled spectrum is obvious. Figure 91b shows the same region of the spectrum at a slightly different sweep rate when the methyl protons are decoupled from the 1-proton. The quartet at the left is the 1-proton. The 2-proton region is partially decoupled in Figure 91b due to the small chemical shift between the 1- and 2-protons (about 15 cps at 60 mc) and the spillover of the large input H_1 ; the 3-proton region is not changed. Figure 92a shows the spectrum of the four vinyl protons of cyclopentadiene:



This complex region would be impossible to analyze completely as is. Figure 92b shows the result of decoupling the down-field vinyl protons from the methylene protons. The up-field vinyl protons are also partially decoupled from the methylene protons because of the small chemical shift (about 7 to 9 cps at 60 mc) between the vinyl protons. For this molecule, the simplification brought about using spin decoupling is quite dramatic. The numerical evaluation of the chemical shifts and coupling constants from the decoupled spectrum of this molecule is currently in progress. The first trial assignments suggest that this particular system of two pairs of two equivalent spin coupled nuclei, designated as an A_2B_2 system, is different from other previously reported similar systems (Ref 57).

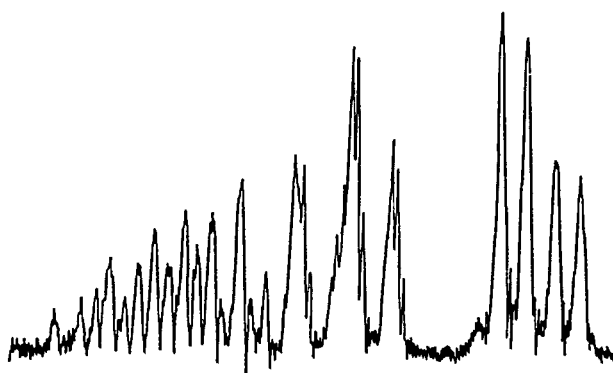
The audio sideband phase detection technique was used to study the NMR spectra of a number of other molecules such as pyridine, bicycloheptadiene allyl acetate, indene, acetaldehyde, acetaldehyde diethylacetal, 1,2-propylene glycol acetonide, and epichlorohydrin. In epichlorohydrin, two groups of protons about 40 cps apart at 60 mc were successfully decoupled. The results of some of these studies will be described at a later time.

2. Numerical Evaluation of NMR Chemical Shifts and Coupling Constants in Proton High-Resolution Spectra

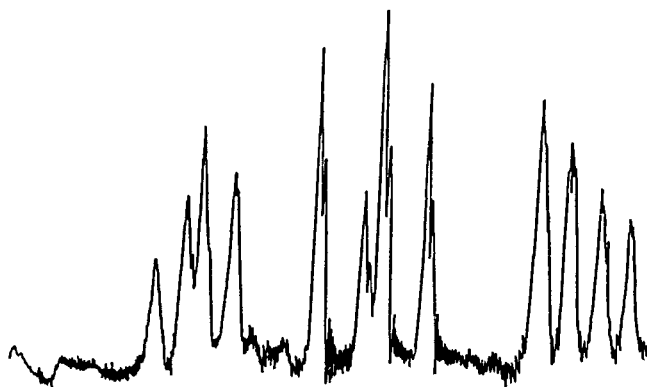
The high-resolution NMR spectrum of a molecule depends on the relative values of two types of parameters, the shielding constants (σ_i) or relative chemical shifts and the electron-coupled spin-spin interactions described by the coupling constants J_{ij} , between various magnetic nuclei. In general, the spectrum of n magnetic nuclei is completely determined by the n different chemical shifts and the $n(n-1)/2$ spin-spin coupling constants. The complete Hamiltonian for the problem is

$$\mathcal{H} = \mathcal{H}^{(0)} + \mathcal{H}^{(1)} = (2\pi)^{-1} \sum_i \gamma_i H_i I_z(i) + \sum_{i < j} J_{ij} \mathbf{I}(i) \cdot \mathbf{I}(j)$$

where γ_i is the nuclear magnetogyric ratio of the i th nucleus, H_i is the static magnetic field including any chemical shift, $I_z(i)$ is the component of the nuclear spin



a. PROPYLENE OXIDE; INCREASING SWEEP TO THE RIGHT



b. DECOUPLED SPECTRUM OF PROPYLENE OXIDE

Figure 91. Spectra of propylene oxide

Table 12. Dimensions of secular equations for systems of spin-coupled nuclei of spin 1/2 for n up to ten

Number of coupled nuclei, n	Dimension of submatrices ^a										
1	1										
2	1	2	1								
3	1	3	3	1							
4	1	4	6	4	1						
5	1	5	10	10	5	1					
6	1	6	15	20	15	6	1				
7	1	7	21	35	35	27	7	1			
8	1	8	28	56	70	56	28	8	1		
9	1	9	36	84	126	126	84	36	9	1	
10	1	10	45	120	210	252	210	120	45	10	1

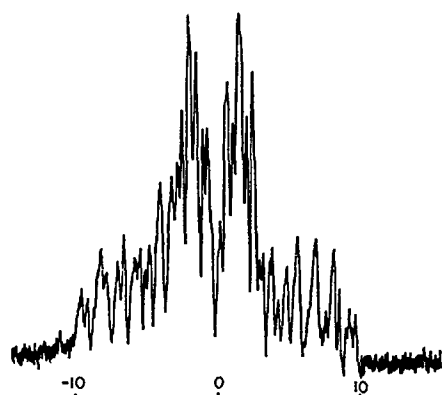
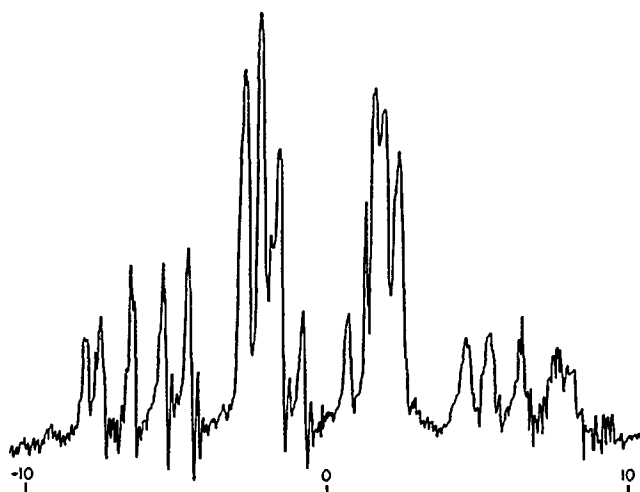
^aEach submatrix contains states of a given total magnetic moment starting with $\frac{n}{2} - 1, \dots, \frac{n}{2}, -\frac{n}{2}$ going from left to right.

Table 13. Number of transitions permitted for n nonequivalent nuclei of spin 1/2

Number of coupled nuclei, n	Number of permitted transitions
1	1
2	4
3	15
4	56
5	210
6	792
7	3003

various numbers of spin-coupled nonequivalent nuclei. Only in the simplest cases where there are only two nuclei, or three or more nuclei with a high degree of molecular symmetry, can an algebraic solution in closed form be obtained. Some of the most interesting and important cases are those where the latter conditions do not exist. To make any progress toward a solution for these systems requires an inordinate amount of numerical computation which can only be realistically attempted on a high speed electronic computer. An IBM 704 program (now being run on the IBM 7090) which is capable of solving problems of up to seven nonequivalent (no molecular symmetry) spin-coupled nuclei of spin 1/2, was obtained from Mellon Institute (Ref 62). A few systems have been completely analyzed for the various chemical shifts and coupling constants using this program, and several of these will be briefly described.

Professor John D. Roberts and his co-workers at the California Institute of Technology (CIT) demonstrated that the methylene protons of systems of the type

**a. VINYL PROTONS OF CYCLOPENTADIENE (60 mc)****b. DECOUPLED VINYL PROTONS****Figure 92. Spectra of vinyl protons**

along H_i , and I_i is the nuclear spin operator. The $\mathcal{H}^{(0)}$ term gives the interaction of the nuclei with the main magnetic field, and the term $\mathcal{H}^{(1)}$ gives the electron coupling of the nuclear spins. Methods for evaluating the matrix elements of the Hamiltonian are well known (Ref 57). For a system of n protons with nuclear spin 1/2, there are 2^n possible states. The 2^n basic product functions lead to a secular equation of order 2^n . There are well known rules (Ref 57) which lead to factorization of this secular equation into $(n+1)$ smaller secular equations whose dimensions go in a binomial manner as shown in Table 12. The presence of molecular symmetry can lead to still further factorization of each of the $n+1$ secular equations (Refs 57, 61). Transitions are only permitted between states whose total spin magnetic moment differs by ± 1 and, furthermore, transitions between states of different symmetry are forbidden (Refs 57, 62). The complexity of the resulting spectra is indicated in Table 13 where the number of spectral lines possible is shown for

$R-CH_2-CR_1R_2R_3$, may be magnetically nonequivalent and display AB rather than A_2 -type spectra (Ref 63). Recently, they found several examples of this type of behavior for ethyl groups (Ref 64), and knowledge of this is important to anyone using NMR for qualitative identification of the ethyl group. Instead of the familiar four-line pattern of spin-spin splitting for the methylene protons (Ref 56), they observed a very complicated pattern as shown in Figure 93. In collaboration with Professor Roberts and his co-workers, we have completely analyzed the spectrum of the ethyl groups of acetaldehyde diethyl acetal as shown in Figure 93 (Ref 64).

The NMR spectra of several simple epoxides have recently been reported by Reilly and Swalen (Ref 65). Since the epoxides studied had groups capable of fairly strong electron withdrawing properties, we felt that it would be interesting to determine the coupling constants of an epoxide that is free from such strong electronic perturbations. About the time that work on this problem was started, Mortimer (Ref 66) reported the C^{13} satellite resonance of ethylene oxide at 40 mc, but it was possible to determine only the *cis*- and *trans*-coupling constants and not the geminal one which has theoretical importance. Some time ago, (Ref 67) Gutowsky investigated at 40 mc the NMR spectrum of propylene oxide, but did not give a full account of the spectrum, and stated that it was

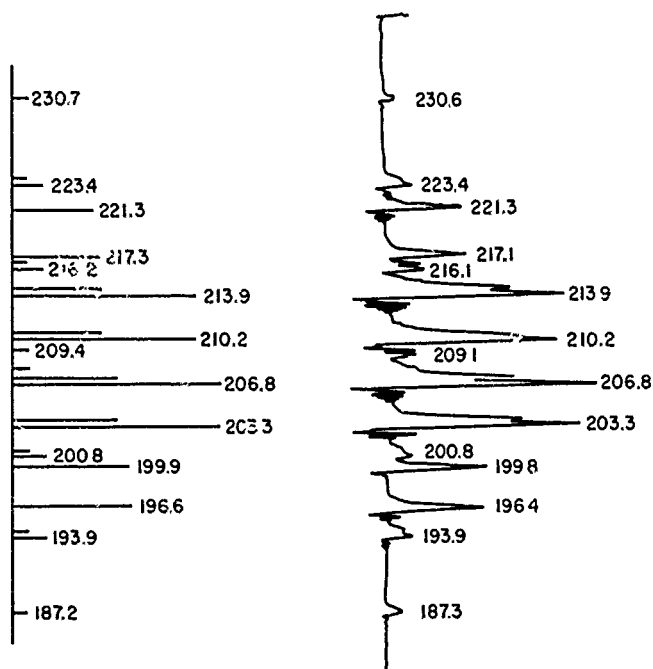


Figure 93. Nuclear magnetic resonance spectra of acetaldehyde diethylacetal at 60 mc with tetramethylsilane as internal reference

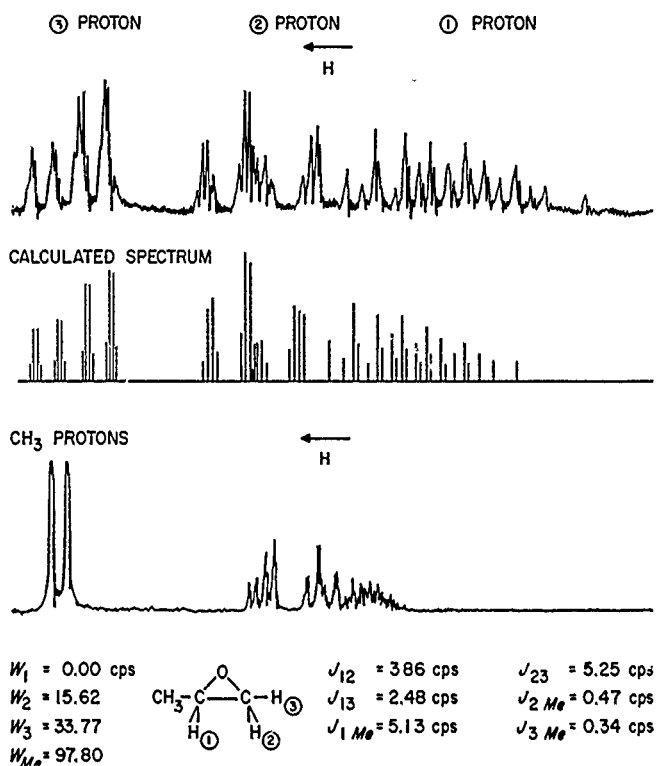


Figure 94. High-resolution NMR spectrum of propylene oxide

too complicated to analyze completely. We have studied the 60-mc NMR spectrum of propylene oxide and carried out a complete analysis of its spectrum. The coupling constants and chemical shifts which were obtained are summarized in Figure 94. An interesting result which we observed was the long-range, spin-spin coupling of the methyl group protons with the 2- and 3-protons on the epoxide ring. Usually, proton spin-spin couplings, except those involving π -electron systems, are negligibly small over more than three bonds (Refs 56, 57).

3. Use of C^{13} Satellite Spectra for the Determination of Proton-Proton Coupling Constants in an Equivalent Set

In a molecule with a single equivalent set of protons bonded to a carbon atom framework, the spectrum will consist of a strong central line and two sets of weak signals on either side of the strong central line. These sidebands result from the fact that although ordinary carbon C^{12} has no nuclear magnetic moments, normal atomic carbon contains about 1% of C^{13} nuclei which have spin $1/2$, and the spin-coupling constant between C^{13} and H^1 directly bonded to it is about 150 cps for systems not containing π -electrons. By detailed analysis of the struc-

ture of C^{13} satellite sidebands, the proton-proton coupling constants in symmetrical molecules can be deduced.

Professor John D. Roberts and Mr. Merlin Howden of CIT have observed the C^{13} satellite spectrum of 1,1-dichlorocyclopropane as shown in Figure 95. In collaboration with them, we have carried out the numerical evaluation of the proton-proton coupling constants. The size of the *cis*- and *trans*-coupling constants, 7.95 and 11.05 cps, respectively, are larger than have been observed before, but this molecule does not contain any large eclipsed groups adjacent to each other as in most of the previously studied cyclopropane derivatives. The analysis of this spectrum has allowed the first direct determination of the H-C-H coupling constant for the cyclopropane ring, and the value of 1.9 cps supports the theory of Karplus et al (Ref 67) that as the H-C-H bond angle becomes greater than $109^{\circ}28'$, the proton-

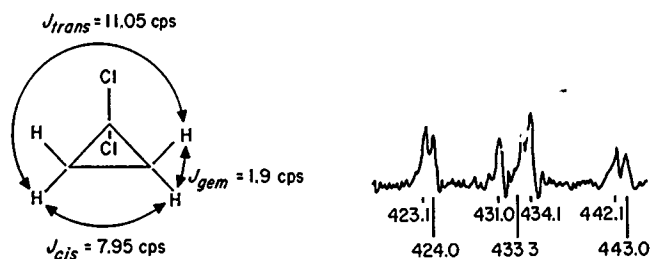


Figure 95. Up-field C^{13} satellite of 1,1-dichlorocyclopropane at 60 mc with chemical shifts relative to benzene $J_{C^{13},H} = 166.4$ cps

proton coupling should become smaller than 12.5 cps. The H-C-H bond angle reported for cyclopropane is about 118 degrees (Ref 68), and Karplus' theory (Ref 67) predicts a coupling constant of about 4 cps.

VI. Physics Research

A. Fission Electric Cells

W. F. Krieve

1. Capsule Irradiation

An experiment has been designed to determine the acceptability of fission electric cell fuel elements (RS 36-4) that have been fabricated by various techniques. Acceptability of sample fuel elements, which are essentially thin layers (3.0 to 10.0 mg/cm²) of fissionable material on suitable base materials, will be determined by following their operating characteristics during irradiation in a high-density neutron flux, and by post-irradiation analysis. Maximum neutron flux intensities that can be tolerated in a typical experiment of this type are available in the pool region of a pool research reactor of the MTR category. Space limitations and environmental conditions in the pool irradiation area have determined the size, shape, and structural material of the fuel element or capsule and, consequently, the magnitude of the currents that are to be measured.

a. Capsule structure. The capsule is formed by a pair of concentric cylinders with the inner space hermetically sealed and evacuated; it contains a cylindrical anode

section supported by quartz rods from the outer cylinder. A portion of the inner cylinder supports the fissionable material and serves as the cathode. A solenoid surrounds the capsule and will be the source of the magnetic field for suppression of the δ - or follow-out electrons that accompany the fission fragments. The shape of the anode, cathode, and magnetic field has been contoured so that fragments that do not reach the anode will be intercepted by the cathode in regions where the magnetic field is perpendicular to the electrostatic field and the magnetic field is of sufficient magnitude to suppress the secondary electrons produced.

The outer shell of the capsule has a 2.00-inch diameter, and the inner cylinder has a 0.50-inch diameter except in regions that are expanded for fragment interception. Total capsule length is 9.0 inches. The fuel layer is deposited in the central 3-inch section of the inner cylinder and has a surface area of 30.4 cm². Nominal wall thicknesses are 0.025 inch, and the material, 6061-T6 aluminum. The anode is 1.50 inches in diameter (except in contracted regions), is 6.10 inches long, and is 0.002 inch thick. Anode material is nickel. Aluminum wire is used for the coil which is canned in an aluminum container that has an ID of 2.16 inches, an OD of 2.685 inches, and a length of 9.5 inches.

An ion pump will be attached to the first capsule, at least, to help maintain the vacuum and to determine if an ion pump will function when located in an intense field of ionizing radiation. The pump and electrical terminals are sealed in a container that is attached to the capsule and coil housing. Electrical leads are strung through an aluminum tube that extends from the pump housing to the pool surface. This distance is approximately 26 feet.

An attempt has been made to minimize the net current loss through lead wire insulation and terminal insulators. Materials and mass ratios between conductors, grounding shield, and insulation have been selected so that the current flow of electrons produced by Compton interactions will be reverse to and of the same magnitude as the current flow due to the conductance of the insulation in the ionizing radiation. Background currents have been minimized by the use of low-density, low-radiative-capture neutron cross section material that is compatible with the environment, and by the use of the thin anode. This gives a low production rate of high-energy electrons and beta rays in the structural material and a low probability that these particles will be stopped in the anode.

b. Experimental procedure. Expected currents from the capsules with various amounts of fissionable material

will be: fission fragment current, i.e., current with magnetic field, +10 to +20 μamp ; δ -electron current, i.e., current without electron suppression, -100 to -200 μamp ; background current due to Compton electrons and beta rays, -0.1 to -0.5 μamp ; and leakage current, -0.5 to +0.5 μamp . The maximum design potential of the capsule is 5 kv.

Following the irradiation and a cooling period, the capsules will be transferred to a hot cell where they will be machined open to allow visual and analytical inspection. Spatial distribution of several of the fragment species typifying both the heavy and light group will be determined on the anode and cathode by gamma count analysis. The ratio of the number of several species of fragments between the anode and cathode will be determined via both gamma spectroscopy and chemical analysis. The amount of fissionable material transferred from the cathode to anode will be measured by chemical analysis. Results of these examinations will not only give information about the operating characteristics of a fuel element, but also energy, charge, and range distribution of fission fragments.

A capsule utilizing an electrostatic grid to suppress the δ -electrons is being designed. This capsule will be used to determine the feasibility of δ -electron suppression via a grid as well as fuel element analysis.

VII. Gas Dynamics Research

A. Stability of a Shear Layer in a Magnetic Field

J. Menkes

It is demonstrated that a uniform magnetic field in a direction normal to the mean flow has a stabilizing influence. A disturbance which propagates with fixed maximum amplitude in the absence of a magnetic field is shown to be damped once the field is applied. The degree of damping is proportional to the Alfvén speed. This confirms a result obtained earlier by Stuart (Ref 69) for the case where the magnetic field is aligned with the mean flow. For the case of infinite conductivity, the flow is absolutely stable for arbitrarily small magnetic fields.

B. Similarity Solution for Stagnation Point Heat Transfer in Low-Density, High-Speed Flow

M. Chahine

The problem considered is that of estimating skin friction and heat transfer to a spherical body at supersonic speeds and under rarefied gas conditions.

When a sphere travels at supersonic speeds, a shock wave is formed close to the front surface, and by confining ourselves to the region close to the stagnation point, the shock wave can be taken to a good approximation as spherical and concentric with the sphere. We will assume that close to the stagnation point, conditions at the outer edge of the boundary layer correspond to those immediately behind the shock. Also, the temperature of the surface T_w is assumed to be constant.

A similarity type solution is obtained for the compressible boundary layer with heat transfer and pressure gradient, and the order of magnitude estimates are those appropriate to the stagnation region of a sphere of radius a .

1. Basic Equations

The equation of state for a perfect gas is

$$P = \rho RT \quad (1)$$

where P is the pressure, ρ is the density, R is the gas constant, and T is the temperature. The Prandtl number, $\sigma = \mu C_p / K$, is taken to be a constant. A spherical system of coordinates (r, θ, ϕ) is used as shown in Figure 96; however, since the body is axisymmetric, the velocity component in the ϕ direction is equal to zero, and subscripts ∞ and 1 denote conditions ahead of and behind the shock wave. In accordance with the oblique shock

relation, the tangential velocity behind the shock v_θ is related to conditions ahead of the shock by the relation

$$v_{\theta_1} = U_\infty \sin \theta \quad (2)$$

Subject to the conditions stated above, we now seek a solution for the steady axisymmetric compressible laminar boundary layer equation for perfect fluids. We assume that the dependent variables have the forms

$$\begin{aligned} v_r &= v(r) \cos \theta \\ v_\theta &= u(r) \sin \theta \\ \rho &= \rho(r) \\ \bar{\mu} &= \mu(r) \cos \theta \\ \rho_\mu &= \text{constant} \end{aligned} \quad (3)$$

with the pressure variation behind the shock given by

$$\frac{-\partial P_1}{\partial \theta} = \rho_1 U_\infty^2 \sin \theta \cos \theta \quad (4)$$

and

$$\frac{\partial P}{\partial \theta} = \frac{\partial P_1}{\partial \theta}$$

The continuity equation

$$\frac{\partial}{\partial r}(\rho v_r) + \frac{1}{a \sin \theta} \frac{\partial}{\partial \theta}(\sin \theta \rho v_\theta) = 0$$

and the boundary condition at the shock are satisfied by

$$\rho r' = - \left(\frac{2 \rho \mu U_\infty}{a} \right)^{1/2} f(\eta) \quad (5)$$

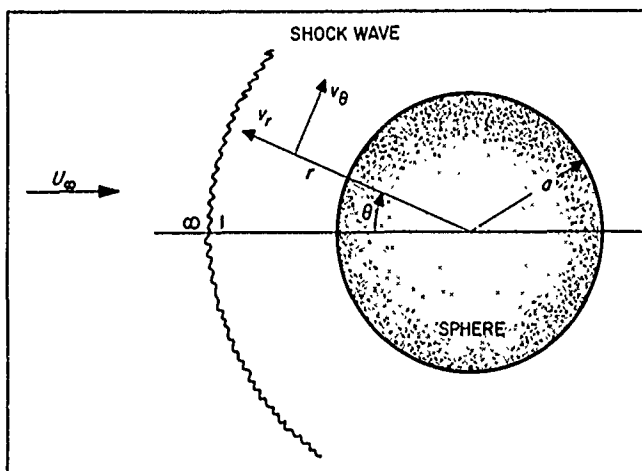


Figure 96. Coordinate system on sphere in hypersonic flow

and the effect of compressibility is made less marked by choosing a Howarth variable

$$\eta = \left(\frac{2U_\infty}{\rho \mu a} \right)^{1/2} \int_a^r \rho ds \quad (6)$$

Substituting Equations (2), (3), (4), and (5) into the momentum and energy equations and reducing the results to the stagnation region, taking into account that the temperature $T(r, \theta)$ is an even function symmetric with respect to $\theta = 0$, the final results read

$$\begin{aligned} f''' + ff'' &= \frac{1}{2} [f'^2 - g] \\ g'' + \sigma f g' &= 0 \end{aligned} \quad (7)$$

where

$$g = \frac{T}{T_1} = \frac{\rho_1}{\rho}$$

Since f and g are not a function of the standoff distance of the shock wave, the boundary conditions at the outer edge of the boundary layer, i.e., conditions at the shock, will be taken at infinity, or

$$\begin{aligned} f(0) &= 0 & f'(0) &= 0 & g(0) &= \frac{T_w}{T_1} \\ f(\infty) &= 1 & g(\infty) &= 1 \end{aligned}$$

This equation was first given by V. M. Falkner and S. W. Skan, and its solutions were studied in detail by C. B. Cohen and E. Reshotko (Ref 70). From these solutions, the variations of the shear function at the wall $f''(0)$ with respect to the heat transfer function g can easily be computed.

The shear function $f''(0)$ is related to the shear stress of the wall τ through the expression

$$\tau = \left(\bar{\mu} \frac{dv_\theta}{dr} \right)_{r=a} = \left(\frac{2 \rho \mu U_\infty^3}{a} \right)^{1/2} f''(0) \sin^2 \theta \cos \theta \quad (8)$$

The value of the skin friction drag coefficient is then obtained by integrating the axial projection of τ over the front surface of the sphere. The resulting relation is

$$C_{f,r} = 8 \frac{(\rho_1/\rho_\infty)^{1/2}}{Re_1^{1/2}} f''(0) \int_0^{\theta_1} \sin^3 \theta \cos \theta d\theta \quad (9)$$

where the upper limit of integration θ_1 is determined experimentally from the unheated case $T_{tr} = T_1$ by matching the theoretical curve with the experimental points, as shown in Figure 97, and by taking the experimental value of the pressure drag coefficient to be 1, or

$$C_{D,theor} = 1 + \frac{9}{8} \frac{(\rho_1/\rho_\infty)^{1/2}}{Re_1^{1/2}} f''(0) \quad (10)$$

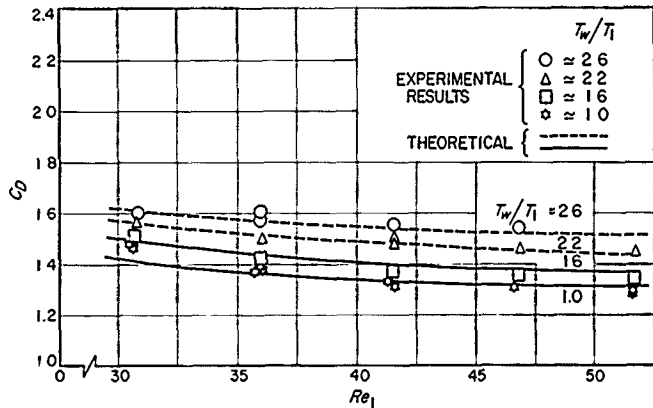


Figure 97. Theoretical and experimental sphere drag, $3.8 < M_\infty < 4.3$; $0.013 < K_n < 0.200$; $1 < T_w/T_1 < 2.6$

Furthermore, Figure 97 serves to indicate that aerodynamic characteristics will be quite seriously affected by the heat transfer conditions and that the trend of these changes is well predicted by Equation (10). However, it should be noted that the curves for $T_w > 2T_1$ are obtained by extrapolation from Reference 70, since $f''(0)$ is given for values of g up to 2 only.

C. Hot-Wire Anemometer in Hypersonic Flow

T. Vrebalovich

The hot-wire technique for measuring fluctuations in supersonic flow has been extended to hypersonic flow in the JPL 21-inch Hypersonic Wind Tunnel where the stagnation temperatures can be as high as 1400°F. The hot-wire probe design for use in this high stagnation temperature flow and some preliminary results follow.

1. Hot-Wire Probe Design

The probes that have been used in supersonic flow fields were designed to tolerate temperatures near room temperature and could not be used in high stagnation temperature flow fields. Therefore, new probes had to be designed for use in the hypersonic tunnel. The hypersonic hot-wire probes are shown in two views in Figure 98. They consist of a 0.25-inch diameter stainless steel body with a nosepiece which has a flat parallel to the air stream. A ceramic adhesive, Temporell 1604, was painted on this flat portion, and the probe was then

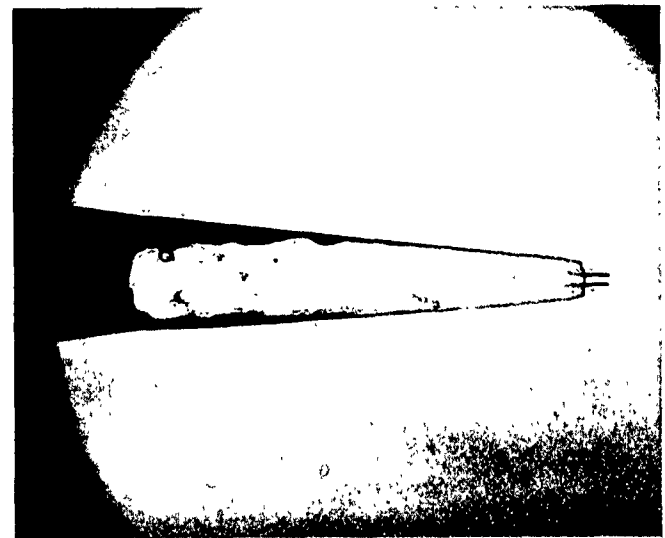


Figure 98. Hypersonic hot-wire probes

baked in an oven. This ceramic was an insulator for a pair of small jewelers' broaches which were placed on the ceramic coat, and more of the ceramic adhesive was used to hold the broaches on the flat portion. The broaches had a tip diameter of 0.002 inch and were spaced 0.012 to 0.015 inch. A wire made of 90% platinum and 10% rhodium and 0.00005 inch in diameter was spot-welded to the broach tips. Glass insulated nickel wires were welded to the broaches and attached to a plug at the base of the probe.

2. Operating Procedure in Hypersonic Tunnel

The hot-wire probe was mounted on a vertical traverse mechanism in the hypersonic tunnel as shown in Figure 99. A second probe with only one broach had 0.001-inch diameter chromel and alumel thermocouple wires

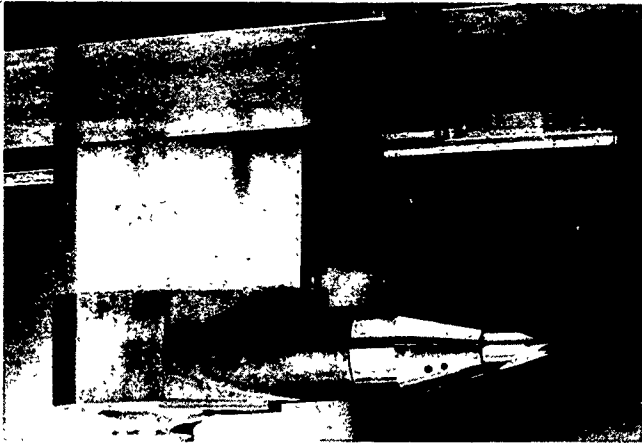


Figure 99. Hot-wire probe in hypersonic tunnel

welded at the tip to determine the recovery temperature of the broach for use in calculating the hot-wire end-loss corrections. The tunnel was started with the wire out of the flow field and in the traverse well. A Shapiro and Edwards Model 50B hot-wire anemometer was used to measure the wire resistance and determine the fluctuations present in the tunnel.

3. Preliminary Results

At a Mach number of 8.5, the tunnel was operated at supply pressures P_t of 130 to 2500 cm Hg and supply temperatures T_t of 750 to 1000°F. For $P_t = 1000$ cm Hg and $T_t = 850$ °F, the wire in the flow increased its resistance by nearly 55% over the room temperature resistance to indicate an average wire recovery temperature of 90% of the stagnation temperature. The broach tip temperature was 85% of the stagnation temperature. The percentage of overheat to which a wire could be heated was dependent mainly on T_t for a given P_t . For the case described above this maximum overheat was about 30% of the recovery resistance, 100% of the room temperature resistance, or an average wire temperature of 1200°F. Measurement of the fluctuating voltage across the wire showed that the mass flow fluctuations were about 2.5% and the total temperature fluctuations were about 0.2%. The wire is in free molecular flow with a Knudsen number based on free stream conditions of 32 for the lowest P_t and, of course, this presents some problems in the reduction of the hot-wire data. These first experiments indicate that the hot-wire technique is applicable to the environment of the 21-inch Hypersonic Wind Tunnel.

ENGINEERING MECHANICS DIVISION

VIII. Materials Research

A. Graphite

W. V. Kotlensky and D. B. Fischbach

1. Graphite Tension Testing

Determination of tensile properties of pyrolytic graphite supplied by Lockheed Missile and Space Division for the purpose of noting lot-to-lot variations has been continued. These tests were made in the manner previously described (RS 36-3, 36-7).

Tensile data from five lots of pyrolytic graphite produced by three different manufacturers are presented in Table 14. The ultimate tensile strengths and elongations for these lots are not markedly different from the data for Lots 158, 159, and 160 previously given (RS 36-7). The relatively low strengths for Specimens 3003, 3006, 3017, 3028, and 3200 may be attributed to either a notch effect caused by nicks along the edges of the gage section or fracture at large growth cones. Because of the limited number of tests, no definite conclusions on the variations in tensile properties from lot-to-lot are apparent.

An examination of the microstructures (Fig 100) reveals little difference, except for Lot 175 which shows a more regenerative structure. The relationship between the microstructure and tensile properties for these eight lots (Table 14 and RS 36-7) is being studied.

Also presented in Table 14 are elongations for room temperature tests which were obtained from a dial indicator clamped to the specimen holders. Elongations of approximately 0.5% would be expected (assuming a modulus of 3 million psi) if the strain were entirely elastic. The difference between the expected and measured strain suggests that about 1% of the measured strain may be due to specimen seating.

Reduction in area data for 5000°F tensile tests for lots shown in Figure 100 are given in Table 15. It is noted that there is a greater reduction in thickness (perpendicular to the basal planes) than in width (parallel to the basal planes) and that the greater the recorded elongation, the greater the reduction in area.

A study of the effect of hot-working pyrolytic graphite on its tensile strength (reported in RS 36-7) has also continued. These data, which are presented in Table 16, show that prestraining at 5000°F and testing at lower temperatures definitely increases the tensile strength of pyrolytic graphite and that the amount of increase in strength is dependent upon the amount of hot-working.

A typical engineering stress-strain curve recorded during the straining at 5000°F, as well as during the testing at 4000°F, is shown in Figure 101.

Earlier data (RS 36-3, 36-4, 36-5) showed changes in X-ray structure and microstructure when pyrolytic

Table 14. Pyrolytic graphite test data

Lot ^a No.	Specimen No.	Test Temperature, °F	Ultimate tensile strength, psi	Recorded elongation, %	Elongation from holders, %	Lot ^a No.	Specimen No.	Test Temperature, °F	Ultimate tensile strength, psi	Recorded elongation, %	Elongation from holders, %	
165	2995	Room	10,000	1.8	1.4	167	3026		17,200	1.4	—	
	2996		12,800	2.0	1.5		3028		8,500 ^b	2.0	—	
	3003		5,200 ^b	1.2	1.1		3030		10,500	0.5	—	
	3006		9,000 ^b	1.6	1.4		175		3193	17,100	—	—
	3007		14,300	1.9 ^c	1.6				3194	21,000	4.1	—
166	3015		14,100	2.1	1.9	3195	3000	19,400	4.2	—		
	3020		11,000	2.0	1.8	166	3017	4000	8,200 ^b	1.8	—	
	3025		10,900	2.0	1.8		3018	16,800	3.2	—		
175	3190		15,000	1.4	1.2	3021		21,800	2.6	—		
	3191		16,300	1.8	1.6	175		3196	18,900	3.1	—	
	3192		16,000	1.7	1.5			3197	21,800	4.6	—	
176	3200		6,300 ^b	1.8	—	3198	21,200	4.5	—			
	3201		14,700	2.5	2.3	3199	26,100	5.0	—			
	3202		17,700	2.4	2.2	176	3204	22,300	3.7	—		
	3203		12,100	1.9	1.8		3205	18,500	3.1	—		
165	2997	3000	11,200	2.7	—	3206	26,300	4.8	—			
	2998		16,000	3.7	—	3207	4000	24,000	4.0	—		
	2999		13,300	2.7	—	165	3005	5000	>60,400 ^c	>32 ^c	—	
	3004		12,500	2.1	—		166	3016	5000	>72,000 ^c	>50 ^c	—
	3008		18,200	1.8	—	3023		5000	>63,500 ^c	>43 ^c	—	
166	3009		14,900	1.9	—							
	3014		18,200	2.7	—							
	3019		11,300	2.1	—							
	3024		16,600	2.3	—							

^aLots 165, 166, 167 produced by High-Temperature Materials, Inc; Lot 175 produced by Raytheon Co; Lot 176 produced by General Electric Co.

^bLow strengths may be due to notch effects or large growth cones.
^cPull rod broke during test.

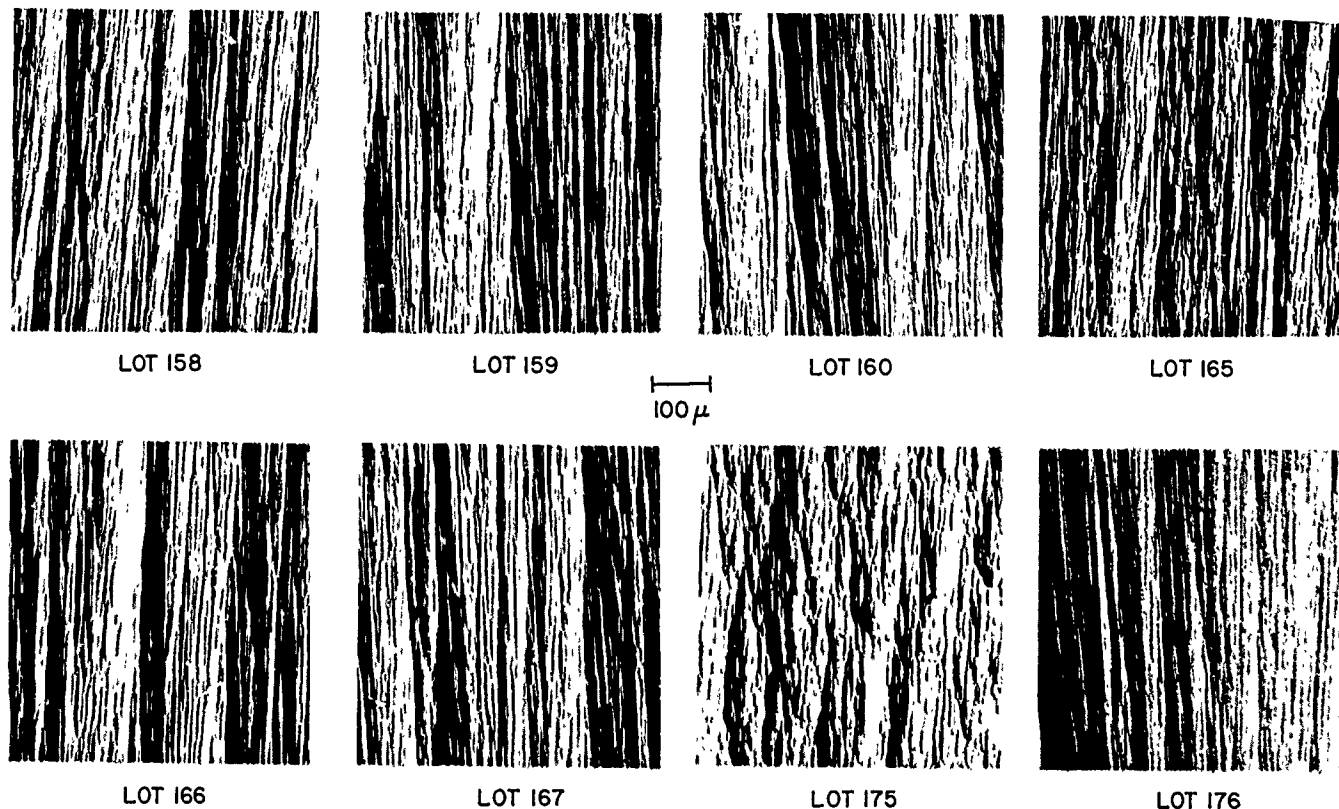


Figure 100. Microstructure of as-deposited pyrolytic graphite, unetched using polarized light

Table 15. Pyrolytic graphite reduction in area data for tests at 5000°F

Lot No.	Specimen No.	Maximum reduction, %			Recorded elongation, %
		Width	Thickness	Area	
165	3005	5.1	14.0	12.5	>32 ^a
166	3016	() ^b	() ^b	() ^b	>50 ^a
	3023	2.6	13.2	14.0	>43 ^a
158	2944	() ^b	() ^b	() ^b	70
	2945	1.8	16.8	17.6	>61 ^a
	2946	4.2	11.2	11.3	>46 ^a
159	2957	4.3	20.2	23.6	>68 ^a
	2958	() ^b	() ^b	() ^b	113
160	2967	9.7	28.9	35.8	>139 ^a
	2968	() ^b	() ^b	() ^b	81
	2970	4.5	14.5	18.4	57

^aPull rod broke during test; elongation greater than value reported.
^bMeasurement not possible because of the type of fracture which occurred.

graphite was deformed. Varying amounts of strain at 5000°F would be expected to show varying structural changes. Evidence that this did occur during straining at 5000°F is presented in Figures 102 and 103. It is noted that only after 36.9% deformation has the growth cone structure disappeared, and the two-dimensional (10) reflection has split into the crystalline (100) and (101) reflections. Although the changes at the smaller deformations are not as marked, they still have an effect on the tensile strength (Table 16).

2. Magnetic Susceptibility of Pyrolytic Graphite

The magnetic susceptibility of pyrolytic carbons is being investigated using the Faraday method. The susceptibility perpendicular (χ_{\perp}) and parallel (χ_{\parallel}) to the plane of the deposit is measured at room temperature as a function of heat treatment temperature. The total susceptibility (the spur of the tensor), $\chi_T = \chi_{\perp} + 2\chi_{\parallel}$ is also computed from these data. This quantity is very useful for comparison purposes since preferred orientation effects are eliminated. Some results were reported previously in RS 36-5 and 36-6; recent results are described below.

The susceptibility apparatus has been modified by replacing the constant gradient magnet pole caps originally used with more suitable constant force ($H dH/dz$ constant) pole caps. These caps provide a small volume of the field in which the results are insensitive to small variations in the sample position. The maximum usable field with these caps, with a gap of 0.5 inch, is about 15,000 oersteds. All measurements are now made in direct comparison to a platinum standard by first measuring the

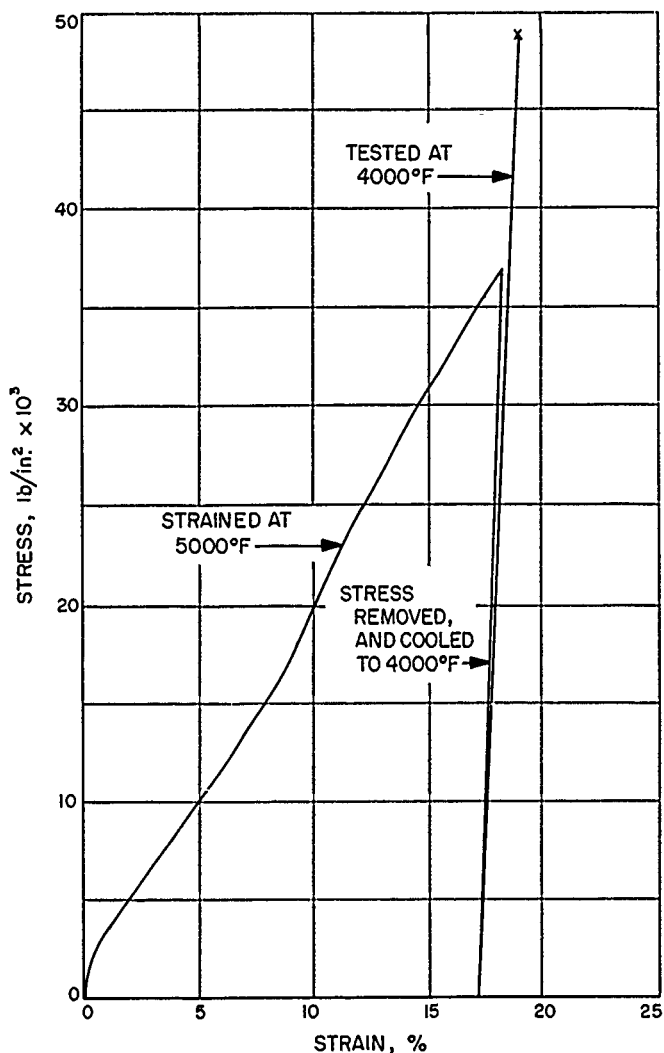


Figure 101. Engineering stress-strain curve for pyrolytic graphite prestrained at 5000°F, tested at 4000°F: stress parallel to basal planes, strain rate $2 \times 10^{-4} \text{ sec}^{-1}$, Block 14701

sample and then the standard under identical conditions. The susceptibility of Pt is taken as 0.971×10^{-6} cgs units per gram (Ref 71). This procedure eliminates the necessity of a direct determination of the quantity $H dH/dz$, which is difficult to measure with precision. Measurements of χ vs H indicate the presence of some ferromagnetic impurity, either in the graphite or the platinum standard. The true susceptibility may be obtained by extrapolation of the plot of χ vs $1/H$ to infinite field strength (Owen-Honda method). Such a plot of the present data indicates that the values obtained at 15,000 to 20,000 oersteds are equal to the extrapolated values within experimental error. Therefore, all measurements have been made at the maximum field strength and no correction applied.

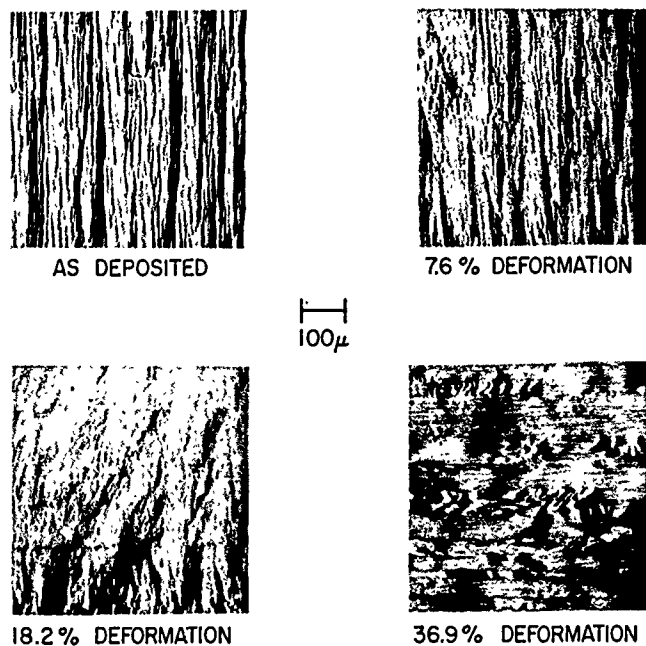


Figure 102. Microstructure of pyrolytic graphite after various deformations at 5000°F, Block 14701 unetched using polarized light

Changes in the room temperature susceptibility resulting from heat treatment at high temperatures (at 3200°C and above, by R. J. Diefendorf of G. E. Research Laboratory) have been observed for several pyrolytic carbons deposited at various temperatures T_D ranging from 1900 to 2300°C. The results are shown in Figure 104 and in Table 17. Samples A, B, and C were cut from flat slabs, Blocks 14601-2593, 14803, and 14124 (by G. E. Research Laboratory, see RS 36-6), respectively; Samples D and E, from hollow cylinders, Lots 140 and 110 (by Avco Manufacturing Co.), respectively. A strong dependence of the heat treatment behavior on the deposition temperature is evident. The values for A and B deposited in the range 2100 to 2300°C fall on the same curve, despite differences in preferred orientation and probable differences in manufacturing technique. The as-deposited and 3400°C values for Sample C also fall on this curve. Measurements of χ_L show that the minimum for Sample C occurs at a temperature about 200°C lower than that of A and B (RS 36-5, Fig 19). Since χ_{11} was not measured for all heat treatments for this material, a complete χ_T curve cannot be plotted. However, the single point at 2900°C is consistent with this temperature shift. The as-deposited susceptibility of these materials is appreciably greater than that of natural single-crystal graphite. The final values, after heating to temperature of 3200°C and above, is within the range (20.5 to 21.2×10^{-6}) found by Eatherly and McClelland (Ref 72) for well-graphitized petroleum

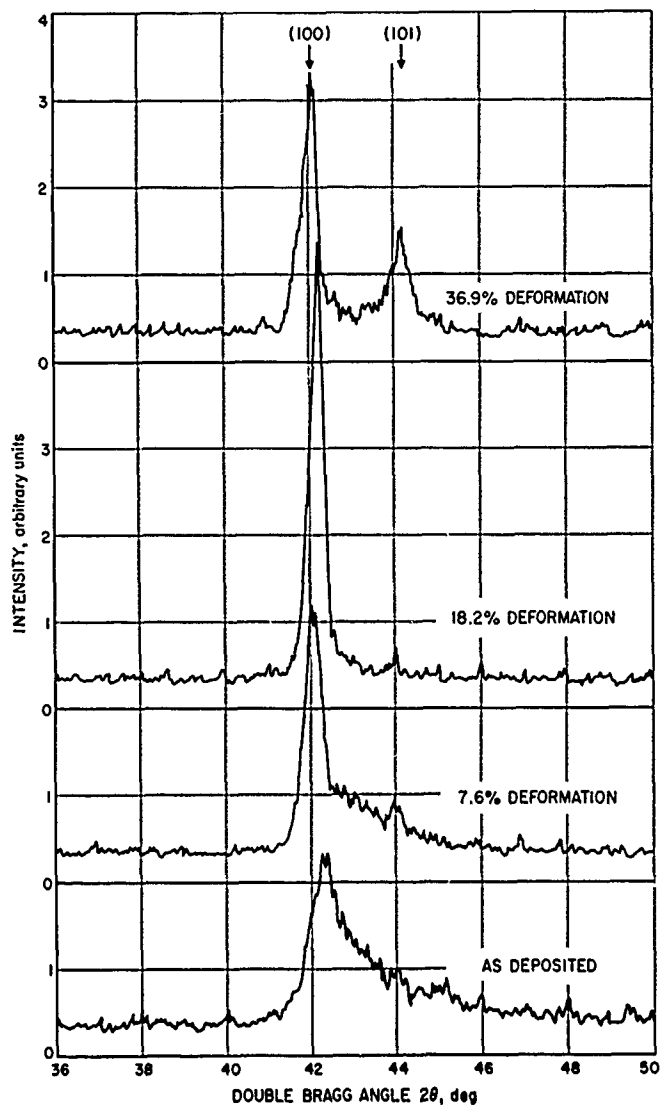


Figure 103. Development of modulations in (10) X-ray reflections of pyrolytic graphite after various deformations at 5000°F, $\text{CuK}\alpha$ radiation, Block 14701

carbons and in reasonable agreement with the recent single-crystal data of Poquet et al (Ref 73). The minimum occurs in the same temperature range as extensive changes in the structure and physical properties. The materials deposited at 1900 and 2000°C have much lower as-deposited susceptibilities. Sample D shows a small susceptibility decrease in the same temperature range as the minimum in Samples A, B and C, but it is not clear from the present data whether there is a minimum. For Sample E there is a small drop occurring at a temperature below 2100°C, after which χ_T is constant. The χ_T values and heat treatment behavior of Samples D and E are in general agreement with recent measure-

Table 16. Tensile properties of hot-worked pyrolytic graphite Block 14701^a

Specimen No.	Hot-working at 5000°F		Tension test		Elongation after test	
	Maximum stress, psi	Recorded Elongation, %	Test temp, °F	Ultimate tensile strength, psi	Recorded, %	Measured, %
3045	None	None	Room	10,000	2.8	0
2990	18,080	7.6	Room	22,700	8.8	—
3046	None	None	3000	15,500	1.6	0
2985	15,200	7.6	3000	20,400	8.2	6.5
2993	35,500	18.2	3000	34,500	18.0	14.5
3044	None	None	4000	12,600	2.4	0.3
2992	None	None	4000	14,900	2.0	0.7
2983	13,700	7.7	4000	24,100	8.5	—
2989	37,000	18.2	4000	49,100	18.9	12.7
2991	59,000	36.9	4000	56,100	36.4	41.1

^aFrom Lot 147, produced by General Electric Co.

Table 17. Magnetic susceptibility values for several pyrolytic carbons in units of (-10^{-6}) cgs units/gram

Sample	$T_D, ^\circ\text{C}$	χ_I	χ_L	χ_{II}	χ_L/χ_{II}
As deposited					
A	2200-2300	27.6	23.4	2.1	11
B	2100	27.6	21.8	2.9	7
C	2100	27.3	21.6	2.8	8
D	2000	20.7	—	—	—
E	1900	20.2	—	—	—
Single crystal (Ref 74)					
Single crystal (Ref 73)					
After heating to 2900°C					
A	—	18.1	16.2	0.9	17
B	—	18.3	15.7	1.3	11
C	—	20.0	17.8	1.1	16
D	—	18.7	—	—	—
E	—	19.4	—	—	—
After heating to 3400°C					
A	—	21.2	20.2	0.5	40
B	—	21.0	19.0	1.0	19
C	—	20.7	19.0	0.8	24

ments by Soule (Ref 75) on pyrolytic carbons deposited at 2000°C.

As-deposited pyrolytic graphite consists of crystallites which tend to be oriented with the (0001) crystallographic plane parallel to the plane of the deposit. The crystallite diameter in the (0001) plane increases with

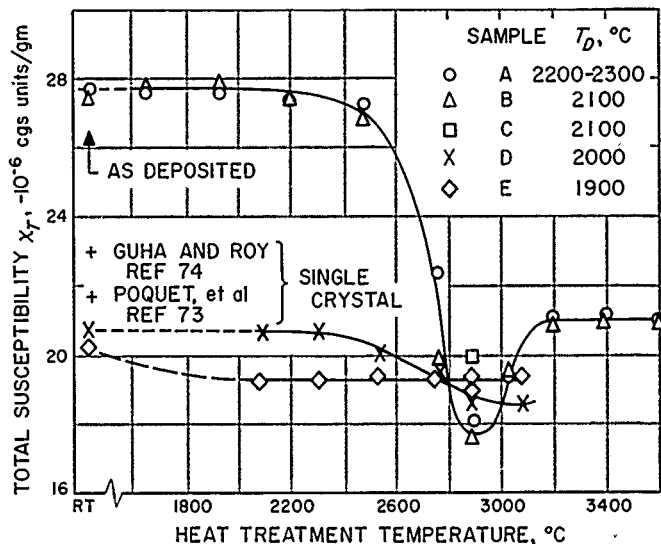


Figure 104. Total diamagnetic susceptibility of pyrolytic carbons deposited at temperatures T_D as a function of heat treatment temperature, values for natural single-crystal graphite shown for comparison

increasing deposition temperature and is larger than 100 Å for $T_D \geq 2100^\circ\text{C}$. The stacking sequence is highly faulted (turbostratic), however. On heat treatment at high temperatures, the material tends to graphitize with an increase in crystallite diameter and preferred orientation and a decrease in the density of stacking faults. Brown and Watt (Ref 76) observed that pyrolytic carbon deposited at 2100°C graphitized much more rapidly than material deposited at 1900°C. It was observed here that heating to temperatures of 3000°C or above produced marked changes in Samples A, B and C. They became softer and began to take on the lustrous, flakey appearance of natural graphite. Such changes were not obvious for Samples D and E after heating to 3100°C.

It appears that the high as-deposited susceptibility of Samples A, B and C is associated with the combination of large crystallite diameter and high density of stacking faults present in these materials. The minimum occurs during the transition from highly faulted to nearly perfect graphite structure and appears to be associated primarily with the disappearance of stacking faults rather than with the concurrent increase in preferred orientation. This minimum could result either from changes in the electronic band structure or from electron trapping during this process. The lower susceptibility values obtained for Samples D and E may result from smaller crystallite diameters. Pinnick (Ref 77) and Adamson and Blyden (Ref 78) have observed the susceptibility of carbons of a variety of types increases with crystallite

diameter up to sizes of 100 to 150 Å. The small response of these materials to heat treatment is consistent with other observations that little change in structure occurs on heat treating pyrolytic carbons deposited in this temperature range.

Work is beginning on the temperature dependence of the susceptibility. Preliminary results on a sample from block 2593 indicate that χ_1 increases from -22.3×10^{-6} at 300°K to -39.8×10^{-6} at 100°K. This temperature dependence is similar to that observed for natural graphite single crystals but is much larger.

It is apparent from the above discussion that the susceptibility of pyrolytic carbons depends sensitively on the detailed structure of the material. A thorough investigation of the susceptibility as a function of both deposition and heat treatment temperature should provide considerable insight into the nature of pyrolytic carbons and the graphitization process in general. Such a study would be particularly valuable if combined with X-ray structure and galvanomagnetic measurements. It is planned to proceed further along these lines.

B. Endothermal Materials

W. V. Kottensky and R. G. Nagler

1. Arc Imaging Furnace

An arc imaging furnace (manufactured by Arthur D. Little Company) has been installed in this laboratory for studies on materials in noncontaminating atmospheres at high temperatures and high heat fluxes. The furnace, which is sketched in Figure 105, can be operated either in the horizontal or vertical positions. It consists of a high-intensity blown arc and an optical system for re-imaging the radiant energy onto a sample. The arc is struck between two carbon electrodes, and the tail flame plasma is concentrated by a ring of impinging air jets. Both electrodes are air and water cooled. The generated plasma is rotated by a magnetic field surrounding the positive carbon, thus giving a relatively symmetrical heat source of great intensity. The radiant energy is first collected on an ellipsoidal projection mirror near the arc and is then re-imaged by a similar mirror onto a sample. The optical path from arc to sample is about 7 feet.

The most useful intensity is concentrated within a re-imaged spot 0.35 to 0.39 inch in diameter. The heat

flux may be varied by using either 300- or 150-ampere electrodes, by a temperature modulator plate, or by moving the sample along the optical axis.

Five 150-ampere electrodes may be burned without interruption for about 1.5 hours of continuous operation; with the 300-ampere electrodes the continuous operation is limited to 7 to 9 minutes.

Table 18 gives heat fluxes and equivalent black-body temperatures (calculated from the heat flux, assuming unity emissivity) which have been measured for the arc imaging furnace operating with the 300- and 150-ampere electrodes. The heat fluxes were measured with no temperature modulation using a cold-wall calorimeter supplied by the manufacturer. Typical heat fluxes for a similar arc imaging furnace have also been included in Table 18 for comparison.

2. Heat Flux Equalization

An attempt has been made to reduce the effect of the uneven flux distribution in the arc imaging furnace caused by the shadows of the anode holder and the specimen holder. As a flux equalizer, the anisotropic thermal conductivity properties of pyrolytic graphite appear to hold promise. The preferred orientation of the pyrolytic graphite provides a high thermal conductivity in the direction parallel to the basal plane and a low thermal conductivity in the direction perpendicular to the basal plane. This distributes the heat flux of the arc imaging furnace over the entire surface of the graphite. Thus, the entire piece of pyrolytic graphite gradually reaches an equilibrium temperature and reradiates the heat flux at that temperature. Exploratory tests have been made using different sizes of pyrolytic graphite separated from thermoplastic specimens by low thermal conductivity spacers. The plastic specimens have degraded evenly over the entire surface during exposure time ranging from 1 to 5 minutes. The average heat fluxes obtainable by this method are very low in comparison with normal arc imaging furnace heat fluxes observed in the focal plane; this extends the heat flux capability of the equipment downward. The pyrolytic graphite-plastic system also appears to have use as a high heating rate insu-

Table 18. Arc imaging furnace heat flux measurements over a 0.37-inch-diameter image

Heat flux, Btu/ft ² /sec		Equivalent black body temperature, °F	Carbon anode typ, amp
Typical	Measured		
553	627	5550	150
884	907	6130	300

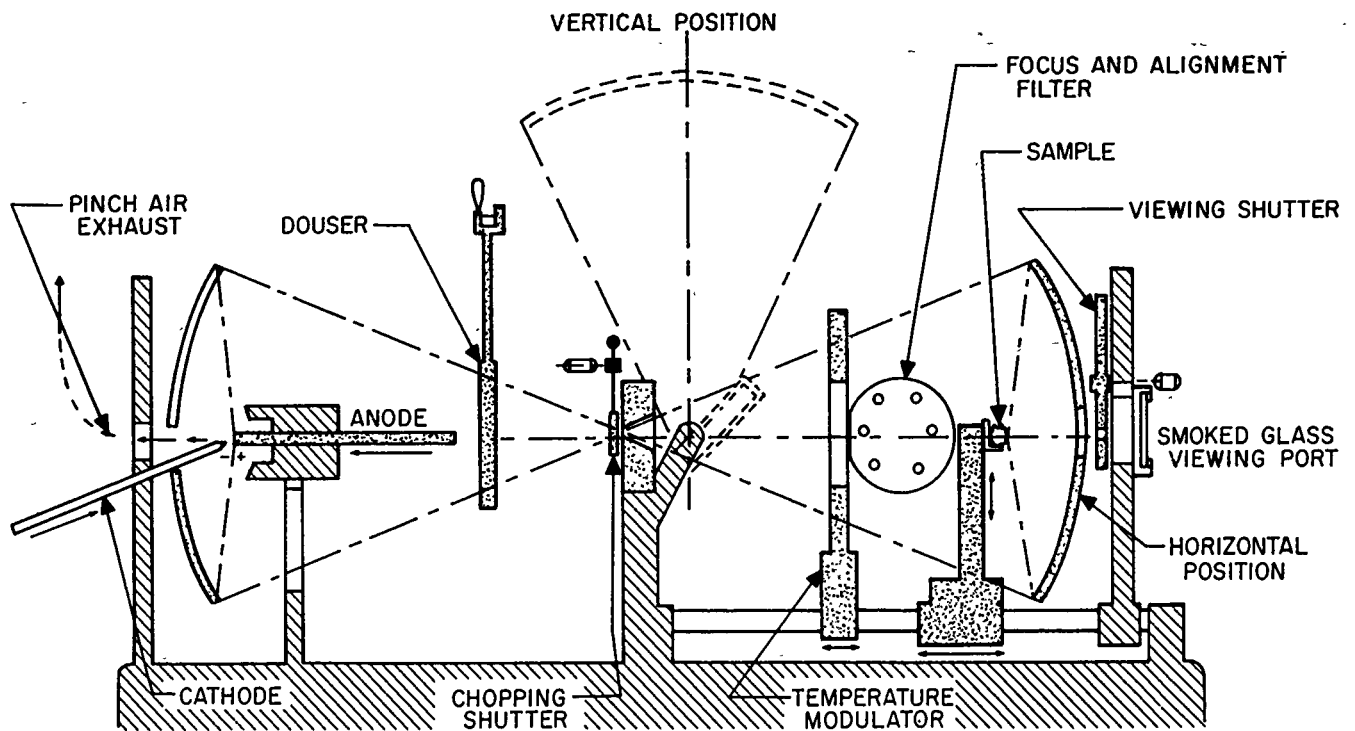


Figure 105. Arc imaging furnace for materials research

lation system for re-entry applications and for rocket nozzles in which advantage can be taken of both the high heat absorption potential of polymeric materials and the highly oriented thermal conductivity and high reradiation properties of the pyrolytic graphite.

C. Behavior of Materials in Space

J. B. Rittenhouse

1. Properties of Simulated Lunar Material

In order to obtain data for the design of future spacecraft and experimental equipment for lunar landing missions, a program was initiated in cooperation with the Department of Geological Sciences, California Institute of Technology, to determine some of the mechanical and physical properties of rock dusts intended to simulate lunar material.

The experiments to be performed at JPL are static and dynamic penetration in both air and vacuum to obtain some information on the behavior of the material under loading. Thermal conductivity and thermal dif-

fusivity of the material will also be measured in vacuum in order to gain some information that may be helpful in the design of the lunar core drill and other surface and subsurface exploration devices. The thermal diffusivity measurements using the simulated lunar material may also prove useful for comparison with astronomical bolometer measurements and may shed some light upon the question of whether the lunar surface is solid rock or material of reduced particle size resulting from some comminution process. Equipment for determining dynamic penetration has been constructed, and some of the initial results will be briefly discussed here. A full report of the results is being prepared. In connection with the dynamic penetration measurements, Fastax motion pictures of the experiments, both in air and in vacuum, were taken. Thermal conductivity apparatus has been designed and constructed; calibration of the equipment is now in progress. Apparatus for measuring static penetration is presently being designed. A number of vacuum degassing experiments were performed preliminary to the actual tests in vacuum with the simulated lunar material.

The material chosen, with the advice of the Department of Geological Sciences personnel, for initial study was an unweathered olivine bearing basalt obtained from Pigsaw Crater, California. This material was crushed in a standard steel jaw crusher. The crushed material was

then sized in a U.S. Standard screen analysis series to determine the distribution of grain sizes resulting from the crushing operation and to separate the material into several selected grain sizes for property measurements. Enough material for the entire series of experiments was crushed and sized in order that the measurements could all be made on the same lot of material.

In a prior test it was found that the clean and empty vacuum system reached an equilibrium pressure of 3×10^{-6} mm Hg in about 3 hours. A sample of 450 grams of crushed and sized material that passed the 60-mesh screen (approx 0.0082 inch) was placed in a large glass Petri dish to observe the vacuum pressure as a function of time in the same vacuum system wherein the equilibrium vacuum pressure in the clean and empty condition had been previously determined. A pressure of 3×10^{-6} mm Hg was reached in 25 hours. The depth of material in the dish was 2 inches, and the exposed surface area was about 12 square inches. A similar sample of material was radiant-heated to a temperature of 400°K during vacuum degassing. A pressure of 3×10^{-6} mm Hg was reached in 15 hours. An interesting observation made during these vacuum degassing experiments was that in the early stages of vacuum pumping, where the relative drop in pressure is quite rapid, there was violent evolution of entrained gas from the crushed rock. This evolution of gas was so rapid that material was expelled from the glass Petri dish container, and explosion craters and crevices were produced in the exposed surface of the material (Fig 106).

The dynamic penetration apparatus used in these experiments is comparable to the scleroscope hardness tester used in determining the hardness of metals and measuring the resilience of elastomers. In these devices, a right-circular, cylindrical penetrator with a 120-degree included angle in one end is dropped from a known height down a guide tube. The height of rebound is then measured with a calibrated scale.

The apparatus that was constructed to measure the dynamic penetration in vacuum of simulated lunar material is shown in Figure 107. As can be seen in the figure, the apparatus consists of an adjustable stand to support the guide tubes and the electromagnetic actuators which permit the penetrators to free-fall into the material below. The depth of penetration was measured after opening the apparatus to the atmosphere. The penetrators were of brass, with the 120-degree included angle in the lower end, in two sizes, 0.35-inch D by 2 inches long weighing 27.5 grams and 0.25-inch D by 2 inches long weighing 11.5 grams.

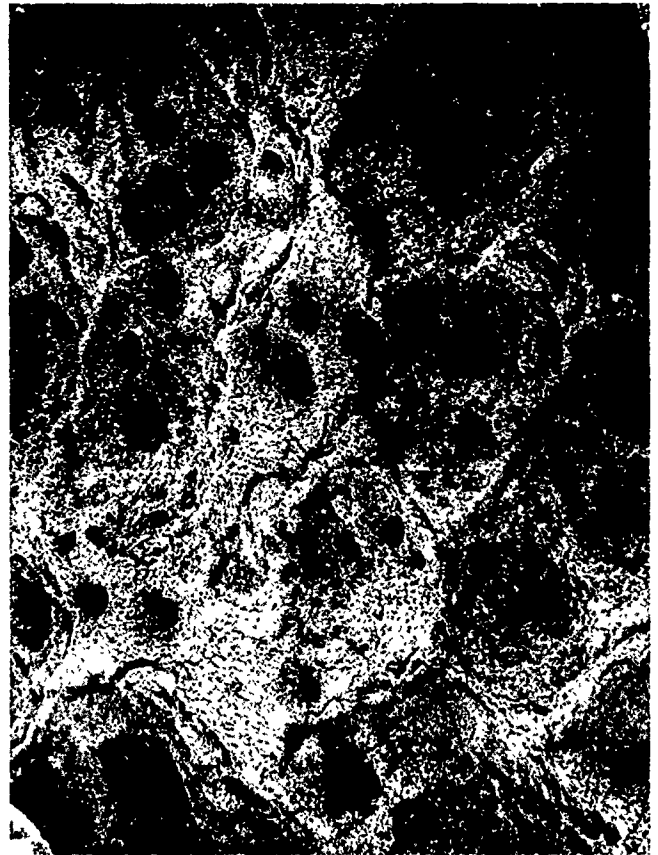


Figure 106. Surface of simulated lunar material after rapid vacuum degassing, crushed and sized California basalt from Pissgaw Crater

There was no appreciable difference between the penetration determined with large and the smaller penetrators. The dynamic penetration in vacuum was not influenced by the material particle size in the range of particle sizes utilized in these measurements. In general, the major factor influencing the dynamic penetration of simulated lunar material was the relative packing of the material.

The dynamic penetration of loose-packed material was less in vacuum than in air. On the other hand, the dynamic penetration of the densely packed material was greater in vacuum than in air.

The probable explanation is that, in the dense condition, displacement of both particles and air must take place rapidly over relatively long distances. Viscous losses in the air increase the energy dissipation, so lower the penetration in air compared to vacuum. This effect is less important with loose packing, where particle displacements are smaller (mostly local motions to a denser local packing), and the interstices for air motion are larger. Here the small viscous losses are more than compensated

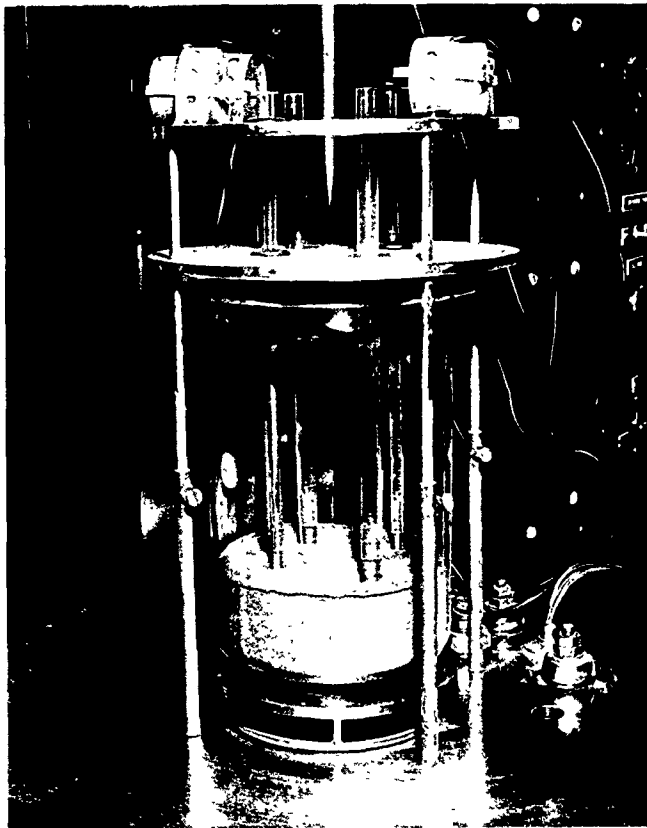


Figure 107. Dynamic penetration apparatus for simulated lunar material

by the decrease in interparticle friction due to air lubrication. Accordingly, with loose packing, penetration is greater in air than in vacuum.

The Fastax motion picture films are presently being edited and will reveal in more detail the action of penetration in all four conditions, loose and dense packing, in air and in vacuum.

D. Structural Materials

W. W. Gerberich

1. Materials Under High Rates of Heating

It has been shown (Refs 80, 81) that the yield and ultimate strengths of materials under high-heating-rate conditions are higher than those obtained from steady-state, high-temperature tensile tests. A coordinated program for determining the steady-state and high-heating-rate

tensile properties of several commonly-used structural materials was initiated to fill some of the existing gaps in the literature. To date, steady-state and high-heating-rate data are available for 17-7 PH stainless steel. The composition and heat treatment of this material are given in Table 19.

For the steady-state tensile tests, the equipment consisted of a 2000°F furnace, an automatic temperature controller, a 300,000-pound universal testing machine, and a high-temperature extensometer. Prior to testing, calibration of shunting resistors for the furnace were made at all temperatures to insure a temperature uniformity of $\pm 5^\circ\text{F}$ over the gage length of the specimen. During a test run, the temperature was monitored by two chromel-alumel thermocouples spot-welded to the center of the gage section. One thermocouple was connected to the controller and the other to a hand-balanced potentiometer. The specimen, as shown in Figure 108, was pulled at a strain rate of approximately 0.004/min to slightly past the yield point and then at a crosshead speed of approximately 0.1 in./min to fracture. A load-deformation curve was recorded to a deformation of about 0.020 inch.

The equipment for the high-heating-rate tests was comprised of a 50 kva transformer with an ignitron pulser for resistance heating, a temperature-control programmer to insure constant heating rates, a 20,000-pound modified creep tester, an extensometer, and a direct-recording oscillograph for measuring the temperature and the deformation. Thermal gradient calibrations of the specimen shown in Figure 108b were made at various heating rates with five chromel-alumel (5 mil) thermocouples evenly spaced over the 2-inch gage length. For a heating-rate range of 40 to 1500°F/sec, the thermal gradient varied from 50 to 15°F, respectively. Below 40°F/sec the thermal gradient was sufficient to affect test results. For a test run, two thermocouples spot-welded to the center

Table 19. Composition and heat treatment of 17-7 PH (1050) stainless steel

Condition	Composition ^a							
	C	Mn	P	S	Si	Cr	Ni	Al
Annealed	0.064	0.70	0.021	0.008	0.44	17.52	7.12	1.21
TH (1050)	Heat treatment ^b							
	1400°F for 1.5 hours; cool to 60°F within 1 hour; hold 0.5 hour; temper at 1050°F for 1.5 hours, air cool.							

^aManufacturer's test report, Electric Steel Co., Los Angeles (HT 56125).

^bPer Armco Steel specification.

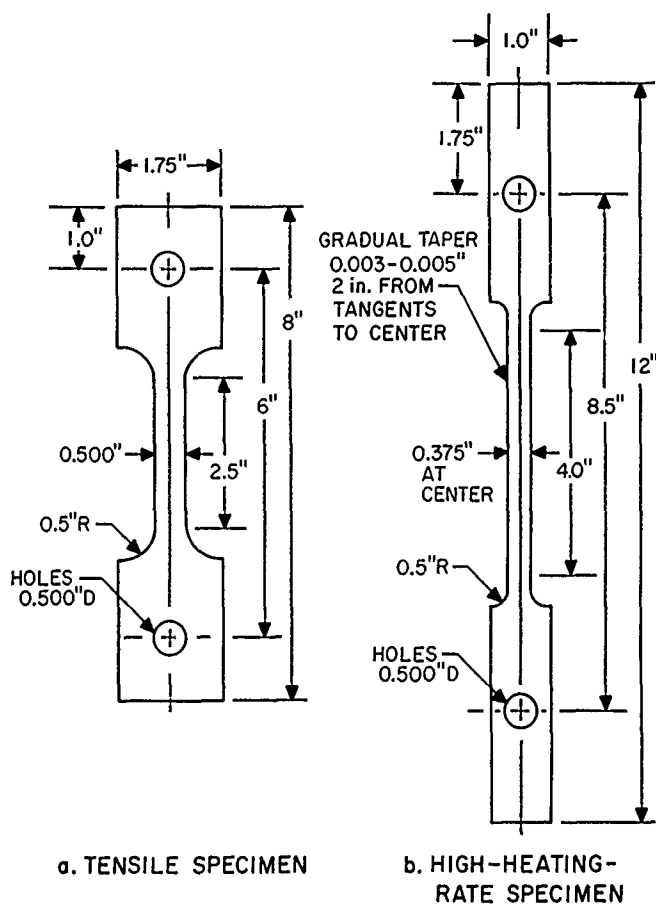


Figure 108. Tensile and high-heating-rate test specimens

of the gage section were used, one for feedback control to the programmer and one to the oscillograph. To eliminate the superimposed resistance heating voltage, a three-wire thermocouple with shunting network was used.

In general, the test procedure was to dead-weight load the specimen and resistance-heat the specimen using a programmed or manual temperature control. As the programmer response was only good up to 500°F/sec, for higher heating rates, a manually operated voltage regulator was used. Temperature-time and deformation-time data were recorded to slightly beyond the yield point. Accuracy of the data was ±5°F for the temperature and ±0.2% for the strain.

Results of the steady-state tensile tests are given in Table 20 and Figures 109 and 110. In Figure 109, typical engineering stress-strain curves at all temperatures are shown to slightly beyond the yield strength. The ultimate, yield, and modulus data are summarized for all temperatures in Figure 110.

Table 20. Tensile test results for 0.063 in. thick sheet of 17-7 PH (1050) stainless steel

Spec No.	Temp, °F	Modulus of elasticity, psi	Yield stress, ksi	Ultimate stress, ksi	Elongation in 2 in., %	Reduction of area, %
D-21	80	27.8 × 10 ⁶	155	178	9.5	33.8
D-22	80	28.4	162	183	10.0	34.6
D-17	415	26.9	—	154	5.7	34.2
D-20	400	27.6	145	156	5.0	25.4
D-11	600	25.6	133	146	5.5	20.8
D-4	800	23.2	114	125	10.0	36.1
D-7	1000	21.2	63.6	81.3	35.3	65.0
D-8	1000	17.4	73.0	84.9	() ^a	58.2
D-1	1000	21.2	86.4	97.5	25.0	45.6
D-9	1200	14.5	21.8	35.8	57.0	81.0
D-19	1200	11.7	26.0	40.1	49.0	78.0

^aBroke at gage point.

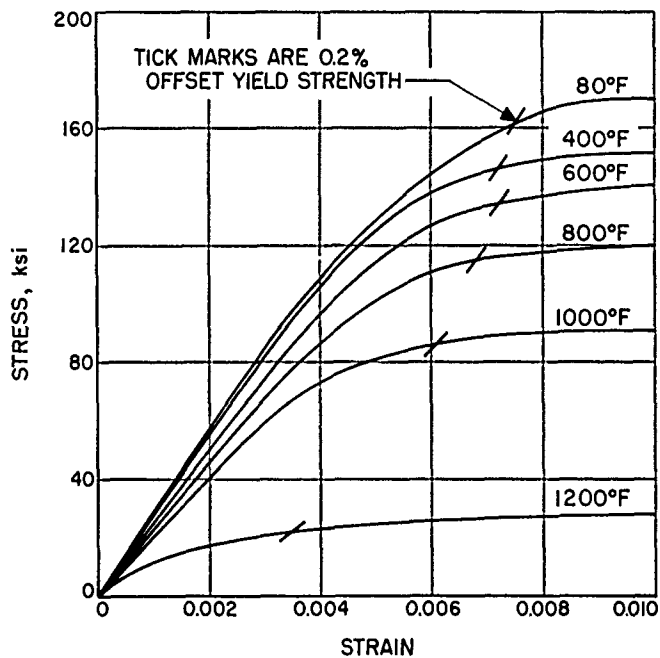


Figure 109. Typical stress-strain curves for 17-7 PH (1050) stainless steel

All of the high-heating-rate data are summarized in Table 21 and illustrated in Figures 111 to 113. Several runs were made in the no-load condition to determine the effect of heating rate on thermal expansion. Figure 111 illustrates this effect. It seems that increasing the heating rate increases the amount of thermal expansion. At first it was thought that the slight thermal gradient that existed caused this, for the higher heating rates had lower thermal gradients. Reading the same temperature

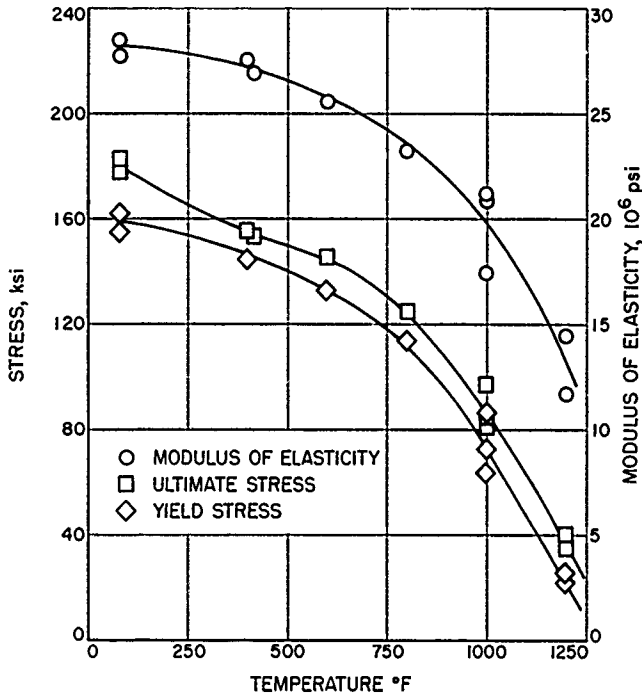


Figure 110. Ultimate stress, yield stress, and modulus data for 17-7 PH (1050) stainless steel at temperatures from 70 to 1200°F

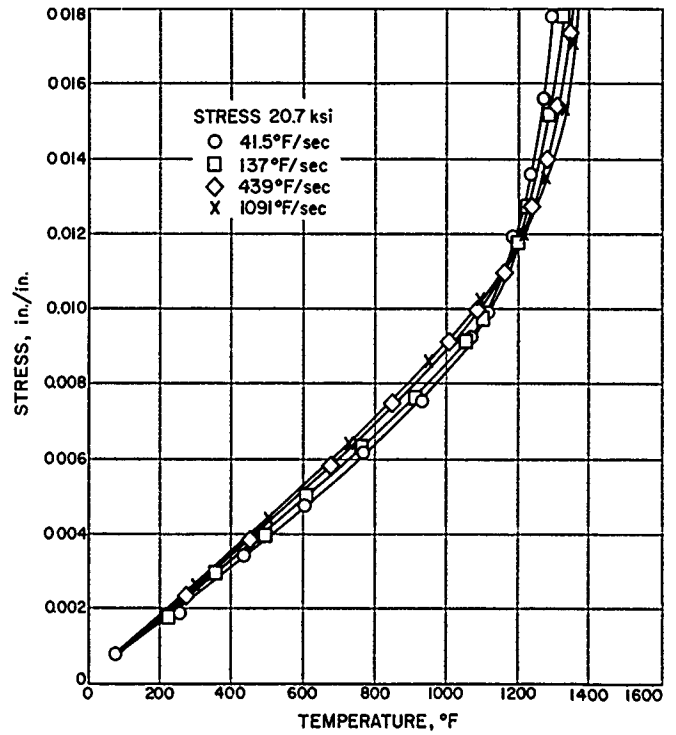


Figure 112. Typical strain-temperature curves at various heating rates for 17-7 PH (1050) stainless steel

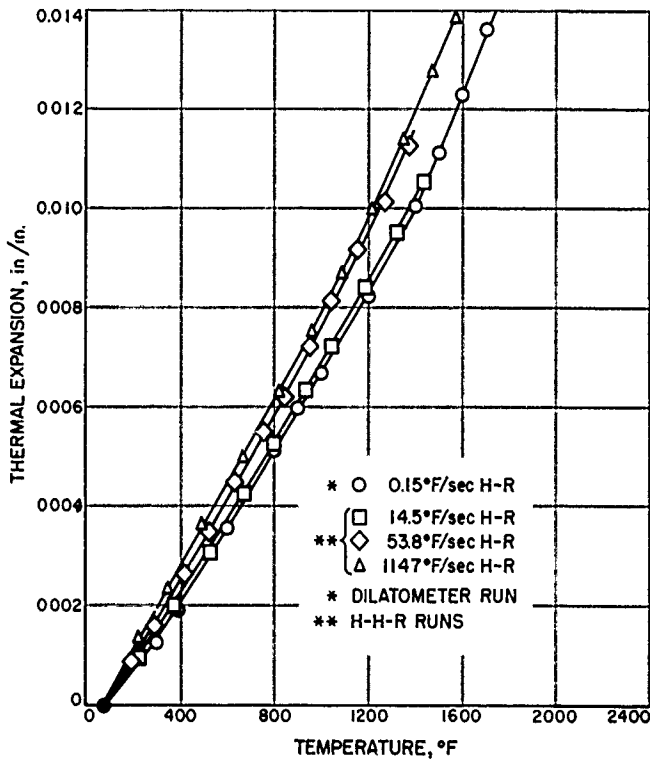


Figure 111. Effect of heating rate on thermal expansion of 17-7 PH (1050) stainless steel

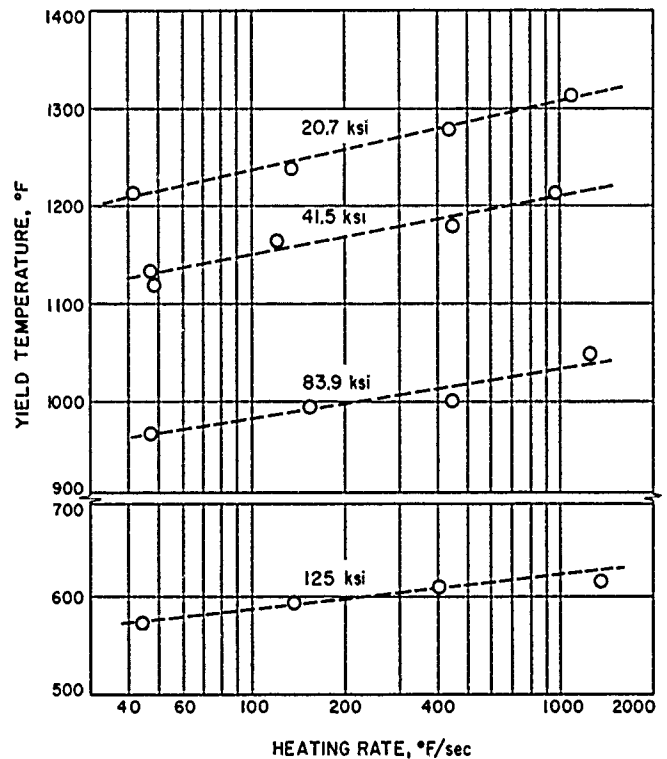


Figure 113. Effect of heating rate on yield temperatures for various stress levels

Table 21. High-heating rate results for 0.063 in. thick sheet of 17-7 PH (1050) stainless steel

Spec No.	Area, in. ²	Load, lb	Stress, ksi	Heating rate, °F/sec	0.2 % Yield temp, °F	Spec No.	Area, in. ²	Load, lb	Stress, ksi	Heating rate, °F/sec	0.2 % Yield temp, °F
A-21 ^a	0.0235	0	0	14.5	—	A-9	0.0238	1000	42.0	121	1167
A-21 ^a	0.0235	0	0	53.8	—	A-15	0.0239	1000	41.8	455	1180
A-2 ^a	0.0242	0	0	190	—	A-11	0.0240	1000	41.7	967	1215
A-21 ^a	0.0235	0	0	524	—	A-19	0.0237	2000	84.4	47.0	968
A-2 ^a	0.0242	0	0	1190	—	A-10	0.0238	2000	84.0	156	995
A-13	0.0244	500	20.5	41.5	1215	A-20	0.0237	2000	84.4	450	1000
A-12	0.0238	500	21.0	137	1240	A-16	0.0242	2000	82.6	1238	1050
A-7	0.0239	500	20.9	439	1280	A-4	0.0236	3000	127.0	44.1	575
A-6	0.0243	500	20.6	1091	1315	A-5	0.0240	3000	125.0	138	595
A-8	0.0244	1000	41.0	47.0	1135	A-1	0.0244	3000	123.0	409	610
A-14	0.0243	1000	41.2	48.4	1120	A-3	0.0242	3000	124.0	1350	615

^aThese tests run for thermal expansion data.

at the center of a specimen with a lower thermal gradient would give a higher thermal expansion than one with a high gradient. However, this was not the case, for two dilatometer runs with no thermal gradient verified the effect shown in Figure 111.

High-heating-rate data under load conditions are shown in Table 21, and a typical set of strain-temperature curves at one stress level is illustrated in Figure 112. The effect of heating rate on thermal expansion is seen in Figure 112, and a crossover occurs when plastic straining starts.

A yield-temperature value is obtained by drawing a 0.2% offset line parallel to the calculated elastic-plus-thermal expansion line. This calculated line is determined from the thermal expansion, and the elastic strain is computed from the applied stress and modulus at temperature taken from Figure 110. The experimental and calculated curves agree up to the point of plastic straining. A plot of 0.2% offset yield temperatures versus heating rate is given in Figure 113. This indicates that for all stress levels, an increase in heating rate allows a higher temperature before yielding occurs.

IX. Engineering Research

A. Liquid Surface Shapes

H. E. Williams, Consultant

As a preliminary step in evaluating the effect of surface tension forces in hydrodynamics, the hydrostatic free surface of a fluid in contact with a vertical wall was investigated. For walls that are parallel flat plates, the solution for the shape of the free surface can be obtained exactly; for circular cylindrical walls, one can obtain an approximation that is appropriate for the free surface shape inside a tube whose radius a is small, compared with the characteristic length of the fluid $\lambda = (\sigma/\rho g)^{1/2}$ where σ is specific surface energy, and ρg is the specific weight of the fluid.

For the two-dimensional channel shown in Figure 114, the form of the free surface must satisfy the well known differential equation (Ref 82)

$$\lambda \frac{d^2 \zeta}{dx^2} - \zeta \left[1 + \left(\frac{d\zeta}{dx} \right)^2 \right]^{3/2} = 0$$

and boundary conditions for $0 \leq x \leq a$

$$\left. \begin{aligned} \left(\frac{d\zeta}{dx} \right)_{(x=0)} &= 0 \\ \left(\frac{d\zeta}{dx} \right)_{(x=a)} &= \alpha \end{aligned} \right\}$$

or for $x \geq a$

$$\left. \begin{aligned} \left(\frac{d\zeta}{dx} \right)_{(x=a)} &= -\alpha \\ \lim_{x \rightarrow \infty} \zeta(x) = \lim_{x \rightarrow \infty} \frac{d\zeta(x)}{dx} &= 0 \end{aligned} \right\}$$

For the region $x \geq a$, the solution can be written as

$$\left(\frac{x-a}{\lambda} \right) = 2 \left[(1 - q_w^2/4)^{1/2} - (1 - q^2/4)^{1/2} \right] - \ln \left[\frac{1 + (1 - q_w^2/4)^{1/2}}{1 + (1 - q^2/4)^{1/2}} \cdot \frac{q}{q_w} \right]$$

where $q = \zeta/\lambda$ and

$$q_w = q_{(x=a)} = \left[2 \left(1 - \frac{1}{(1 + \alpha^2)^{1/2}} \right) \right]^{1/2} \leq \sqrt{2}$$

An important observation can be made regarding the general shape of this curve. As the sign of $d^2\zeta/dx^2$ is the

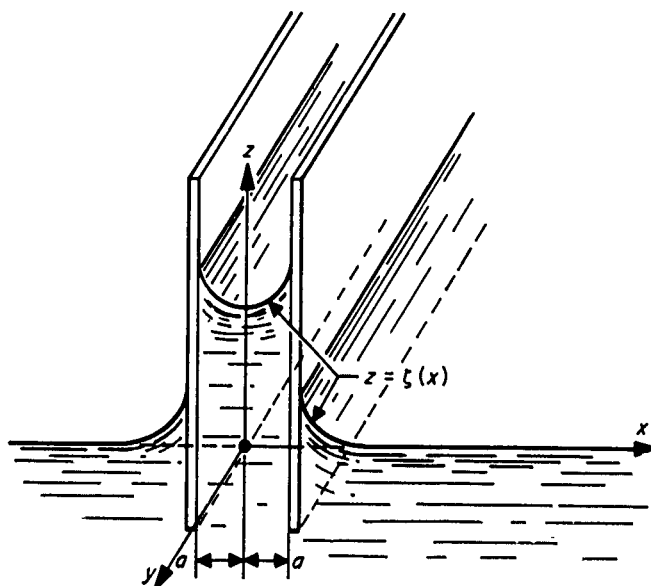


Figure 114. Free liquid surface on inside and outside of two-dimensional channel

same as the sign of ζ from the differential equation, it can be concluded that the free surface shape is a monotonic function of distance from the wall. Thus, whether the deflection ζ is positive or negative, the shape of the curve is dependent only on the absolute value of the slope of the surface at the wall. In addition, one can conclude that for an external wall, the fluid will not overhang the edge but will, at most, assume the shape corresponding to an infinite slope in the limiting case.

From an experimental standpoint, the fact that the surface shape is independent of the sign of the deflection allows one greater freedom as an external edge is more accurately observed than an internal edge for a given value of wall slope. In addition, one can obtain arbitrary wall slopes by varying the degree of overfilling the container. It should be remarked that it is not necessary to have parallel walls exactly, but only to approximate the two dimensional character of the wall locally. This can be done in a circular container provided that the radius of the container is very much greater than λ .

For the region $x \leq a$, the shape of the fluid surface can be expressed in terms of elliptic functions. This is worked out in detail in Reference 83. In the limiting case that $(a/\lambda)^2 \ll 1$, the shape of the fluid surface can be shown to approach the limit of a circular cylinder.

For circular cylindrical walls that are not appropriate to a two-dimensional approximation, one cannot obtain an analytical solution to the differential equation except in the limiting case corresponding to the fluid surface shape in the interior of a tube whose radius is very much smaller than the characteristic length. In this limiting case, the free surface shape assumes a spherical shape.

In the above, no reference has been made to formulating the appropriate basic equations, such as the relationship between the pressure discontinuity at the surface and the local curvature. A fundamental formulation of both the dynamical and kinematical free surface boundary conditions is presented in Reference 84.

B. Free-Fall Capsule to Study Weightless Liquid Behavior

E. A. Zeiner

In order to experimentally observe the statics and dynamics of liquids in free fall during which surface forces dominate, a prototype capsule system which is

dropped from a hovering helicopter was developed and tested. Three basic design requirements were outlined that the system should provide: (1) the liquid and its container should make the transition from 1 g to free fall in such a way that minimum angular and translational momentum is transferred to the liquid; (2) the accelerations on the liquid and its container should not exceed 10^{-3} g during the experimental interval; (3) the time for the experimental interval should allow for possible slow rate effects to be observed. (This is estimated to be about 10 seconds.) It was decided that photographic data be used, at least in the initial phases of the experimentation, because of the random nature of some of the flow processes.

The system constructed consisted of a hollow, bomb-shaped, fin-stabilized capsule, 5 feet long and 1 foot in diameter, weighing 204 pounds. The weight was concentrated in the nose section, while the middle and tail sections were made of Lucite (to provide internal light) and fiberglass, respectively. The primary objective of this first system was to evaluate the adequacy of the initial release conditions and the aerodynamics of the capsule during its fall. The capsule was suspended vertically under the helicopter and released from a hovering altitude of 800 feet above the ground.

The basic capsule scheme is illustrated in Figure 115. Falling inside the capsule shell as the shell is falling, is the experimental package. If, as shown in Figure 115a, the experiment and capsule shell are released simultaneously, the experiment will make a single pass through the inside of the shell. The relative motion is caused by the external air drag on the capsule shell. Employing the technique sketched in Figure 115b, the shell is given a small velocity increment greater than the experiment, by delaying the experiment's release a few milliseconds or giving the shell a slight push. The experiment will make two passes through the shell cavity: the first pass due to the initial relative velocity, and the second because of air drag deceleration on the shell. Using the double-pass technique gives roughly a 30% increase in the time available for experimentation. The release mechanism that was devised held the shell and the experiment independently and could be adjusted to provide a controlled time delay in the drop sequence.

In this prototype system, the experimental package was a slender triangular rod marked and mirrored so that the relative motion between the shell and the rod could be determined for all 6 degrees of freedom. To observe this, a sequence camera was attached to the shell half-way along its length. A stopwatch was placed inside the shell cavity and was always visible to the camera so

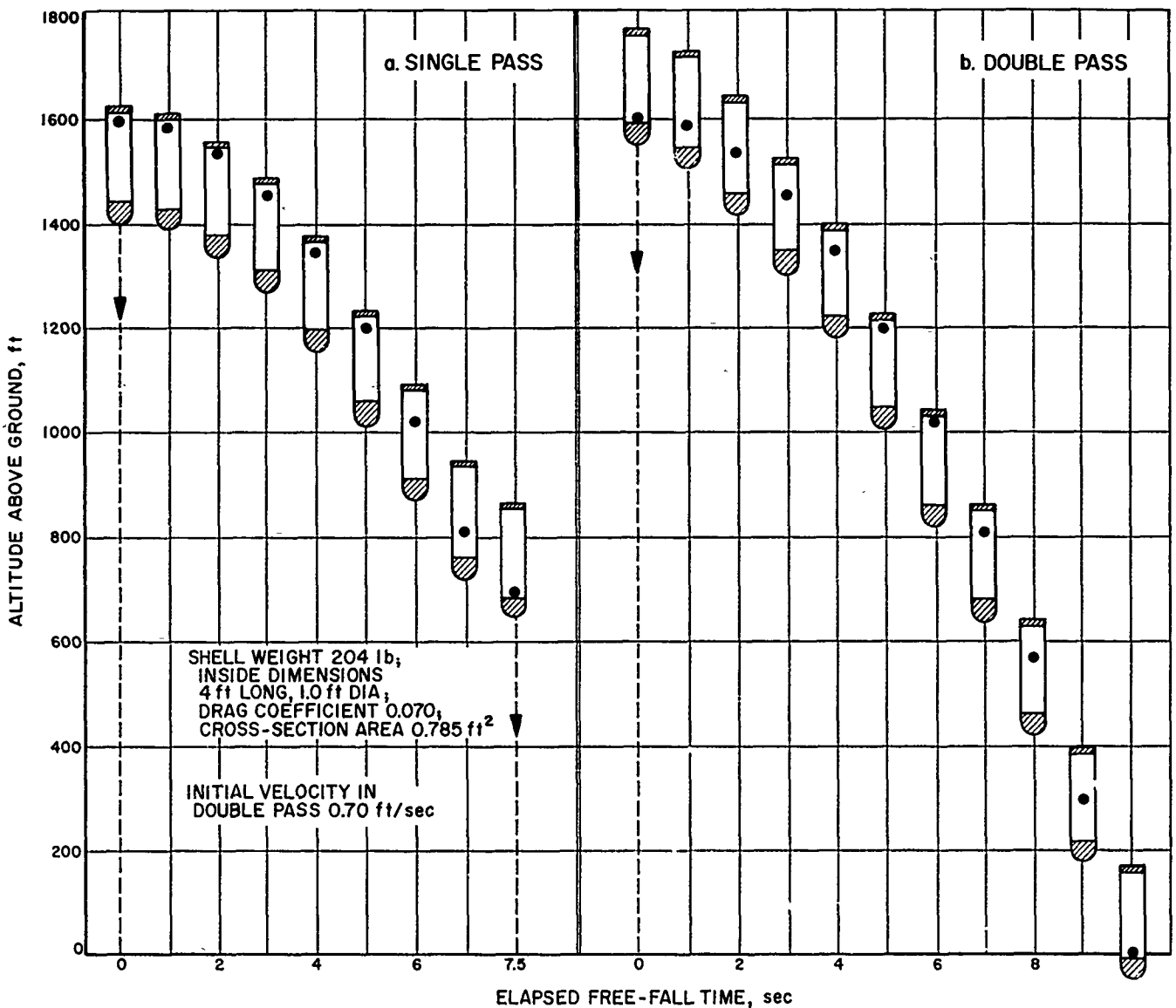


Figure 115. Relative vertical displacement between experiment and capsule shell for single- and double-pass techniques

that it was possible to get values of each of the coordinates as a function of time. By comparing these data with that predicted, it is possible to determine the limitations of the prototype system and what can be done to improve it. A special sequence camera was developed for recording the internal relative displacements since the size and ruggedness of existing commercial cameras were unsatisfactory. The details of the design and construction of the camera are covered in *Space Programs Summary 37-7*. Also, a landing platform and associated handling equipment were constructed and attached to a portable trailer. The entire assembled system suspended from the helicopter and ready for launch is shown in the photograph (Fig 116).

The drop test was performed at the U.S. Army Yuma Test Station, Yuma, Arizona, where ample area of very soft ground was available, as well as three tracking cameras. The purpose of these cameras was to provide very large capsule displacements as a function of time that would be beyond the capabilities of the internal instrumentation. At impact, the backing plate of the internal camera sheared off and caused the films taken to be over-exposed. However, data was provided by the tracking cameras which give the position of the capsule to an accuracy of about ± 3 feet. The angular attitude displacements were not discernible to the tracking cameras and, thus, only visual observations of these motions was possible.

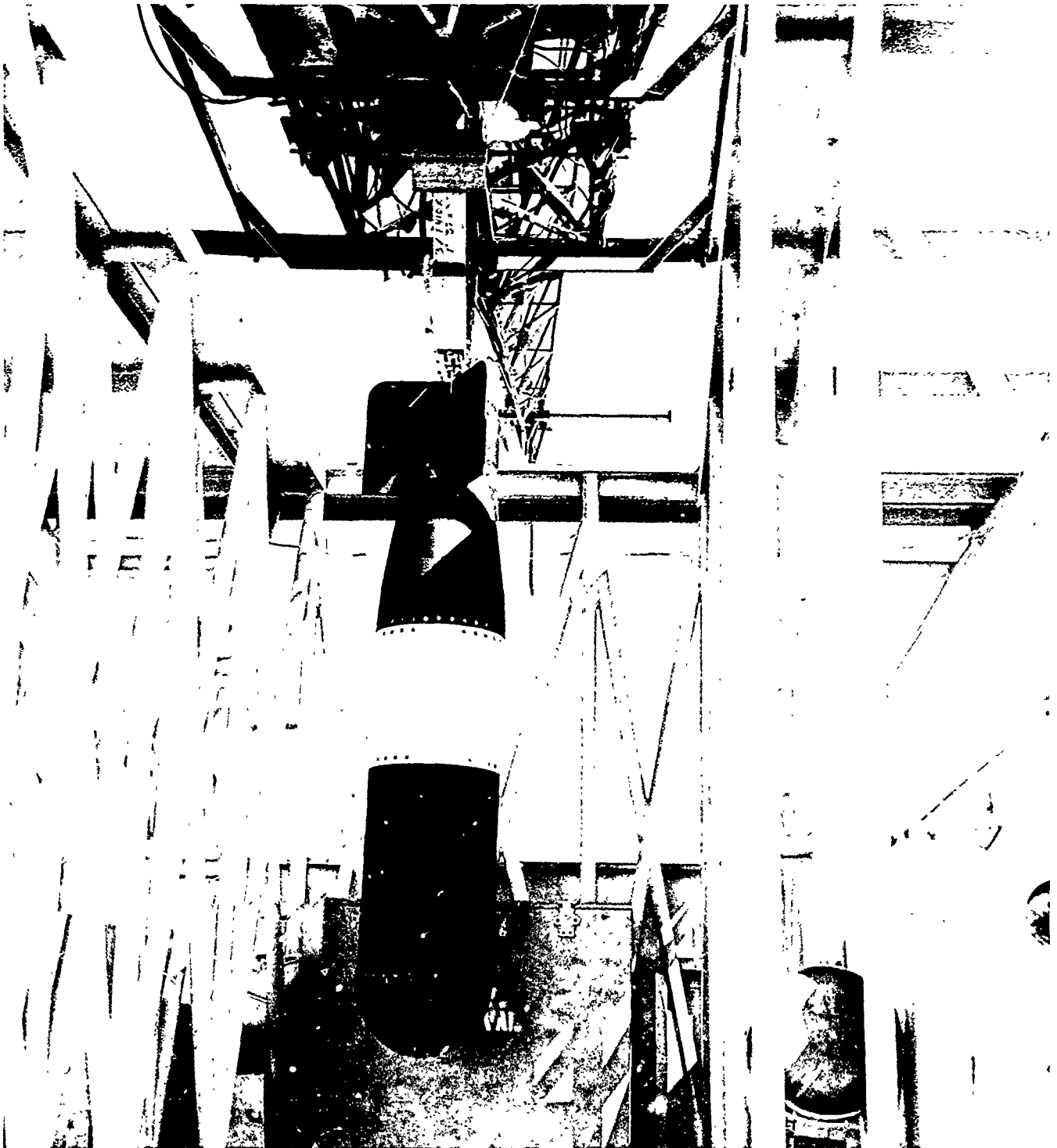


Figure 116. Complete assembled free-fall capsule system

No deviation from a true vertical path was noticed within the errors indicated for the cameras. This accuracy is sufficient only to indicate that no gross errors were made in the aerodynamic design and fabrication of the capsule. The internal relative displacements would

have to have been obtained to accurately affirm the functional capabilities of the system. Visual estimates of the capsule's attitude uncovered a problem involving excessive pitching rates introduced into the capsule from the vibrations of the helicopter, which is being studied.

ENGINEERING FACILITIES DIVISION

X. Wind Tunnel and Environmental Facilities

A. 20-Inch Supersonic Wind Tunnel

G. Goranson

Test 20-C36B was completed during March in the 20-inch supersonic wind tunnel in order to determine the maximum practical Mach number for this tunnel. It was found that $M = 5.6$ can be run satisfactorily if the effects of air condensation are neglected. Because the supply temperature of the air in the 20-inch tunnel is limited to 150°F , air condensation starts occurring at about $M = 5.2$. However, information gained from the 21-inch hypersonic tunnel indicates that air condensation effects can be neglected in some types of test work such as coarse

configuration studies which constitute a large share of the wind tunnel testing time. Operation at $M = 6$ was attempted, but the resulting supersonic air flow in the test section was unsatisfactory due to insufficient diffuser throat adjustment. Design work has been completed for a modification of the diffuser throat which will permit the necessary additional adjustment.

After completion of the high Mach number work, a few runs were made at $M = 2.21$ and 4.54 to obtain flow field and wake information for a mockup of a typical blunt body dynamic stability model and its supporting structure. The tunnel started and operated satisfactorily without any adverse interactions between the tunnel sidewalls and the model.

XI. Instrumentation

A. Instrumentation Facilities

J. Z. Inskeep

1. Instrumentation Systems for Edwards Test Station

Connection of Test Stands B and C to the Edwards Test Station instrumentation system described previously in *Research Summary 5* (p 86) was completed recently. System design and construction was contracted to Consolidated Systems Corporation, Monrovia, California. The types of measurements provided for and the equipment selected are identical to those previously described for Test Stand D, and the numbers of channels are approximately the same.

The instrumentation circuits for Test Stands B and C are connected directly to the blockhouse, and no terminal room such as the one at D-stand is used. Only the thermocouple reference junction is located in the test stand area. Transducer to conditioning equipment distance is 450 feet for Test Stand B, and 350 feet for Test Stand C.

a. Blockhouse control area for Stands B and C. Figure 117 shows the Test Stand C firing control console and monitor area. In the vertical racks from left to right are (1) flowmeter pulse-rate converters (shared with Test Stand B); (2) monitor meters; (3) closed circuit television monitor and control panel, scaling and select panel, digital voltmeter with selector and amplifier panel, and thermocouple calibration panels; (4) manual nulling digital voltmeter, and bridge balance and calibration panels; (5) dc amplifiers and monitor patch panels; and (6) a 36-channel oscillograph with series/shunt resistor panel.

With few exceptions the Test Stand B control console and monitor areas are identical. A checkout scaling and select panel is located in each monitor area. Up to ten transducer signals may be connected through the monitor patch board to the panel, where each signal is attenuated with a potentiometer to produce an output reading on a digital voltmeter which corresponds numerically to the transducer input in engineering units (psi, °F). One signal at a time may be selected by push button from either the test console or the scaling and select panel. The capability to precisely monitor prerun propellant tank and other system pressures has been received with enthusiasm by the test operators.

b. Blockhouse common-equipment area. The common area system prepatch board has been enlarged to 4896

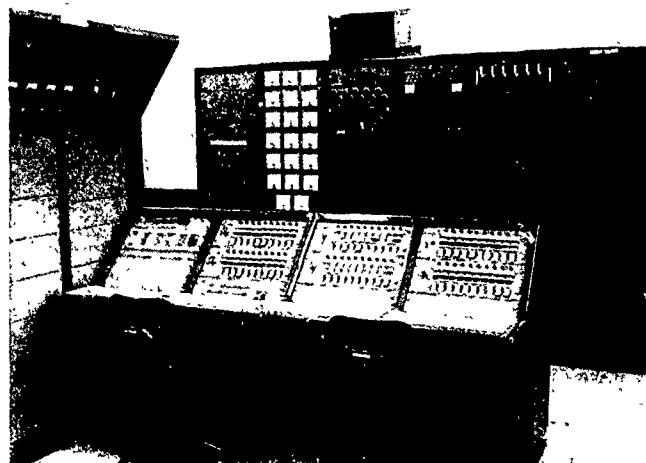


Figure 117. Test Stand C firing control console and monitor area

contacts to provide for inputs from a maximum of five test stands. Twenty additional Neff differential dc amplifiers have been added for use with grounded thermocouples, providing a total of 30 amplifiers. A JPL constructed two-channel flow register has been added to the MicroSADIC which provides for the digital recording of accumulated pulses from turbine flowmeters or other pulse or frequency-output devices. Average pulse rates for any time interval equal to an integral multiple of the sampling interval or the MicroSADIC (approx 18 ms) may be obtained during the digital computer data reduction process.

c. Blockhouse high-frequency data recording area. The high-frequency signal conditioning and recorder input and output connections are made through a 1632 channel prepatch system in the common-equipment area. High-frequency data is recorded on a 14-track CEC Datatape recorder using wide-band FM recording. Transducer inputs are received from Photocon high-frequency pressure gages, turbine flowmeters, and vibration pickups. The ac component of the Photocon pressure channels is recorded in addition to the dc-10-kc signal. These components are obtained by passing the Photocon Dynagage output through Dynamics Instrumentation Co. Model 1634 amplifiers having a passband of 2 cps to 200 kc. Six channels of bandpass filters and rms converters are available as a system for describing the noise or roughness of rocket motor combustion. In this system, each complete high-frequency pressure signal is passed through a filter with a 10-cps to 8-kc passband, and the output is then fed to a device which produces an output proportional to the rms of this signal for recording on a galvanometer oscillograph. Automatic prerun calibration of the Photocon (variable capacitance) system is accomplished with coaxial relays and shunt capacitors applied at the coaxial input connection. Electronic equipment for terminating a test in the event of rocket motor instability is energized by one of the Photocon Dynagage outputs. The actuation level of the equipment can be preset for any steady-state (dc) value within the range of the pressure measurement and also for any fluctuating level above a selectable frequency in the range from 400 to 2000 cps, with a time delay of 10 to 250 milliseconds before actuation of the shutoff relay. Six KinTel-111 dc amplifiers are available for amplification of flowmeter outputs before recording, and for coupling tape playback amplifiers to galvanometers. A six-channel Hathaway cathode-ray oscillograph with recording response from dc to 50 kc is available, although seldom used, since galvanometer-oscillograph recording of high-frequency data can conveniently be accomplished using reduced-speed playback techniques with the magnetic tape

recorder. A time base for all blockhouse recording is generated by a Hewlett-Packard Model 522 electronic counter and a frequency divider which produces blanked and correlated timing pulses in decades from 0.1 to 10,000 pps.

B. Instrument Performance Studies

J. Earnest

1. Evaluation of ETS Six-Component Thrust Stand

An evaluation has been made of an Aeroscience six-component thrust stand installed at Edwards Test Station. This thrust stand is enclosed in a vacuum chamber with diffuser, as described briefly in RS 36-7 (Vol III). Characteristics investigated included interaction of force measuring struts, mechanical distortion under load, alignment of stand and motor, hysteresis, repeatability, and accuracy.

The thrust stand, a dummy motor, and calibration units are shown in Figure 118. The six struts supporting the cradle utilize Aeroscience load cells with flexure joints on both sides of each cell to minimize interaction between measurements. There are two vertical cells, two horizontal cells, a forward horizontal roll cell, and a main axial cell, whose outputs fully define the forces and moments produced by the rocket motor during firing.

The main calibration unit consists of a pneumatically actuated drive motor which applies tension to the flexured calibration cell (Fig 118) and thereby induces compression on the main axial load cell. An indicating device calibrated directly in pounds permits monitoring of the calibration force applied. A similar system is used for the auxiliary calibrator, which applies a side force to the dummy motor (Fig 118) through a flexured link. The five load cells in the side struts are thereby subjected to specific forces which can be calculated from the known load applied and the moment equations of the stand geometry. Figure 119 shows the thrust stand in the vacuum chamber with a mockup motor. The specifications require this thrust stand to measure thrust vector magnitude at 6000 pounds with an accuracy of $\pm 0.25\%$, and thrust angle in the range from zero to several degrees with an accuracy of ± 0.1 degree. The accuracy of thrust vector magnitude is dependent primarily on the characteristics of the main calibrator, while the accuracy of thrust vector angle is dependent upon accurate motor alignment and measurement of side forces to ± 3 pounds.

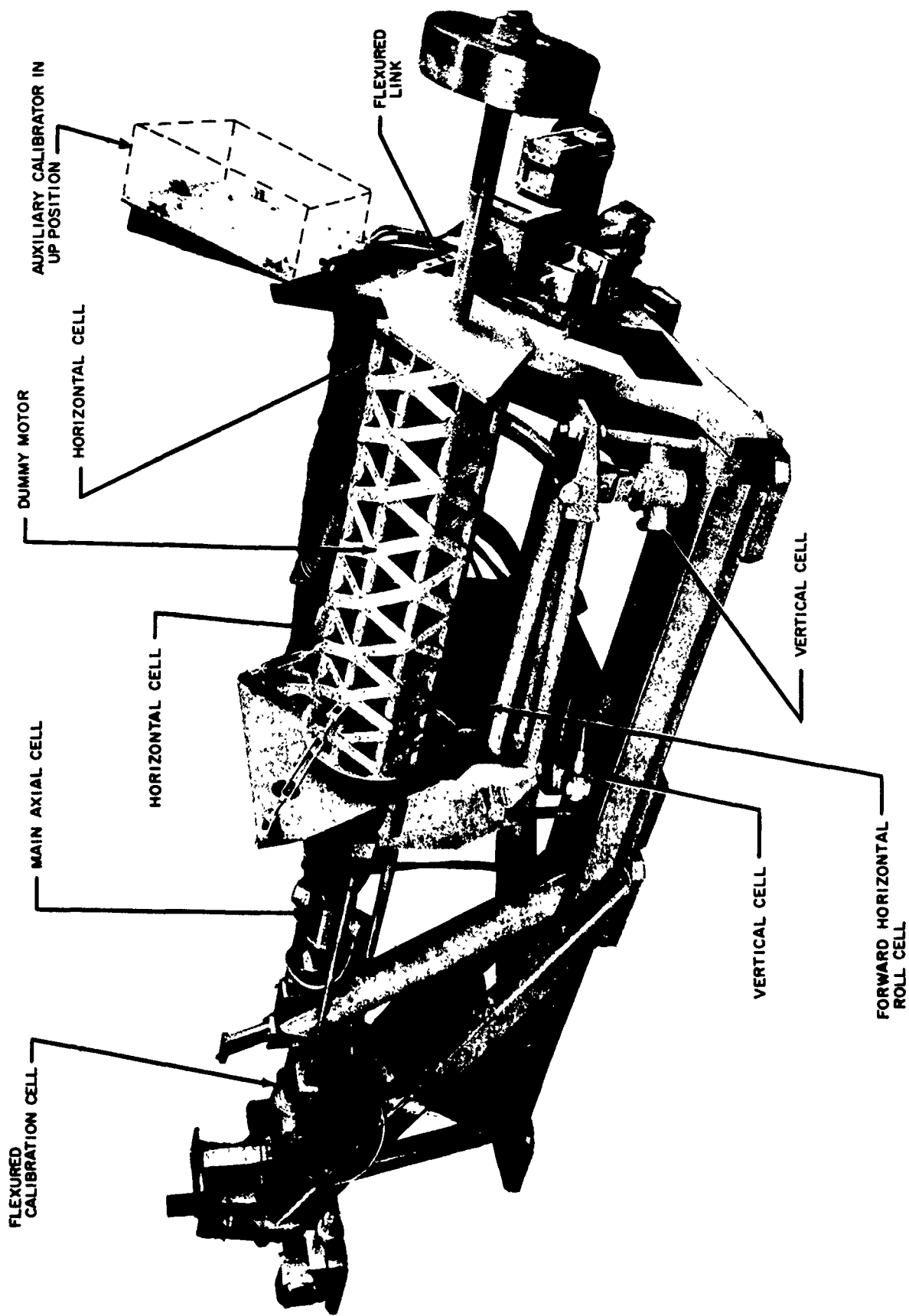


Figure 116. Aerospace six-component thrust stand with dummy motor and calibration units

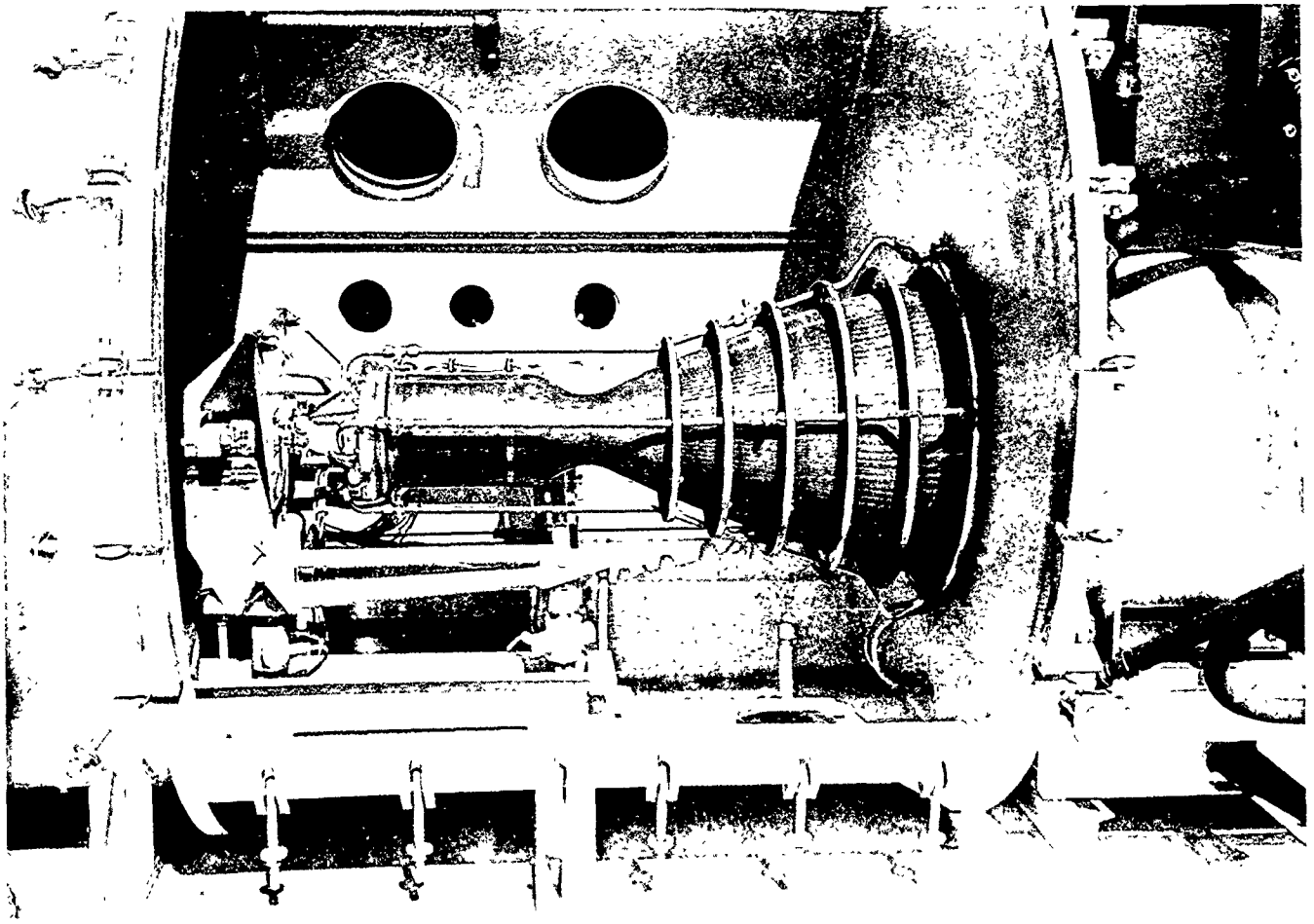


Figure 119. Thrust stand in vacuum chamber with mockup motor

The load cells were vented at the factory and vacuum-filled at JPL with Dow Corning 200 fluid to minimize ingestion of corrosive fumes during operation. Venting the load cells to the ambient vacuum-chamber pressure eliminated zero shift. Since small forces of 50 to 100 pounds were to be measured on load cells of 1000- and 2000-pound range, a typical shift of 6% of load cell range from ambient pressure to vacuum would have the same order of magnitude as the output due to load. Oil-filled stand pipes were used to contain the oil in the vented cells. Dial gages were used to determine cradle movement under calibration load. The axial movement was approximately 0.018 inch for a 6000-pound load. Cradle movement for side loads was approximately 0.001 inch for 110 pounds. An extreme condition during firing might consist of 200 pounds tension on a forward strut and 200 pounds compression on a corresponding rear strut. This would cause a misalignment of only 0.01 degree. The use of high-capacity load cells for small side force measurements thus eliminated thrust stand distortion, but at the expense of data resolution.

The operational ETS instrumentation (RS 5, p 86) was used for thrust stand evaluation, and permitted a resolution of approximately ± 0.5 pounds in the side force measurements. Precision weights (10 and 50 pounds) were used to check the laboratory calibration of the side load cells and the operation of the auxiliary calibrator. The laboratory calibrations were accurate to better than 0.25% and agreed with the field calibration of the load cells in the stand. The auxiliary calibrator was shown to be in error from 0 to 8% because the axis of the calibration cell is fixed, while the link connecting the cell to the dummy motor is flexured at either end. Any misalignment due to deflection of the dummy motor permits application of small side loads to the column of the calibrate cell causing erroneous readings. The auxiliary calibrator will not be usable until it is redesigned with flexures at either end of the calibration cell. No hysteresis was evident in any of the six load cells within the limits of measuring resolution. Repeatability was excellent except that some non-repeatability occurs in the 0- to 10-pound region when calibrating from tension to compression

through the zero point of a load cell. This uncertainty was of the order of ± 1 pound for the front vertical strut, which permitted this type of test.

Initially, it was believed that the two calibrators would permit interaction studies and the setup of a calibration matrix for data correlation. From a practical standpoint, several features prohibited this procedure. As mentioned, the auxiliary calibrator is incorrectly designed. Also, the readout devices for both calibration cells are servo-mechanisms utilizing mechanical counters, repeatable to only ± 1 count, which corresponds to ± 10 pounds on the main calibration cell and ± 1 pound on the auxiliary calibration cell. This resolution combined with the resolution inherent in the six operational load cells is of the same magnitude as the interactions to be determined, especially in the low side-force region expected for normal operation. Further, the auxiliary calibrator yields only sets of conditions instead of permitting force to be applied to one or two cells at a time. By the use of weights, pulleys and wires, 50-pound forces were applied over the axes of each of the five side struts with no indication of cross coupling to any other cell. The more important interaction of main thrust to any specific side force was minimized by proper alignment of the thrust stand. The alignment procedure used insures minimum thrust to side force interaction but does not align the

cradle. This is unimportant so long as the real motor is aligned within the cradle to be parallel to the axis of the main load cell. The dummy motor was optically aligned for initial tests and scribe marks transferred to the chamber wall for prefring alignment of the operational motor. It is estimated that this method of alignment may be in error by as much as ± 0.5 degree. At present, the accuracy with which the true thrust vector angle may be determined will depend primarily upon the accuracy of motor alignment during firing. The final accuracy with which axial thrust can be measured is estimated to be $\pm 0.5\%$.

After completion of the evaluation, a 6000-pound thrust $N_2O_4-N_2H_4$ liquid-rocket engine was tested in the thrust stand and vacuum chamber. All thrust parameters were recorded during this run with no apparent instrumentation failures. Several days after the run, however, two load cells were found to be inoperative due to open circuits in the strain gage bridge. A second firing resulted in two more inoperative load cells. A current investigation indicates severe internal corrosion of the metallic strain gage elements. Apparently moisture of high acid content has entered the load cells through the vented standpipes, either in the form of water or fumes. The thrust stand is currently being used only with an unvented main axial load cell whose output is corrected for zero shift due to ambient pressure conditions.

PROPULSION DIVISION

XII. Liquid Propellant Propulsion

A. Combustion and Injection

G. I. Jaivin

1. Atomization and Injection Hydraulics

In RS 36-4 (Vol II), it was noted that sheet velocity and velocity profile were pertinent variables which may be significant in determining the breakup of liquid sheets. A ballistic trajectory method for evaluating sheet velocities was discussed in RS 36-5 (Vol II). The utilization of a flat plate probe for the determination of velocity profile in the sheet is currently being planned.

The pressure distributions produced by the perpendicular impingement of free liquid jets upon a flat plate have been previously evaluated for three reference streams (CBS 43, 44, 47, and 52). These reference conditions were obtained from jets produced by known flow conditions, i.e., fully developed laminar flow and fully developed turbulent flow, as well as the jet produced by a sharp-edged orifice. These data have proved useful in categorizing jets of unknown dynamic characteristics.

The dynamic-head probe used in the investigation (Ref 85) essentially consists of a small hole in the center of a flat plate. The pressure is measured by a pressure-sensing element bounding one side of a small cavity

located behind the hole in the plate. The pressure distribution resulting from the jet impingement is determined by moving the plate in a plane perpendicular to the stream centerline. Relative to the stream diameter, the hole should be small and the plate large, in order to assure that the flow configuration produced by the impingement of the stream on the plate does not change as the probe is moved from point to point in the pressure field. In that initial set of experiments, the diameter of the probe hole ranged from 0.013 to 0.022 inch.

In the course of some current work, it became evident that certain anomalies existed in the data obtained with the flat plate probe. In particular it was noted that measured pressure distributions were inconsistent with other experimental results; the empirical data obtained with the probe lead to results which indicate that the observed pressures are too high.

In order to explain this effect it was reasoned that, in the presence of a large pressure gradient, the streamline pattern in the region of the hole can become sufficiently disturbed to significantly affect the measured pressure. This phenomenon can be understood when it is realized that any finite hole in the retaining surface will produce some curvature of the streamlines due to removal of the constraining boundary. The streamlines will dip into the hole producing a centripetal force field which tends to

raise the tap pressure above stream pressure. The hole will feel a pressure gradient across it in the direction of flow arising from various flow conditions and the changing curvature of the streamlines at various points inside the hole. The hole integrates these pressures across its entry to give the measured pressure. The measurement inaccuracies resulting from this effect diminish with decreasing hole size. Due to its dependence upon the pressure gradient field, reducing the hole diameter-stream diameter ratio should also be significant in minimizing errors.

Experiments were performed to evaluate the effect of these parameters upon the measured pressure field. Several flat plate probes having different hole sizes were built and run with two different reference jets. The experimental procedure was identical to that described in Reference 85 with the exception of the pressure transducer used. A Statham gage (Model P24-50A-100) was employed rather than a Photocon transducer in order to eliminate the zero shift difficulties previously encountered. No attempt was made to obtain high-frequency response data (i.e., turbulence measurements) during the course of these tests. Figure 120 illustrates the change resulting from decreasing the probe hole diameter from 0.022 to 0.0016 inch for the case of uniform velocity profile jet impingement. The pressure distributions shown in Fig-

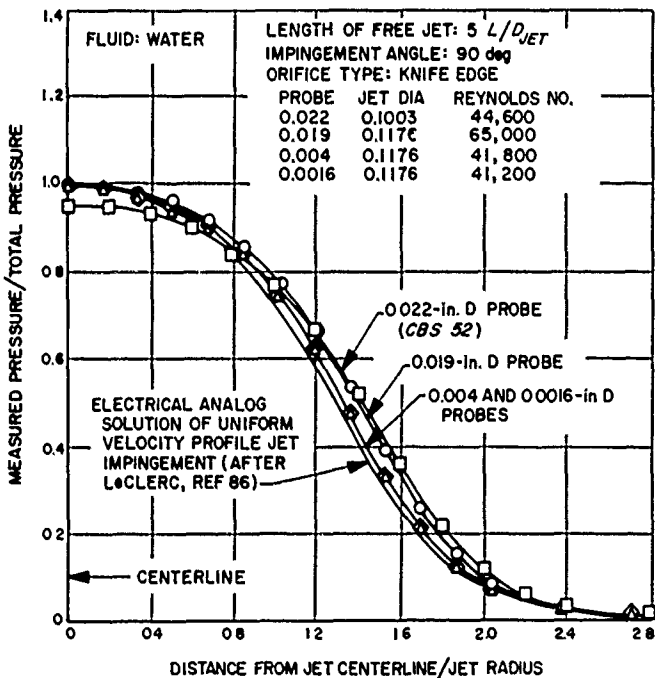


Figure 120. Pressure distribution produced by a free liquid jet with uniform velocity profile, impinging on a flat plate

ure 121 were produced by impingement of a fully developed turbulent profile jet and show the change caused by decreasing the hole diameter from 0.019 to 0.0016 inch. It should be noted that the pressures plotted on the ordinate of the plots have been divided by the centerline stagnation pressure that would be obtained if the jet had a uniform velocity profile.

An electrical analog solution as proposed by LeClerc (Ref 86) has been included in Figures 120 and 121 for comparative purposes, and it is interesting to note the degree of agreement between the analog solution and the other experimental data shown. In Figure 120 the differences noted in the 0.022-inch diameter data may be due to the flow system geometry which, in this case, differed somewhat from that used for the other data shown.

No further change in the pressure profile was noted when the diameter was reduced from 0.004 to 0.0016 inch. Mindful that experimental inaccuracies in probe location become increasingly important when the diameter of the probe hole becomes small, the good reproducibility of the data at these two points lends credence to this experimental result. These data imply that, within the experi-

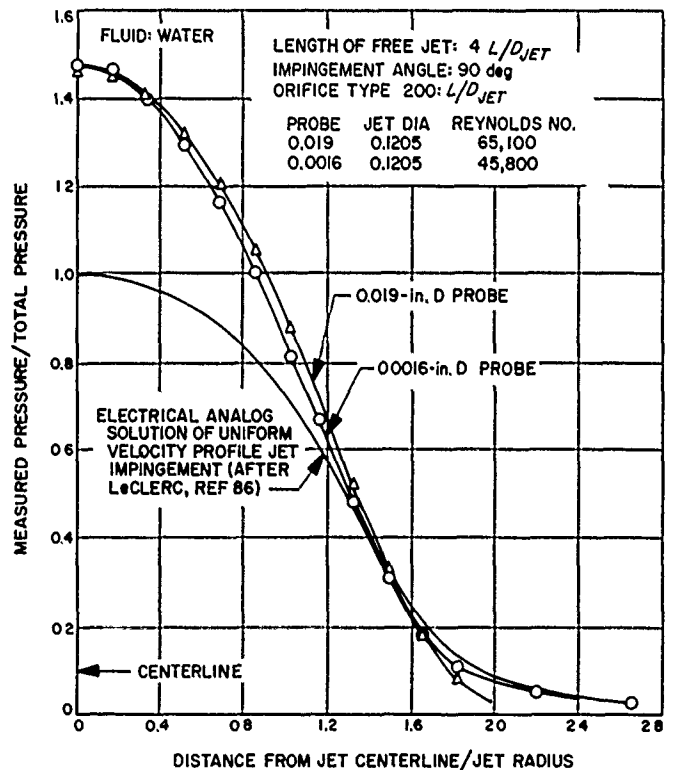


Figure 121. Pressure distribution produced by a free liquid jet with fully developed turbulent profile, impinging on a flat plate

mental accuracy of the measurements, a minimal error is introduced if the hole size is kept below a critical value. In the case of an impinging jet, this critical size would be a function of the jet diameter and the type of jet (since different jets produce different pressure gradient fields).

The use of the flat plate probe seems feasible for use in the liquid sheet investigation if the diameter of the probe hole can be reduced to 0.001 inch and the minimum sheet thickness is approximately 0.025 inch. This sheet thickness is considerably larger than the thickness obtained in the uniform, reproducible sheets produced to date (RS 36-5, Vol II), but it is expected that a modification of the present hardware will result in the desired sheet configuration.

B. Heat Transfer and Fluid Mechanics

A. B. Witte

1. Heat Transfer in Rocket Motors

An experimental investigation of heat transfer in rocket engines is being conducted to determine the effect of injector configuration, thrust-chamber geometry, and operating conditions on the axial heat flux distribution. These tests are being made at chamber pressures between 100 and 300 psia, with hydrazine (N_2H_4) and nitrogen tetroxide (N_2O_4) as bipropellants at a nominal mixture ratio of 1.0. Steady-state experimental values of heat flux are measured calorimetrically by passing cooling water through axially short, circumferential coolant passages which form the thrust-chamber walls. Comparisons between the analytical and experimental values of local heat flux have been made with 1.64-to-1, 4-to-1, and 8-to-1 contraction-area-ratio nozzles and reported in Reference 87.

Recently, calorimetric heat transfer measurements were made on a 1.64-to-1 contraction-area-ratio nozzle (throat dia = 3.9 inches) to determine the effect of change in characteristic combustion chamber length L^* near 200 psia chamber pressure on semi-local values of heat flux. Tests were made at 17.0, 23.6 and 30.1-inch L^* which was accomplished by changing combustion chamber length. An eight-orifice-pair, splash-plate type injector was used. A description of the thrust-chamber operational appara-

tus, the thrust chamber assembly, the injector, and the operating procedure is given in Reference 87. The results of six tests have been tabulated in Table 22 in terms of chamber pressure p_c , mixture ratio r , characteristic velocity c^* , characteristic combustion chamber length L^* , maximum experimental heat flux $q_{max\ expt}$, and the ratio of $q_{max\ expt}$ to calculated maximum analytical heat flux $q_{max\ anal}$. The results indicate that, as expected, c^* increases with increasing values of L^* (a result observed also for a 4-to-1 and an 8-to-1 nozzle reported in Ref 87). The experimental heat flux maxima, which occurred slightly upstream of the nozzle throat, also increased with increasing c^* and L^* . The $q_{max\ anal}$ was based on experimental c^* since both the heat transfer coefficient determined by the method of Reference 88 and the enthalpy difference between the stagnation and wall condition as determined by the method used in Reference 87 are given as a function of c^* . Consequently, to determine the sole effect of these changes of L^* and $q_{max\ expt}$, the heat flux ratio $q_{max\ expt}/q_{max\ anal}$ was calculated. The last column in Table 22 shows that the $q_{max\ expt}/q_{max\ anal}$ values for 17.0 and 23.6-inch L^* indicate random scatter of approximately 4% with no apparent effect of L^* on $q_{max\ expt}/q_{max\ anal}$ at these conditions. The tests at 30.1-inch L^* show values of this ratio about 8% above the average value of the first four tests. An increase of heat flux ratio with an increase in L^* of this magnitude has not been observed previously with other nozzles, and no apparent explanation can be given for this result. Furthermore, the chamber pressures for all tests were within 2% of the average value.

Results of an 8-to-1 and 4-to-1 nozzle operating at 38- and 62.8-inch and 23.7- and 39.7-inch L^* , respectively, were compared in a similar way (Ref 87) to this investigation. The 8-to-1 nozzle showed a decrease of 10 to 20% of the heat flux ratio as L^* was increased from 38.0 to 62.8 inches; however, the 4-to-1 nozzle showed no change of heat flux ratio when L^* was increased from 23.7 to 39.7 inches.

A comparison of all these results seems to indicate that for the particular thrust-chamber geometries tested, the

Table 22. Experimental heat transfer in rocket engines

Test No.	p_c , psia	r	c^* , ft/sec	L^* , in.	$q_{max\ expt}$, Btu/in. ² sec	$q_{max\ expt}$ / $q_{max\ anal}$
6031A	198	1.03	5300	17.0	6.91	1.23
6031B	199	1.02	5280	17.0	7.00	1.26
6102	202	1.01	5300	23.6	7.27	1.28
6103	201	1.06	5420	23.6	7.28	1.23
6105	205	1.04	5460	30.1	8.01	1.34
6106	203	1.04	5450	30.1	8.00	1.35

effect of changes in L^* (aside from the changes in c^* with L^*) had little or no effect on heat flux maxima for the 1.64-to-1 and 4-to-1 contraction-area-ratio nozzles; however, with the 8-to-1 contraction-area-ratio nozzle, changes in L^* significantly affected the heat flux maxima. Since the Mach number at the entrance to the 8-to-1 nozzle is 0.08 compared to 0.24 and 0.4 for the 4-to-1 and 1.64-to-1 nozzles, one may speculate that combustion nonuniformities may well significantly perturb the one-dimensional,

uniform flow at the entrance to the 8-to-1 nozzle. It also seems reasonable to hypothesize that increasing L^* (further separating the injector from the nozzle entrance at a given contraction area ratio) would improve the uniformity of flow at the entrance to the nozzle. This effect would account for the decreasing heat flux maxima with increasing L^* as was observed for the 8-to-1 nozzle but does not explain the reverse trend that apparently occurred for the 1.64-to-1 nozzle.

References

1. Tross, C., "Astronomical Constants and Their Importance in Lunar Trajectory Determination," *Journal of the American Rocket Society*, 30: 938-941, 1960.
2. Magness, T., Space Technology Laboratories, work performed under Space Systems Analysis Study Contract No. 950045, 1961.
3. Herrick, S., Westrom, G., and Makemson, M. W., *Astrodynamic Report No. 5*, University of California, Los Angeles, 1959.
4. Rabe, E., "Derivation of Fundamental Astronomical Constants from the Observations of Eros," *Astronomical Journal*, 55: 112, 1949.
5. Price, R., et al, "Radar Echoes from Venus," *Science*, 129: 751, 1959.
6. Irving, J., *Space Technology*, Chap 10, ed. H. Seifert, John Wiley and Sons, Inc., New York, 1959.
7. Melbourne, W., *Interplanetary Trajectories and Payload Capabilities of Advanced Propulsion Vehicles*, Technical Report No. 32-68, Jet Propulsion Laboratory, Pasadena, March 31, 1961.
8. Kizner, W., *A Method of Describing Miss Distances For Lunar and Interplanetary Trajectories*, External Publication No. 674, Jet Propulsion Laboratory, Pasadena, August 1, 1959.
9. Noton, A. R. M., *Statistical Analysis of Space Guidance Systems*, Technical Memorandum No. 33-15, Jet Propulsion Laboratory, Pasadena, June 15, 1960.
10. Meisenholder, G. W., *An Introduction to the Operation and Testing of Accelerometers*, Technical Memorandum No. 33-2, Jet Propulsion Laboratory, Pasadena, October 3, 1960.
11. Jensen, L. K., Evans, B. H., Clark, R. B., *Evaluation of Precision Gyros for Space Boost Guidance Applications*, presented as ARS 1175-60 at American Rocket Society Semi-Annual Meeting, May 9-12, 1960.
12. *Preliminary Descriptive Material on the GG8001B Miniature Integrating Gyro*, U-ED 9841, Minneapolis Honeywell Aeronautical Division, March 28, 1960.
13. *Preliminary Description Document, GG177 Hinged Pendulous Accelerometer*, U-ED 9870, Minneapolis Honeywell Aeronautical Division, October 6, 1960.
14. Smythe, W., *Static and Dynamic Electricity*, Second Edition, Section 11.14, pp 408-411, McGraw-Hill, New York, 1950.
15. Harding, J. T., *Force and Torque on a Superconducting Ellipsoid in an Axially Symmetric Magnetic Field*, Technical Release No. 34-242, Jet Propulsion Laboratory, Pasadena, February 6, 1961.
16. Laub, J. H., *Hydrostatic Gas Bearings*, Progress Report No. 20-353, Jet Propulsion Laboratory, Pasadena, October 3, 1958.
17. Menyuk, N., and Goodenough, J. B., "Magnetic Materials for Digital-Computer Components. I. A Theory of Flux Reversal in Polycrystalline Ferromagnetics," *Journal of Applied Physics*, 26: 8-18, 1955.
18. Gyorgy, E. M., "Rotational Model of Flux Reversal in Square-Loop Ferrites," *Journal of Applied Physics*, 28: 1011-1015, 1957.
19. Humphrey, F. B., *Journal of Applied Physics*, 28: 284, 1958.
20. Humphrey, F. B., and Gyorgy, E. M., *Journal of Applied Physics*, 30: 935, 1959.
21. Gyorgy, E. M., and Rogers, J. L., *Proceedings of Magnetism Conference*, Boston, AIEE T-91, p 637, 1959.
22. Hagedorn, F. B., "Partial Switching of Thin Permalloy Films," *Journal of Applied Physics*, 30: 254S, 1959.
23. Sarles, F. W., Jr., *A Magneto-Optic Apparatus for the Dynamic Study of Ferromagnetic Surface Domains*, PhD Thesis, Massachusetts Institute of Technology, EE Dept, January 9, 1961.
24. Olson, C. D., and Pohm, A. V., "Flux Reversal in Thin Films of 82% Ni, 18% Fe," *Journal of Applied Physics*, 29: 274-282, 1958.
25. Dietrich, W., Proebster, W. E., and Wolf, P., *IBM Journal of Research*, 4: 189, 1960.
26. Silver, S., *Microwave Antenna Theory and Design*, p 383, McGraw-Hill Book Co., New York, 1949.
27. *Measurement of Relative Phase Shift at Microwave Frequencies*, Engineering Notes, Vol II, No. 1, Huggins Laboratories, Sunnyvale, 1961.
28. Cumming, R. C., "The Serrodyne Frequency Translator," *Proceedings of the IRE*, 45: 175-186, February 1957.
29. Maserjian, J., *A Semiconductor Approach to Microelectronics*, Technical Release No. 34-206, Jet Propulsion Laboratory, Pasadena, December 2, 1960.
30. Robbins, H., Hughes Aircraft Co., personal communication, 1961.
31. Silver, S., *Microwave Antenna Theory and Design*, p 145, McGraw-Hill Book Co., New York, 1949.
32. Tartakovskii, I. B., "Side Radiation from Ideal Paraboloid with Circular Aperture," *Radiotekhnika i elektronika*, 4(No. 6): 920-929, 1959.
33. Singer, J. R., Chairman, *Second International Conference on Quantum Electronics*, University of California at Berkeley, March 23-25, 1961, to be published.
34. Schawlow, A. L., and Townes, C. H., "Infrared and Optical Masers," *Physical Review*, 112: 1940-1949, December 15, 1958.
35. Shannon, C. E., and Weaver, W., *The Mathematical Theory of Communication*, University of Illinois Press, Urbana, 1949.
36. Lorens, C. S., and Viterbi, A. J., *Optimum Filtering*, External Publication No. 633, May 15, 1959.
37. Black, H. S., *Modulation Theory*, Van Nostrand Co., New York, 1953.
38. Woodward, P. M., and Davies, I. L., "Information Theory and Inverse Probability in Telecommunications," *Proceedings of the IEE*, 99(Part III): 37, 1952.
39. Viterbi, A. J., *On Coded Phase-Coherent Communications*, Technical Release No. 32-25, Aug. 15, 1960, to be published in *IRE Transactions on Space Electronics and Telemetry*, March 1961.
40. Zierler, N., "On Decoding Linear Error-Correcting Codes. I," *IRE Transactions of PGIT*, IT6(No. 4): 450-459, September 1960.
41. Zierler, N., "On Decoding Linear Error-Correcting Codes. II," to appear in *Proceedings of the Fourth London Symposium on Information Theory*, 1961.
42. Viterbi, A. J., "On Coded Phase-Coherent Communications," Technical Report No. 32-25, Jet Propulsion Laboratory, Pasadena, August 15, 1960.
43. Lawton, J. G., "Theoretical Error Rates of Differentially Coherent Binary and Kineplex Data Transmission Systems," *Proceedings of the IRE*, 47: 333-334, February 1959.
44. Cahn, C. R., "Comparison of Coherent and Phase Comparison Detection of a Four-Phase Digital Signal," *Proceedings of the IRE*, 47: 1662, September 1959.
45. Glenn, A. B., "Comparison of PSK-AM Versus FSK-AM and PSK Versus FSK Binary Coded Transmissions," *IRE Transactions on Communications Systems*, CS-8(No. 2): 87, June 1960.
46. Doelz, M. L., Heald, E. T., and Martin, D. L., "Binary Data Transmission Techniques for Linear Systems," *Proceedings of the IRE*, 45(No. 5): 656-661, May 1957.

47. Barry, G., and Garabedian, A., *Performance of Predicted Wave Systems in the Presence of Additive, White Gaussian Noise*, Engineering Report No. CER-W592, Collins Radio Co., Newport Beach, Calif., January 29, 1958.
48. Landee, R. W., *A Method of Generating an Unambiguous Local Phase Reference for Data Detection Applications*, Technical Memorandum, Collins Radio Company, December 19, 1960.
49. Coggshall, J. C., and Nybo, R., *Technical Report on the TE-290 Data Terminal Set*, Collins Radio Company, Newport Beach, Calif., 1960.
50. *Performance of Predicted Wave Systems in the Presence of Additive, White Gaussian Noise*, Collins Radio Company, Cedar Rapids, Iowa, January 29, 1958.
51. *Theoretical Comparison of Binary Data Transmission Systems*, Report No. CA-1172-S-1, Cornell Aeronautical Laboratory, Inc., May 1958.
52. *Study and Development Program for an Advanced Telemetry System*, Final Report SEC-4R-1, Space Electronics Corp., Glendale, May 19, 1959.
53. Jaffee, R., and Rechin, E., "Design and Performance of Phase-Locked Circuits of Near Optimum Performance over a Wide Range of Input Signal and Noise Levels," *IRE Transactions on Information Theory*, IT-1: 66-76, March 1955.
54. Davenport, W. B., "Signal-to-Noise Ratios in Band-Pass Limiters," *Journal of Applied Physics*, 24(No. 6): 720-727, June 1953.
55. Andrew, E. R., *Nuclear Magnetic Resonance*, Cambridge University Press, New York, 1955.
56. Roberts, J. D., *Nuclear Magnetic Resonance, Applications to Organic Chemistry*, McGraw-Hill, New York, 1995.
57. Pople, J. A., Schneider, W. G., and Bernstein, H. J., *High-Resolution Nuclear Magnetic Resonance*, McGraw-Hill, New York, 1959.
58. Anderson, W. A., "Nuclear Magnetic Resonance Spectra of Some Hydrocarbons," *Physical Review*, 102: 151-167, 1956.
59. Bloom, A. L., and Shooley, J. N., "Effects of Perturbing RF Fields on Nuclear Spin Coupling," *Physical Review*, 97: 1261-1265, 1955.
60. Kaiser, R., "Double Resonance Technique for Elimination of Proton Spin-Spin Splitting," *Review of Scientific Instruments*, 31: 963-965, 1960.
61. Corio, P. L., "The Analysis of Nuclear Magnetic Resonance Spectra," *Chemical Reviews*, 60: 363-429, 1960.
62. Grateful acknowledgement to Dr. Aksel A. Bothner-By, Assistant Director of Research, Mellon Institute.
63. Nair, P. M., and Roberts, J. D., "Nuclear Magnetic Resonance Spectra," *Journal of American Chemical Society*, 79: 4565, 1957.
64. Shafer, P. R., Davis, D. R., Vogel, Martin, Nagarajan, K., and Roberts, J. D., *Journal of American Chemical Society*, in press.
65. Reilly, C. A., and Swalen, J. D., *Journal of Chemical Physics*, 32: 1378-1385, 1960.
66. Mortimer, F. S., *Molecular Spectroscopy*, 5: 199-205, 1960.
67. Gutowsky, H. S., Karplus, M., and Grant, D. M., *Journal of Chemical Physics*, 31: 1278-1289, 1959.
68. Goldish, E., *Journal of Chemical Education*, 36: 408-416, 1959.
69. Stuart, J. T., "On the Stability of Viscous Flow Between Parallel Planes in the Presence of a Coplanar Magnetic Field," *Proceedings of the Royal Society of London, A*, 221: 189-205, 1954.
70. Cohen, C. B., and Reshotko, E., *Similar Solutions for the Compressible Boundary Layer with Heat Transfer and Pressure Gradient*, NACA Report No. 1293(TN3325), National Aeronautics and Space Administration, Washington, 1956.
71. Hoare, F. E., and Walling, J. C., "An Absolute Measurement of the Susceptibility of Tantalum and Other Metals," *Proceedings of Physical Society, (London)*, 64B: 337-341, 1951.
72. Eatherly, W. P., and McClelland, J. D., "Anisotropic Susceptibility of Polycrystalline Graphite," *Physical Reviews*, 89: 661(L), 1953.
73. Poquet, E., et al, "Etude du diamagnétisme de mono cristaux de graphite," *Journal de Chimie Physique*, 57: 866, 1960.
74. Guha, B. C., and Roy, B. P., "The Principle of Magnetic Susceptibility of Graphite," *Indian Journal of Physics*, 8: 345, 1934.
75. Soule, D. E., Research Laboratories, National Carbon Company, private communication.
76. Brown, A. R. G., and Watt, W., "The Preparation and Properties of High-Temperature Pyrolytic Carbon," *Industrial Carbon and Graphite (Society of Chemical Industry, London)*, p. 86, 1958.
77. Pinnick, H. T., "The Magnetic Susceptibility of Carbons and Polycrystalline Graphites, I," *Physical Review*, 94: 319-326, 1954.
78. Adamson, A. F., and Blayden, D. H., "The Magnetic Susceptibility of Mesomorphous Carbons and Graphites," *Industrial Carbon and Graphite (Soc. of Chem. Industry, London)*, p. 28, 1958.
79. Kirshman, K. S., and Ganguli, N., "The Temperature Variation of the Abnormal Unidirectional Diamagnetism of Graphite Crystals," *Nature*, 139: 155, 1937.
80. Helmerl, G. J., Kurg, I. M., and Inge, J. E., *Tensile Properties of Inconel and RS-120 Titanium-Alloy Sheet under Rapid-Heating and Constant-Temperature Conditions*, NACA TN3731, National Aeronautics and Space Administration, July 1956.
81. Kurg, I. M., *Tensile Properties of AZ31A-0 Magnesium-Alloy Sheet under Rapid-Heating and Constant Temperature Conditions*, NACA TN3752, National Aeronautics and Space Administration, August 1956.
82. Champion, F. C., and Davy, N., *Properties of Matter*, Philosophical Library, New York, 1959.
83. Williams, H. E., *On Hydrostatics with Surface Tension*, Technical Report No. 32-89, Jet Propulsion Laboratory, Pasadena, May 15, 1961.
84. Rupe, J. H., *A Dynamic-Head Probe for Evaluating the Properties of Free Liquid Jets*, Progress Report No. 20-299, Jet Propulsion Laboratory, Pasadena, May 23, 1956.
86. LeClerc, A., *Deflection of a Liquid Jet by a Perpendicular Boundary*, Thesis, Department of Mechanics and Hydraulics, State University of Iowa, Iowa City, 1948.
87. Welsh, W. E., Jr., and Witte, A. B., *Comparison of Analytical and Experimental Local Heat Fluxes in Liquid-Propellant Rocket Thrust Chambers*, Technical Report No. 32-43, Jet Propulsion Laboratory, Pasadena, February 1, 1961.
88. Bartz, D. R., "A Simple Equation for Rapid Estimation of Rocket Nozzle Convective Heat Transfer Coefficients," *Jet Propulsion*, 27(No. 1): 49-51, January 1957.